



HAL
open science

Synthesis of light-harvesting polymeric nanoparticles and their applications in biosensing and bioimaging

Caterina Severi

► **To cite this version:**

Caterina Severi. Synthesis of light-harvesting polymeric nanoparticles and their applications in biosensing and bioimaging. Polymers. Université de Strasbourg, 2021. English. NNT: 2021STRAF018 . tel-04398226

HAL Id: tel-04398226

<https://theses.hal.science/tel-04398226>

Submitted on 16 Jan 2024

HAL is a multi-disciplinary open access archive for the deposit and dissemination of scientific research documents, whether they are published or not. The documents may come from teaching and research institutions in France or abroad, or from public or private research centers.

L'archive ouverte pluridisciplinaire **HAL**, est destinée au dépôt et à la diffusion de documents scientifiques de niveau recherche, publiés ou non, émanant des établissements d'enseignement et de recherche français ou étrangers, des laboratoires publics ou privés.

ÉCOLE DOCTORALE DES SCIENCES CHIMIQUES
Laboratoire de Bioimagerie and Pathologies – UMR 7021

THÈSE présentée par :

Caterina SEVERI

soutenue le : 31 mai 2021

pour obtenir le grade de : **Docteur de l'université de Strasbourg**
Discipline/ Spécialité : Chimie/ Chimie moléculaire – chimie supramoléculaire

**Synthèse de nanoparticules polymères
fluorescentes récolteuses de lumière et
leurs applications dans la biodétection
et la bioimagerie**

THÈSE dirigée par :

M. KLYMCHENKO Andrey
M. CHABERT Philippe

Directeur de recherches CNRS, Université de Strasbourg
Ingénieur de Recherche CNRS, Université de Strasbourg

RAPPORTEURS :

Mme. ISHOW Eléna
M. MONNEREAU Cyrille

Professeur, Université de Nantes
Maître des conférences, ENS de Lyon

AUTRES MEMBRES DU JURY :

M. GAUTIER Arnaud

Professeur, Sorbonne Université

Acknowledgements

First and foremost, my deepest gratitude goes to my supervisor, Dr. Andrey Klymchenko for his guidance during the pursuit of my PhD; his great knowledge, positive attitude and unwavering support helped me to overcome the challenges I faced during these three years. Thanks to him I learned an invaluable amount of knowledge about science and research.

Dr. Philippe Chabert is acknowledged for his help in translating the part in French of this thesis.

I would like to thank the jury members, Prof. Eléna Ishow, Prof. Cyrille Monnereau and Prof. Arnaud Gautier for accepting my request to evaluate this work.

My thanks go to everyone in the UMR 7021 whom I had the pleasure to work with, I am especially grateful to Dr. Andreas Reisch for his help with polymer chemistry, Dr. Mayeul Collot for his insights in organic synthesis and Dr. Jurga Valanciunaite for helping me with fluorescence microscopy and FCS setups. I am grateful to the PACSI team for NMR and mass analysis and to Dr. Corinne Crucifix from the FRISBI platform for helping me with TEM characterization. Many thanks to Ingrid Barthel and Marlyse Wernert for their kindness and help.

I am grateful to all the postdocs and PhD students with whom I collaborated. My thanks go to Dr. Bogdan Andreiuk and Dr. Nina Melnychuk for teaching me nanoparticle preparation and characterization techniques. I want also to thank Prof. Tero Soukka, Dr. Julie Karpenko and Dr. Yosuke Niko for their collaboration and fruitful discussion on the projects reported in this work.

My thanks go to my friends and labmates: Alex, Kyong, Rajhans, Sasha, Anil, Liliia, Tania, Raphaël, Francesco, Sophie, Vitalii, Masashi, Hanna, Stefano, Ilya, Mario, Antoiine, Lazare, Paraskevi, Viola, Gianluca, Elisabete, Rémi and Lucie; thank you for all the fun we had in the lab and outside.

A big thanks too goes to my family and my friends back in Italy who supported me from afar.

This work was done thanks to the financial support of European Research Council ERC Consolidator grant BrightSens 648528. École doctorale des Sciences Chimiques is acknowledged for the formation provided during my doctorate.

–Caterina

Déclaration sur l'honneur *Declaration of Honour*

J'affirme être informé que le plagiat est une faute grave susceptible de mener à des sanctions administratives et disciplinaires pouvant aller jusqu'au renvoi de l'Université de Strasbourg et passible de poursuites devant les tribunaux de la République Française.

Je suis conscient(e) que l'absence de citation claire et transparente d'une source empruntée à un tiers (texte, idée, raisonnement ou autre création) est constitutive de plagiat.

Au vu de ce qui précède, **j'atteste sur l'honneur que le travail décrit dans mon manuscrit de thèse est un travail original et que je n'ai pas eu recours au plagiat ou à toute autre forme de fraude.**

I affirm that I am aware that plagiarism is a serious misconduct that may lead to administrative and disciplinary sanctions up to dismissal from the University of Strasbourg and liable to prosecution in the courts of the French Republic.

I am aware that the absence of a clear and transparent citation of a source borrowed from a third party (text, idea, reasoning or other creation) is constitutive of plagiarism.

*In view of the foregoing, **I hereby certify that the work described in my thesis manuscript is original work and that I have not resorted to plagiarism or any other form of fraud.***

Nom : Prénom : SEVERI Caterina

Ecole doctorale : ED222

Laboratoire : Laboratory of Bioimaging and Pathologies

Date : 25/06/21

Signature :

Contents

<i>Acknowledgements</i>	3
<i>Contents</i>	6
<i>List of used abbreviations</i>	8
<i>General introduction</i>	10
Chapter 1. Bibliographical overview	12
1.1. Fluorescence: principles and techniques	12
1.1.1. Basics of fluorescence.....	12
1.1.2. Quenching and excitation energy transfer.....	17
1.1.2.1. Kinetics aspects.....	17
1.1.2.2. Energy transfer.....	18
1.1.3. Fluorescence single-molecule techniques	22
1.1.3.1. Fluorescence correlation spectroscopy.....	22
1.1.3.2. Fluorescence microscopy	23
1.2. Fluorescent dyes and nanoparticles	25
1.2.1. Organic dyes	26
1.2.2. Fluorescent proteins	26
1.2.3. Quantum Dots	27
1.2.4. Upconversion nanoparticles.....	28
1.2.5. Carbon dots	30
1.2.6. Dye-based nanoparticles	30
1.2.6.1. Strategies for preventing dye self-quenching	31
1.2.6.2. Dye-doped silica nanoparticles	35
1.2.6.3. Conjugated polymer nanoparticles (PDots)	36
1.2.6.4. Dye-loaded polymeric nanoparticles.....	37
1.3. Fluorescence signal amplification in biosensing	41
1.3.1. Chemical signal amplification strategies.....	41
1.3.2. Optical signal amplification using nanomaterials	43
1.4. Fluorescence smartphone-based detection	46
1.4.1. Principles of smartphone-based detection.....	46
1.4.2. Smartphone-based spectrometers.....	49
1.4.3. PoC assays and microfluidics	50
1.4.4. Fluorescence sensors for biomarkers based on a smartphone.....	51
1.4.5. Smartphone-enabled fluorescence microscopy.....	57
1.5. Specific targeting of fluorescent nanomaterials	62
1.5.1. Ligand approach.....	62
1.5.2. Molecularly imprinted polymer (MIP) approach	66
1.5.2.1. Preparation techniques of nanoMIPs.....	68
1.5.2.2. NanoMIPs for targeted imaging applications.....	70
<i>Aim of this PhD work</i>	76
Chapter 2. Results and discussion	78
2.1. New dyes inside NPs: Synthesis of green-emitting nanoparticles for smartphone assisted detection of nucleic acids	78

2.1.1.	Article 1. Smartphone-assisted detection of nucleic acids by light-harvesting FRET-based nanoprobe.....	82
2.2.	New counterions inside NPs: Synthesis of dye-loaded nanoparticles using a family of lanthanide-based counterions	83
2.2.1.	Article 2 (manuscript). Lanthanide-based bulky counterions for preparation of highly fluorescent dye-loaded polymeric nanoparticles	86
2.3.	Design of NPs surface for specific targeting.....	105
2.3.1.	Synthesis of PEGylated nanoparticles for the targeting of lipids and proteins	105
2.3.1.1.	Synthesis of stealth nanoparticles	106
2.3.1.2.	Synthesis of targeting nanoparticles.....	107
2.3.2.	Synthesis of nanoparticles with a protein like surface and investigation of their potential targeting abilities	112
2.3.2.1.	Synthesis of polymers grafted with amino acids.....	112
2.3.2.2.	Preparation and characterization of AA-decorated NPs.....	115
2.3.2.3.	Investigation of the effects of high salinity in nanoparticle formation.....	120
Chapter 3.	Conclusions and perspectives.....	123
Chapter 4.	Materials and methods	126
4.1.	Materials	126
4.1.1.	Chemicals.....	126
4.1.1.1.	Dyes	127
4.1.1.2.	Counterions	128
4.1.1.3.	Polymers	128
4.1.1.4.	Dye salts.....	141
4.1.1.5.	Clickable PEG derivatives	143
4.1.2.	Oligonucleotides	144
4.2.	Methods.....	145
4.2.1.	Nanoparticles preparation	145
4.2.1.1.	DNA nanoprobe preparation	145
4.2.1.2.	Nanoparticle surface functionalization via Cu-free click chemistry	147
4.2.2.	Nanoparticles characterization	147
4.2.3.	Fluorescence microscopy.....	148
4.2.3.1.	Immobilization protocols	149
4.2.3.2.	Data treatment of microscopy images.....	149
4.2.4.	Transmission electron microscopy.....	150
4.2.5.	Cellular studies.....	150
4.2.5.1.	Cell culture.....	150
4.2.5.2.	Apoptosis protocol	150
4.2.5.3.	Cytotoxicity assays	150
4.2.5.4.	Flow cytometry	151
4.2.5.5.	Fluorescence microscopy on cells.....	151
4.2.6.	Calculation of limit of detection (LOD) and limit of quantification (LOQ)	152
4.3.	NMR spectra.....	153
	Résumé de la thèse en français	169
	References.....	185
	List of publications	201
	List of presentations	201

List of used abbreviations

AA	Amino acid	ESA	Excited-state absorption
ACQ	Aggregation caused quenching	ETU	Energy transfer upconversion
AIE	Aggregation induced emission	EWG	Electron withdrawing group
APBA	Acetyl phenylboronic acid	FBS	Fetal Bovine Serum
API	1-(3-aminopropyl)imidazole	FCS	Fluorescence correlation spectroscopy
ATRP	Atom transfer radical polymerization	FP	Fluorescent protein
BCN	Bicyclononyne	FR	Folate receptor
Boc	Tert-Butyloxycarbonyl	FRET	Förster resonance energy transfer
CBT	Carbetocin	GFP	Green fluorescent protein
CD	Carbon dot	GPCR	G-protein coupled receptor
CI	Counterion	HER2	Human epidermal growth factor receptor 2
CMC	Critical micellar concentration	HOBt	Hydroxybenzotriazole
CMOS	Complementary metal–oxide–semiconductor	HOMO	Highest unoccupied molecular orbital
CR	Cross relaxation	HRP	Horseradish peroxidase
CSU	Cooperative sensitization upconversion	IC	Intersystem crossing
DBCO	Dibenzocyclooctyne-amine	ICG	Indocyanine green
DCM	Dichloromethane	IFAST	Immiscible phase filtration assisted by surface tension
DIPEA	N,N-Diisopropylethylamine	IR	Infrared
DMAP	4-Dimethylaminopyridine	LAMP	Loop-mediated isothermal amplification
DMEM	Dulbecco's Modified Eagle Medium	LED	Light-emitting diode
DMF	Dimethylformamide	LOD	Limit of detection
DMSO	Dimethyl sulfoxide	LOQ	Limit of quantification
DLS	Dynamic light scattering	LUMO	Lowest unoccupied molecular orbital
dPCR	Digital polymerase chain reaction	MIP	Molecularly imprinted polymer
eDHFR	Escherichia coli dihydrofolate reductase	miRNA	Micro RNA
EDG	Electron donor group	MNP	Magnetic nanoparticle
EGF	Epidermal growth factor	MTT	3-(4,5-dimethylthiazol-2-yl)-2,5-diphenyltetrazolium bromide
EGFR	Epidermal growth factor receptor	NA	Nucleic acid
EISPT	Excited-state intramolecular proton transfer	NADP⁺	Nicotinamide adenine dinucleotide phosphate
ELISA	Enzyme-linked immunosorbent assay		

NP	Nanoparticle	UCNP	Upconverting nanoparticle
OTR	Oxytocin receptor		
PB	Phosphate buffer		
PBA	Phenylboronic acid		
PBS	Phosphate buffered saline		
PCR	Polymerase chain reaction		
PDot	Polymer dot		
PEG	Polyethylene glycol		
PEI	Polyethylenimine		
PEMA-MA	Poly(ethyl methacrylate)-co methacrylic acid		
PFBT	Poly(9,9-dioctylfluorene-alt- benzothiadiazole)		
PLGA	Poly(lactic-co-glycolic acid)		
PMMA-MA	Poly(methyl methacrylate)-co methacrylic acid		
PNA	Peptide nucleic acid		
PoC	Point of care		
PVP	Polyvinylpyrrolidone		
QD	Quantum dot		
QY	Quantum yield		
RAFT	Reversible addition-fragmentation chain-transfer		
RBC	Red blood cell		
RCA	Rolling circle amplification		
RGB	Red green blue		
RGD	Arg-Gly-Asp		
ROI	Region of interest		
SA	Sialic acid		
TAC	Tetrameric antibody complex		
TCS	Target competitive sequence		
TEM	Transmission electron microscopy		
TEOS	Tetraethoxysilane		
TFA	Trifluoroacetic acid		
TICT	Twisted intramolecular charge transfer		
TIRF	Total internal reflection fluorescence		
TMP	Trimethoprim		
TPB	Tetraphenylborate		

General introduction

The subject of the present work is fluorescent dye-loaded polymeric nanoparticles applied to sensing and bioimaging. Nanomaterials are complex systems whose properties arise not only from the substance(s) they are composed of, but also from their nanometric size by virtue of quantum confinement effects or the increased surface to volume ratio, to nominate a few. Fluorescence-based biosensing is a quite complex and multidisciplinary field too; requiring knowledge in: (i) synthetic chemistry and photophysics of fluorescent reporters; (ii) molecular biology, cell biology and nanotechnology for predicting and understanding the interactions of nanomaterials within a biological environment and efficiently designing the surface of the nanoprobe in order to obtain a spectral change upon a biomolecular recognition event; (iii) physics, optics and statistics for constructing a sensor and developing a robust data analysis workflow.

Most frequently, the focus is usually done on one of the multiple aspects that designing a fluorescent nanoreporter entails. However there still is an intimate connection between all the multiple subjects comprising the problem, making it impossible to separate in neat domains of expertise the phases of the conception of a fluorescent biosensing nanoprobe.

It is therefore clear that any work dealing with a multidisciplinary subject on nanoparticle based fluorescent probes will touch on many different fields.

In this exploratory work we aimed towards a sort of “all-encompassing approach” towards the conception of new probes based on dye-loaded polymeric nanoparticles. The first part of this work is therefore more focused on the design of nanoparticles with specific photophysical properties, namely color, brightness and FRET properties through rational design of fluorescent dyes and bulky counterions. The search for new dyes allowed to develop biosensors compatible with RGB camera of a smartphone, while new counterions added new functionalities to the particle core attractive for multimodal imaging. The second part is focused on applying these fluorescent nanomaterials in a biological context, this section being centered more on cellular studies and the rational design of nanoparticles surface to ensure a biological activity.

These two aspects of nanoprobe design cannot exist one without the other, for a nanoparticle-based fluorescent sensor requires both optimal photophysical properties and an

appropriate surface in order to interact as needed with the surrounding biological environment and provide the desired spectroscopic response.

Chapter 1. Bibliographical overview

1.1. *Fluorescence: principles and techniques*

1.1.1. *Basics of fluorescence*

Photoluminescence is the phenomenon of light emission by a material upon absorption of light (Lakowicz and Masters, 2008). Photoluminescent molecules are called *fluorophores*. After absorbing one photon, the fluorophore transitions from its energetic ground state (S_0) to an excited singlet state, either S_1 or S_2 depending on the energy of the absorbed photon, then the molecule quickly relaxes to the lowest vibrational level of S_1 via an *internal conversion* (IC) process. At this point the system has several deactivation paths: the transition $S_1 \rightarrow S_0$ is spin-allowed and can be either radiative (*fluorescence*) or a non-radiative relaxation. Otherwise, if the singlet and triplet excited states are close in energy, the intersystem crossing process will be favoured, and the system will then return to the ground state through a spin-prohibited transition $T_1 \rightarrow S_0$ either by *non-radiative decay* or by emitting a photon (*phosphorescence*).

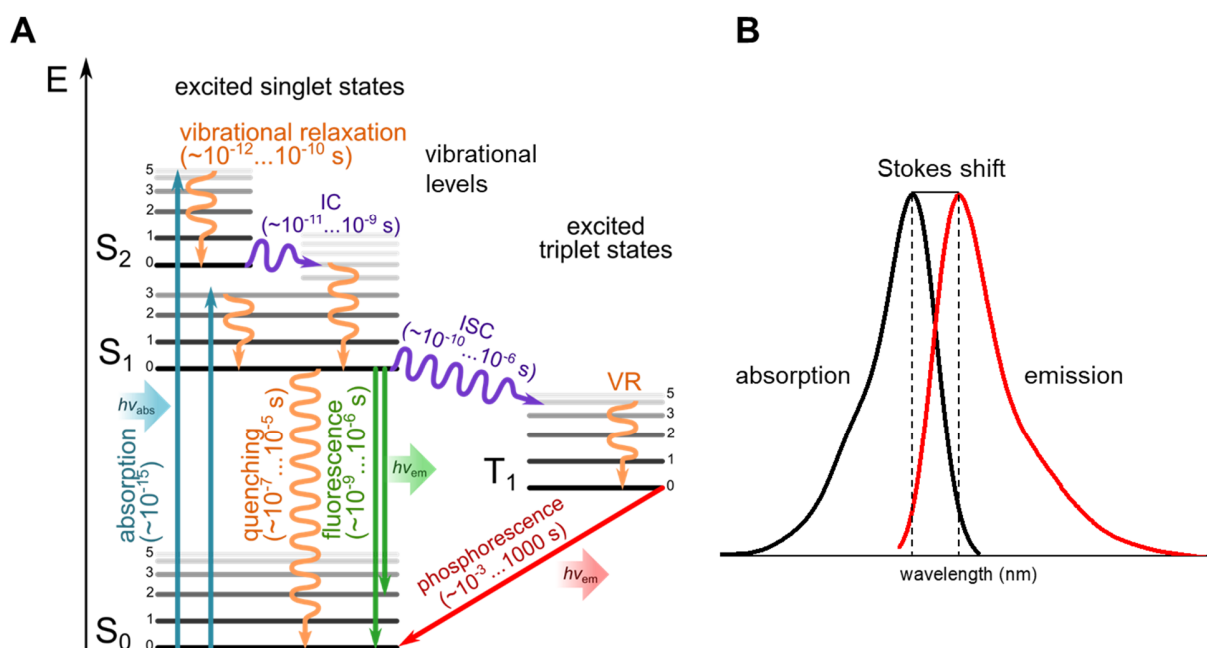


Figure 1.1 (A) The Jablonski diagram is used for illustrating the electronic transitions a fluorophore can undergo upon absorption of a photon. (B) Stokes shift is a phenomenon related to vibrational relaxation of the fluorophore.

1.1. Fluorescence: principles and techniques

Phosphorescence being a spin-forbidden process has a longer lifetime in respect to fluorescence; molecules featuring heavy atoms (such as heavy metals or bromine and iodine) due to a strong spin-orbit coupling tend to have higher rates for ISC and thus display phosphorescence.

Internal conversion, being the quickest among all the processes a fluorophore can undergo (Figure 1.1A), makes so that all further deactivation processes will always start from the lowest vibrational level of the lowest excited state (S_1) (*Kasha's rule*). This results in the emission spectrum being independent from the excitation wavelength and since a part of the excitation energy is always lost due to IC the emission peak being always shifted towards longer wavelengths in respect to the absorption (*Stokes shift*) (Figure 1.1B). The vibrational structure of the electronic levels results in both emission and absorption spectra broadening as absorption can start and end from/in different vibrational levels, and the emission process can land on vibrational levels higher than 0 (Figure 1.1A).

Organic fluorophores are generally molecules featuring aromatic groups and/or extensive π -conjugated systems (Figure 1.2). Conjugation lowers the energy gap between the highest occupied molecular orbital (HOMO) and the lowest-unoccupied molecular orbital (LUMO) and therefore only molecules with large delocalized orbitals have energy gaps small enough to fall in the visible range. Some fluorophores, especially the ones bearing electron donating (EDG) or electron withdrawing groups (EWG) display absorption and emission shifts as a function of the solvent polarity. This phenomenon is called *solvatochromism* can be either *bathochromic* (or *positive solvatochromism*), *i.e.* the shift is towards longer wavelengths upon increase of solvent polarity, or *hypsochromic* (or *negative solvatochromism*), *i.e.* the shift is towards shorter wavelengths. Compounds whose ground states have a separation of charge exhibit negative solvatochromism due to the higher ground state stabilization offered by polar environments compared to apolar ones (which results in a blue shift). Since biological systems feature a multiplicity of environments with different polarity, solvatochromic dyes are employed as probes to study the local polarity or changes in it, such as reorganization of membranes or binding of proteins (Klymchenko, 2017).

1. Bibliographical overview

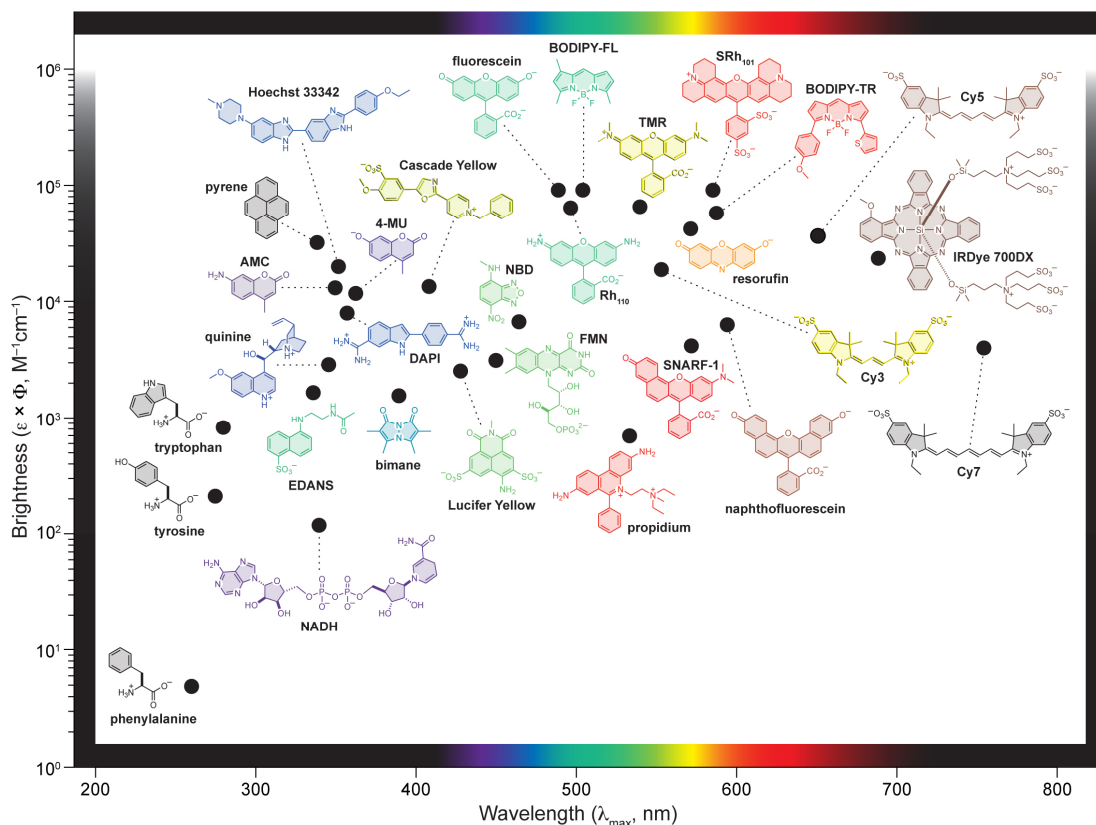


Figure 1.2 Most commonly used fluorescent dyes. Image adapted from: <https://www.janelia.org/lab/lavis-lab/research>.

Two important quantities associated to every fluorophore are the *molar absorption coefficient* and the *fluorescence quantum yield*.

Molar absorption coefficient (ϵ) defines the intrinsic ability of a fluorophore to absorb light at a given wavelength. Absorbance (A) is the light absorbed by a sample and it is proportional to the molar absorption coefficient, the concentration of the absorbing specie (c) and the length of the optical pathway (b) according to the Beer-Lambert law:

$$A = \epsilon \cdot b \cdot c \quad (1.1)$$

Fluorescence quantum yield (Φ) is defined as the ratio between the photon emitted over the photon absorbed. An analogous definition can be made in terms of kinetic rate constants of deactivation processes:

$$\Phi_r = \frac{k_r}{k_r + k_{nr}} \quad (1.2)$$

1.1. Fluorescence: principles and techniques

Where k_r is the deactivation constant for the radiative process, while k_{nr} is the constant for every non-radiative deactivation process, which could be a photoreaction (*photobleaching*) or a non-radiative relaxation, which in turn can be either vibrational or rotational. The vibrational relaxation is a deactivation path always available to a fluorophore, and it becomes preponderant when molecules have long and flexible groups. This is the reason cyanine 7 has a lower quantum yield than cyanine 3: the longer π -conjugated bridge has more vibrational deactivation pathways available in respect to the shorter one cy3 has (Figure 1.2). Moreover, dyes with a simple carbon-carbon bond connecting two big moieties are particularly susceptible to a rotational deactivation. This class of compounds is called *molecular rotors*. They are not fluorescent in non-viscous environments; however, in viscous solution, the solid state, or in any other situation in which the bond rotation is hindered (*e.g.* if the probe is bound in a receptor pocket) the rotational deactivation pathway is not available anymore, therefore the quantum yield increases (Klymchenko, 2017; Yang et al., 2014).

Fluorescence lifetime is a measure of the average time a fluorophore spends in the excited state. The decay processes follow a negative exponential kinetic equation:

$$S_1(t) = S_1(0) \cdot e^{-kt} \quad (1.3)$$

The lifetime of a molecule τ is defined by the time taken by a population of excited fluorophores to decrease its number of a factor e . From this definition it is possible to derive a formula for τ exclusively as a function of the kinetic rate constant of the deactivation processes.

$$\tau = \frac{1}{k_r + k_{nr}} \quad (1.4)$$

From this expression it is immediately clear that in presence of non-radiative deactivation pathways the lifetime decreases. Fluorescence lifetime can be used as a useful indication for the presence of quenching species (molecular oxygen being one of the most common quenchers in biological environments).

Fluorescence anisotropy refers to the phenomenon by which electronic transition dipole moments in fluorophores possess a specific direction. Fluorescence anisotropy is defined as:

$$r = \frac{I_{\parallel} - I_{\perp}}{I_{\parallel} + 2I_{\perp}} \quad (1.5)$$

1. Bibliographical overview

I_{\parallel} and I_{\perp} are the emission intensities parallel and perpendicular to the polarization of the excitation source. In ordinary fluorescence measurements the excitation light is not polarized, therefore this phenomenon is not immediately evident. However, if an ensemble of fluorophores is illuminated by polarized light, only the molecules whose dipole transition moment is aligned with the excitation (*photoselection*) will actually get excited. If the emitting species are free to rotate, the polarization is quickly lost and the light emission will not possess any polarization, generally, small molecules in fluid solution have fluorescence anisotropy values close to 0. On the other hand, if the fluorophore rotates at a timescale larger than the emission process, the preferential direction is maintained and the fluorescence anisotropy increases (Figure 1.3). For these reasons, fluorescence anisotropy-based techniques can provide valuable information about the viscosity of the probe environment, or whether the probe is bound to large objects, such as proteins or particles.

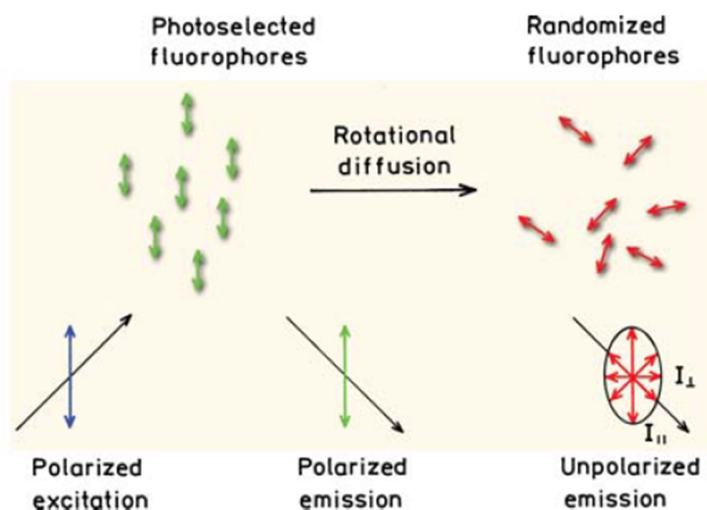
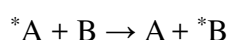
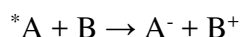
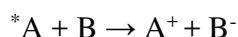


Figure 1.3 Influence of the fluorophore rotation on the polarization of the emission. Image adapted from: (Lakowicz and Masters, 2008).

1.1.2. *Quenching and excitation energy transfer*

As discussed in the previous section, the excited state of a fluorophore can decay by itself through *intramolecular* paths. However, under certain conditions, the excited state *A can deactivate by interacting with another compound B. The two main interaction modes between the two species are the *energy transfer* and the *electron transfer*.



These processes are also called *quenching* processes because they are in competition with the radiative deactivation process of *A , and therefore in practice they quench its fluorescence. Electron transfer can result in either an oxidation or reduction of the fluorophore A, while energy transfer results in generation of the excited state *B of the quenching species B which will then undergo other deactivation processes. If *B decays by fluorescence it is said that B emission is *sensitized* by A.

1.1.2.1. *Kinetics aspects*

Quenching can occur by two mechanisms, which are governed by different kinetic laws: *static* and *dynamic* quenching. Dynamic quenching occurs when the lifetime of *A is sufficiently long for it to diffuse in solution and encounter a quencher molecule B. It is a bimolecular process and it is governed by the *Stern-Volmer equation*.

$$\frac{\tau^0}{\tau} = 1 + \tau^0 k_q [B] \quad (1.6)$$

Which expresses the ratio of the lifetime of *A in absence and presence of B (τ^0 and τ) as a function of the constant of the quenching process k_q and the concentration of B, the product $\tau^0 k_q$ is also called Stern-Volmer constant (k_{sv}).

In static quenching at a certain concentration of B a certain fraction A will be already associated to B, the amount of the complex A-B is determined by the constant of association (k_{ass}). In this situation the complex A-B will not be fluorescent (and therefore quantum yield of the system

1. Bibliographical overview

will decrease), however, the free fraction of A will possess the same lifetime τ^0 of the unquenched fluorophore. Fluorescence lifetime analysis can therefore easily distinguish between the two.

1.1.2.2. *Energy transfer*

Energy transfer can take place with different mechanisms: *radiative* and *nonradiative*. Radiative energy transfer involves the emission of a photon from *A and the reabsorption by B, this is also called *trivial energy transfer* and its efficiency does not depend on the distance between the fluorophore pair, but only on the concentration of B, the optical path length and the spectral overlap between A emission and B absorption. A radiative energy transfer process will not change the lifetime of the donor, but it will result in the loss of donor fluorescence where the acceptor absorbs, such distortion of the donor emission spectrum is called *inner filter effect*.

Nonradiative transfer occurs without the emission of photons, and it is the result of multiple interaction mechanisms, such as: long-range dipole interaction (coulombic, or Förster's mechanism) (Figure 1.4A), short-range multipolar interactions, electron exchange (Dexter-like mechanism) (Figure 1.4B) and charge resonance interactions. It is a process strongly dependent on the distance, and it usually occurs at distances less than 10 nm (Balzani et al., 2014).

Dexter energy transfer, also called Dexter-electron exchange, is an energy transfer process by which the electron in the LUMO of *A jumps in the LUMO of B, at the same time one electron in the HOMO of B jumps in the HOMO of *A , leaving *B in an excited state and quenching A (Figure 1.4B). This energy transfer mechanism depends on the spectral overlap of the dye pair and it required orbital overlap to occur. Therefore, it is strongly dependent on the distance between dyes and it usually does not occur for distances superior to 20 Å.

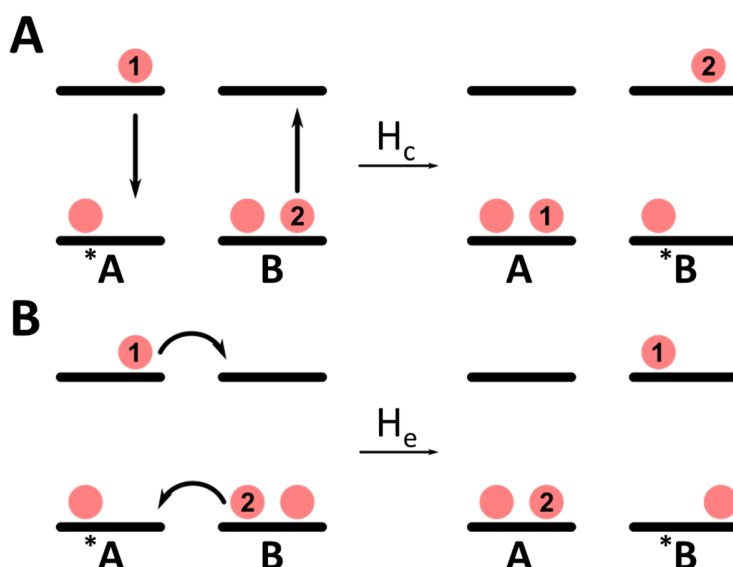


Figure 1.4 Possible mechanisms for energy transfer. (A) Coulombic mechanism, also called resonance energy transfer. (B) Exchange mechanism, also called Dexter-like.

Förster Resonance Energy Transfer (FRET) as discussed before, is a nonradiative energy transfer process occurring through long-range dipole-dipole interaction. The FRET rate constant can be expressed with the following equation:

$$k_{FRET} = 8.8 \cdot 10^{-25} \frac{K^2 \phi}{n^4 r_{AB}^6 \tau} J_F \quad (1.7)$$

Where K^2 is an orientation factor which can range from 0 to 4. Generally, for randomly oriented fluorophores it is equal to $2/3$, if the partners are perpendicular the value equals 0 and no dipole-dipole interaction occurs, while the biggest interaction is achieved when the dipoles are oriented head-to-tail ($K^2 = 4$). ϕ and τ are respectively the fluorescence quantum yield and fluorescence lifetime of the donor in absence of acceptor. n is the solvent refractive index, r_{AB}^6 is the distance (in Å). J_F is the *Förster overlap integral* between the fluorescence spectrum of the donor and the absorbance spectrum of the acceptor:

$$J_F = \frac{\int F(\lambda) \varepsilon(\lambda) \lambda^4 d\lambda}{\int F(\lambda) d\lambda} \quad (1.8)$$

1. Bibliographical overview

From this equation, it is immediately clear that the more the emission spectrum of the donor and the absorption spectrum of the acceptor overlap, the more efficient is the FRET process (Figure 1.5A)

The expression for k_{FRET} can be rewritten to regroup most of the terms of expression 1.7:

$$k_{FRET} = \frac{1}{\tau} \left(\frac{R_0}{r_{AB}} \right)^6 \quad (1.9)$$

Where R_0 is a quantity called *Förster radius* and it represents the distance for which the energy transfer efficiency is equal to 50%, typical values for R_0 are in the range of 2-6 nm.

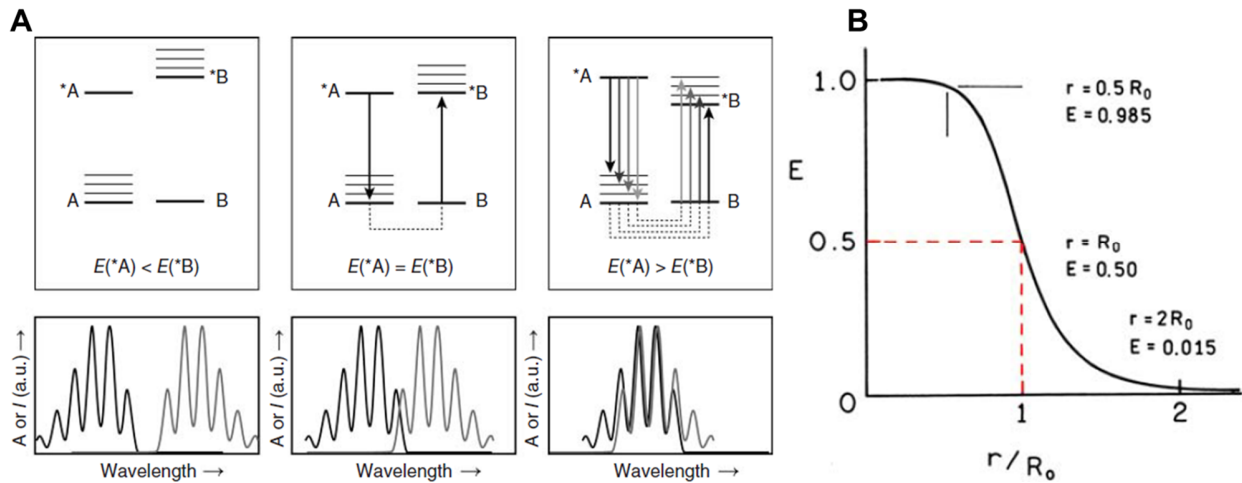


Figure 1.5 (A) There is a relationship between the energy levels of the donor-acceptor pair and the spectral overlap. (B) FRET efficiency as a function of the ratio between the pair distance and the Förster radius. Images adapted from: (Balzani et al., 2014; Lakowicz and Masters, 2008).

FRET efficiency (E) can be expressed as the ratio between the photons transferred to the acceptor and the total photons absorbed by the donor:

$$E = \frac{k_{FRET}(r)}{\tau^{-1} + k_{FRET}(r)} \quad (1.10)$$

Combining the 1.9 and 1.10 equations it is possible to obtain an expression for E in terms of R_0 and r_{AB} :

$$E = \frac{R_0^6}{R_0^6 + r_{AB}^6} \quad (1.11)$$

1.1. Fluorescence: principles and techniques

The dependence on r_{AB}^{-6} causes Förster Resonance Energy Transfer to be a process decaying very quickly for values $r_{AB} > R_0$ (Figure 1.5B), due to this FRET has been extensively used as a “molecular ruler”, to study the conformation of nucleic acids (Preus and Wilhelmsson, 2012) and interaction between proteins (Fernández-Dueñas et al., 2012).

Experimentally, there are several routes to measure FRET efficiency; E might be expressed as a function of the donor emission:

$$E = 1 - \frac{I_D^A}{I_D} \quad (1.12)$$

Where I_D^A and I_D are the donor intensities respectively in presence and absence of the acceptor, it should be noted that both terms have to be normalized by their absorption to avoid errors in the calculation linked to the difference in concentration between the two samples, moreover, the two quantities should also be recorded in the exactly the same experimental conditions.

As previously mentioned, the decrease in fluorescence intensity due to energy transfer is generally followed by a decrease in the donor fluorescence lifetime, therefore E can be calculated by measuring the donor lifetimes:

$$E = 1 - \frac{\tau_D^A}{\tau_D} \quad (1.13)$$

Where τ_D^A and τ_D are the donor lifetimes in presence and absence of acceptor, respectively. Expression 1.13 has the advantage that lifetimes are independent from fluorophore concentration; therefore, this calculation method is less prone to errors in respect to expression 1.12. On the other hand, if the donor has multiple lifetimes this formula is not applicable anymore.

E might also be expressed as a function of the acceptor emission:

$$E = \frac{I_A^D \cdot A_A^A - I_A^A \cdot A_A^D}{I_A^A \cdot A_D^D} \quad (1.14)$$

Where I_A^D and I_A^A are the acceptor emission upon respectively donor and acceptor excitation, A_A^A is the absorption of the acceptor at the acceptor excitation wavelength and A_A^D and A_D^D are the absorbance of respectively acceptor and donor at the donor excitation wavelength.

1. Bibliographical overview

Lastly, the semi-empirical FRET ratio has been widely used in literature:

$$E^{rel} = \frac{I_A}{I_D + I_A} \quad (1.15)$$

Since this ratio does not depend exclusively on the efficiency of the FRET process, but also on the quantum yields of donor and acceptors, this expression should not be used quantitatively, but only for monitoring qualitatively relative changes in FRET efficiency in the same system.

1.1.3. *Fluorescence single-molecule techniques*

While ensemble fluorescence measurements are useful and routinely used both inside and outside research laboratories, their intrinsic limitation lies in the fact that the measured property is always an average of a large number of emitting species. Single-molecule techniques can help to bridge this knowledge gap.

1.1.3.1. *Fluorescence correlation spectroscopy*

Fluorescence correlation spectroscopy (FCS) is the most common single molecule spectroscopy technique. Usually it is performed in solution on fluorescent species that are free to diffuse. A laser beam is focused in solution and the emission of the fluorophores in the *confocal volume* is recorded (Figure 1.6A). The size of the illumination spot is quite small (in the order of hundreds of nanometers), therefore, only a small number of emitters will be present in the confocal volume at any given time. With the diffusion of the fluorophores some will enter the illumination spot while others will exit it, meaning that the total fluorescence intensity recorded will fluctuate (Figure 1.6B). These fluctuations of intensity depend on the number of fluorophores in the confocal volume (which is directly proportional to their concentration) and their size. Autocorrelation analysis is performed on the acquired fluorescence traces and from the autocorrelation curves it is possible to obtain the emitting species diffusion coefficient (Figure 1.6C).

1.1. Fluorescence: principles and techniques

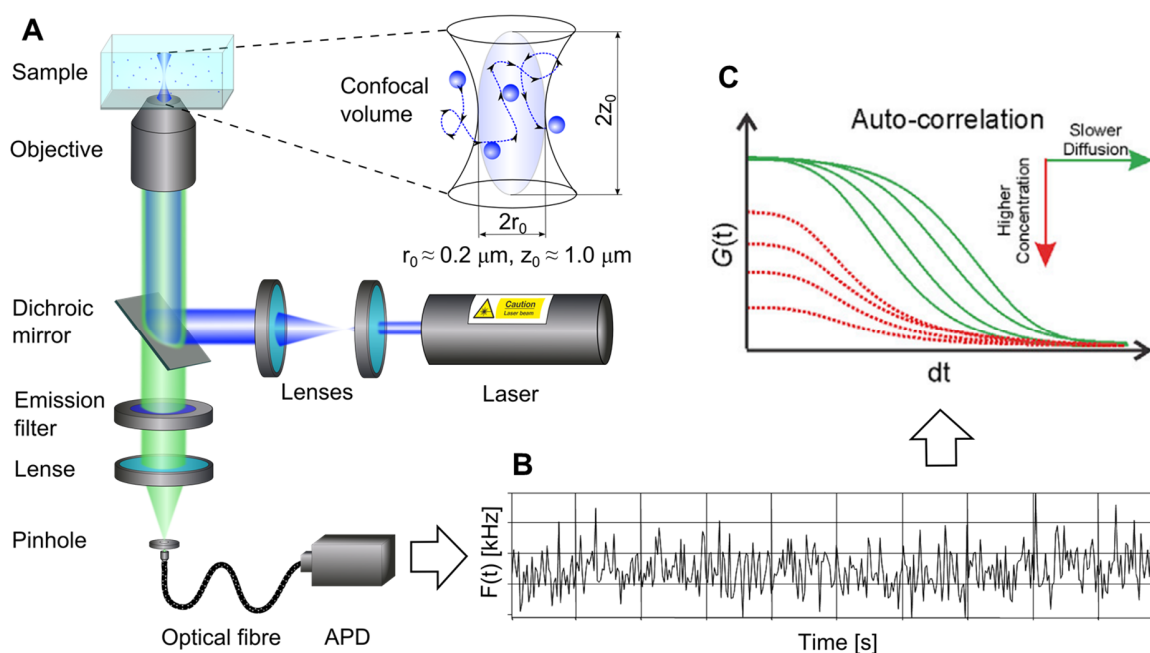


Figure 1.6 FCS working principle. (A) In a typical confocal FCS configuration a laser beam is focused in a very small volume of the sample (also called *confocal volume*). (B) The fluorescence fluctuations caused by the species entering and exiting the confocal volume are recorded. Images adapted from: (Koyanov and Butt, 2012). (C) The autocorrelation curve of the fluorescence trace recorded varies according both to the size and the concentration of fluorescent species. Image adapted from (Liu et al., 2015).

FCS is a powerful technique in biological settings due to the high number of processes that change the diffusion coefficient of fluorophores, such as: DNA hybridization (Schwille et al., 1997), protein interactions, mobility of labelled species on plasma membrane, ligand-receptor binding (Lippincott-Schwartz et al., 2001). More generally, FCS is useful in the study of fluorescent nanomaterials too, since it can provide information about the size, concentration and brightness (Wöll, 2014).

1.1.3.2. Fluorescence microscopy

Imaging single molecules can be achieved with single-molecule microscopy techniques (Coelho et al., 2013). Single-molecule microscopy represented a major step forward in the world of bioimaging and biosensing, offering insights on biological processes that would otherwise be inaccessible by ensemble measurements.

Wide-field epifluorescence microscopy is by far the simplest and most commonly used technique in bioimaging. The instrumental setup consists of illuminating the sample with a light source through an objective and collecting the resulting fluorescence signal. As seen in Figure

1. Bibliographical overview

1.7A, the illumination volume is relatively large (Moerner and Fromm, 2003), with the consequence that even fluorescent species outside of the focal plane contribute to the recorded fluorescence. Thus, to achieve a high signal to noise ratio with this technique, it is necessary to operate at high dilution of fluorescent species.

Total internal reflection fluorescence (TIRF) microscopy is a technique in which the sample is illuminated with a laser beam at an angle greater than the critical angle of reflection (B), resulting in the total internal reflection between the thin glass surface (where the sample is deposited) and the medium covering the sample. This phenomenon produces an *evanescent field*: a stationary electromagnetic field localized in close proximity of the glass surface. The sample is therefore excited by this evanescent field only very close to the reflecting surface, eliminating the background fluorescence of the out of focus emitters (Figure 1.7B).

Epifluorescence and TIRF microscopy yield valuable information in the study of fluorescent nanomaterials, like single macromolecules and nanoparticles, like brightness, photostability and their homo/heterogeneity (Kondo et al., 2017).

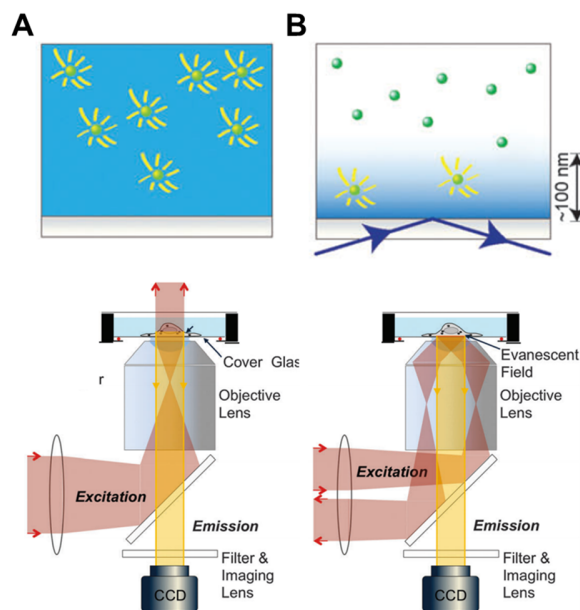


Figure 1.7 (A) Epifluorescence microscopy. Top: illumination scheme. Bottom: optical setup. (B) TIRF microscopy. Top: illumination scheme. Bottom: optical setup. Images adapted from: (Coelho et al., 2013) and (Park et al., 2015)

1.2. *Fluorescent dyes and nanoparticles*

In bioimaging applications there are several requirements a fluorescent probe should fulfil.

Brightness is defined as:

$$B = n \cdot \varepsilon \cdot \phi \quad (1.16)$$

Where ε is the molar absorption coefficient, ϕ is the quantum yield and n is the number of individually emitting fluorophores per probe. Higher brightness allows collecting more photons, therefore improving the signal-to-noise ratio.

Quantum yield. A high quantum yield (QY) is not only desirable because the brightness of the system is directly proportional to it, but also because if ϕ is high, then alternative relaxation processes –such as photobleaching– will be less probable.

Absorption and fluorescence wavelengths. The fluorescent probe should be compatible with excitation sources commonly used in fluorescent-based measurement setups. While imaging cells and tissues wavelength longer than 460 nm should be used in order to avoid cell autofluorescence. If deep tissue penetration is needed, then the optimal excitation window is in the near infra-red (NIR) region. Fluorescence emission should be sufficiently separated from its absorption in order to avoid light-scattering effects.

Photostability. This key characteristic for a fluorescent probe is usually expressed in number of photons emitted before photobleaching. Indeed, every fluorophore eventually photobleaches; this is due to the high reactivity of the excited state. Molecular oxygen can interact with triplet state of organic dyes to photobleach them. Organic fluorophores generally display limited photostability, while inorganic nanoparticles (NPs) such as quantum dots and upconversion nanoparticles feature a much higher photostability. High photostability allows longer and/or stronger illumination, improving the signal to noise ratio.

Blinking. While in some cases blinking might be a desirable characteristic (*i.e.* in single molecule localization microscopy), in most contexts it decreases the signal-to-noise ratio. Moreover, for single-particle tracking applications it renders more difficult the tracking.

Size. A probe of large size can pose a host of problems in a bioimaging context. If the probe is attached to a targeting group and its size is too large, this might have consequences on its

1. Bibliographical overview

targeting specificity. In addition, a fluorescent label of too large size might have issues diffusing in a complex biological environment, leading to inhomogeneous staining.

1.2.1. *Organic dyes*

As briefly mentioned before, fluorescent organic dyes are an indispensable tool in bioimaging and biosensing. They find large usage in cellular staining and in the study of the properties and processes in biological environments (Lakowicz and Masters, 2008; Lavis and Raines, 2008). Their small size allows their incorporation in biological structures such as DNA helix (Wilhelmsson, 2010), plasma membrane (Klymchenko and Kreder, 2014; Shynkar et al., 2007) and various organelles (Danylchuk et al., 2021) with minimal perturbation on the cell activity.

Fluorescent dyes that respond to stimuli in the environment (*e.g.* changes in polarity, presence of oxygen, local viscosity) are called *sensors* or *probes*, while fluorophores that do not are *labels*. Generally, fluorophores with rigid skeletons, such as *rhodamines*, *fluoresceins* and *cyanines*, feature high quantum yields due to the scarcity of vibrational relaxation pathways and very little dependence of their optical properties from the surrounding environment. Meanwhile, as discussed before, dyes bearing charge separation, such as –Nile Red, Prodan and Laurdan– are known to be solvatochromic (Klymchenko, 2017). Another class of compounds responsive to polarity are dyes able to undergo an *excited state intramolecular proton transfer* (EISPT), such as 3-hydroxyflavones (Klymchenko et al., 2004). Molecular rotors are sensitive to the environment viscosity due to the *twisted intramolecular charge transfer* (TICT), occurring while the molecule is in the excited state (Haidekker and Theodorakis, 2007). Molecular flippers have been employed as mechanosensors (Dal Molin et al., 2015), while pyrene dyes, known to form stable excimers which have radically different spectroscopical properties in respect to the monomeric excited dye, have been employed in the sensing of ions (Sivaraman et al., 2014; Zhao et al., 2016). A large palette of molecular probes have been developed for a variety of scopes: pH (Qi et al., 2015), temperature (Chandrasekharan and Kelly, 2001), oxygen (Papkovsky and Dmitriev, 2013), etc.

1.2.2. *Fluorescent proteins*

In terms of photophysical properties, fluorescent proteins (FPs) have similar characteristic to organic dyes. Their structure consists essentially of an organic fluorophore surrounded by a

1.2. Fluorescent dyes and nanoparticles

peptidic barrel (Figure 1.8A), which both protects it from quenching from other molecules and it fixes its conformation, maintaining its quantum yield high (Cranfill et al., 2016; Giepmans, 2006). Historically, the first fluorescent protein to be sequenced and cloned was a *green-fluorescent protein* (GFP) from the jellyfish *Aequorea victoria* (Prasher et al., 1992).

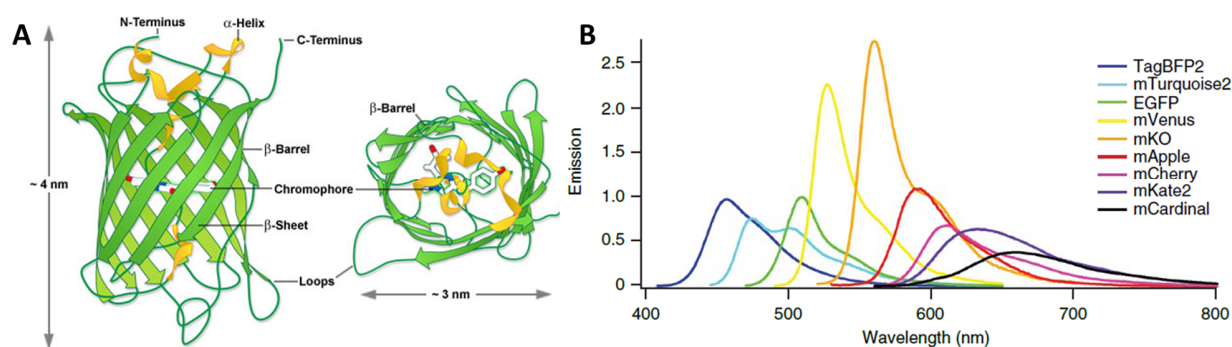


Figure 1.8 (A) Green-fluorescent protein from *A. victoria* structure. Image adapted from: <http://zeiss-campus.magnet.fsu.edu/articles/probes/jellyfishfps.html>. (B) Emission spectra of some commonly used fluorescent proteins. Image adapted from: (Cranfill et al., 2016).

Nowadays a vast library of FPs covering the whole visible spectrum is available (Cranfill et al., 2016) (Figure 1.8B). Fluorescent proteins are most commonly used to label proteins and monitor their expression. This is achieved by transfecting cells with plasmids containing sequences corresponding to the target protein and the fluorescent protein.

1.2.3. Quantum Dots

Quantum Dots (QDs) are nanometric semiconductor crystals, with sizes typically in the 2-20 nm range. The most used materials for QDs are metal chalcogenides (such as CdS, CdSe, CdTe, ZnS, PbS). Bulk semiconductors have two distinct energy bands: a *valence band* occupied by electrons, and a *conduction band* that is unoccupied. At the nanoscale, due to the small number of atoms composing the QD, these levels become discrete, and therefore the bandgap of the nanomaterial is wider than the bulk material (Figure 1.9B). The width of the bandgap is dependent on the composition, the shape and the size of the nanocrystal: QD sizes in the previously mentioned range allow obtaining bandgaps falling in the visible (Figure 1.9C-D) (Alivisatos, 1996, 2004). Upon absorption of light one electron gets excited in the conduction levels, forming an electron-hole pair. While in bulk material the pair can easily dissociate, in QDs it is confined, increasing the probability of recombination and the emission of a photon (Michalet, 2005).

1. Bibliographical overview

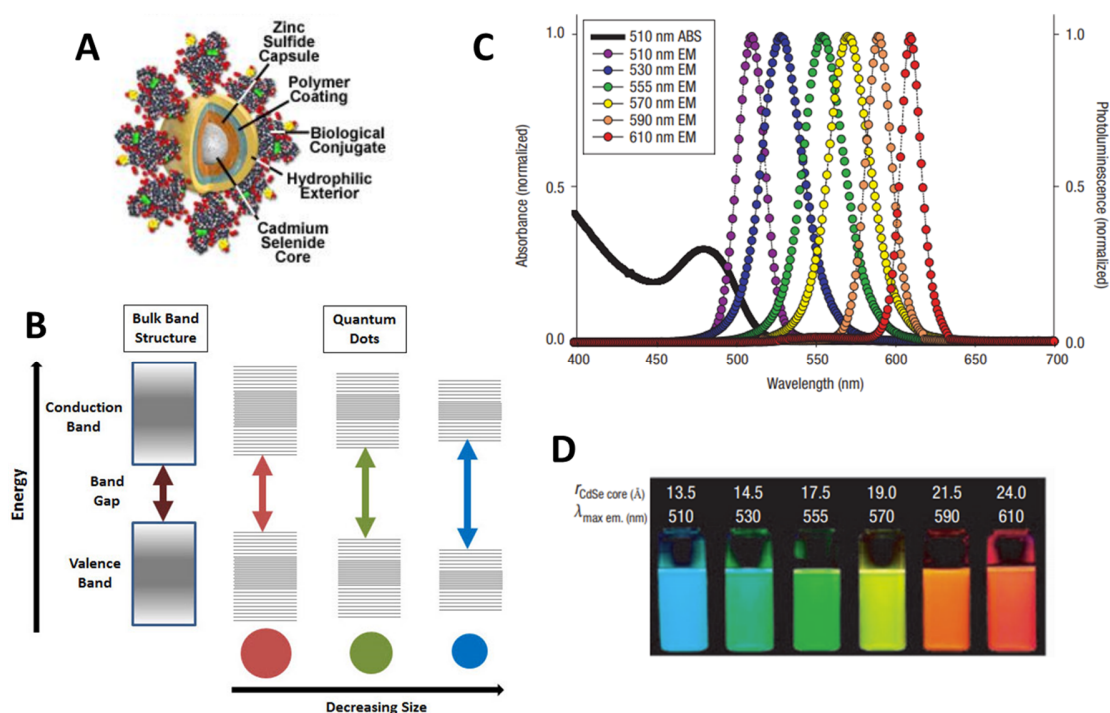


Figure 1.9 (A) Structure of a coated Quantum Dot. Image adapted from: <https://www.olympus-lifescience.com/> (B) Energy levels in the bulk material vs the nanostructured material. Image adapted from: <https://www.sigmaaldrich.com> (C) Emission spectra of CdSe QDs of different sizes. (D) Photography of the samples reported in (C) Images adapted from: (Medintz et al., 2005).

QDs are ideal candidates for bioimaging, due to their high molar absorption coefficients (10^5 - $10^7 \text{ M}^{-1}\text{cm}^{-1}$), high quantum yields (0.3-1), narrow emission band profile (Figure 1.9C) and high photostability. However, their blinking behaviour (*i.e.* the rapid switching between emissive and nonemissive states) poses some limitations (Kuno et al., 2000).

Furthermore, most of the compounds QDs are constituted of are highly toxic; and therefore, to be employed in a biological setting they need to be coated (Hardman, 2006). Usually this is achieved by coating the particle with surfactants, silica shell or polymer. This coating can bear further synthetic handles to attach any biologically active compound needed.

1.2.4. Upconversion nanoparticles

Upconversion nanoparticles (UCNPs) are a class of nanomaterials which features and anti-stokes emission behaviour. Their size does not exceed the 100 nm. They are a host-guest system, composed of an inert matrix (typically NaYF_4 and NaGdF_4) doped with lanthanide ions (Figure

1.2. Fluorescent dyes and nanoparticles

1.10A), in part *sensitizer ions* (the most commonly employed being Yb^{3+} due to its strong absorption at 980 nm) in part *emitter ions* (typically Er^{3+} , Tm^{3+} and Ho^{3+}). UCNPs absorb red and NIR light to emit at shorter wavelength through a wealth of nonlinear processes (Figure 1.10B-C) (Chen et al., 2014).

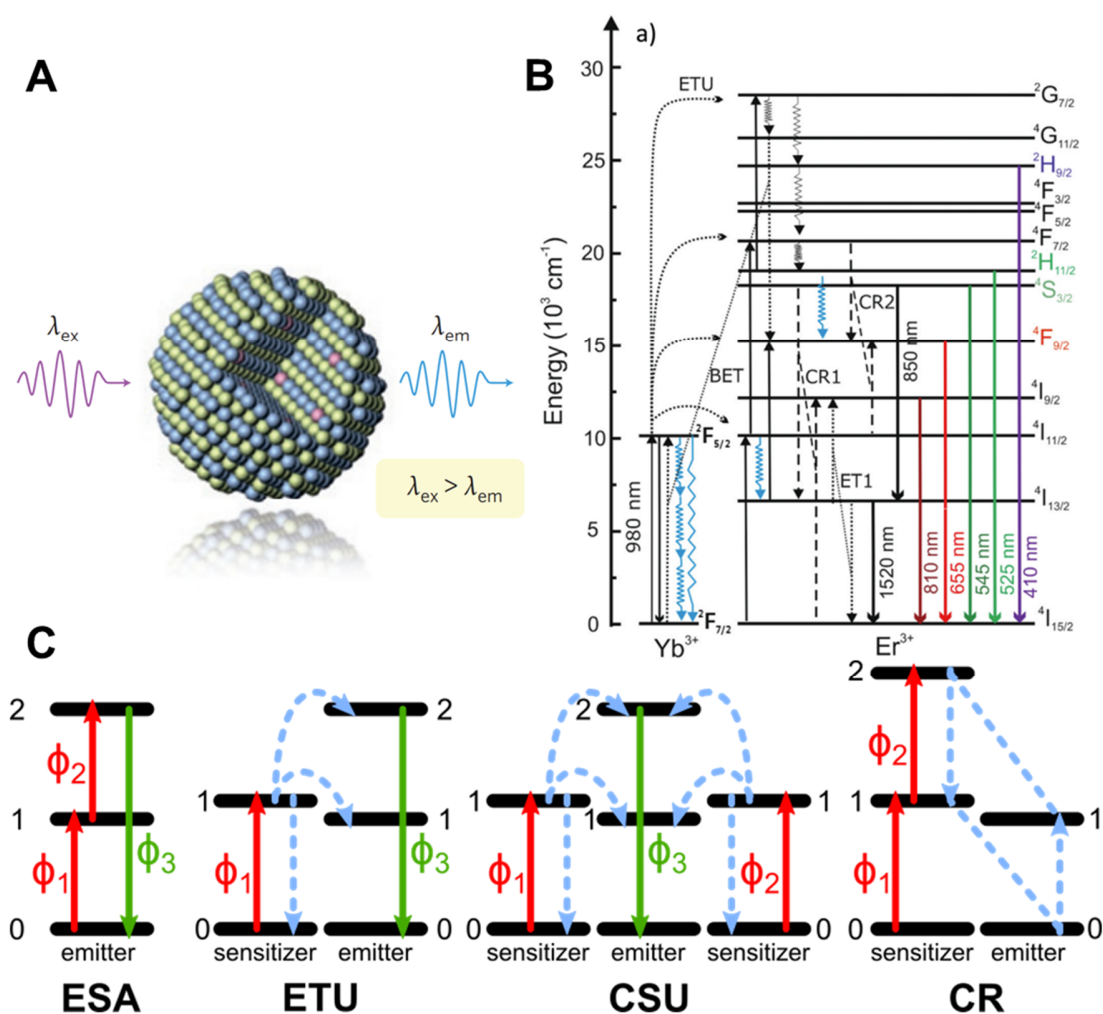


Figure 1.10 (A) Scheme of an upconverting nanoparticle. Image adapted from: (Zhou et al., 2015). Scheme of all the electronic transitions which lead to emission in a $\text{Yb}^{3+}/\text{Er}^{3+}$ UCNP. Image adapted from: (Würth et al., 2017). (C) Scheme of all the possible mechanism which lead to upconversion.

Excited-state absorption (ESA) is the successive absorption of two photons by the same ion, this process is made possible by the fact that lanthanide ions feature a very complex electronic structure with multiple energy levels close to each other due to f orbitals being occupied and long fluorescence lifetimes due to the forbidden nature of their electronic transitions.

1. Bibliographical overview

Energy transfer upconversion (ETU) is the process by which the sensitizer ion transfers its excitation energy to an excited state of the emitter.

Cooperative sensitization upconversion (CSU) is a process analogous to ETU, but it involves three ions simultaneously: two sensitizer ions transfer their excitation energy to the emitter.

Cross relaxation (CR) is a non-radiative process by which an ion can decay from a higher energy state to an intermediate state and in the process excite a nearby ion to a higher energy level as well.

Due to their unique optical properties, UCNPs found an application in several different fields. In bioimaging they feature several desirable characteristics, such as the possibility to be excited in the NIR, to which biological tissues are transparent to, their high photostability, the narrow emission bands and the absence of blinking behaviour (Zhou et al., 2015).

1.2.5. *Carbon dots*

Carbon dots (CDs), also called *carbon quantum dots*, are small fluorescent clusters of carbon (with sizes below 10 nm) containing small variable fractions of oxygen and nitrogen. The origin of their fluorescence is in part the same as QDs (hence the name *carbon quantum dots* being sometimes used): the discretization of the energy levels when the material is composed of only few atoms leads to the energy bandgap to fall into visible, which leads to a dependence of the emission wavelength on the size of the CD; however it is believed that most of the fluorescence is due to the electron-hole recombination on the surface of the CDs, this explains why CDs are quenched both by donor and acceptor groups and the increase in QY when their surface is coated (Luo et al., 2013). There are two viable synthetic routes for preparing CDs, *top-down* approaches such as exfoliation or laser ablation of graphite (Lim et al., 2015) or *bottom-up* routes, like the pyrolysis of small organic molecules (one of the most popular being citric acid) (Zhai et al., 2012). In terms of photophysical properties they are quite photostable, feature good quantum yields and have been used in multiple bioimaging applications (Dong et al., 2012; Lim et al., 2015).

1.2.6. *Dye-based nanoparticles*

Dye-based NPs designate a class of compounds where organic dyes are in some way confined in a nanoparticle. This strategy is useful to increase the brightness of fluorescent

1.2. Fluorescent dyes and nanoparticles

nanomaterials, due to the possibility confining up to thousands (Trofymchuk et al., 2017) fluorophores per nanoparticle. Another point of interest is the possibility of obtaining nanoparticles of virtually any color, since a vast choice of organic fluorophores is available.

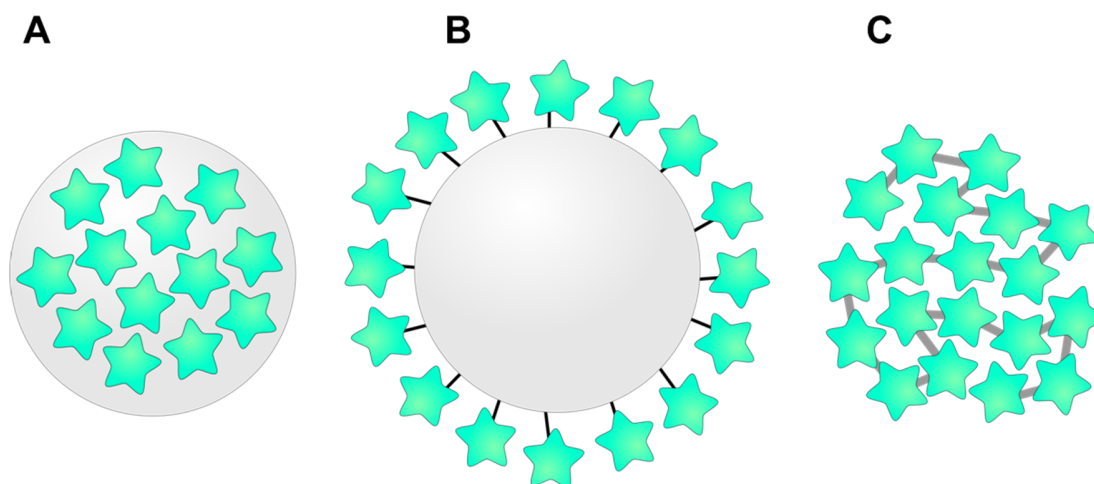


Figure 1.11 Viable strategies of confining fluorophores within a nanoparticle. (A) In dye-loaded nanoparticles fluorophores are encapsulated inside the NP matrix. (B) Fluorophores can be grafted on the surface of NPs. (C) Conjugated polymer nanoparticles (PDots) contain the fluorescent group in the polymer backbone.

Fluorophores can be contained within the NPs in different ways: encapsulated inside the nanoparticle matrix (Figure 1.11A), grafted on its surface (Figure 1.11B), or by employing a fluorescent polymer in the nanoparticle formulation (C). Sometimes the distinction between the adjectives *dye-doped* and *dye-loaded* is done, and it lies mostly on the dye concentration achievable in the nanoparticle, with dye-doped nanoparticles featuring generally lower amount of fluorophores in respect to dye-loaded NPs.

The most widespread materials of choice for dye-based nanoparticles are silica and polymer; both of them are hydrophobic, non-toxic and with easy to functionalize surfaces, making them ideal candidates for bioimaging applications.

1.2.6.1. *Strategies for preventing dye self-quenching*

In the case of fluorescent NPs encapsulating dyes a common problem is the fluorophores undergoing *aggregation-caused quenching* (ACQ), also called *self-quenching*, a phenomenon by which dyes in close proximity quench each other's fluorescence, limiting the overall brightness of the system. Several strategies have been developed to avoid this phenomenon, the most

1. Bibliographical overview

straightforward being the use of *aggregation induced emission* (AIE) dyes, which –as the name might suggest– do not quench but rather enhance emission of dyes in close proximity with each other (Hong et al., 2011; Zhang et al., 2014) (Figure 1.12).

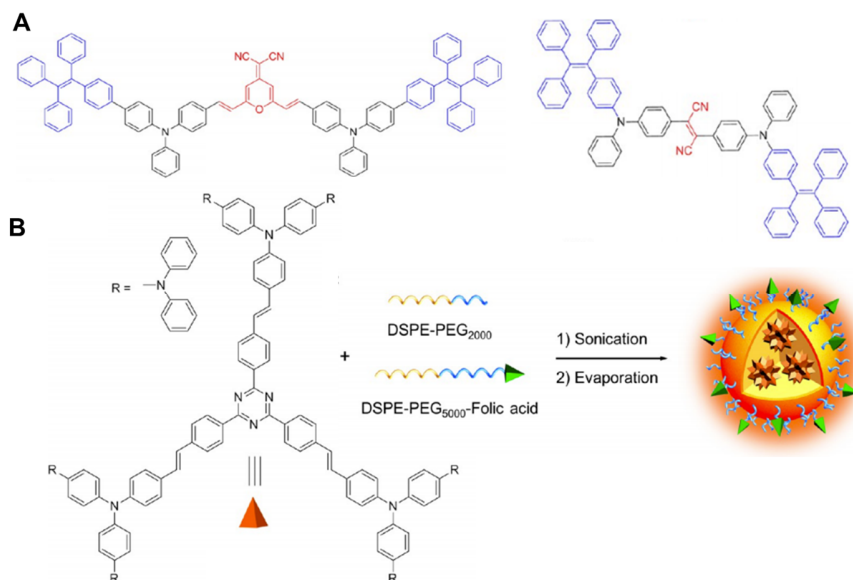


Figure 1.12 (A) Most AIE dyes possess simple carbon-carbon bonds, upon aggregation their rotation is hindered and the radiative deactivation pathway becomes preponderant. (B) Preparation scheme of an AIE dye-loaded nanoparticles. Images adapted from: (Ding et al., 2013).

Another viable approach is the encapsulation of bulky dyes. Fluorophores have been functionalized with bulky groups that prevent their π -stacking (and thus self-quenching). This strategy has been successfully applied on BODIPY dyes and perylene bisimides (Schmidt et al., 2019; Trofymchuk et al., 2019, 2014; Zhang et al., 2017). Recently, another way to space fluorophores not requiring any covalent chemistry has been presented and it relies on the employment of bulky spacers to prevent the fluorophore to come in close proximity.

1.2. Fluorescent dyes and nanoparticles

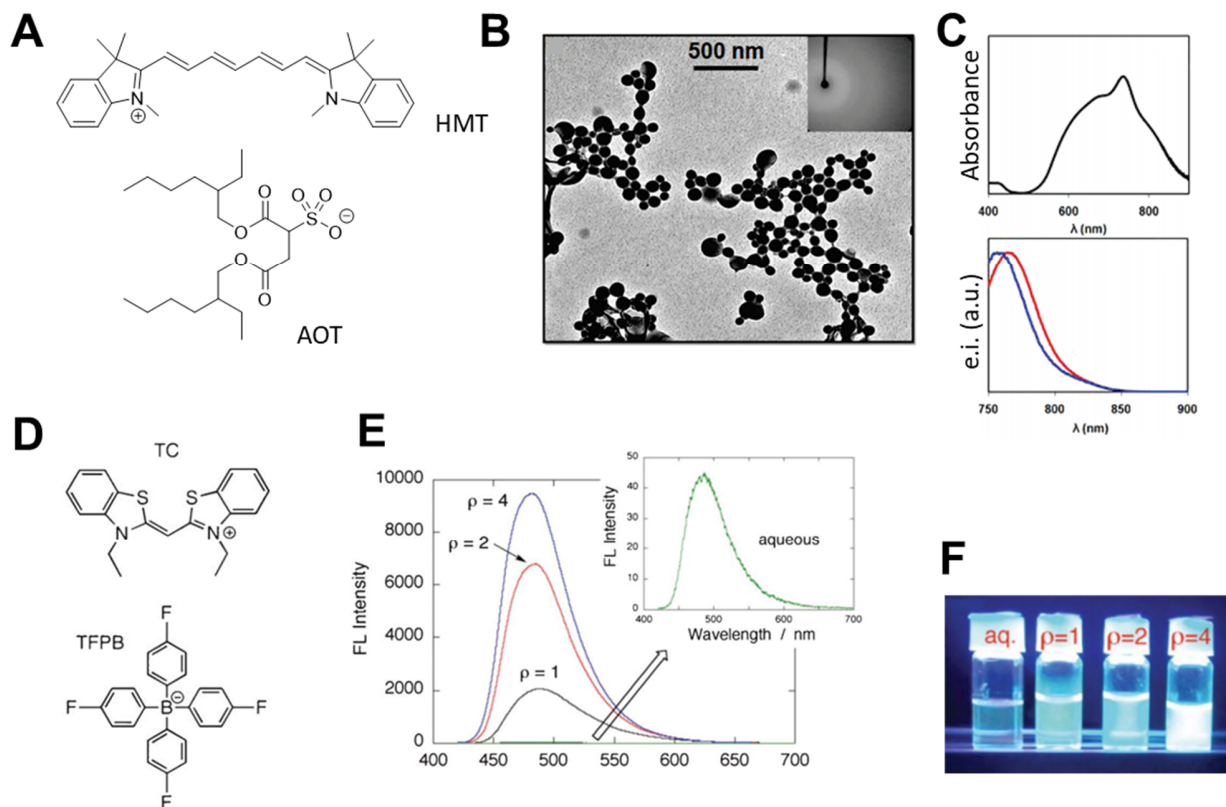


Figure 1.13 (A-C) Warner's group pioneered the use of bulky hydrophobic counterions in the preparation of GUMBOS. (A) The ion pair employed in the preparation of fluorescent nanocrystals, it is composed of a cationic NIR-emitting cyanine dye and of a hydrophobic sulfosuccinate derivative. (B) TEM images of the nanoGUMBOS constituted by [HMT][AOT]. (C) Above: absorption spectrum of the nanoparticles shown in (B). Below: normalized emission spectra of [HMT][AOT]-constituted nanoGUMBOS (in blue) vs the freely dissolved [HMT][AOT] in ethanol (in red). Images adapted from (Bwambok et al., 2009). (D-F) Yao and Ashiba introduced the use of tetraphenylborates as counterions for the preparation of ion-associated nanoparticles. (D) The ion pair employed in the preparation of nanoemitters, based on a cationic blue-emitting cyanine and a fluorinated tetraphenylborate anion. (E) Fluorescence intensity of nanocrystals prepared with different ratios between counterion and dye, the inset shows the fluorescence of the cyanine in aqueous solution. (F) Photograph of the fluorescence of the samples shown in (E) when irradiated with 365 nm UV light. Images adapted from (Yao and Ashiba, 2011).

Some groups employed cationic dyes paired with bulky hydrophobic counterions (Andreiuk et al., 2017b, 2019; Bwambok et al., 2009; Reisch et al., 2014; Yao and Ashiba, 2011).

This strategy was pioneered by Warner's group with the development of a Group of Uniform Materials Based on Organic Salts (GUMBOS). The first example reported was an organic salt composed of a cationic NIR-emitting cyanine dye paired with bis(2-ethylhexyl)sulfosuccinate (Figure 1.13A). By nanoprecipitating the ion pair with a process similar to the one commonly used for polymeric nanoparticles, stable and NIR-emissive nanocrystals of ~70 of diameter were obtained (Figure 1.13B-C) (Bwambok et al., 2009). In a later work, Yao and Ashiba introduced

1. Bibliographical overview

tetraphenylborates (Figure 1.13D) for preparation via so-called ion association technique of fluorescent nanoparticles, which were stabilized by a hydrophilic polymer (Figure 1.13E-F) (Yao and Ashiba, 2011).

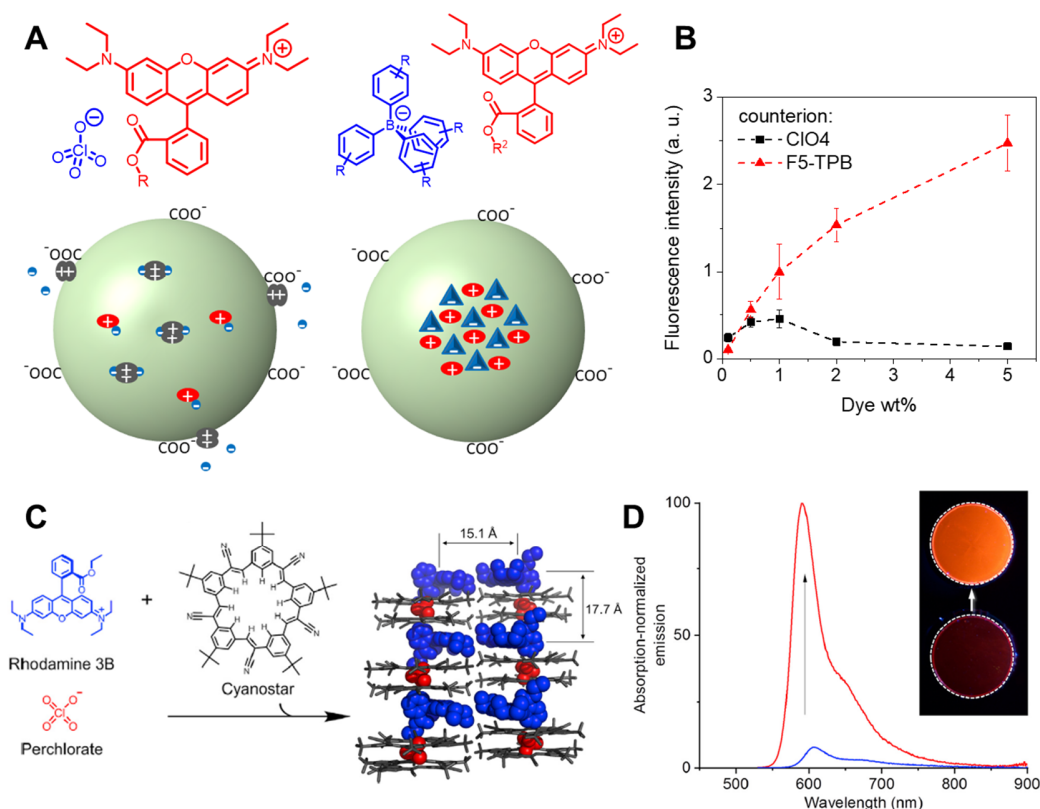


Figure 1.14 Preventing ACQ through bulky hydrophobic counterions. (A) and (B) bulky hydrophobic counterion approach. (A) Left: ion pair of Rhodamine B and perchlorate – a small hydrophilic counterion (top) and its hypothesized distribution inside the matrix of a polymeric nanoparticle, dye is poorly encapsulated and mostly quenched (bottom). Right: ion pair of Rhodamine B and a tetraphenylborate derivative – a bulky hydrophobic counterion (top) and its hypothesized distribution in the polymeric matrix, dye is well encapsulated and not quenched due to the counterion acting as a spacer (bottom). Images adapted from: (Andreiuk et al., 2019) (B) NPs fluorescence intensity as a function of dye loading for Rhodamine B perchlorate (in black) and tetraphenylborate (in red). At higher loadings the perchlorate NPs are almost non-emissive, while the tetraphenylborate NPs display a good fluorescence. Images adapted from: (Reisch et al., 2014). (C) and (D) Inert spacer approach. (C) Rhodamine 3B perchlorate is co-crystallized with cyanostar, an inert spacer. (D) The material prepared with cyanostar (red spectrum) is ten times more emissive than the one prepared without (blue spectrum). Images adapted from: (Benson et al., 2020).

This approach not only spaces the dyes in such a way that reduces their self-quenching (Figure 1.14A-B), but also improves the encapsulation of cationic dyes in the hydrophobic polymeric matrix preventing dye leaching (Andreiuk et al., 2017b, 2019), showing that the efficiency of encapsulation correlates well with the NPs quantum yield. This approach was first validated for tetraphenylborates (Reisch et al., 2014), being a class of compounds bulky

1.2. Fluorescent dyes and nanoparticles

hydrophobic counterions, also called as weakly coordinated anions (Krossing and Raabe, 2004). More recently, this concept has been extended to less expensive alkoxyaluminates (Andreiuk et al., 2017b), indicating the possibility to use metal complexes bearing more functionalities other than being simple spacers. Others groups employed neutral inert receptor to complex the small hydrophilic counterion to co-crystallize with fluorophores and enhance their fluorescence in the bulk material (Figure 1.14C-D) (Benson et al., 2020).

However, up to date there are no reports of the use of bulky hydrophobic counterions which bear any additional functionality besides being a mere bulky hydrophobic spacer. Indeed, the counterion approach could be an opportunity to construct multifunctional platforms, where one component of the ion pair functions as a fluorescent contrast agent, while the other could have other theranostic functions.

Lastly, another way of controlling the spatial disposition of fluorophores inside a nanoparticle relies on covalently fix the dye molecule to the polymer chain constituting the particle (Grazon et al., 2014).

1.2.6.2. *Dye-doped silica nanoparticles*

A good host material for dye-based nanoparticles is silica. Silica is photophysically inert and optically transparent, therefore it does not interfere with the fluorophore emission (Bonacchi et al., 2011). Indeed, all the relevant photophysical properties of said NPs, such as emission and absorption wavelength or fluorescence lifetimes, are mostly defined by the encapsulated dyes. Moreover, its synthetic versatility allows to easily encapsulate a lot of different species, such as organic dyes, metal-organic frameworks, or metal-based nanoparticles, yielding the possibility of preparing a vast array of multifunctional systems (Montalti et al., 2014). Silica nanoparticles might also be coated with different surfaces, like bioactive molecules or fluorescent dyes, but in this case ACQ has been observed in some instances.

1. Bibliographical overview

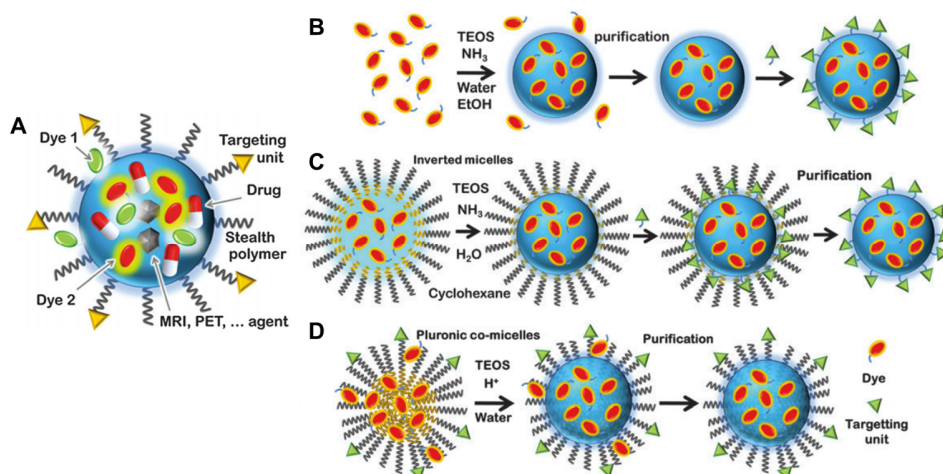


Figure 1.15 (A) Scheme of a multifunctional dye-doped silica NP. Image adapted from (Montalti et al., 2014). There are several synthetic routes available for silica NPs: (B) direct TEOS condensation, (C) in inverted emulsion, (D) in amphiphilic polymer micelles. Image adapted from: (Bonacchi et al., 2011)

Several strategies are available for synthesizing dye-doped silica nanoparticles, the oldest one pioneered by Stöber and van Blaaderen was developed in the 60s and it is based on condensing trialkoxysilane derivatives of fluorescent molecules with tetraethoxysilane (TEOS), yielding nanoparticles where the fluorescent dye is covalently linked to the silica matrix (Figure 1.15B) (Stöber et al., 1968; Van Blaaderen and Vrij, 1992). More recently other strategies based on TEOS condensation in inverted emulsion (*i.e.* water in oil emulsions) as a nanoparticle template or surfactant micelles featuring a hydrophobic core have been proposed (Figure 1.15B-C) (Montalti et al., 2014).

1.2.6.3. Conjugated polymer nanoparticles (PDots)

Fluorescent nanoparticles can be also built from conjugated polymers. Conjugated polymers are polymeric chains featuring long π -conjugated system, where, π electrons are delocalized over a significant portion of the polymeric chain. Moreover, all conjugated polymers are functionalized with long aliphatic chains to prevent π -stacking and the quenching of fluorescence (Figure 1.16A).

1.2. Fluorescent dyes and nanoparticles

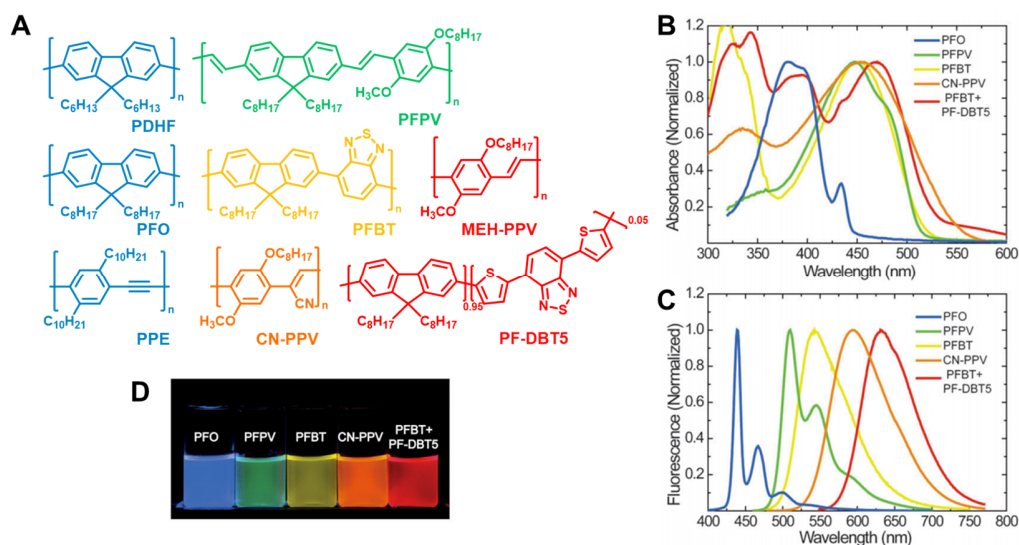


Figure 1.16 Conjugated polymer nanoparticles. (A) Conjugated polymers commonly used in the formulation of PDots. (B) Absorption and (C) emission spectra of aqueous PDots prepared with different polymers. (D) Photographs of the samples shown in (B) and (C). Images adapted from: (Wu and Chiu, 2013).

Their size is generally in the range of 5-30 nm and they feature broad absorption spectra due to the heterogeneity in length of the chain constituting the particles, relatively narrow emission bands and high quantum yields (in the range of 0.1-0.6). Changing the nature of the conjugated system allows tuning the emission wavelength (Figure 1.16). PDots are usually prepared either by nanoprecipitation or by direct polymerization (Braeken et al., 2017).

1.2.6.4. Dye-loaded polymeric nanoparticles

Dye-loaded polymeric nanoparticles are a class of nanomaterials where the organic fluorophores are encapsulated in a polymeric matrix.

1. Bibliographical overview

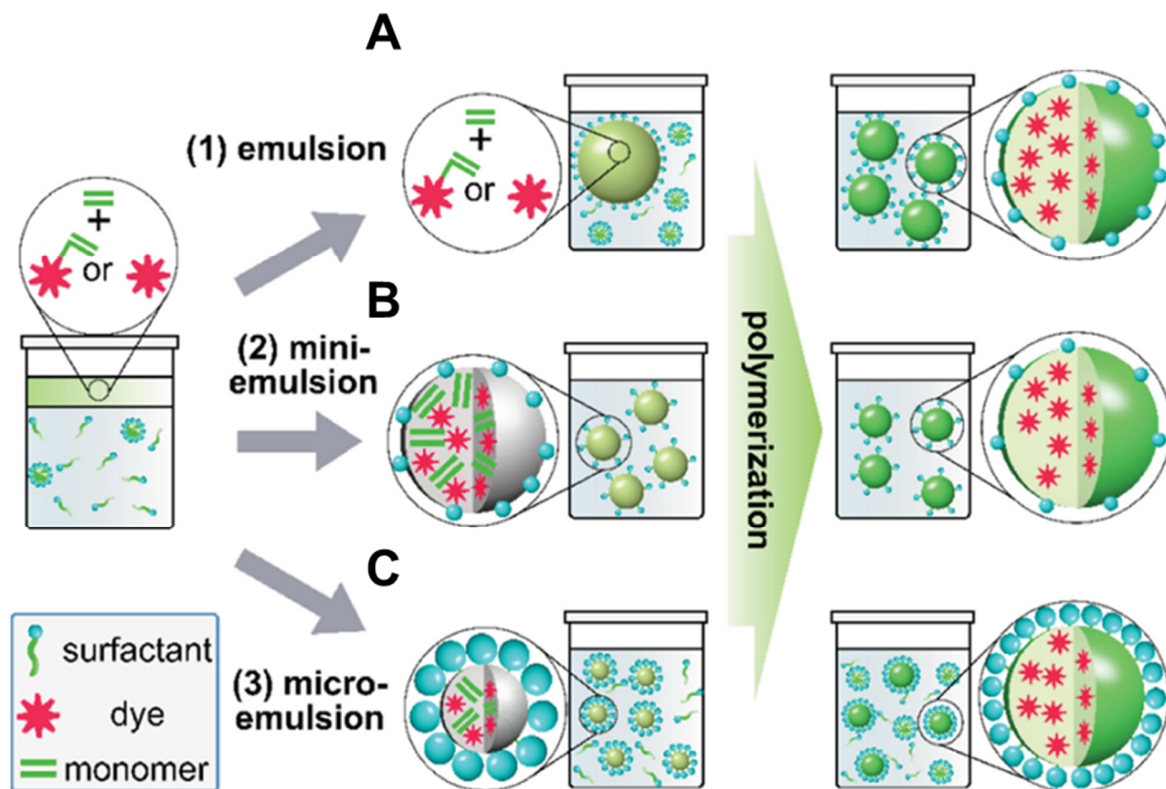


Figure 1.17 Polymeric NPs preparation by polymerization *in situ*. Polymerization can be performed in (A) conventional emulsion, (B) mini-emulsion or (C) micro-emulsion. The type of the obtained emulsion depends on the surfactant concentration and the stirring method. Image adapted from: (Reisch and Klymchenko, 2016a).

Polymeric nanoparticles can be prepared by direct polymerization of monomers in emulsion. The low water soluble monomers and dyes are dispersed in an aqueous phase with a surfactant. The fluorescent dye can be functionalized with the monomer to obtain a nanosystem in which the fluorophore is covalently linked to the matrix, much like in the case of the aforementioned silica nanoparticles. Alternatively, it can be embedded in the polymeric matrix as the polymerization proceeds. The size of the micelles in the emulsion governs the final size of the nanoparticles (Figure 1.17). In the so-called *conventional emulsion*, NPs with diameters in the range of 50-300 nm are obtained. *Mini-emulsions* are obtained by strong mechanical stirring and/or sonication, which allow to obtain smaller nanoparticles, while *micro-emulsions* are thermodynamically stable emulsions of monomer in the aqueous phase which are then subsequently polymerized, through this last approach is possible to obtain very small nanoparticles (5-50 nm) (Reisch and Klymchenko, 2016a).

1.2. Fluorescent dyes and nanoparticles

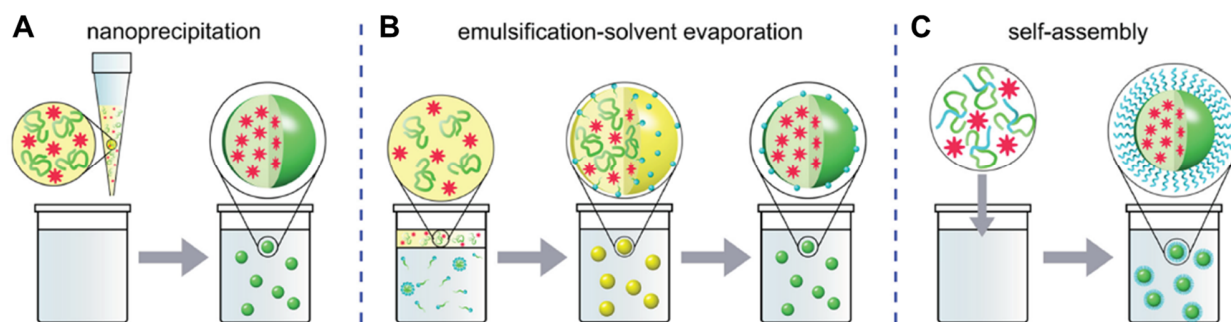


Figure 1.18 Polymeric NPs preparation with pre-synthesized polymer. Organic phase shown in yellow, aqueous phase in blue, polymer in green and fluorophores in red. Image adapted from: (Reisch and Klymchenko, 2016a).

Another approach to polymeric nanoparticles preparation relies on the use of pre-synthesized polymers (Figure 1.18), in this case several approaches have been developed. In *nanoprecipitation* (also called *solvent displacement*) (Figure 1.18A) polymer and dye are dissolved in an organic solvent soluble in water. Then, the organic phase is injected in an aqueous solution. The polymer is not soluble in water, and therefore, once in aqueous phase, it forms hydrophobic nanoparticles. Being a kinetically controlled process, many variables such as polymer type and concentration, speed of mixing and ratio of organic and aqueous phase influence the size of the obtained nanoparticles, sizes ranging from 5 to 100 nm are obtainable. In this preparation the choice of dye is fundamental: a too hydrophilic fluorophore would be poorly encapsulated, leading to dye leaching; while a dye too hydrophobic during nanoprecipitation would form a core composed of aggregated dyes surrounded by a polymeric layer (Trofymchuk et al., 2019), which could limit the system brightness due to ACQ.

Emulsification solvent evaporation consists of dissolving a polymer and a dye in a water immiscible solvent and dispersing the organic phase in the aqueous phase and creating an emulsion with the help of surfactants by mixing or sonication (Figure 1.18B). The organic solvent is left to slowly evaporate, leaving behind polymer nanoparticles. NPs obtained with this method are usually in the range of 100-200 nm.

While nanoprecipitation is a kinetically controlled process, some amphiphilic polymers can spontaneously self-assemble into NPs in the form of micelles (Collot et al., 2020; Shulov et al., 2016b). In this case, again, an organic phase of polymer is dispersed in an aqueous phase, if the polymer concentration exceeds the *critical micellar concentration* (CMC) it will assemble in

1. Bibliographical overview

nanoparticles, which can be then cross-linked with a dye, yielding stable NPs (Figure 1.19A). Alternatively, amphiphilic polymer bearing fluorescent dyes can spontaneously fold into micelle-like polymeric nanoparticles (Figure 1.19B). With these approaches, nanoparticles of very small size around 10 nm can be obtained. Organic fluorophores can be encapsulated in the hydrophobic core of the NPs, or can be covalently linked to the polymer to avoid dye leaching.

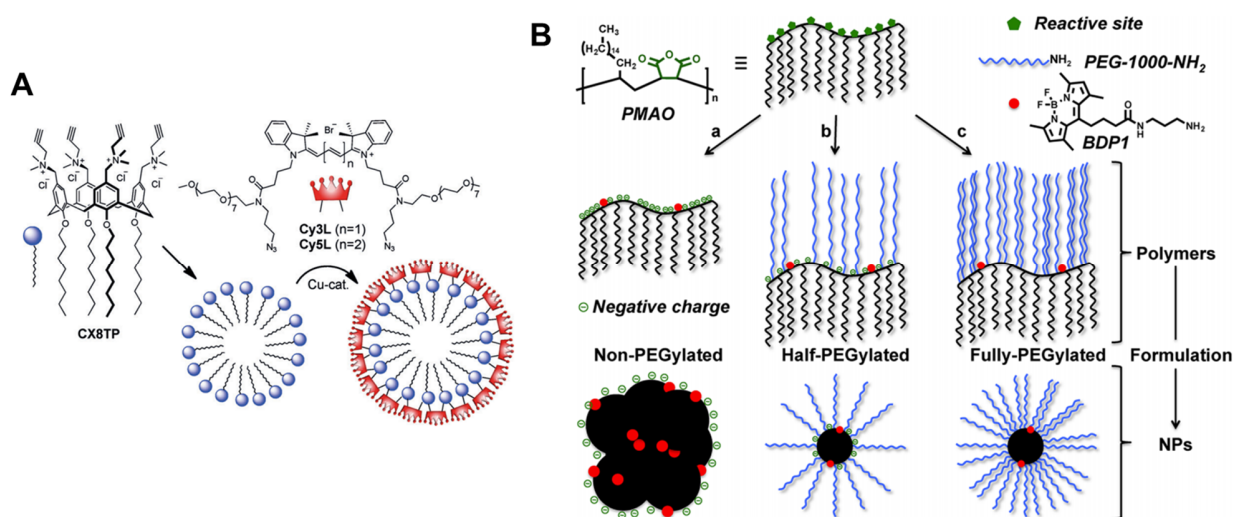


Figure 1.19 Self-assembly of amphiphilic species. (A) Calixarenes with a hydrophobic tail and a charged head can self-assemble in micelles on which an azide-functionalized fluorophore can be grafted on. Image adapted from: (Shulov et al., 2016b). (B) Amphiphilic polymers with a brush-like structure can fold in nanoparticles exposing the PEG chain and hiding the aliphatic chains. Image adapted from: (Collot et al., 2020).

1.3. *Fluorescence signal amplification in biosensing*

Fluorescence-based assay can be quite sensitive, however to detect ultra-low quantities of analyte and push further the boundaries of biosensing, several strategies have been developed.

The most straightforward approach relies on employing instead of single dyes fluorescent nanoparticles that are several orders of magnitude brighter. This solution is effective especially in *in vitro* tests, where neither size nor toxicity of the fluorescent reporter poses an issue. As a matter of fact, a good portion of the assays reviewed in this and the following sections employ some kind of fluorescent NP as reporter. However, nanomaterials always possess a degree of inhomogeneity in their properties, and sometimes their surface functionalization for biological applications can be tricky, therefore organic fluorophores still have a place in the world of biosensing.

A number of amplification strategies for the analyte of interest have been developed, and they can be divided in (i) *chemical* and (ii) *physical* amplification strategies. Chemical strategies rely on multiplying the number of analyte or reporter species, in order to increase the fluorescence signal associated to the presence of analyte.

1.3.1. *Chemical signal amplification strategies*

Nucleic acids (NAs) due to their structure, naturally lend themselves to amplification through chemical routes. A great number of NA amplification techniques have been developed: polymerase chain reaction (PCR, Figure 1.20A) being the first (Mullis et al., 1986) and still being used routinely nowadays and simpler approaches which do not require thermal cycling (Daubendiek et al., 1995; Notomi et al., 2000). Among the molecular amplification techniques for nucleic acids, loop-mediated isothermal amplification (LAMP) has been used in many works (Chen et al., 2017; Hu et al., 2020; Priye et al., 2018; Stedtfeld et al., 2012). It is a one-step technique, which does not require thermal cycling (unlike PCR) and it is highly sensitive and selective towards the target sequence (Figure 1.20B). All these features greatly reduce the equipment and the operator proficiency required. Rolling circle amplification (RCA) is another molecular amplification technique that has been widely used (Kühnemund et al., 2017; Lu et al., 2018). Similarly to LAMP, it is an isothermal technique (Figure 1.20C), but its strongest feature is that it is suitable for DNA detection on solid supports, (such as beads, surfaces or well plates) opening the way of further streamlining the analytical workflow. Digital PCR (dPCR) is a variant of PCR where single

1. Bibliographical overview

molecules are isolated in individual droplets and amplified separately, the concentration of a certain sequence quantified by counting the fluorescent droplets. dPCR and other digital NA amplification techniques have been proven to be more sensitive, allowing also to reduce the errors associated to operator inexperience.

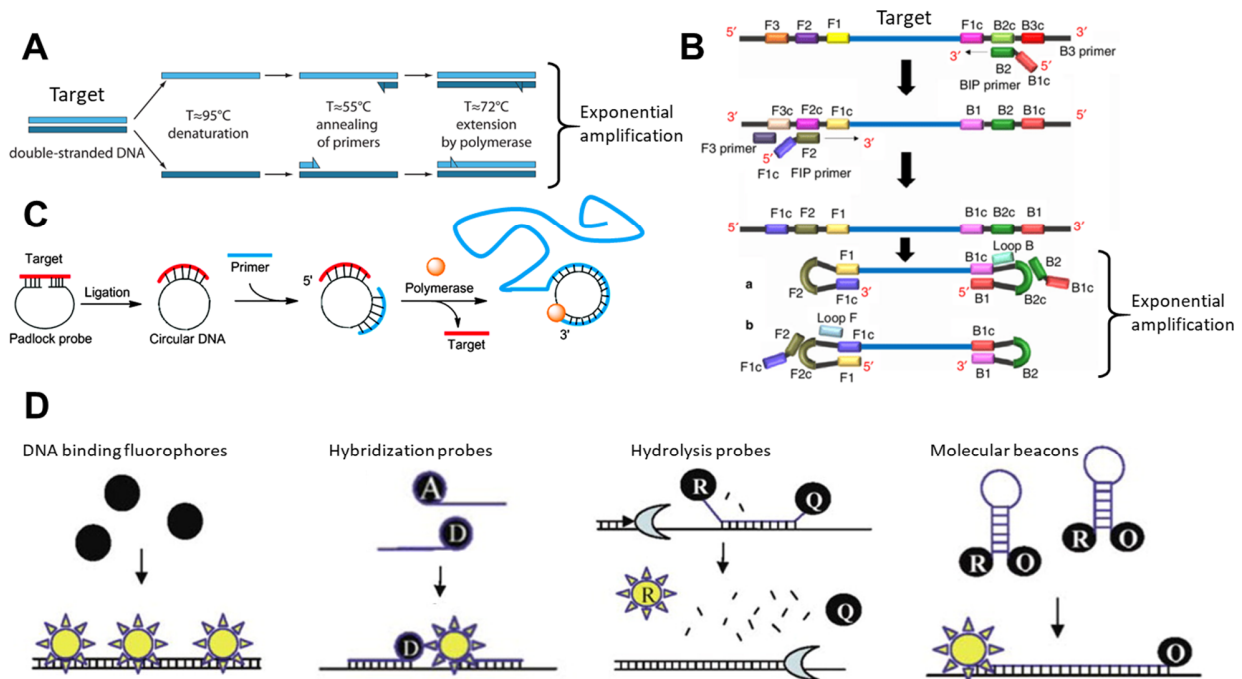


Figure 1.20 DNA amplification techniques. (A) Working principle of PCR. Image adapted from: <https://microfluidics.stanford.edu/Projects/Archive/OnChipPCR.html> (B) Working principle of LAMP. Image adapted from: (Wong et al., 2018) (C) Working principle of RCA. Image adapted from (Yan et al., 2014) (D) Methods for fluorescence quantification of the amplified DNA. Image adapted from: (Wong and Medrano, 2005).

Another chemical amplification strategy, this time for antigens, proteins, peptides and hormones, are enzyme-linked immunosorbent assays (ELISA). Briefly, the analyte is deposited on a glass surface (either directly in direct ELISA or captured by antibodies deposited on the surface in sandwich ELISA) and an antibody-enzyme conjugate and an enzyme substrate is subsequently added. The enzyme (usually horseradish peroxidase – HRP) converts the substrate in either a coloured or fluorescent species (Figure 1.21). If fed enough substrate molecules the enzyme produces reporter species indefinitely, thus amplifying the color or fluorescence associated to even very small concentrations of analyte. However, antibodies are notoriously difficult to produce and not very stable at ambient conditions, making ELISA somewhat suboptimal for point of care (PoC)

1.3. Fluorescence signal amplification in biosensing

settings, with groups consequently seeking alternative assays more compatible with low resources areas.

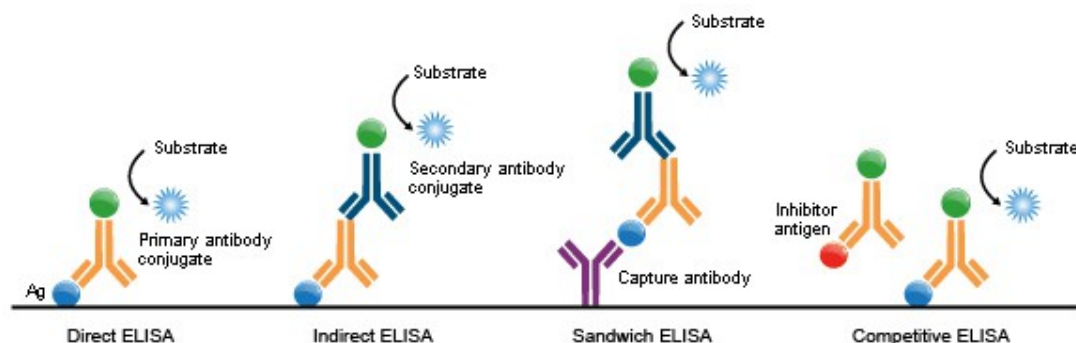


Figure 1.21 Simplified scheme of the main ELISAs. Image adapted from: <http://www.abnova.com/support/resources.asp?switchfunctionid={70196CA1-59B1-40D0-8394-19F533EB108F}>.

1.3.2. Optical signal amplification using nanomaterials

Physical optical amplification, on the other hand, is the *direct* amplification of the fluorophore signal. The simplicity of the concept renders it attractive for PoC applications. There are mainly three established means of fluorescent signal amplifications: (i) plasmonic nanostructures, (ii) light harvesting conjugated polymers and (iii) light harvesting dye-loaded polymeric nanoparticles. Plasmonic nanostructures (*i.e.* gold and silver nanomaterials) have been shown to greatly enhance the fluorescence of organic dyes when positioned at the proper distance and orientation (Figure 1.22A) (Novotny and van Hulst, 2011) and found applications in smartphone microscopy (Wei et al., 2017) and DNA detection (Ochmann et al., 2017; Trofymchuk et al., 2020). In conjugated polymer nanoparticles the large numbers of π -conjugated aromatic units are positioned at a close distance one from each other, allowing a very fast and efficient excitation energy transfer to one or few energy acceptor (Figure 1.22B) (Jiang and McNeill, 2017; Rochat and Swager, 2013; Thomas et al., 2007). Light-harvesting dye-loaded polymeric nanoparticles operate under a similar working principle: the dyes are dispersed in the polymeric matrix at an intramolecular distance allowing the ultrafast excitation energy migration of thousands of donors towards one energy acceptor (Figure 1.22C) (Trofymchuk et al., 2017). This system performs better than plasmonic antennas in terms of fluorescence enhancement, yielding the highest signal amplification of a single dye reported up to date, the design has been exploited for DNA detection (Melnychuk et al., 2020; Melnychuk and Klymchenko, 2018).

1. Bibliographical overview

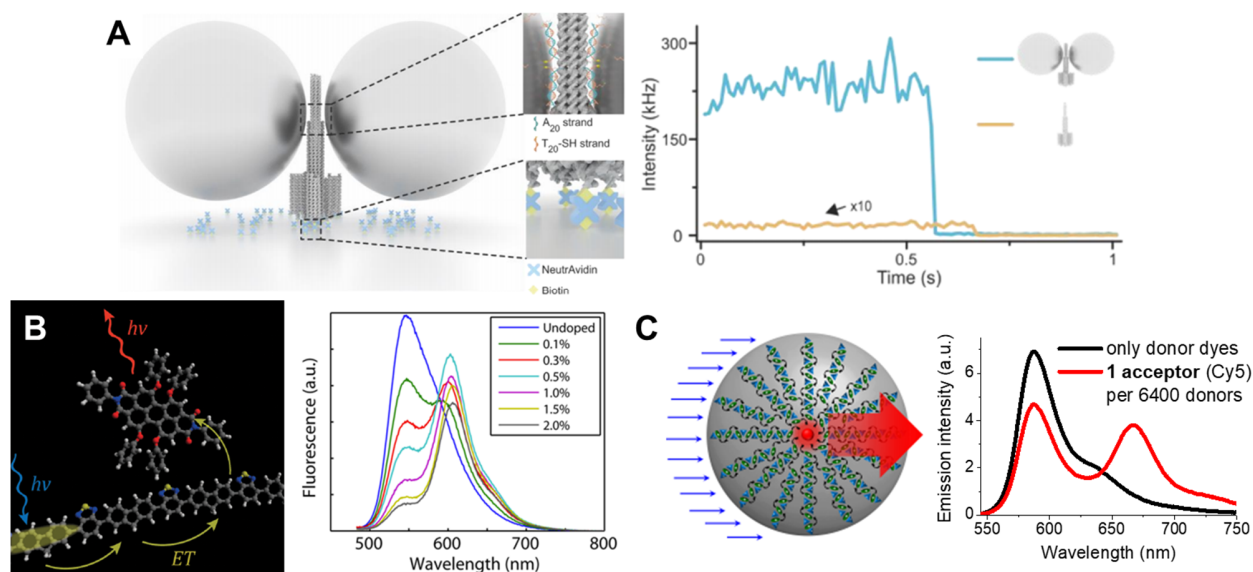


Figure 1.22 Optical amplification techniques. (A) Plasmonic nanostructures greatly enhance both absorption and fluorescence rates of fluorophores located at precisely controlled distances, increasing their fluorescence intensity up to 300 times. Images adapted from: (Trofymchuk et al., 2020). (B) In conjugated polymers the excitation energy can quickly migrate and be transferred very efficiently towards FRET acceptors; the emission spectra on the right show how a very small quantity of dopant, 2%, (in this case Perylene Red) in PFBT can result in an energy transfer efficiency of 86%. Images adapted from: (Groff et al., 2013). (C) In giant light harvesting polymeric antennas organic dyes are located at the optimal intramolecular distance in order to produce an ultra-fast excitation energy transfer towards a single FRET acceptor. The emission spectra on the right show that 6400 octadecyl-rhodamine B can transfer their excitation energy towards a single FRET acceptor (cy5) with an efficiency of 30%. Images adapted from: (Trofymchuk et al., 2017).

Biosensing enabled by nanomaterials is an ever-expanding field, many sensors for biomarkers have been developed, such as: nucleic acids (Chen et al., 2018; Hildebrandt et al., 2017), proteins (Hildebrandt et al., 2017; X. Huang et al., 2018), metabolites (X. Huang et al., 2018), *etc.*

In the field of NA detection many progresses have been made in the development of detection methods which do not require the chemical amplification of the target species. A notable example comes from Tinnefeld group, where with the aid of DNA origami it was possible to place a single molecular beacon at the proper distance from a silver nanoparticle to greatly enhance its fluorescence in presence of the target sequence (specific of the Zika virus) (Ochmann et al., 2017). Another interesting DNA nanoprobe which is based instead on dye-loaded polymeric nanoparticles is described by our team (Melnychuk and Klymchenko, 2018). The system exploits the light-harvesting antenna effect previously described: but in this case the FRET acceptor is not inside the nanoparticle, but on its surface. DNA decorated NPs are prepared, and the acceptor is introduced

1.3. Fluorescence signal amplification in biosensing

in the system by annealing an acceptor-bearing target competitive sequence (TCS). In presence of the target sequence, that encodes a fragment of survivin, an important cancer marker (Altieri, 2003; Stobiecka et al., 2019), the acceptor is displaced and the FRET turns off (Figure 1.23A).

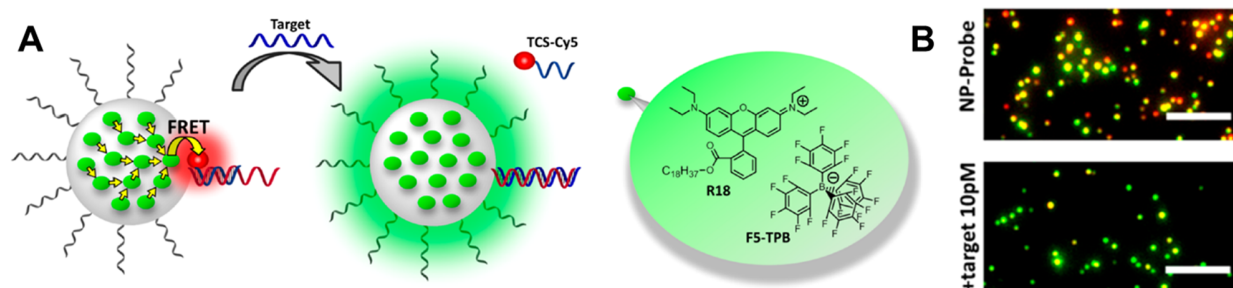


Figure 1.23 Dye-loaded polymeric nanoantennas for the detection of DNA. (A) Design of the DNA sensor. (B) Single-particle microscopy image of the nanoprobes without any target sequence (top) and in presence of 10 pM of target (bottom). Scale bars: 5 μm . Images adapted from (Melnychuk and Klymchenko, 2018).

This system works remarkably well, featuring high acceptor signal amplification, very low limit of detection (LOD in solution was 5 pM, while on surfaces it reached 0.25 pM), high specificity and the ability to function even in complex biological matrices, such as serum. In a later work, the authors challenge even further the capabilities of this system, reaching single-molecule sensitivity (Melnychuk et al., 2020).

1. Bibliographical overview

1.4. *Fluorescence smartphone-based detection*

Most of biological assays for diagnosing disease require skilled personnel and sophisticated instrumentation, which are not accessible everywhere, especially in remote areas, lower resources areas and high population areas. For this reason, the concept of point of care assay has been emerging as a way to ensure healthcare in lower-resources settings through robust, quick and easy assays. Many point of care assays have been developed for a great number of analytes such as proteins (Luppa et al., 2011), metabolites (Lauks, 1998; Luppa et al., 2011), nucleic acids (Niemz et al., 2011), human cells (Basabe-Desmonts et al., 2010), pathogens (Clerc and Greub, 2010), drugs and toxins (Wong and Tse, 2005) using a variety of techniques, like colorimetry (Yetisen et al., 2013), fluorescence (Gubala et al., 2012) and various electrochemical methods (Warsinke et al., 2000). In this growing research field, smartphones have attracted interest as potential instrumentation due to: (i) their almost universal prevalence – it is estimated that roughly 40% of the world population owns one; (ii) their ever-growing processing power, which allows to treat complex collected data; and (iii) and their storage and connectivity, which allows to store and transmit analysis results. For all these reasons a multitude of smartphone-based PoC setups have been developed (McGonigle et al., 2018; Roda et al., 2016; Zhang and Liu, 2016). In particular, smartphone cameras are progressively becoming better and better, opening the possibility to use them as detectors for optical measurements. There is an ever-increasing number of colorimetric and fluorescence based assays employing smartphones presented in scientific literature such as: blood analysis (Breslauer et al., 2009), pathogen agents detection (Wei et al., 2013; Zhu et al., 2012), detection of biomarkers as nucleic acids (Wei et al., 2014; Xu et al., 2020), proteins (Coskun et al., 2013) and metabolites (Yu et al., 2018).

1.4.1. *Principles of smartphone-based detection*

Constructing a point of care smartphone-based setup capable of sensing is an interdisciplinary challenge. Ideally, the system should be as sensitive as traditional setups, while being inexpensive, portable and easy to use. It should be noted that fluorescence smartphone-based detection can be achieved through something as simple as taking a picture of a fluorescent object and measuring its color and/or intensity, or as complicated as quantifying fluorescence microscopy images. In the first case no particular hardware is required outside the smartphone itself and possibly a sample holder, although careful calibration of the system should be performed and a

1.4. Fluorescence smartphone-based detection

robust data acquisition and quantification routine should be put in place to avoid instrumental errors. For the microscopy applications, some consideration should be placed also on the setup hardware (Breslauer et al., 2009; Cho et al., 2016; Ghosh et al., 2011). In this regard, 3D printing is an emerging technology that helped immensely with the speed of prototyping and costs of production.

When dealing with fluorescence, filters are usually an essential part of the setup, having multiple functions, such as filtering out the excitation light, or separating the FRET donor emission from the acceptor in order to perform ratiometric analysis. The detector of modern consumer-grade cameras is composed of an active pixel sensor array based on a complementary metal-oxide semiconductor (CMOS) light sensor, on which a color filter array which let pass red, green and blue (RGB) light (Takayanagi, 2006). This design allows the simultaneous detection of three channels and has been extensively exploited for both colorimetric and fluorescence assays (Figure 1.24). Colorimetric RGB analysis is outside of the scope of this introduction but some notable examples of smartphone-based colorimetric detection for biomarkers should be mentioned, with the development for systems for the detection of cancer markers (Hosu et al., 2017; J.-Y. Huang et al., 2018; Vashist et al., 2015), metabolites (Calabria et al., 2017; Jia et al., 2015) and electrolytes (Yetisen et al., 2017). RGB analysis in fluorescence based assays has been used for multiplexing (*i.e.* the intensity registered in one channel corresponds to one analyte) (Petryayeva and Algar, 2014; Priye et al., 2018; Xu et al., 2015) and ratiometric analysis (*i.e.* the ratio between the intensity registered in two channels is proportional to the concentration of the analyte) (Arts et al., 2016; Hou et al., 2019). RGB analysis has been applied for a variety of scopes, such as the quantification of beta-estradiol (Lee et al., 2017), proteins (Petryayeva and Algar, 2014) (Figure 1.24A-C), metabolites (Yu et al., 2018), the measurement of pH and oxygen concentration (Xu et al., 2015) (Figure 1.24D-E), and the quantification of antibodies (Figure 1.24F-G).

1. Bibliographical overview

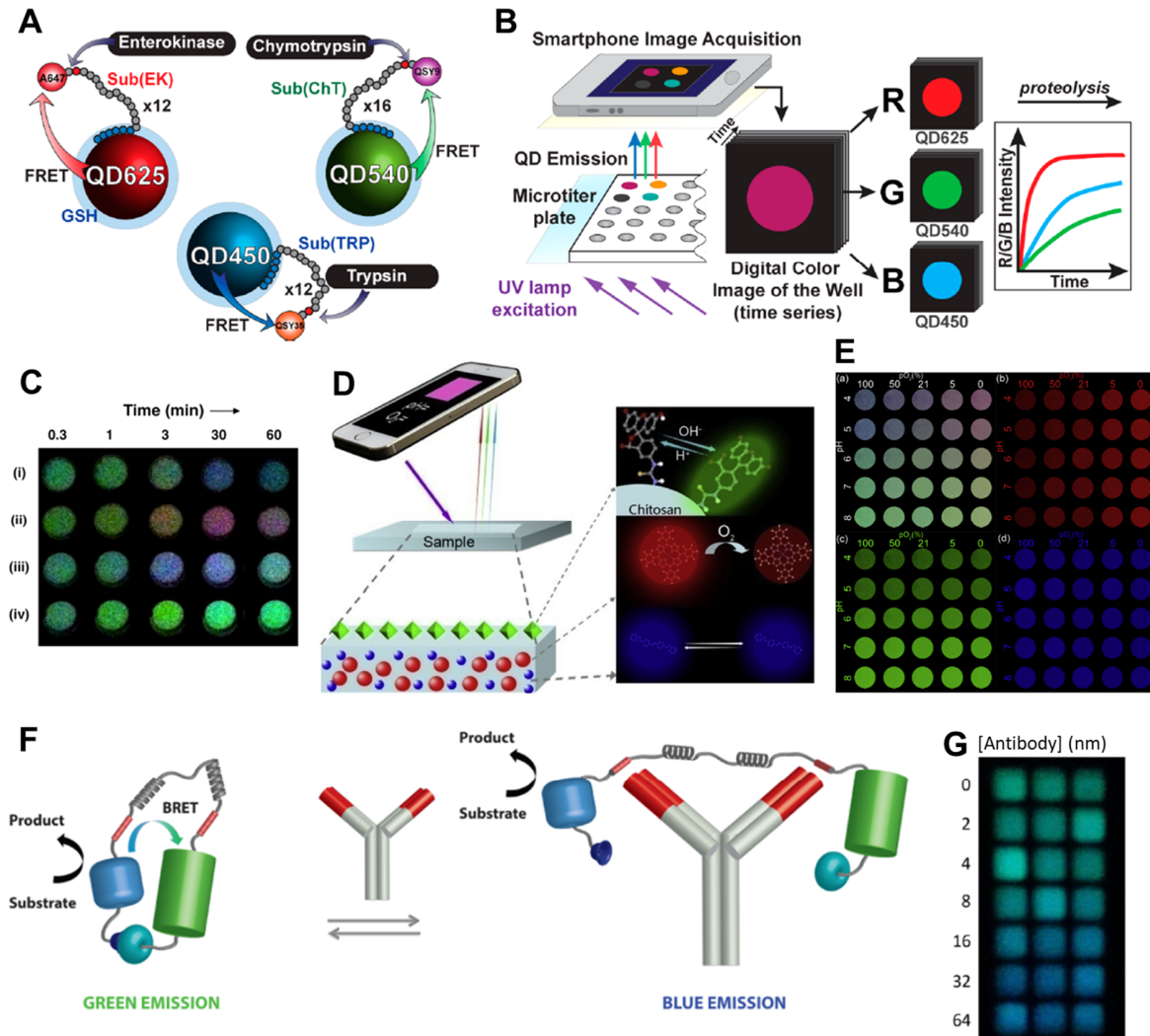


Figure 1.24 RGB analysis in smartphone-based detection. (A) Multiplexed detection scheme for three different proteolytic enzymes. Three QDs of different colors are functionalized with three different quencher-bearing peptidic sequences. Each enzyme is selective towards one of the peptides and if present in the sample it will cleave it, restoring the fluorescence. (B) Sample analysis workflow: a multiwell plate is imaged over time, the resulting RGB image is decomposed in its three channels and the recovery of each channel intensity is reconstructed. (C) Smartphone image of four samples at different timepoints, the recovery of fluorescence is evident. Images adapted from (Petryayeva and Algar, 2014). (D) Schematic of a paper-based assay for the simultaneous measurement of pH and $p(\text{O}_2)$. Fluorescein (in green) is brightly green in basic conditions and nonemissive when protonated, platinum-porphyrin complexes (in red) display a red fluorescence which is quenched by oxygen. A stilbene-based dye (blue) is insensitive to both conditions and is used as a reference. (E) Multichannel images of test papers at different pH and $p(\text{O}_2)$. Red channel intensity is inversely proportional to $p(\text{O}_2)$, green channel intensity is directly proportional to pH, while blue channel is insensitive to both. Images adapted from (Xu et al., 2015). (F) Scheme for the ratiometric measurement of antibody concentration. A chimera protein consisting of a NanoLuc, a GFP, a helper domain and an epitope domain displays a green emission due to the FRET from the NanoLuc towards the GFP in absence of the target antibody. In presence of the analyte, the antibody binds to the epitope and distances the two luminescent domains, rendering the sensor fluorescence blue. The concentration of the antibody is derived by evaluating the ratio between the blue and green channels. (G) Smartphone photos of fluorescent well plates with increasing dengue 1 antibody concentration. Images adapted from: (Arts et al., 2016).

1.4. Fluorescence smartphone-based detection

1.4.2. Smartphone-based spectrometers

As previously discussed, quantification of the RGB channels of the acquired fluorescence images has proven itself useful as means of multiplexing and ratiometric analysis. However, camera RGB filters are fixed, restricting the choice of fluorophores to ones whose emissions fall in the ideal spectral windows; moreover, smartphone cameras have an infrared (IR) blocking filter preventing the use of NIR emitters that are widely used in biological settings due to NIR light not being absorbed by biological samples. In this regard, Cunningham's group developed a smartphone handheld fluorometer (Yu et al., 2014) (Figure 1.25), a green laser pointer works as an excitation source and a monochromator separates in its wavelength components the light emitted by the sample (Figure 1.25A-B). The raw emission intensity data acquired with such setup are obviously not a plot of intensity vs wavelength, but they appear as an image of a spectral band (Figure 1.25D) from which can be later reconstructed the more familiar plot of intensity vs wavelength (Figure 1.25E).

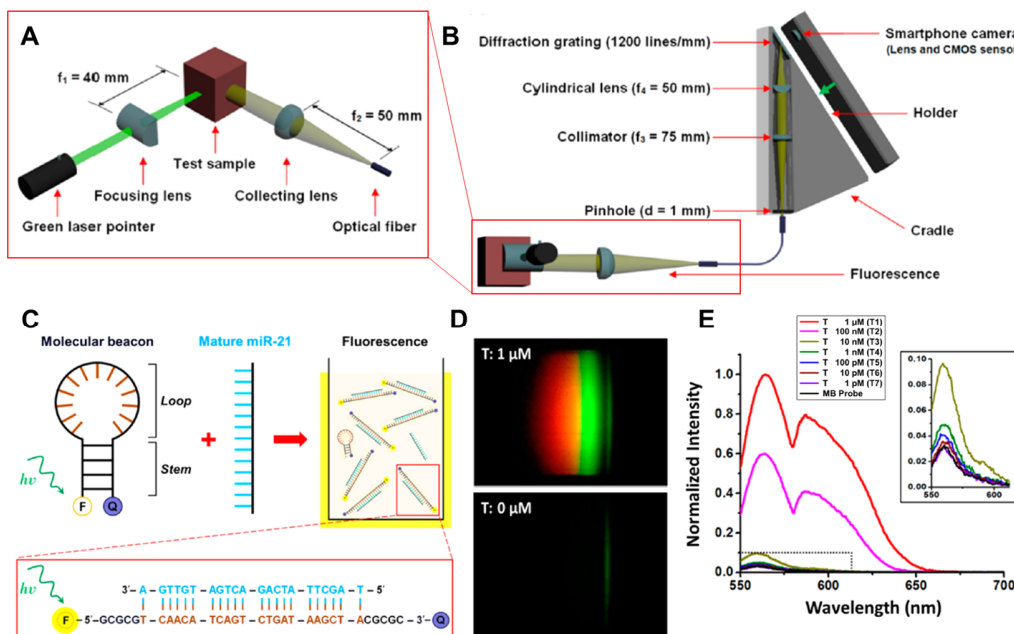


Figure 1.25 A smartphone-based fluorometer. (A) Optical configuration of the sample holder: a green laser excites the sample and its emission is collimated in an optical fiber. (B) Optical setup of the entire device, the sample holder shown in (A) is circled in red. (C) Sensing principle for the detection of miRNA: in absence of target the molecular beacon is in the hairpin conformation and its fluorescence is quenched, in presence of target fluorophore and quencher are spatially separated and an increase of fluorescence is observed. (D) Pictures recorded with the smartphone-based fluorometer of samples with and without target. (E) Spectra recorded *via* smartphone of samples at increasing concentration of target. Images adapted from: (Yu et al., 2014).

1. Bibliographical overview

The setup was used for detecting, as a proof of concept, miRNA using a molecular beacon probe (Figure 1.25C) with a LOD of 1.3 pM. The authors claim that the strong point the device is its flexibility, and potentially it could be a universal platform for every fluorescence-based assay. However, the capability of selecting the exciting wavelength is a fundamental feature of fluorometers. Even a smartphone-based one should be equipped with multiple excitation sources to achieve the broad applications range the authors envision. Due to the advanced technical challenges the construction of a smartphone-based fluorometer entails, there are few examples in literature of such devices. Smith *et al.* report the conception of a smartphone-based microscope and fluorometer for educational purposes (Smith et al., 2011), while Hossain *et al.* constructed dual smartphone-based fluorometer and spectrophotometer equipped with two light emitting diodes (LEDs) at 370 and 450 nm and a white broadband LED as excitation sources. The device was used to measure the fluorescence of a Zn²⁺ sensitive probe and a pH probe (Hossain et al., 2015).

1.4.3. PoC assays and microfluidics

It is clear that careful consideration should be put in designing the components of a biosensing smartphone-based setup, hardware should be well-performing yet inexpensive; software analysis should be carefully validated. Finally, the fluorophores chosen should be bright enough to be detected by consumer-grade cameras and have emission compatible with the available RGB channels.

However, it is also vitally important that the analysis is sufficiently simple and robust: a lot of biological assays require multiple steps of careful pipetting and washing, which could be difficult to perform accurately by unskilled personnel. Some groups circumvented this obstacle by developing alternative, simpler one-step assays (Arts et al., 2016), while a more common approach is designing microfluidic chips to render these operations simpler and almost completely automated (Alves and Reis, 2019; Stedtfeld et al., 2012; Wang et al., 2019; Zeinhom et al., 2018). A notable example of smartphone-based technology marrying microfluidic technology comes from Stedtfeld *et al.*, where the authors describe the construction of a platform for the simultaneous detection of multiple pathogens. This device, called Gene-Z, consists of a microfluidic chip with multiple arrays of 15 reactions well each mounted on a platform which includes a heating aluminium plate, an array of LEDs and a multichannel fluorescence sensor (Figure 1.26A-C). In each well, different primers for loop-mediated isothermal amplification. The sample is injected in the sample inlet and

1.4. Fluorescence smartphone-based detection

the LAMP is carried out in the wells, the chip is then illuminated by an array of LEDs and photographed by the Gene-Z device (Figure 1.26D). Data are analysed with an iPod Touch using a custom-built app (Stedtfield et al., 2012). It should be remarked that in this work in particular the fluorescence image is not acquired with a smartphone, but by custom-built platform. However, nowadays smartphone cameras should be sensitive enough to acquire the fluorescence images and treat them afterwards, reducing the complexity, and thus the cost, of the Gene-Z device.

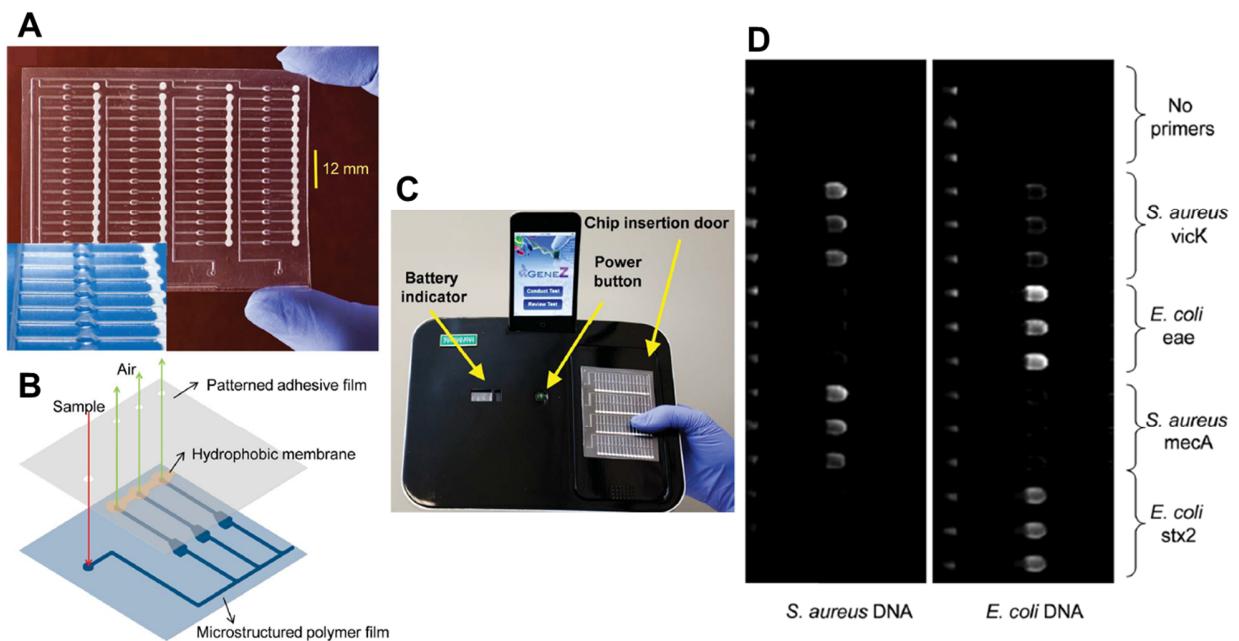


Figure 1.26 Microfluidics for simultaneous detection of multiple pathogens. (A) Photo of the Gene-Z microfluidic chip. (B) Microfluidic chip structure: the sample is loaded through an inlet and its equally distributed in 15 reaction wells (only three are shown for simplicity), each well is loaded with LAMP reagents with primers for different sequences. (C) Picture of the Gene-Z device, each well is individually illuminated by a LED. (D) Fluorescence images of two chip rows for two different samples demonstrating the selectivity of the device. Images adapted from: (Stedtfield et al., 2012).

1.4.4. Fluorescence sensors for biomarkers based on a smartphone

Antibodies. Arts *et al.* (Arts et al., 2016) developed a bioluminescent sensing protein for detection of antibodies for HIV1-p17 and dengue 1 in plasma. The fluorescence assay is meant to be a simple, one-step alternative to ELISA assays and it is based on a synthetic fluorescent protein. The sensor protein is composed of two domains, NanoLuc (which emits in the blue region of the spectrum) and mNeonGreen (emitting in the green), the two domains are joined on one end by an epitope which has a strong affinity for the target antibody, on the other end a helper domain keeps

1. Bibliographical overview

the two fluorescent moieties in close proximity. In absence of antibody NanoLuc and mNeonGreen are in close proximity, and upon excitation of NanoLuc the energy is transferred to mNeonGreen, rendering the color of the sensor green. If the target antibody is present in the sample it will bind the epitope, separating the two fluorescent domains, and turning off the FRET and rendering the sensor color blue. The assay is carried in solution by taking a picture of the fluorescent wells; the presence of the antibody is quantified by evaluating the ratio between the blue and the green RGB channels. The LOD for the HIV1-p17 antibody was calculated to be 10 pM.

Chi *et al.* (Chi et al., 2017) concentrated their efforts on how to increase the fluorescence signal produced in an ELISA. The authors report the conception of an ELISA for human IgG with a modified support that amplifies the fluorescence reporter signal. The support consists of a pseudo-paper constituted by patterned nitrocellulose with an inverse opal structure (Figure 1.27). Opal and inverse opal structures are widely known for their photonics properties, and their capability to amplify the fluorescence of dyes in their cavities, in this work the fluorescence signal was 57 times stronger in respect to non-patterned nitrocellulose paper, which allowed a limit of detection of 3.8 fg/mL.

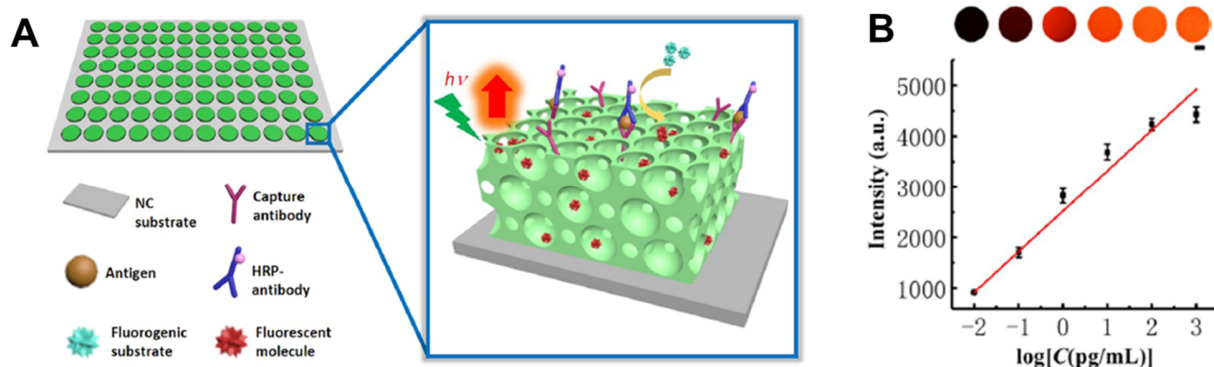


Figure 1.27 (A) Inverse opal structures can greatly amplify the fluorescence of emitters. (B) Fluorescence intensity measured as a function of concentration of human IgG. Images adapted from: (Chi et al., 2017).

Nucleic acids. Chang *et al.* (Chang et al., 2020) developed a semisynthetic sensor for detection of miRNA based on NanoLuc. A luciferase-peptide nucleic acid (PNA) conjugate is annealed with a short sequence bearing a bioluminescence inhibitor moiety (Figure 1.30A-B). In presence of the target sequence the inhibitor sequence gets displaced and the fluorescence turns on (Figure 1.30C-D). Lu *et al.* (Lu et al., 2018) developed an assay for miRNA based on magnetic

1.4. Fluorescence smartphone-based detection

beads functionalized with DNA fishhook probes. The beads are incubated with the sample and after the target sequence is captured by the probe the magnetic beads are used as a mean of concentrating and washing the sample before the rolling circle amplification reaction takes place. The reduced volume of the sample increases the sensitivity of the assay (Figure 1.28).

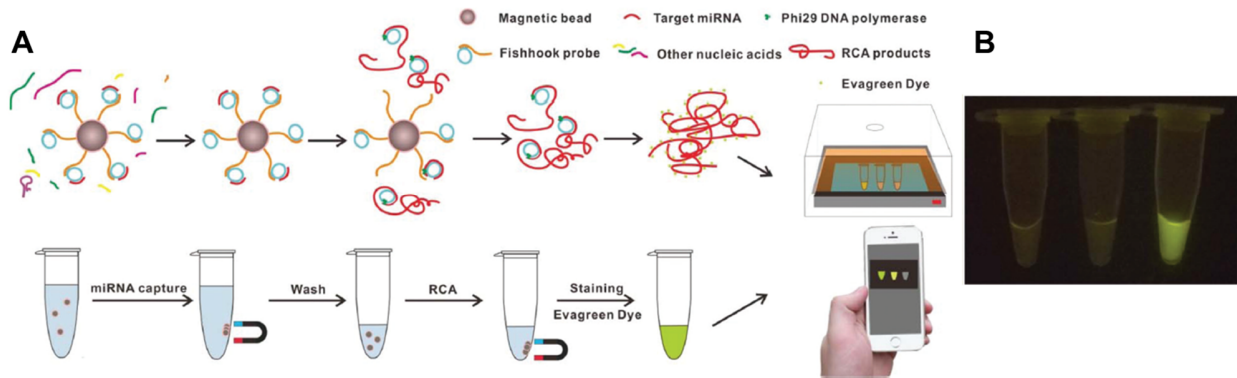


Figure 1.28 Smartphone-based setup for the detection of miRNA. (A) Solid-phase RCA functioning principle and Sample treatment workflow. (B) Smartphone images of sample containing the target sequence (right) vs two blank samples (center and left). Imaged adapted from: (Lu et al., 2018).

Proteins. Petrayayeva and Algar developed a FRET-based assay for proteolytic enzymes in blood. The system consists of a quantum dots functionalized with an acceptor-bearing peptidic chain (Petrayayeva and Algar, 2015, 2014, 2013). In absence of proteolytic enzymes, the peptide is not cleaved and the system undergoes FRET. While in presence of the target analyte the acceptor is displaced and the QD regains its fluorescence. The authors showcase the great versatility of this design by creating first a paper-based multiplexed assay, where three different color QDs (QD450: blue, QD540: green, and QD625: red) are functionalized with different acceptor-bearing peptides sensitive to three proteolytic enzymes: enterokynase, chymotrypsin and trypsin. Each QD color is monitored by one of the three RGB channels of the smartphone camera (Petrayayeva and Algar, 2014). It should be noted that despite being a FRET-based assay, the FRET acceptors are quenchers for both QD450 and QD540, while the emission of QD625 acceptor (alexa647) is filtered out by a short-pass filter. The presence of proteolytic enzyme is quantified by the recovery of QD fluorescence compared to a reference quantum dot of the same color without the acceptor.

1. Bibliographical overview

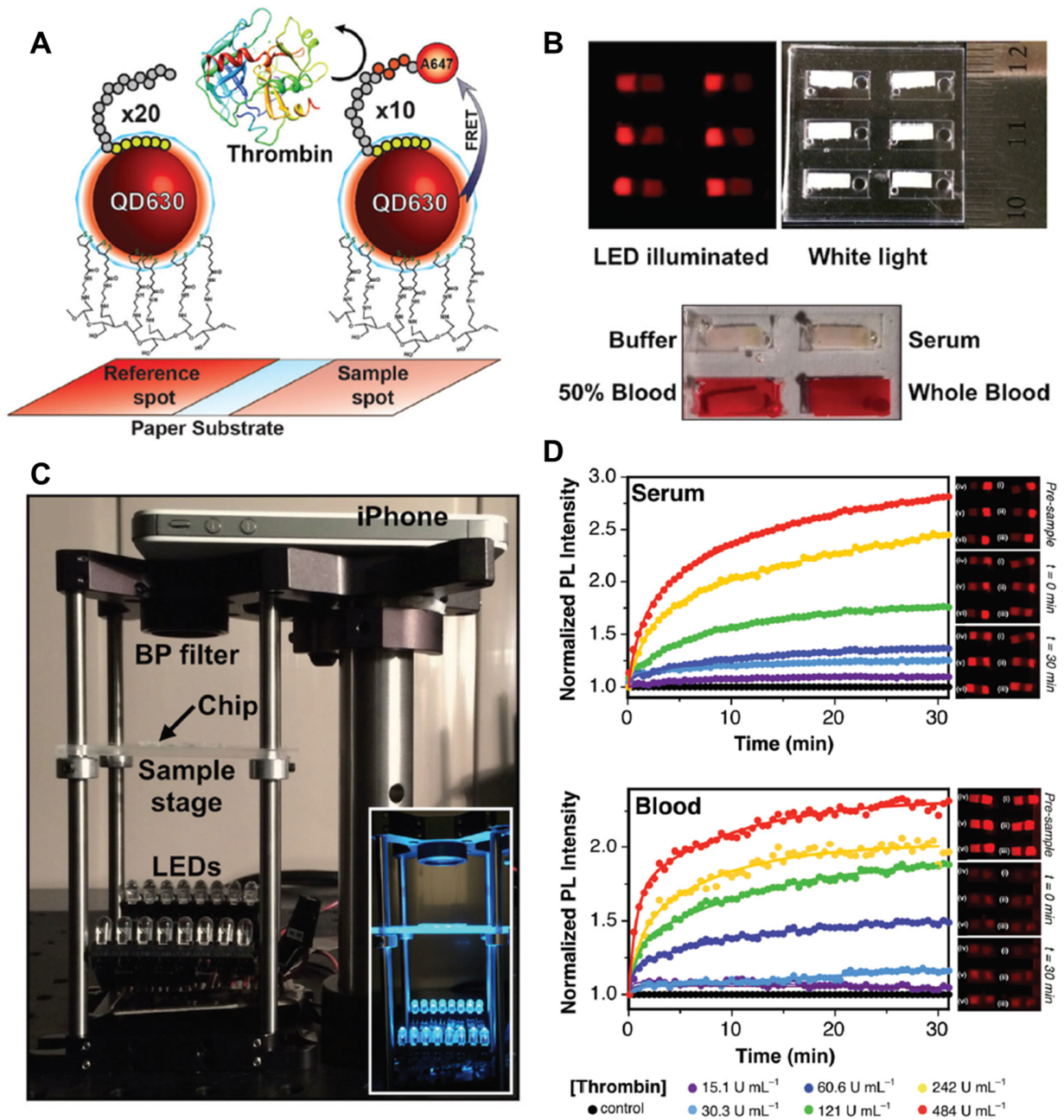


Figure 1.29 Smartphone-based detection setup for proteolytic enzymes. (A) Scheme of detection of thrombin based on QDs: QD630 is functionalized with a peptide with an IR emitting FRET acceptor on the other end. In absence of thrombin the excitation energy is transferred from the QD to the acceptor, while in presence of thrombin the peptide gets cleaved, removing the FRET acceptor. (B) Top: smartphone pictures of the QD-based test paper under LED illumination (left) and white light (right). Bottom: smartphone pictures of the test papers imbued with: buffer, serum, diluted blood, and whole blood. It should be noted that the latter has a very strong absorption in the visible. (C) Smartphone-based setup for the thrombin concentration measurement. (D) Left: Photoluminescence curves measured *via* smartphone imaging as a function of time at different thrombin concentrations in serum and whole blood. Right: smartphone pictures of the test papers from which the PL curves were derived. Images are adapted from: (Petryayeva and Algar, 2015).

1.4. Fluorescence smartphone-based detection

The authors further challenge this system by developing a setup for detecting thrombin in serum and directly in whole blood (Figure 1.29A-B). Due to blood being a strong absorber nearly everywhere in the visible spectrum, and the construction of mobile phone cameras, featuring an IR-blocking filter, leaves only the red spectral window available to detect the QD fluorescence. The multiplexing possibility is thus lost, but in exchange the authors report the conception of an extremely simple and quick point of care assay directly in a complex matrix like blood (Petryayeva and Algar, 2015) (Figure 1.29C-D).

Metabolites pose too an interest in terms of diagnostics, since many of them can be linked to disease, *e.g.* phenylalanine in phenylketonuria or glutamate in ischemic strokes. Unfortunately, the detection of many of these species is not easy or reliable, especially in complex matrices like blood. Yu *et al.* (Yu et al., 2018) present an elegant approach for point of care detection of potentially every metabolite than can be oxidized by cofactor nicotinamide adenine dinucleotide phosphate (NADP⁺), the authors validated the assay for phenylalanine, glucose, and glutamate. The assay relies on the detection of NADPH –which is produced stoichiometrically upon oxidation of the analyte– by a semisynthetic sensor protein. The sensor is composed of a NanoLuc domain, a receptor domain (Escherichia coli dihydrofolate reductase – eDHFR) and a fluorescent probe (cy3) covalently linked through a SNAP-tag. The fluorescent probe is functionalized with the ligand trimethoprim (TMP). eDHFR has a NADPH-dependent affinity for TMP, thus in presence of the analyte of interest it will bind to the receptor's domain pocket, bringing the cy3 close to the NanoLuc domain, resulting in the FRET from NanoLuc to cy3 (Figure 1.30E). The semisynthetic sensor protein was absorbed on paper, and showed high stability in time; moreover, the data obtained by photographing and quantifying the fluorescence color of the paper were in excellent agreement with the ones obtained by traditional methods, opening the way towards a quick and flexible point of care detection of metabolites (Figure 1.30F).

1. Bibliographical overview

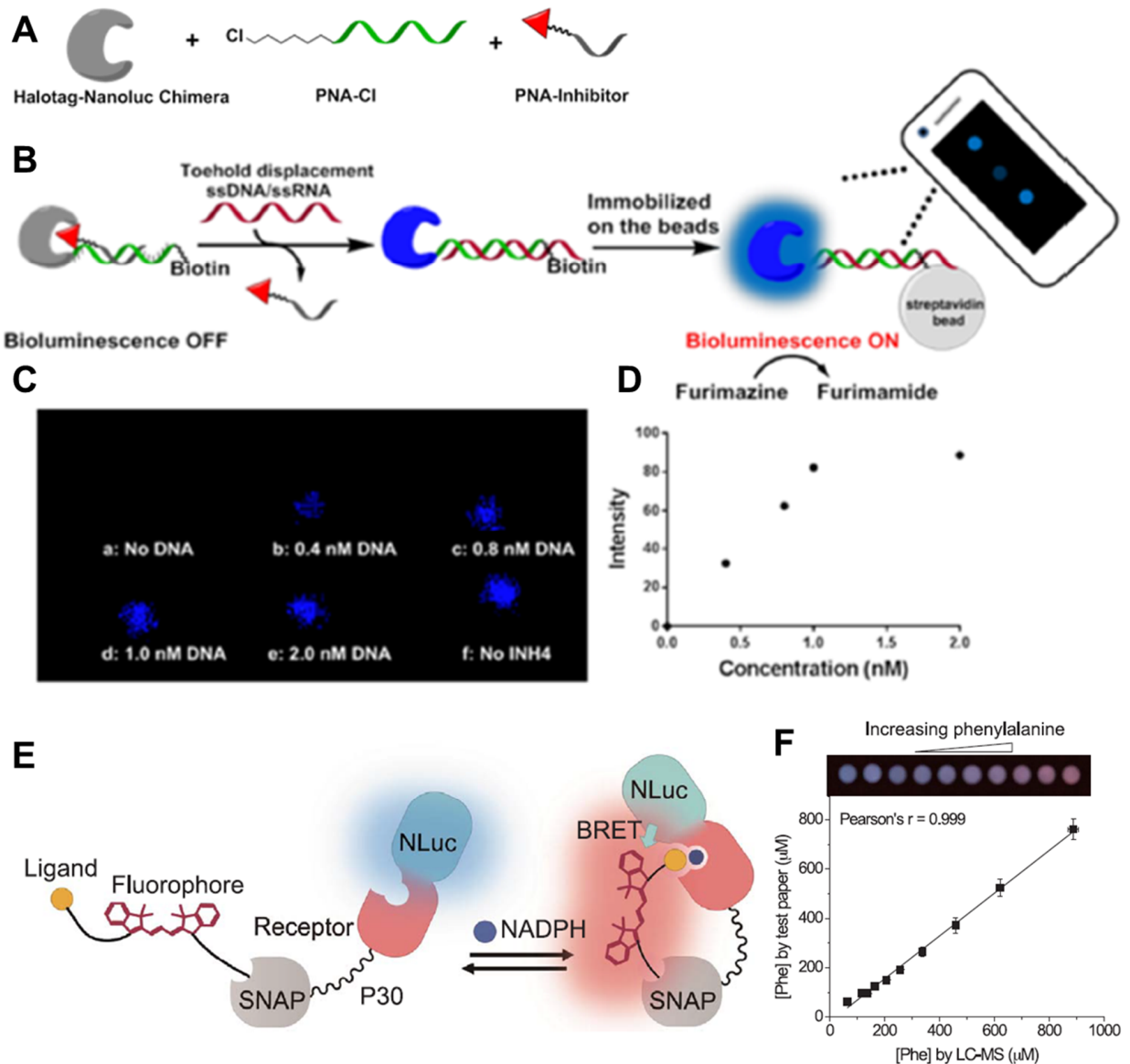


Figure 1.30 Semisynthetic protein sensors found a wide usage in fluorescence-based smartphone-enabled sensing. (A) Preparation scheme of a DNA sensor, an Halotag-NanoLuc chimera is tagged with a chloroalkane-functionalized PNA filament and subsequently annealed with a complementary short sequence bearing a bioluminescence inhibitor. (B) Sensor functioning scheme: in presence of the target sequence the inhibitor-bearing sequence gets displaced and the NanoLuc turns on, a biotin group at the end of the PNA filament allows the sensor immobilization on streptavidin beads. (C) Smartphone images of samples with increasing concentration of target (first five images) and of the sensor without inhibitor (last image). (D) Fluorescence intensity quantification of the images acquired in (C). Imaged adapted from (Chang et al., 2020). (E) Semisynthetic sensor for the detection of metabolites that can be oxidized by the cofactor NADP⁺. A protein chimera of a NanoLuc domain and a receptor domain is functionalized with a ligand-fluorophore conjugate through a SNAP tag. The receptor has a NADPH-dependent affinity for the ligand. In presence of the analyte NADPH gets produced, leading to the ligand getting complexed by the receptor pocket, resulting the NanoLuc transferring its excitation energy to the fluorophore. (F) Detection of phenylalanine using this system. At low concentrations the sensor is blue (NanoLuc emission), while at high concentration it becomes pink (cy3 emission). The PA concentration measured by this method is in good agreement with LC-MS. Imaged adapted by: (Yu et al., 2018).

1.4. Fluorescence smartphone-based detection

1.4.5. *Smartphone-enabled fluorescence microscopy*

Fluorescence microscopy in respect to fluorescence spectroscopy sensing provides more context, as it can better illuminate on the conformation of a sample and its homo/heterogeneity. However, with the wealth of information that comes with microscopy techniques, there is a price to pay in terms of technical challenges to overcome. The key point to address is the higher complexity of the setups required for microscopy in respect to simpler paper and solution-based assays. Lenses, mirrors and sources of illumination need to be cheap but of sufficient quality to ensure a good sensitivity with a consumer-grade camera. Moreover, the analysis of microscopy images is more complex than a simple color and intensity readout of an ensemble measurement, requiring –as discussed previously– the development of robust algorithms for the individuation of the regions of interest (ROIs) on which perform then the actual analysis.

Fluorescence microscopy with smartphone setups have been constructed and successfully tested for a number of different applications, such as cell imaging and counting (identification of pathogens like bacteria (Müller et al., 2018), viruses (Minagawa et al., 2019; Wei et al., 2013) and parasites (Koydemir et al., 2015; Snow et al., 2019), imaging of organs (Cho et al., 2016; Hong et al., 2016) and DNA/RNA detection (Kühnemund et al., 2017; Wei et al., 2014).

Nucleic acids (NAs). Kühnemund *et al.* (Kühnemund et al., 2017) present a smartphone-based, portable, dual-mode, fluorescence microscope for DNA sequencing (Figure 1.31D-E). The setup employs rolling circle amplification to distinguish between wild-type and mutant of the KRAS gene. The authors validated their setup both at the single molecule level and directly inside cells to detect mutation sites. The detection of the mutation comes from color: as the wild type DNA label is based on cy3 and it is selective towards G in the mutation position (corresponding to the wild-type KRAS) and A selective label (mutant type) is based on cy5. The assay was performed on a smartphone-based-microscopy setup both on slide and inside tumor cells. It was found that this setup is able to detect KRAS mutant cells at ratios as low as 1:1000 mutant to wild type cells (Figure 1.31F-G).

Another interesting example of smartphone-based imaging of nucleic acids comes from Wei *et al.* (Wei et al., 2014), in this work double strands of DNA were successfully imaged with a smartphone for the first time, and an algorithm for detecting and measuring their length was developed. Said analysis showed a good agreement with traditional microscopy data, especially for

1. Bibliographical overview

longer strands, while showing a slight inaccuracy for very short sequences (5 kbp) (Figure 1.31A-C).

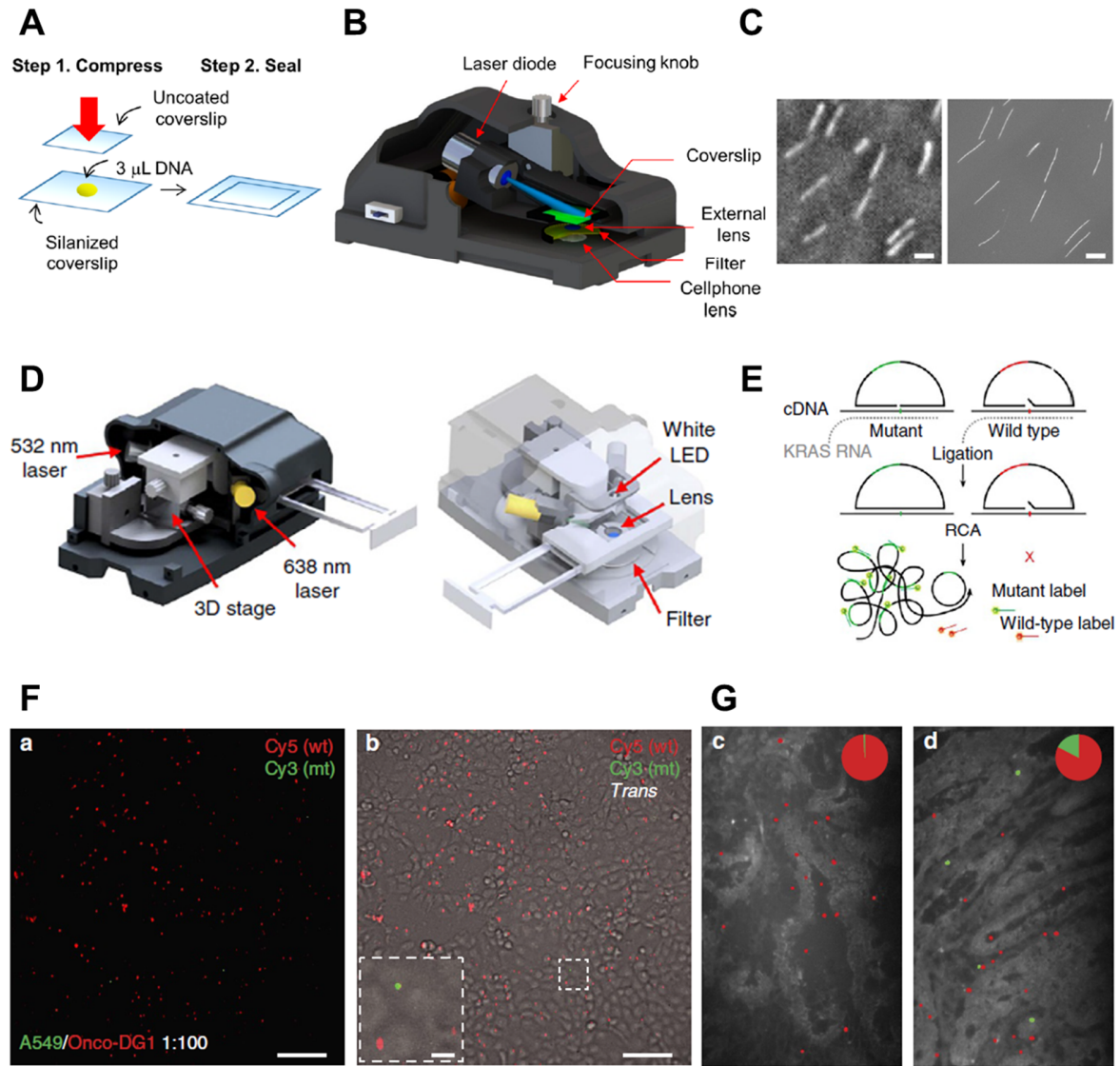


Figure 1.31 Smartphone-enabled fluorescence microscopy for DNA detection. (A) Scheme for stretching labeled DNA filaments on a glass coverslip. (B) Portable setup for imaging the DNA filaments. (C) Smartphone-acquired image of the stretched DNA filaments. Images adapted from: (Wei et al., 2014). (D) Dual-mode portable smartphone microscope for targeted DNA sequencing. (E) Scheme for in situ point mutation detection. The KRAS RNA is converted in complementary DNA on which is targeted by single-base-discriminating padlock probes. The probes are then ligated and amplified through RCA. (F) In situ KRAS mutation detection on A549 cells carrying the mutant KRAS gene and Onco-DG1 cells carrying the wildtype mixed in 1:100 proportion. Mobile-phone fluorescence image alone (left) and with bright-field channel superimposed (right). (G) In situ KRAS mutation detection in two different colon cancer tissue sections. The pie charts show the ratios between the wild type (red) and mutant (green). Scale bars are 100 μ m. Images adapted from: (Kühnemund et al., 2017).

1.4. Fluorescence smartphone-based detection

Hu *et al.* (Hu et al., 2020) constructed a setup compatible with smartphone for digital PCR and digital LAMP. It consists of a microfluidic device in which the NAs are first purified from other components in the sample using the immiscible phase filtration assisted by surface tension (IFAST) by which NA capturing magnetic beads pass through an oil phase, leaving behind all the water soluble impurities (Figure 1.32A). Then the purified DNA is mixed with PCR reagents and micro-droplets of this PCR solution are formed. The droplets arrive in a droplet tiling region which is imaged by the smartphone (Figure 1.32B). Then, a custom built application counts the number of fluorescent droplets and outputs as a result the concentration of the target sequence, since the number of fluorescent droplets correlates with the concentration of the target sequence (Figure 1.32C).

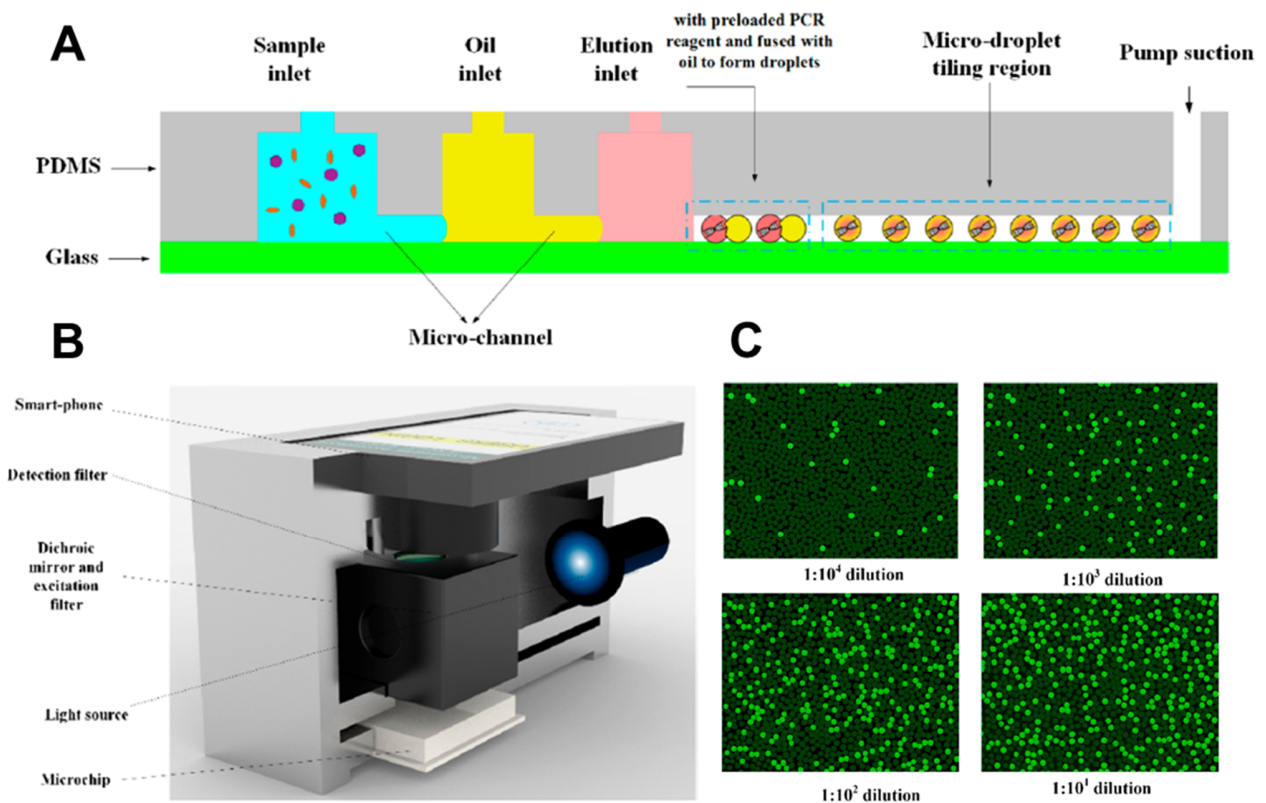


Figure 1.32 Smartphone-based setup for dPCR. (A) Sample treatment scheme: the NAs are first purified by IFAST, then mixed with PCR reagents and confined in droplets. (B) Device for imaging the qPCR droplets. (C) images of fluorescent droplets at different dilutions of target NA. By counting the fluorescent droplets, it is possible to calculate the NA concentration. Images adapted from: (Hu et al., 2020).

Cell imaging and counting. If the object of interest of the analysis is a complex structure like cells, then fluorescence-based assays are not sufficient anymore, and fluorescence microscopy

1. Bibliographical overview

is a more suitable technique. Zhu *et al.* (Zhu *et al.*, 2011) describe the construction of a lightweight and cheap optofluidic attachment for performing flow cytometry using a smartphone and they use it for counting white blood cells in whole blood after staining them with SYTO16. The results obtained with this setup are in good agreement with the ones obtained by traditional methods, with just a slight tendency to undercount, caused by, the authors believe, losses in the smartphone cytometry device.

Knowlton *et al.* (Knowlton *et al.*, 2017) developed a multimodal cytometry setup, by which it is possible to image the cells in brightfield, darkfield or fluorescence and to separate them based on their density, thanks to magnetic focusing (Figure 1.33A). The authors challenged this setup to distinguish two different populations of cells based on their density and their fluorescence color (Figure 1.33B-C). The results obtained were in good accordance with the ones obtained with traditional cytometers.

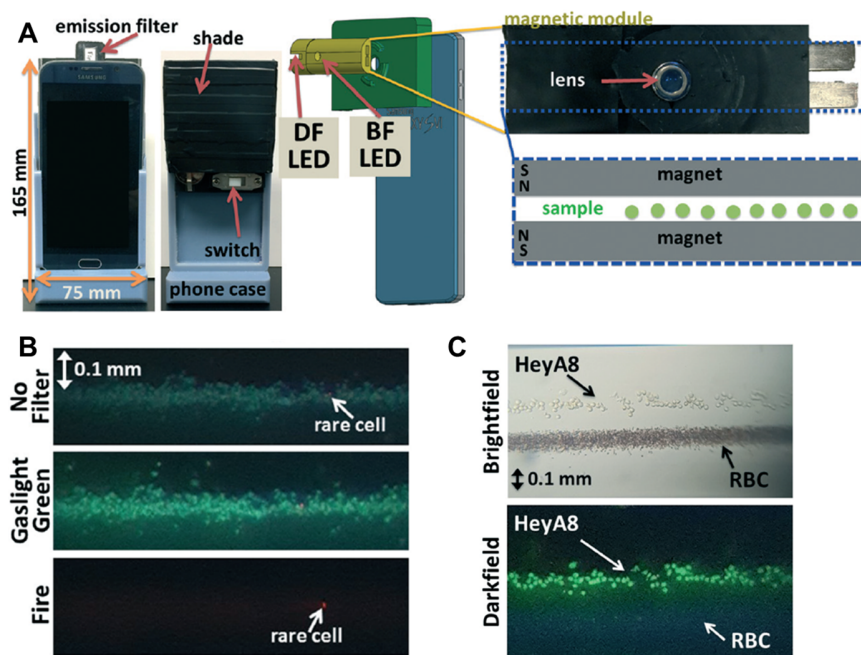


Figure 1.33 Smartphone-based flow cytometer. (A) Flow cytometer setup. (B) Imaging of a mixture of cancer cells HeyA8 stained with calcein and HeyA8 cells in a much smaller proportion stained with Qtracker 625. RGB analysis allows to distinguish cells even when present in low quantity. (C) Brightfield and darkfield images of HeyA8 cells stained with calcein and unstained red blood cells (RBC). The two populations are distinguished by density (top) and fluorescence (bottom). Images adapted from: (Knowlton *et al.*, 2017).

Tran *et al.* (Tran *et al.*, 2019) proposed a method for cell separation and phenotyping alternative to cytometry. The authors describe the preparation of magnetic nanoparticles (MNPs)

1.4. Fluorescence smartphone-based detection

coated with dextran functionalized with 1-(3-aminopropyl)imidazole (API) which are then self-assembled with quantum dots to form MNPs-QDs conjugates (MNP@QD). These nanoparticles are then used as an immunostaining contrast agent for SK-BR3 cells (which overexpress the human epidermal growth factor receptor 2, HER2), by binding them to the cell membrane with tetrameric antibody complexes (TACs). One end of the TAC binds to the QD dextran coating, while the others target HER2. SK-BR3 cells are isolated from the non-labelled cells *via* magnetic separation (Figure 1.34A), then imaged and counted by recording the QD fluorescence with a smartphone camera (Figure 1.34B). The possibility to prepare MNPs@QDs conjugates with different QDs colors offers the possibility to perform multiplex analysis (Figure 1.34C).

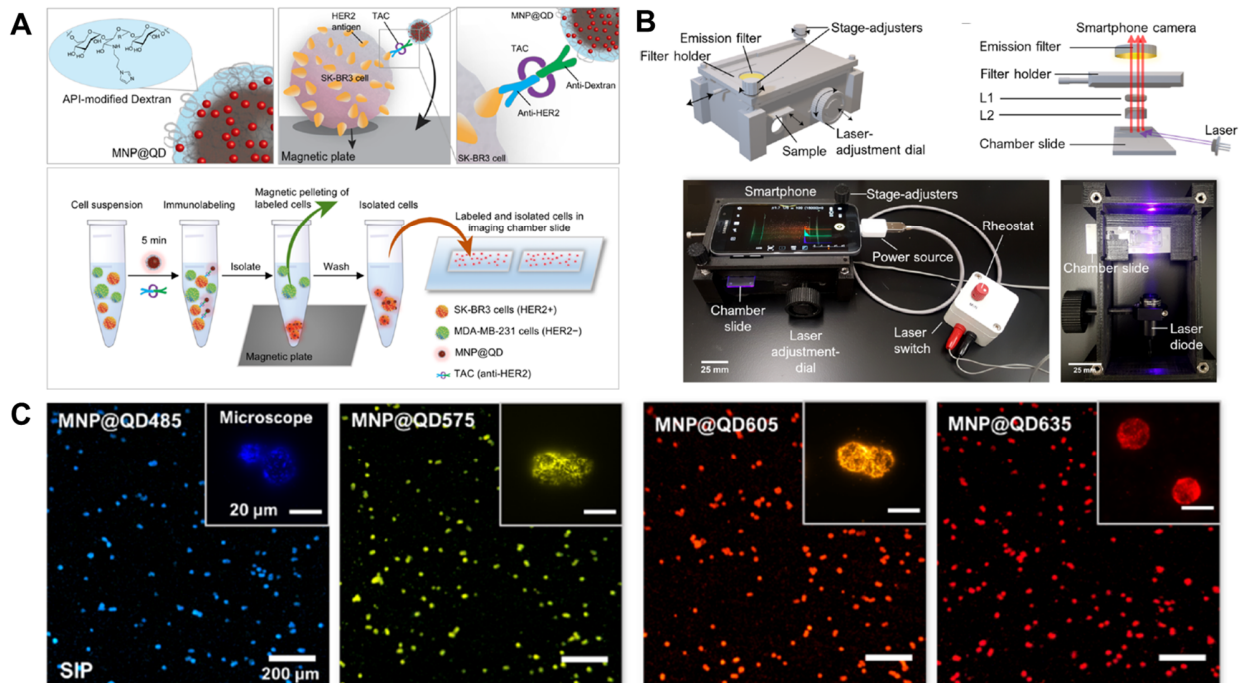


Figure 1.34 (A) Scheme of MNP@QDs conjugates, their use for immunolabeling and sample treatment. (B) Smartphone-based microscope for imaging of labeled cells. (C) Smartphone-acquired fluorescence images of SK-BR3 cells labeled with MNP@QDs of different colors. Images adapted from (Tran et al., 2019).

1. Bibliographical overview

1.5. *Specific targeting of fluorescent nanomaterials*

The capability of distinguishing between different tissues or even different cell types is of fundamental importance in biosensing. In a drug delivery context, it is vital to deliver the therapeutic agent only in the area of interest, while for targeted imaging it is desirable to have fluorescent probes as selective as possible towards the imaging target. Cellular membranes are extremely complex structures, with a variety of proteins, lipids and sugars present on their surfaces. A useful way to distinguish between different cells and tissues is to target specific species on the cell surface. This has been achieved in mainly two ways: by functionalizing the fluorescent nanoreporter with a ligand known to bind to the target species, or by “imprinting” a nanomaterial on the desired target to obtain a targeting ability.

1.5.1. *Ligand approach*

Receptor-mediated targeting is a strategy that has been extensively used to selectively accumulate an agent in a specific tissue, either for drug delivery or targeted imaging. One of the fields in which this approach is the most promising is the treatment for cancer, since cancerous cells present altered patterns of receptor expression. Due to its high incidence in rich countries and its multifaceted and aggressive nature, a massive quantity of receptors has been investigated for targeting and a multitude of targeted imaging and drug delivery systems has been developed. The topic is too vast to be treated exhaustively in this section which will be limited to a brief discussion on fluorescent nanosystems targeting the most studied receptors.

Most of the nanocarriers developed for this scope are composed of soft and organic materials such as: liposomes (Guo et al., 2018), micelles and organic nanoparticles (Duan et al., 2020). These formulations have higher chances of being biocompatible (while inorganic nanoparticles might be toxic (Hardman, 2006) or even dissolve at physiological conditions (Dukhno et al., 2018)). Since the majority of the approved nanoparticle drug formulations for cancer consist of drug-loaded PEGylated liposomes (Anselmo and Mitragotri, 2019), new liposomal nanocarriers might have a chance to be approved more quickly than other systems. The surface of self-assembled nanoparticles is easy to decorate, requiring just to functionalize the amphiphilic building blocks. Moreover, organic nanoparticles can be simultaneously loaded with both fluorophores and drugs to achieve multifunctional platforms; additionally, self-assembled nanostructures once they accumulate in the target tissue can be disrupted by irradiating with a NIR

1.5. Specific targeting of fluorescent nanomaterials

laser, causing them to release the drug in a controlled manner. However, when the dye or the drug are not covalently bound to the nanocarrier, leaching of the cargo can occur, causing only a limited quantity to reach the target tissue. When the cargo is covalently linked to the carrier the bond should be cleavable once it reaches the target tissue, meaning that careful design consideration should be done (Srinivasarao and Low, 2017). Among inorganic NPs fluorescent silica nanoparticles (Watermann et al., 2019), UCNPs (Xiong et al., 2009) and gold nanoparticles have been employed in the receptor targeting.

Folate receptors (FR) expression is very low or absent in the majority of healthy tissues, while its overexpression has been observed in a lot of different cancers, such as ovarian, cervix, brain, lung, kidney, endometrium, and head and neck (Sega and Low, 2008). It is estimated that FR overexpression is common in one third of human cancers: this might be linked to the increased demand of coenzyme folic acid, which plays a fundamental role in the synthesis of both amino acids and nucleic acids (Zaki and Tirelli, 2010). Moreover, folic acid displays a high binding affinity for FR (in the picolomolar range) (Kamen, 2004) and its carboxylic acid moiety makes it easy to functionalize. For all the aforementioned reasons FR is a popular target in the field of drug delivery and cancer imaging. Various imaging and multifunctional platforms targeting the folate receptor have been reported, both employing organic fluorophores and fluorescent nanoparticles (Guo et al., 2018; Hu et al., 2014; Liu et al., 2011; Miki et al., 2010).

Miki *et al.* (Miki et al., 2010) report the synthesis of amphiphilic copolymers subsequently grafted with folate and indocyanine green (ICG). The authors found that in aqueous solution the copolymers self-assembled in particles with diameters in the order of ~150 nm, and that when injected in live mice they would accumulate in cancerous tissue efficiently and selectively. Meanwhile, later Guo *et al.* report the conception of a self-assembled multifunctional platform: the authors prepared phospholipid liposomes featuring a surface functionalized with methotrexate, an anticancer drug with a structure very close to folic acid. Embedded in the lipid bilayer magnetic nanoparticles and cy5.5, while doxorubicin is encapsulated in the aqueous core of the liposomes (Figure 1.35A). When the nanoparticles reach the tumoral tissue an alternating magnetic field and a local precise NIR laser irradiation are applied which results in the disruption of the liposomes and release of the doxorubicin. The efficient uptake both *in vitro* and *in vivo* was monitored by fluorescence imaging of both the cy5.5 and doxorubicin (Guo et al., 2018) (Figure 1.35B).

1. Bibliographical overview

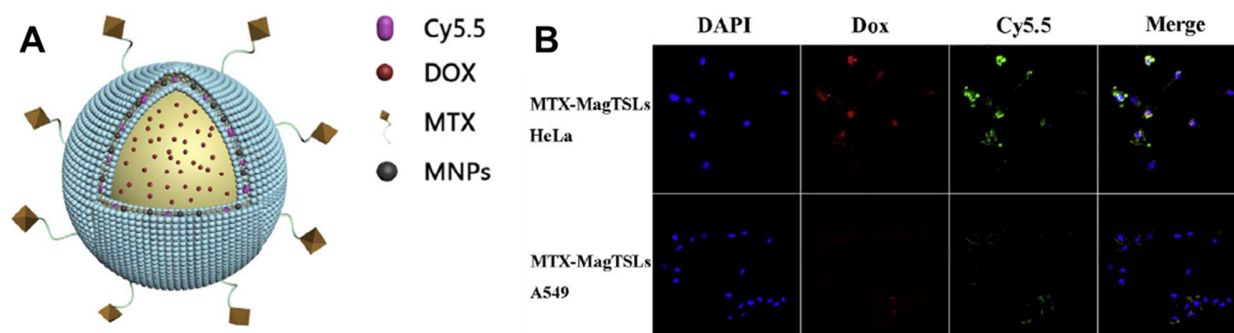


Figure 1.35 Multifunctional nanocarrier for targeting folate receptors. (A) Structure of the folate targeting liposomes: the surface is functionalized with methotrexate (MTX), a folate-targeting anti-cancer drug; in the lipid bilayer are embedded cy5.5 and magnetic nanoparticles (MNPs); while the core is loaded with doxorubicin (DOX). (B) Cellular uptake images of the nanocarriers incubated with HeLa (overexpressing FR) and A549 (not overexpressing FR) cells, showing that the liposomes internalize only into HeLa cells. Images adapted from: (Guo et al., 2018).

Epidermal growth factor receptors (EGFR) are implicated in a variety of pathways that result in apoptosis inhibition, cell proliferation, promote *angiogenesis* (the process of growing new blood vessels, on which cancer progression is dependent) and overall promote cancer survival and metastasis generation (Rocha-Lima et al., 2007). An overexpression of EGFR is generally linked to cancer aggressiveness and proliferation. Due to this, a great deal of effort has been dedicated to the design of agents targeting this receptor. EGFR can be targeted with multiple ligands, most common being EGFR-targeting antibodies (Lurje and Lenz, 2009). Watermann *et al.* report the synthesis of 45 nm silica nanoparticles with the surface functionalized with both fluorescein isothiocyanate and EGFR-targeting antibodies (Figure 1.36A). Said particles were used in confocal microscopy on both healthy and cancer cells and tissues, finding a good targeting ability (Figure 1.36B), potentially useful, the authors hope, to define quickly and reliably the tumor borders in real time (Watermann et al., 2019). Another viable route for EGFR targeting is the employment of the native ligand EGF, being a relatively small protein (6 kDa for 53 residues) in respect to antibodies, Kang *et al.* report the synthesis of magnetic NPs functionalized with a fragment of EGF and doxorubicin as an effective mean to target A549 cells (Kang et al., 2017).

1.5. Specific targeting of fluorescent nanomaterials

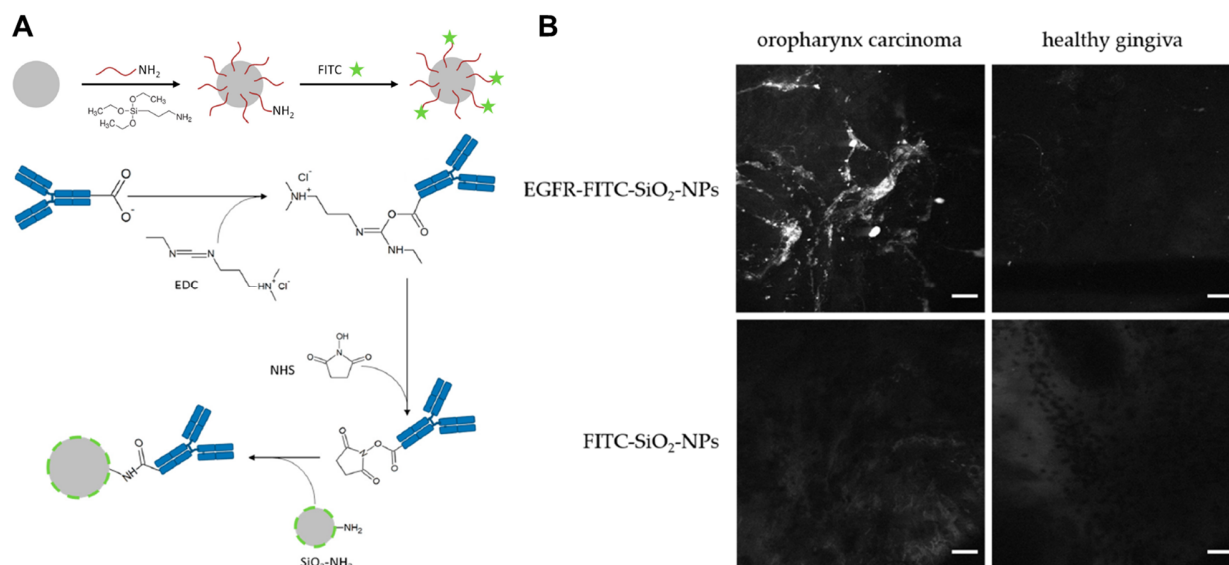


Figure 1.36 Silica nanoparticles for EGFR targeting. (A) Scheme of functionalization of silica NPs. Top: Silica NPs are reacted with APTES to graft reactive amine groups on their surface which in turn react with fluorescein isothiocyanate. Bottom: EGFR specific antibodies are activated with EDC and subsequently with NHS to graft them on the surface of silica NPs. (B) Confocal laser endoscope microscopy images of oropharynx carcinoma and healthy gingiva tissues incubated with NPs functionalized with and without EGFR targeting antibodies (top and bottom rows), incubation time was 2 minutes and NPs concentration 100 $\mu\text{g}/\text{mL}$. A preferential accumulation of targeting NPs in EGFR-overexpressing tissues is evident. Images adapted from: (Watermann et al., 2019).

Integrin receptors are implicated in angiogenesis like EGFR. Integrin receptors constitute a family of heterodimeric proteins, in mammals 18 α and 8 β subunits were identified, yielding a total of 24 receptors (Hynes, 2002). Among them $\alpha_v\beta_3$ has been the most targeted, due to its overexpression in a number of different cancers, such as melanoma, glioblastoma, ovarian, prostate and breast cancer. The most widespread ligand for $\alpha_v\beta_3$ are peptides based on either the linear or cyclic Arg-Gly-Asp (RGD) motif. Xiong *et al.* report the synthesis of a upconversion nanoparticles grafter with a cyclic RGD-containing peptide, showing targeting towards cells lines overexpressing integrin receptors both *in vitro* and *in vivo* (Xiong et al., 2009). Another impressive work on the topic is by Duan *et al.*, where the authors describe the conception of a multifunctional platform, which allows targeting of glioblastoma cells and their multimodal imaging both *in vitro* and *in vivo*. The system is composed of a poly(lactic-co-glycolic acid) (PLGA) based polymeric nanoparticle with encapsulated inside iron oxide NPs, which have the function of magnetic resonance imaging (MRI) contrast agents, and a conjugated polymer suited for photoacoustic imaging. The PLGA NPs are coated with a glioblastoma cells modified with azide groups at the plasma membrane. The membrane is stained with a NIR fluorescent dye (DiR) and cyclic RGD-containing peptides

1. Bibliographical overview

functionalized with bicyclononyne (BCN) are clicked on top of the modified plasma membrane (Figure 1.37A). Authors show that the coating consisting of a phospholipidic bilayer of glioblastoma cells allows the NPs to cross the blood-brain barrier and to accumulate in the brain tumor location in live mice (Figure 1.37B-D) (Duan et al., 2020).

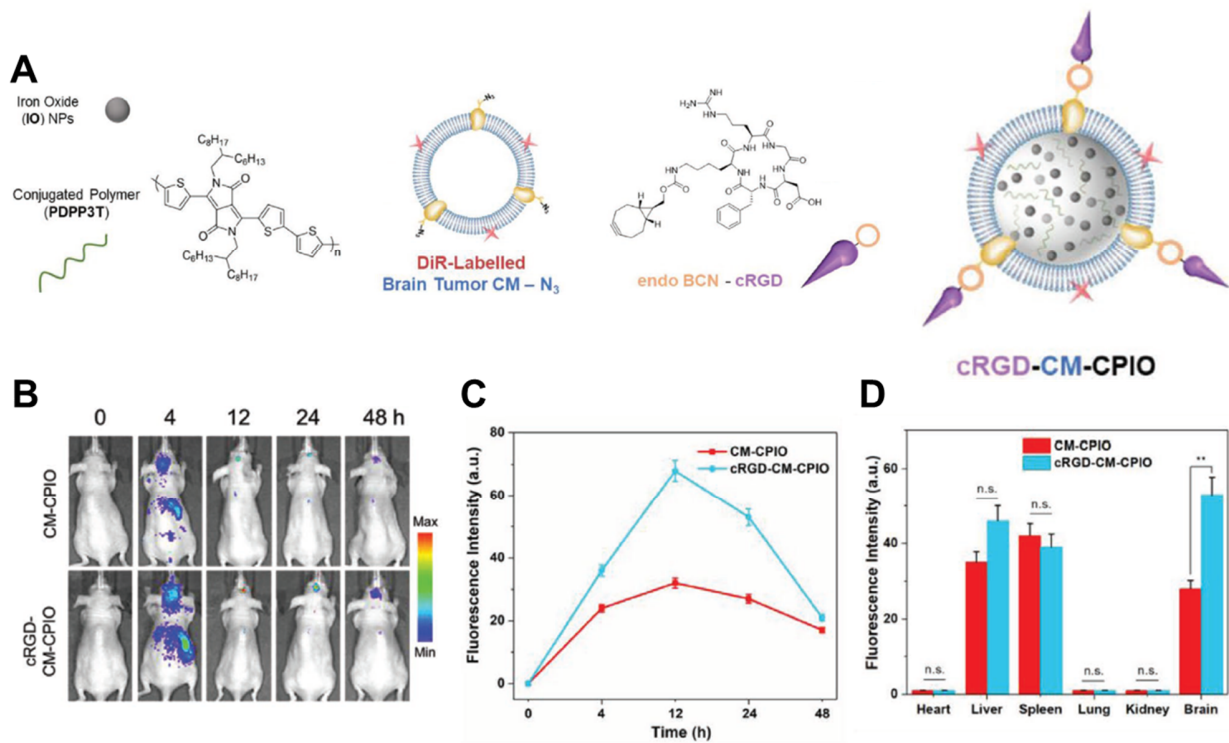


Figure 1.37 Multifunctional nanoimaging agents targeting integrin receptors. (A) Components for multifunctional PLGA-based NPs. (B) In vivo fluorescence imaging images for non-targeting NPs (top row) and targeting NPs (bottom row) at different times. (C) Fluorescence intensity in the brain tumor region at different injection times for targeting NPs and controls. (D) Fluorescence intensity in the main organs after 12 h from injection. (n = 3, ** p < 0.01, n.s.: not significant). Imaged adapted from: (Duan et al., 2020).

1.5.2. Molecularly imprinted polymer (MIP) approach

An alternative to the ligand approach to targeting is *molecular imprinting*. A great deal of effort has been devoted to produce synthetic materials able to mimic natural antibodies by binding a target species with affinity, specificity and selectivity similar to a natural system. In the last fifty years the research field of *molecularly imprinted polymers* (MIPs) has undergone an extensive development; MIPs for a variety of applications have been developed: sensing (Uzun and Turner, 2016; Whitcombe et al., 2011), imaging (Piletsky et al., 2020) and drug delivery (Wang and von Recum, 2011).

1.5. Specific targeting of fluorescent nanomaterials

The concept behind MIPs is as simple as elegant: the polymerization is carried out in presence of the target species, in order to obtain a material imprinted on the desired target. The polymerization mixture usually contains monomers able to complex the target in such a way that the monomers polymerize around the target, effectively creating a binding pocket in the material (Figure 1.38).

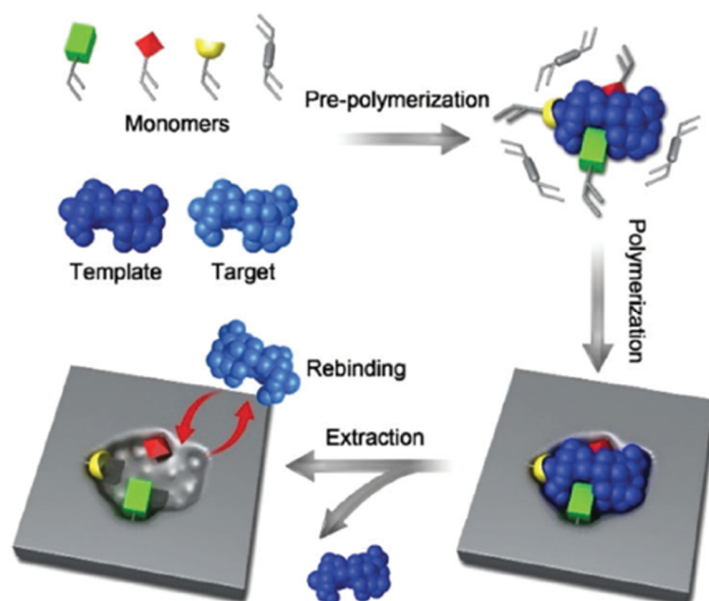


Figure 1.38 In molecular imprinting the polymerization mixture is tailored in such a way that some monomers (shown in green, red and yellow) form a complex with template (in blue), while the polymerization is carried out by a cross-linker (in grey). After a washing step to remove the template, the material has a pocket able to bind the target molecule. Image adapted from: (Pan et al., 2018).

Molecularly imprinted polymers have been developed both in form of films and nanoparticles (nanoMIPs) (Figure 1.39). MIP films are macroscopic objects and in biosensing have mainly been used for whole-cell imprinting and recognition. They are typically produced by *microcontact printing*, a technique consisting in depositing the target cells on a flat and solid support, then covering with either monomers or a soft pre-formed polymer. The mixture is then cross-linked and the as-obtained film surfaces retain shapes and selectivity towards the template cells. The affinity of these structure can be finely tuned, producing impressive results. A notable example is the imprinting of polyvinylpyrrolidone (PVP) for the recognition of erythrocyte subgroups A₁ and A₂, which present on their surface the same antigen type and differ exclusively for their glycolipids density. This work represents an important proof of concept, because it

1. Bibliographical overview

demonstrates that –unlike antibodies which target specifically antigens– MIP surfaces interact with the whole cells, allowing a degree of recognition which would be not achievable with other targeting methods (Seifner et al., 2009). On the other hand, MIP film imprinted on mature cells can direct the fate of stem cells cultured on them (Bonakdar et al., 2016; Mahmoudi et al., 2013; Mashinchian et al., 2014). The literature on this topic is rich of fascinating works demonstrating the power of this approach, which is, however, outside of the scope of this introduction.

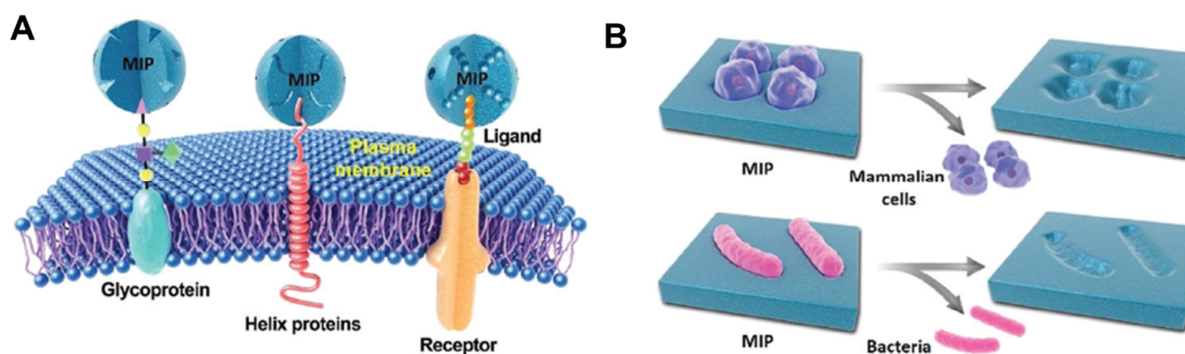


Figure 1.39 There are two main strategies to synthesize MIPs for cell recognition. (A) NanoMIPs imprinted on cell membrane proteins. (B) Whole-cell imprinted surfaces. Image adapted by (Pan et al., 2018)

1.5.2.1. Preparation techniques of nanoMIPs

A variety of techniques have been developed for the synthesis of nanoMIPs, most of them are based on free radical polymerization.

Precipitation polymerization is quite a straightforward and robust technique, which does not require the addition of stabilizers or other additives and can be performed on simple setups. The solvent plays a key role: it should be chosen in such a way that monomers, template and initiators, are well solubilized, while the polymer is not. During polymerization the chains grow until they become insoluble and precipitate. NPs synthesized *via* precipitation polymerization can have sizes ranging from 100 nm to several μm . (Wang et al., 2003; Ye et al., 1999).

High dilution polymerization like precipitation polymerization is a homogeneous technique in which a good solvent efficiently dissolves monomers, template and initiators. In this case the monomers are extremely diluted, therefore the cross-linked polymer forms into nanometric particles, instead of becoming a macroscopic gel (Figure 1.40A). Particles as small as 14 nm have been synthesized using this technique (Çakir et al., 2013).

1.5. Specific targeting of fluorescent nanomaterials

Emulsion polymerization for MIPs is quite similar to the technique described in section 1.2.6.4. One of the most notable differences is the presence of a templating agent in the polymerization mixture: which can either be in solution inside the micelles, and in this case some of the target binding sites might be inside the as-synthesized nanoparticle (Figure 1.40B); or the surfactant head itself can be the templating agent, and in this case the binding pockets of the nanoparticle are guaranteed to be exposed on its surface (Figure 1.40C) (Zeng et al., 2010).

Core-shell approaches are useful techniques to obtain multifunctional platforms, the core idea relies on synthesizing a layer of molecularly imprinted polymer on the surface of a core nanoparticle, such as, polymeric NPs (Marchyk et al., 2014), silica NPs (Shinde et al., 2015), QDs (Yang et al., 2016), upconversion NPs (Wang et al., 2017) and carbon dots (Zhang et al., 2020). The MIP shell can be grafted to the core particle by initiating the polymerization from the nanoparticle surface. This can be done *via* living polymerization, such as reversible addition–fragmentation chain-transfer (RAFT) polymerization or atom transfer radical polymerization (ATRP), or by using an iniferter coupled with an initiator grafter on the nanoparticle surface (Figure 1.40D). Another viable route is to physically encapsulate the core particle in the polymeric shell by locally initiating a photopolymerization process. It has been shown that the light emitted by single QDs, UCNPs and CDs could trigger the photopolymerization of the MIP shell.

Solid-phase synthesis is a rather innovative technique offering several advantages in nanoMIPs synthesis, namely the ease of purification and the yield of higher affinity nanoparticles. To date it has been used to produce molecularly imprinted polymers for the targeting of both small molecules (Poma et al., 2013) and proteins (Ambrosini et al., 2013). It relies on binding the templating agent on a solid phase (glass beads being the most widespread platforms) and performing the polymerization around said template. Once the reaction is over the nanoMIPs are purified through several washings (Figure 1.40E). The first rinsing at room temperature removes the unreacted monomer and the low affinity polymeric products, while the successive ones are performed at higher temperatures (60-70 °C), in order to separate the templating agent from the nanoMIPs. When performing MIP solid-phase synthesis some key points should be addressed: the high temperature washing step might be too harsh for some thermolabile templates (*e.g.* proteins) rendering impossible to reuse them multiple times.

1. Bibliographical overview

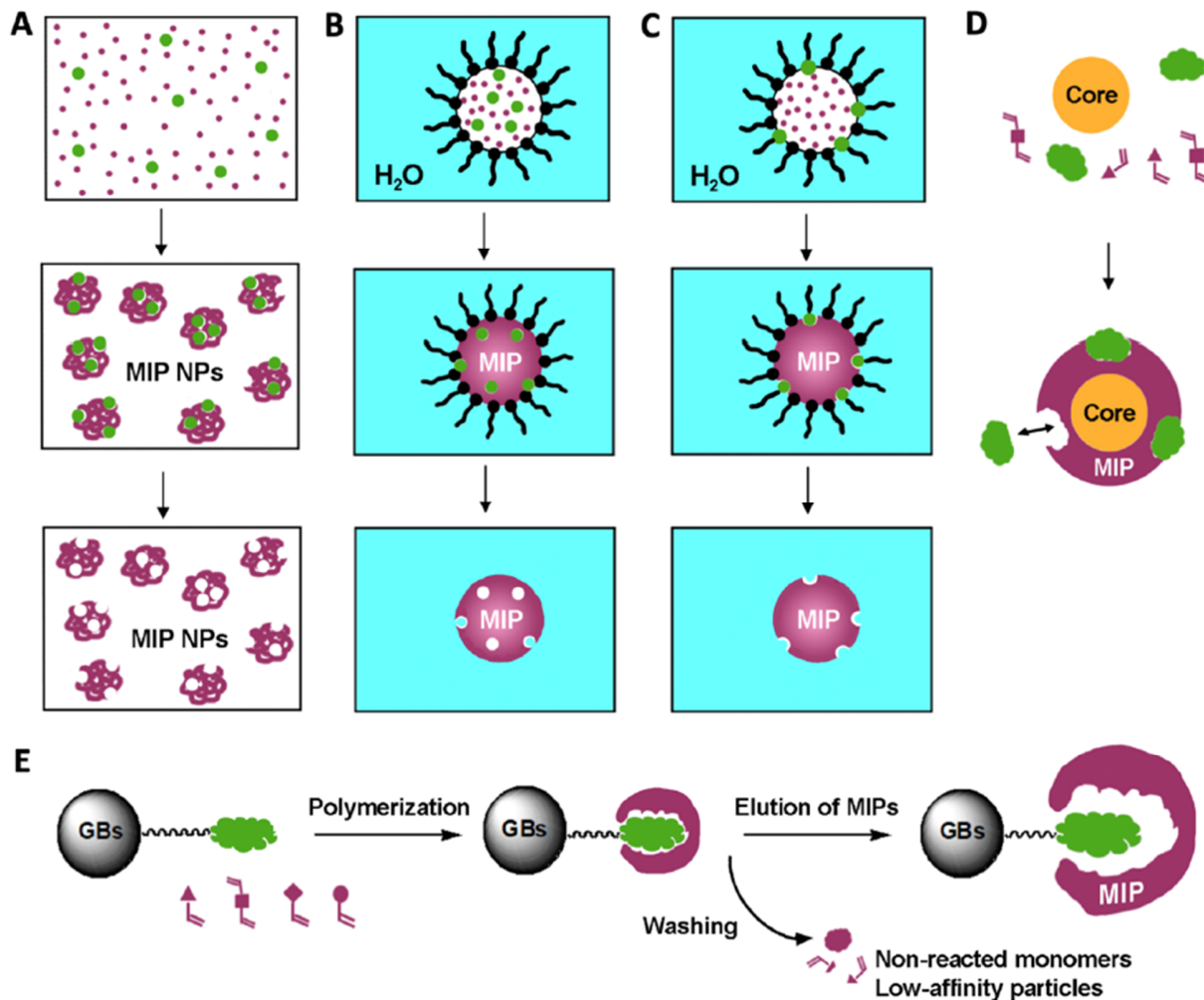


Figure 1.40 NanoMIPs synthesis techniques. (A) Precipitation polymerization. (B) and (C) Emulsion polymerization with templating agent in (B) solution and (C) bound to the surfactant head. (D) Core-shell MIP synthesis scheme. (E) Solid phase synthesis. Image adapted from (Haupt et al., 2020)

Moreover, when immobilizing proteins, usually the protein surface group of choice for linking it to the solid support is either an amino or a carboxyl group. If more than one of these groups is present on the protein surface, this could lead to the proteins to be bound in multiple different configurations, leading to the formation of nanoMIPs with different binding pockets.

1.5.2.2. *NanoMIPs for targeted imaging applications*

NanoMIPs sensitive to a variety of targets have been developed, both biological and not, with a vast number of different detection techniques (Chen et al., 2016). The topic is vast, and a good part

1.5. Specific targeting of fluorescent nanomaterials

of it outside the scope of this section, which will be limited to MIP-based fluorescence targeted imaging in biological contexts.

Glycans are important biological targets due to the process of *glycosylation* (*i.e.* the enzymatic attachment of glycans to either lipids or proteins on the cell surface) being a ubiquitous process, linked to all sorts of growth and development processes. Abnormal levels of glycosylation have been linked to diseases like cancer (Fuster and Esko, 2005), and in particular sialic acids (anionic monosaccharides located at the end of cell membrane glycans) overexpression has been associated with metastasis generation in a number of cancers (Bernacki and Kim, 1977; Dennis et al., 1982). Glycans are difficult substrates to detect by antibodies due to their weakness as antigens. Their difficulty to be detected through more traditional methods has made MIPs attractive candidates for their targeting. Panagiotopoulou *et al.* (Panagiotopoulou et al., 2017) report the synthesis nanoMIPs composed of 4-acrylamidophenyl(amino)methaniminium acetate, methacrylamide as complexing monomers and ethylene glycol dimethacrylate as a crosslinker and labelled with a polymerizable rhodamine B. These nanoMIPs were imprinted on both D-glucuronic acid and N-acetylneuraminic acid to image hyaluronan and sialylation sites on fixed cells. Another notable instance of glycan sensitive nanoMIPs has been reported by Liu *et al.*, where a fluorescent conjugated polymer, Poly(9,9-dioctylfluorene-*alt*-benzothiadiazole) (PFBT), grafted with phenylboronic acids (PBA) was employed to synthesize nanoparticle imprinted on sialic acid (SA) (Figure 1.41A), and subsequently employed for the imaging of cancer cells overexpressing SA (DU 145). The authors found that the prepared nanoMIPs stained selectively the DU 145 cells, without interacting with control HeLa cells (Figure 1.41B) (Liu et al., 2017).

1. Bibliographical overview

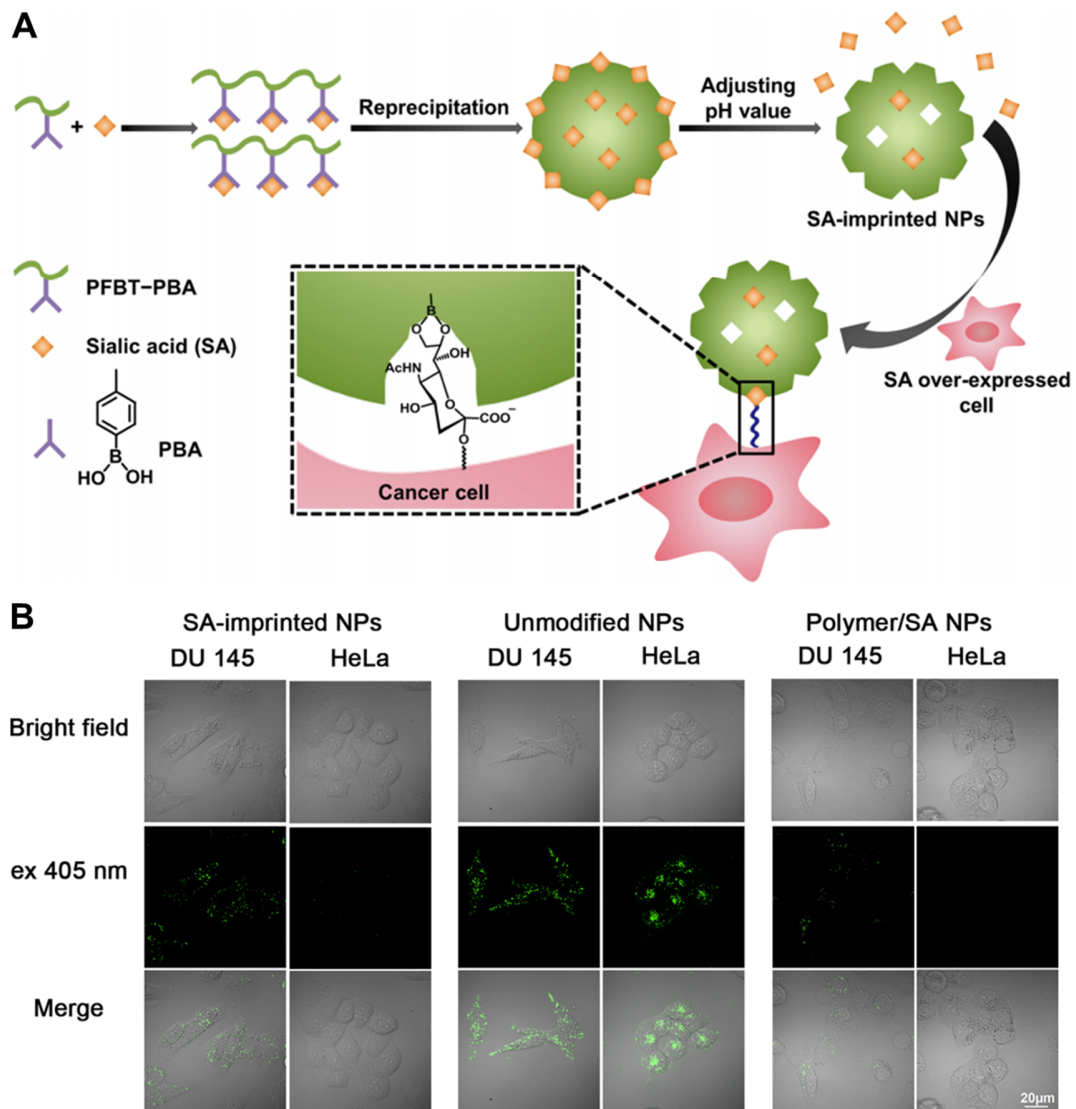


Figure 1.41 Use of MIPs to target glycans on the cell membrane. (A) Scheme of preparation of a conjugated polymer nanoparticle imprinted using sialic acid as a template. (B) Imaging of cells with surface rich in SA (DU 145) or not (HeLa) with imprinted and nonimprinted polymers. Image adapted from (Liu et al., 2017).

Proteins, especially membrane proteins are ideal targets for targeted imaging of cells. Whole proteins have been used for nanoMIPs imprinting (Piletsky et al., 2020), however, most membrane proteins are quite expensive, and therefore their employment as imprinting templates is not feasible. A much more widespread approach when producing protein targeting MIPs, is to imprint the material not on the whole protein, but on a short peptide sequence (called *epitope*), which in the protein of interest represents the region exposed to the surface. Epitope imprinting proved itself as an effective approach to target membrane proteins. Canfarotta *et al.* report a solid

1.5. Specific targeting of fluorescent nanomaterials

phase synthesis protocol to synthesize nanoMIPs imprinted on a linear epitope of epidermal growth EGFR. Doxorubicin is fed into the polymerization mixture to yield nanoparticles loaded with it, obtaining a system which doubles as an imaging and drug delivery platform (Figure 1.42A). A strong fluorescence signal was detected from cell lines that overexpress EGFR (*i.e.* MDA-MB-468), while in control cells (*i.e.* MDA-231 and SKBR3) the fluorescence signal was absent (Figure 1.42B) (Canfarotta et al., 2018).

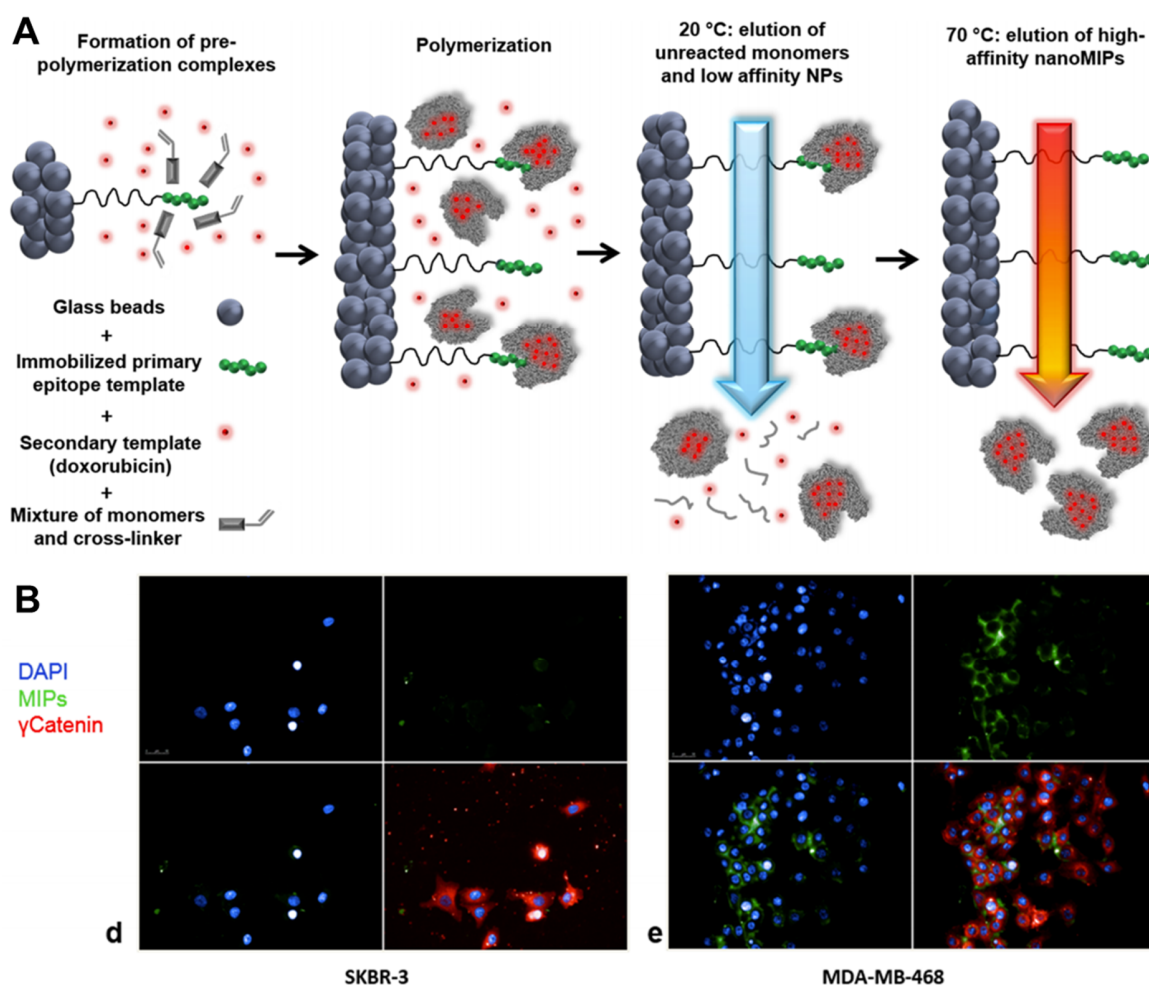


Figure 1.42 Protein targeting MIPs. (A) Preparation scheme of MIPs imprinted on the epitope of epidermal growth factor receptor. (B) Confocal microscopy of the MIPs incubated with cells not expressing EGFR (left) and overexpressing EGFR (right). Images adapted from (Canfarotta et al., 2018).

Whole cells. In the field of MIPs, a great deal of effort has been dedicated to imprint the material on whole cells, and not only on small biological molecules, with the intent of obtaining a sort of “total recognition” of the target system. Due to their size, most of the systems imprinted on

1. Bibliographical overview

whole cells are surfaces and not nanoparticles. As discussed before imprinted surfaces have, obviously, different applications than targeted imaging, and they are mainly used for cell concentration and separation as well as tissue engineering. Nevertheless, some notable examples of non-surface MIPs imprinted on whole cells can be found in literature. Magennis *et al.* presented a polymer synthesized through a copper-catalyzed ATRP. Some clinically relevant strains of bacteria such as *E. coli* and *P. aeruginosa* are known to metabolically reduce Cu(II) to Cu(I) and the authors found that the Cu(I) generation rate was high enough to promote a bacterial induced ATRP and synthesize polymer chains imprinted on the bacterial membrane, while control polymer was synthesized *via* conventional ATRP (Figure 1.43A-B). The ability to sequester bacterial cells by the imprinted and control polymers was tested by fluorescence microscopy, where the capability of the polymers to form large aggregates of bacterial cells was evaluated (Figure 1.43C) (Magennis *et al.*, 2014).

1.5. Specific targeting of fluorescent nanomaterials

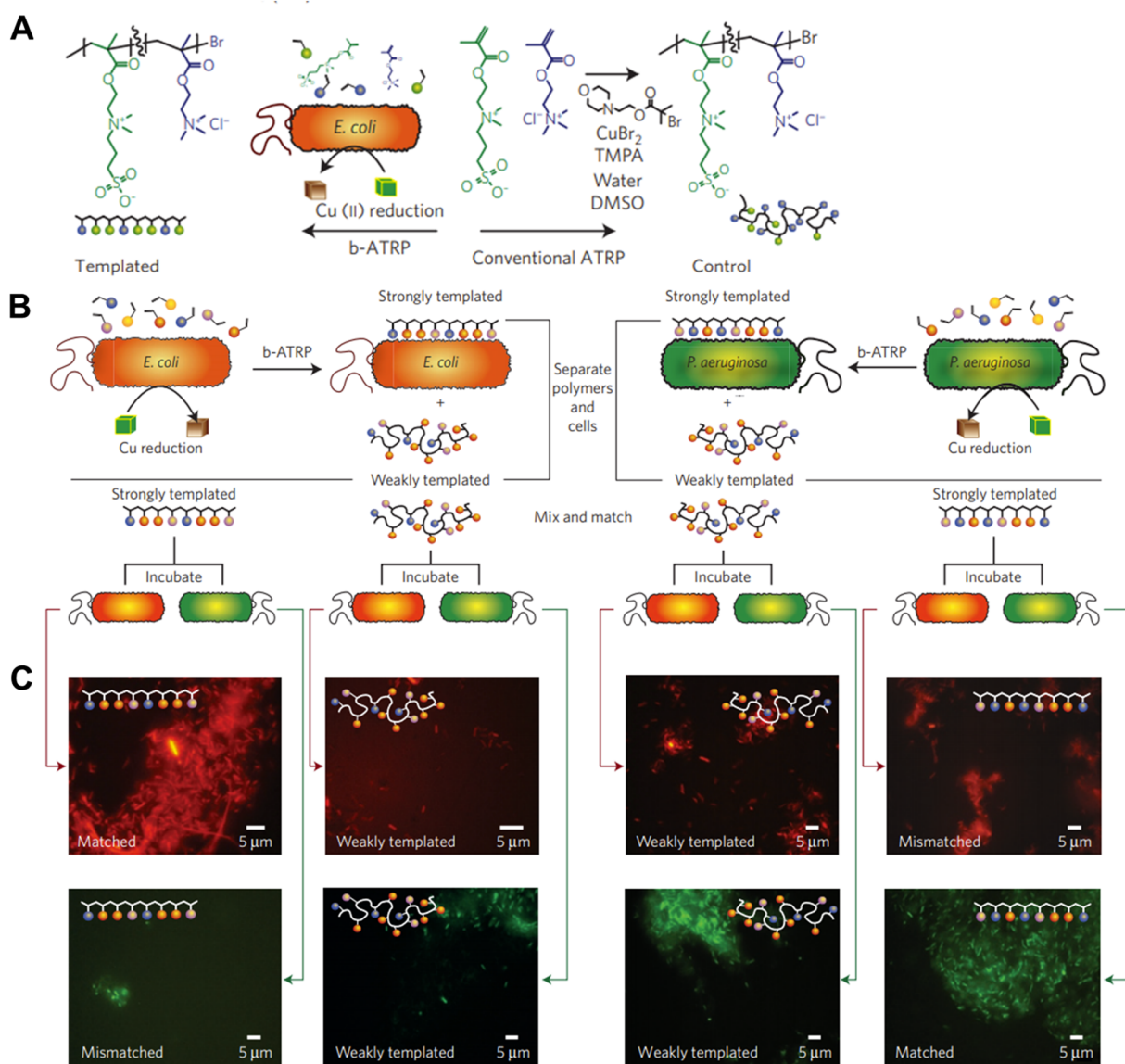


Figure 1.43 MIPs for bacterial recognition. (A) Structure of the monomers used for ATRP. Bacterial metabolism produces Cu(I) at a sufficient rate to catalyze polymerization at the cellular surface, yielding polymers imprinted on bacteria. Conventional ATRP obviously produces non-imprinted polymers. (B) Experiment scheme of molecular imprinting on two strains of bacteria to produce strongly templated polymers (at the surface) while weakly templated polymers are obtained through conventional ATRP, these polymers are then incubated with *E. coli* (expressing mCherry) and *P. aeruginosa* (expressing GFP). (C) Fluorescence microscopy images showing that bacterial strains incubated with their matched MIP aggregate to a higher degree in respect to when incubated with the mismatched MIP and the non-imprinted polymer. Images adapted from: (Magennis et al., 2014).

Aim of this PhD work

Dye-loaded polymeric nanoparticles are excellent candidates for bioimaging applications thanks to their high brightness, small size, available surface chemistry and biocompatibility. Our group developed a class of ultrabright polymeric nanoparticles.

Their size is finely tuneable in a range between 10 and 100 nm thanks to the choice of polymer and the pH of the medium used for nanoprecipitation (Reisch et al., 2015). The ACQ phenomenon in these NPs is mitigated by pairing cationic dyes with bulky hydrophobic counterions (Andreiuk et al., 2019; Reisch et al., 2014). Moreover, the counterion spaces the dyes at the optimal distance to enable the ultrafast excitation energy transfer between fluorophores (Reisch et al., 2014).

This phenomenon was exploited to synthesize a light-harvesting nanoantenna system capable of transferring the excitation energy of thousands of donor dyes towards a single FRET acceptor, greatly amplifying its signal (Trofymchuk et al., 2017). Moreover, our group also developed a robust and easy protocol to functionalize the surface of polymeric nanoparticles *via* copper-free click chemistry (Melnychuk and Klymchenko, 2018). A DNA-sensor based on these two principles was constructed for microRNA detection in cell lysates (Egloff et al., 2021; Melnychuk et al., 2020).

Dye-loaded polymeric nanoparticles are a complex system composed of multiple parts that can be individually addressed to achieve new properties and find new applications.

The first part of this work focuses on tuning the *core* properties of dye-loaded polymeric nanoparticles, *i.e.* the properties that arise from the ion pair encapsulated in the polymeric matrix. Initially we devoted our efforts to adapt the previously developed DNA-sensor to smartphone-based detection, this was achieved by developing new green-emitting dyes to be encapsulated. Afterwards we dedicated our attention to test new counterions bearing more functionalities than just mere hydrophobic spacers with the aim to obtain multi-functional platforms.

The second part of this work focuses on the *surface* properties of dye-loaded polymeric nanoparticles, with an emphasis of obtaining bioactive surfaces to achieve targeting systems. This question was tackled by two different approaches: a ligand-based approach, where ligands were grafted on the surface of nanoparticles and their ability to target specific membrane lipids and

proteins was tested. Finally, we made an attempt to develop a MIP-like approach, where nanoparticles with a surface decorated with amino-acids were developed and their capabilities to adapt to their environment were studied.

Chapter 2. Results and discussion

2.1. New dyes inside NPs: Synthesis of green-emitting nanoparticles for smartphone assisted detection of nucleic acids

Our first motivation was to change the optical properties of our dye-loaded polymeric nanoparticles with the aim to adapt them to sensing using portable devices. Indeed, testing for biomarkers at very low concentration is fundamental for the early detection of multiple diseases. To date a great deal of effort has been dedicated to the development of fluorescence-based assays for a large number of biomarkers, such as: blood analysis (Breslauer et al., 2009), pathogen agents detection (Wei et al., 2013; Zhu et al., 2012), detection of biomarkers as nucleic acids (Wei et al., 2014; Xu et al., 2020), proteins (Coskun et al., 2013) and metabolites (Yu et al., 2018). To push further the detection limit, many signal amplification strategies were proposed: either chemical, entailing the multiplication of either the analyte or the reporter species (such as PCR for nucleic acids or ELISA for proteins, antibodies and antigens); or physical, where the fluorescence signal associated to the presence of analyte is amplified by a physical effect (to this end nanostructures such as conjugated polymers, plasmonic nanoantennas and light-harvesting nanoparticles have been applied). In a point-of-care setting physical amplification strategies are more desirable, because generally the signal amplification requires less time, steps and reagents, making this approach attractive in low resources situations.

Our group recently developed a FRET-based DNA sensor constructed from dye-loaded polymeric nanoantennas (Melnychuk et al., 2020; Melnychuk and Klymchenko, 2018). Dye-loaded nanoparticles are decorated with DNA sequences complementary to the target sequence (a fragment of the sequence that encodes survivin, an important cancer marker), the FRET acceptor is introduced by annealing a short acceptor-bearing target competitive sequence (TCS). This system is able to transfer the excitation energy of thousands of encapsulated donors to few FRET acceptors on the NP surface. In presence of the target sequence the acceptor is displaced and the FRET turns off. This probe design has some remarkable points of strength, it is as bright 100 Qdot-605, the maximum acceptor signal amplification reached was of 75-fold, and its LOD is of 0.25 pM. Moreover, it also enabled detection down at the single sequence level (Melnychuk et al., 2020) and in cell lysates (Egloff et al., 2021).

2.1. Article: Preparation of green-emitting nanoparticles

However, this probe is based on rhodamine B derivatives (emitting in the orange) as FRET donors, and far-red emitting acceptors, meaning that the color change detection is not easy to detect with consumer-grade cameras and requires scientific-grade equipment such as beam splitters. The objective of the work presented in this section is to adapt this system to point-of-care settings, *i.e.* to synthesize a system whose color change can be detected by RGB cameras.

To obtain a system which is compatible with RGB detection it is necessary to select a FRET pair where emission of the donor and the acceptor is compatible with two distinct RGB channels with minimal crosstalk (Figure 2.1C-D). To this end, we designed as the FRET donors the green-emitting octadecyl ester of Rhodamine 110 (R110-C18) and the yellow-emitting octadecyl ester of Rhodamine 6G (R6G-C18). ATTO647N (Figure 2.2A) was chosen as the FRET acceptor because its absorption overlaps well with the emission of the donor dyes, thus ensuring an efficient FRET. Moreover, its emission is compatible with the red channel of RGB camera (Figure 2.1D), commonly used in smartphones.

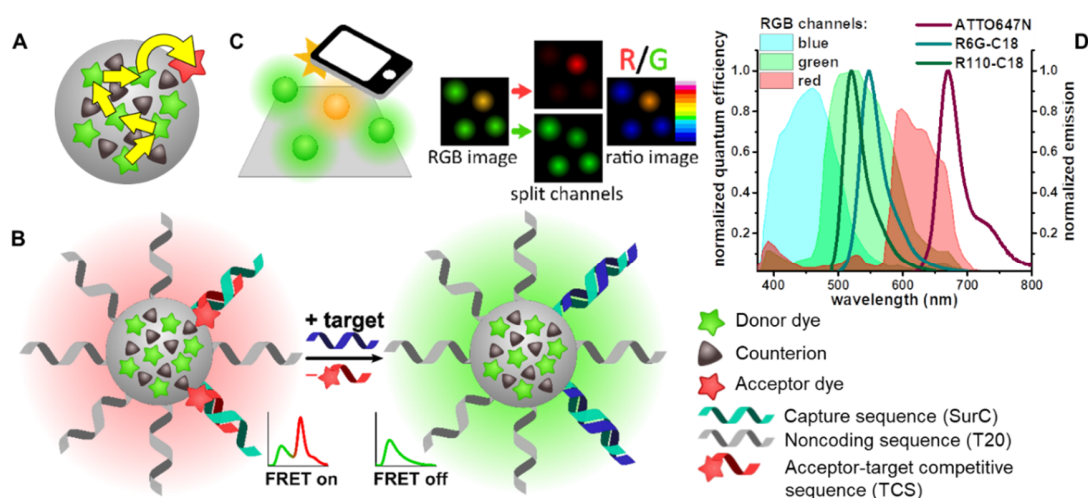


Figure 2.1 (A) Scheme depicting ultrafast intramolecular energy transfer and light harvesting of the FRET acceptor. (B) Nanoprobe design: the green donor inside NP transfer part of their excitation energy towards FRET acceptor at the surface, making the fluorescence from the nanoprobe yellow-orange. In presence of the target sequence the FRET acceptor bearing sequence is displaced, turning off FRET and switching the emission color to green. (C) Smartphone-based data analysis workflow: an RGB image is taken and the ratio between the red and green channel is evaluated; this ratio is a function of target concentration. (D) Comparison between the spectral response (quantum efficiency) of the RGB channels of the color camera (Nikon DS-Fi3) with the emission spectra in ethanol of the donor and acceptor dyes selected to the nanoprobe design.

2. Results and discussion

Polymeric NPs were prepared based on a derivative of poly(methyl methacrylate-co-methacrylic acid (PMMA-MA, 1.6% methacrylic acid) (Figure 2.2A), bearing azide groups (PMMA-AspN₃) as was previously described (Melnychuk and Klymchenko, 2018) and loaded with donor dye paired with a bulky hydrophobic counterion (Figure 2.2A-B). We chose to test two different counterions: one based on a fluorinated tetraphenylborate (F12) and tetrakis(perfluoro-tert-butoxy) aluminate (F9-Al) (Krossing, 2001), because of their already established effectiveness (Andreiuk et al., 2017a, 2017b) (Figure 2.2A).

The photophysical properties of these donor-loaded NPs were studied and the two best performing pairs, R6G-C18/F12 and R6G-C18/F9-Al were selected to prepare a FRET-based DNA nanoprobe based on previous works of our group (Melnychuk et al., 2020; Melnychuk and Klymchenko, 2018) (Figure 2.2C). Briefly: the donor-loaded NPs were decorated with DNA sequences by Cu-free click reaction, then the FRET acceptor was introduced by annealing the acceptor-bearing target competitive sequence (ATTO647N-TCS) on the surface of the nanoparticle (Figure 2.2C). In presence of the target sequence (in this work we used a fragment of the sequence which encodes survivin, an important cancer marker) the acceptor gets displaced and the FRET turns off (Figure 2.1B). The spectroscopic properties of these probes were studied (Figure 2.2D) and the best performing sample in terms optical properties and FRET-based signal amplification was determined to be R6G-C18/F9-Al.

Target detection capabilities of this system were tested both via fluorescence spectroscopy and at the single-particle level (Figure 2.2E-F). In particular, concerning single-particle measurements, we tested the capability of three different sensors to detect the color change of this probe upon addition of the target sequence: (i) our benchmark setup, a monochrome sCMOS camera equipped with a beam splitter at 640 nm, (ii) a scientific-grade RGB camera, and (iii) a consumer-grade RGB camera from a smartphone. The limit of detection (LOD) for spectroscopy in solution was found to be 3 pM, while for fluorescence microscopy (tested with the previously mentioned three different sensors) was <10 pM in all three cases. While, unsurprisingly, the sCMOS camera proved itself to be the most sensitive detector, the RGB smartphone camera performed better than the RGB scientific-grade camera. Indeed, the color change was better detected by the smartphone, opening the possibility of developing a point-of-care assays based on this system. Based on the results described in this paragraph, an article has been published: Severi,

2.1. Article: Preparation of green-emitting nanoparticles

C., Melnychuk, N. & Klymchenko, A. S. Smartphone-assisted detection of nucleic acids by light-harvesting FRET-based nanoprobe. *Biosensors and Bioelectronics* 168, 112515 (2020). A detailed description of the work can be found in the following enclosed article.

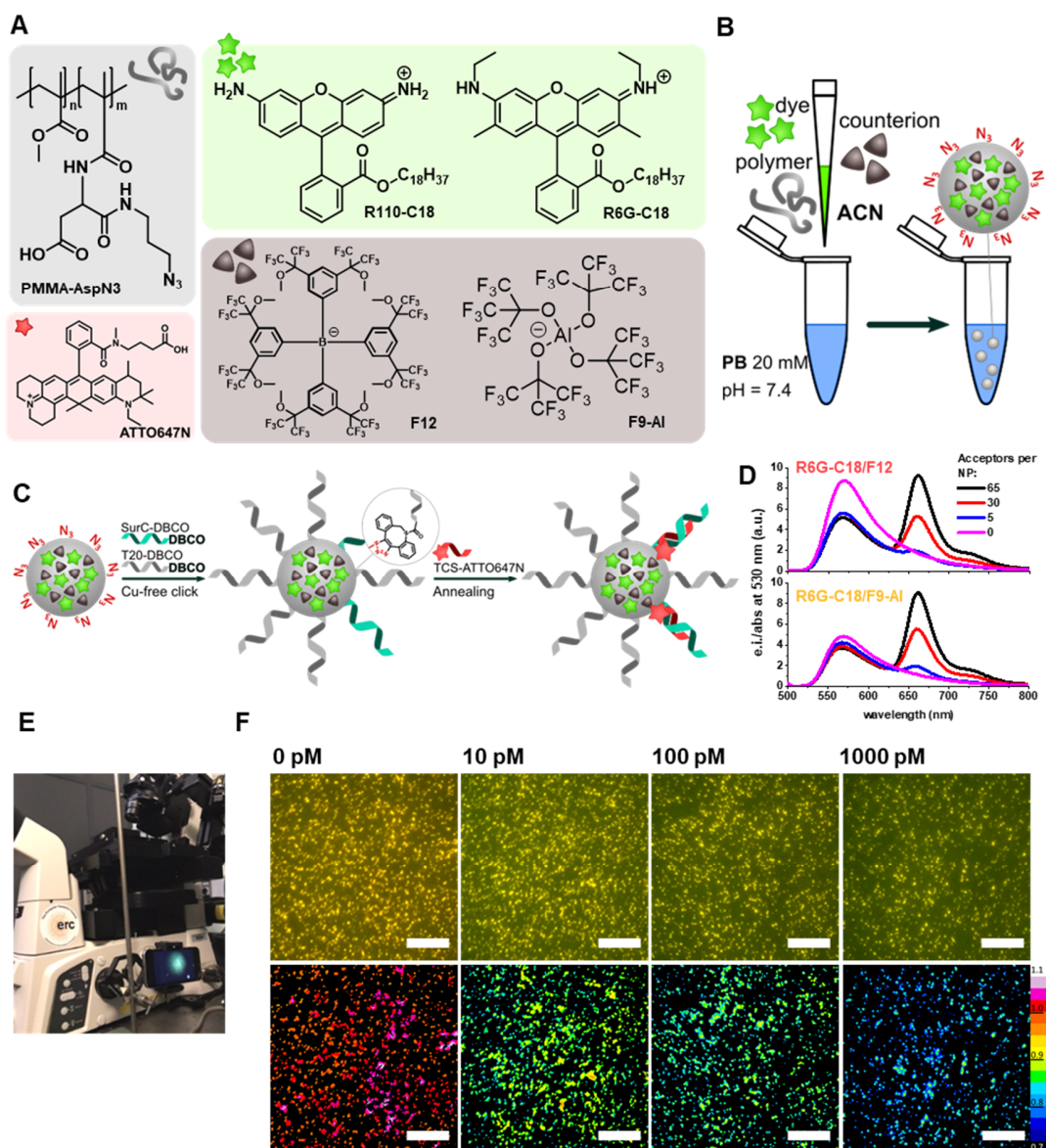


Figure 2.2 (A) Azide bearing polymer PMMA-AspN3 (top left), donor dyes (top right), counterions (lower right) and acceptor (lower left) used for the DNA nanoprobe preparation. (B) Donor-loaded NPs preparation scheme. (C) DNA nanoprobe preparation scheme. (D) Fluorescence spectra of the FRET nanoprobe loaded with two different ion pairs at increasing concentrations of acceptor. (E) Smartphone-assisted microscopy setup for detection of the DNA target sequence with probes immobilized on a glass surface. (F) Upper row: RAW RGB images acquired with a smartphone. Lower row: Ratiometric images of the red channel and the green channel of the images shown above. Images were acquired after 3 hours of incubation at room temperature with different target concentrations. Scale bars: 25 μm .

2. Results and discussion

2.1.1. Article 1. Smartphone-assisted detection of nucleic acids by light-harvesting FRET-based nanoprobe



Smartphone-assisted detection of nucleic acids by light-harvesting FRET-based nanoprobe

Caterina Severi, Nina Melnychuk, Andrey S. Klymchenko*

Laboratoire de Biophotonique et Pathologies, Faculté de Pharmacie, UMR 7021, CNRS, Université de Strasbourg, 74, Route du Rhin, 67401, Cedex, Illkirch, France

ARTICLE INFO

Keywords:

Smartphone-based detection
Detection of nucleic acids
Fluorescence microscopy
Polymeric nanoparticles
Nanoantenna
Point-of-care diagnostics

ABSTRACT

Point-of-care assays for optical detection of biomolecular markers attract growing attention, because of their capacity to provide rapid and inexpensive diagnostics of cancer and infectious diseases. Here, we designed a nanoprobe compatible with a smartphone RGB camera for detection of nucleic acids. It is based on light-harvesting polymeric nanoparticles (NPs) encapsulating green fluorescent donor dyes that undergo efficient Förster Resonance Energy Transfer (FRET) to red fluorescent acceptor hybridized at the particle surface. Green-emitting NPs are based on rhodamine 110 and 6G dyes paired with bulky hydrophobic counterions, which prevent dye self-quenching and ensure efficient energy transfer. Their surface is functionalized with a capture DNA sequence for cancer marker survivin, hybridized with a short oligonucleotide bearing FRET acceptor ATTO647N. Obtained 40-nm poly(methyl methacrylate)-based NP probe, encapsulating octadecyl rhodamine 6G dyes with tetrakis(perfluoro-tert-butoxy)aluminate counterions (~6000 dyes per NP), and bearing 65 acceptors, shows efficient FRET with >20% quantum yield and a signal amplification (antenna effect) of 25. It exhibits ratiometric response to the target DNA by FRET acceptor displacement and enables DNA detection in solution by fluorescence spectroscopy (limit of detection 3 pM) and on surfaces at the single-particle level using two-color fluorescence microscopy. Using a smartphone RGB camera, the nanoprobe response can be readily detected at 10 pM target in true color and in red-to-green ratio images. Thus, our FRET-based nanoparticle biosensor enables detection of nucleic acid targets using a smartphone coupled to an appropriate optical setup, opening the way to simple and inexpensive point-of-care assays.

1. Introduction

Point-of-care (PoC) diagnostics is a forefront research direction devoted to greatly accelerate early diagnostics of diseases (Yang et al., 2019). Ideally, point-of-care testing devices should be inexpensive, portable and easy to use while still being sensitive and selective towards the target species. A great deal of efforts has been devoted to the construction of the electrochemical biosensors, which match these requirements (Chen and Chatterjee, 2013; Dakshayini et al., 2019; Roy et al., 2019; Shetti et al., 2019). Smartphones are exceptional candidates in the biosensor development due to their almost universal prevalence (Zhang and Liu, 2016). Fluorescence smartphone-based detection systems were developed for a variety of scopes, such as: blood analysis (Breslauer et al., 2009), detection of viruses (Wei et al., 2013), bacteria (Zhu et al., 2012), cells (Breslauer et al., 2009), proteins (Coskun et al., 2013), nucleic acids (Wei et al., 2014; Xu et al., 2020) and DNA sequencing (Kühnemund et al., 2017). However, smartphone cameras

are generally less sensitive than the devices commonly used in research, featuring sensitivity down to single-molecule detection (Kanchi et al., 2018). Sensitivity is a vital quality of point-of-care devices, in order to permit the detection of very low concentration of an analyte, thus allowing early diagnosis of diseases.

The inherent limitation of fluorescence-based assays is the limited brightness of fluorescent dyes (Grimm et al., 2015). This has led to the development of many amplification strategies for which single molecular recognition event triggers a response equivalent to hundreds of fluorescent dyes (Scrimin and Prins, 2011). This amplification can be achieved by increasing the number of target molecules, as in polymerase chain reaction (PCR) and methods based on enzymatic amplification or hybridization chain reactions (Ali et al., 2014; Choi et al., 2010). An alternative approach is direct amplification of the fluorescence signal from the dye, which is attractive for PoC applications owing to its simplicity. In this respect, three systems have already been established: (i) plasmonic nanostructures, which amplify the fluorescence of single

* Corresponding author.

E-mail address: andrey.klymchenko@unistra.fr (A.S. Klymchenko).

dyes located at a precisely controlled distance (Acuna et al., 2012; Wei et al., 2017); (ii) light-harvesting with conjugated polymers (Jiang and McNeill, 2017), in which a large number of π -conjugated aromatic units efficiently transfer the excitation energy to one energy acceptor (Rochat and Swager, 2013) and (iii) light-harvesting with dye-loaded fluorescent polymeric nanoparticles (Trofymchuk et al., 2017).

Previously, we developed dye-loaded polymeric NPs encapsulating hundreds of rhodamine dyes paired with a bulky hydrophobic counterion (Reisch et al., 2014; Reisch and Klymchenko, 2016). The use of the bulky counterion ensures efficient dye encapsulation without leakage in biological media, prevents aggregation-caused quenching of dyes at high loading and at the same time assembles dyes inside the polymeric matrix with relatively short spacing, inducing a collective behavior of dyes inside the nanoparticle (Andreiuk et al., 2019; Reisch et al., 2017). This collective behavior was exploited to design a giant light-harvesting nanoantenna that undergoes efficient Förster Resonance Energy Transfer (FRET) from $\sim 10,000$ donor dyes to very few acceptors inside the nanoparticle, yielding an amplification of the acceptor signal of ~ 1000 times (Trofymchuk et al., 2017). These nanoantennas were then functionalized with DNA yielding nanoprobe for nucleic acids, stable in physiological conditions and operating by FRET with strand displacement mechanism (Melnychuk and Klymchenko, 2018). The obtained nanoprobe, being ~ 100 times brighter than QDot-605, produced a donor/acceptor ratio response to single hybridization events (Melnychuk et al., 2020).

In a single-molecule FRET detection, highly sensitive monochromatic cameras are used with an image splitting module (Roy et al., 2008), which is a highly costly and difficult to handle considering point of care devices. Modern consumer grade cameras are comprised of a color filter array for red, green and blue light (RGB) overlaid on an active pixel sensor array based on a complementary metal-oxide semiconductor (CMOS) light sensor (Takayanagi, 2006). These cameras allow the simultaneous detection of three spectral channels and can provide a rapid and simple detection of color change in FRET nanoprobe (Wang et al., 2011). FRET detection assays with the RGB camera of a smartphone is an emerging field (Noor and Krull, 2014; Petryayeva and Algar, 2015; Yan et al., 2018). However, smartphone-based FRET detection at the single nanoparticle level has not been achieved so far, which would open the opportunity to ultrasensitive point-of-care detection. Light-harvesting dye-loaded polymeric NPs, owing to their exceptional brightness, offer this opportunity; but in these nanoprobe both donor and acceptor emit in the red region (Melnychuk et al., 2020; Melnychuk and Klymchenko, 2018), which make these probes not compatible with common RGB cameras.

In this work, we redesigned these light-harvesting nanoprobe for nucleic acids to make them compatible with RGB detection. We selected a donor-acceptor FRET pairs with emissions compatible with the red and green channels of the RGB camera and designed nanoprobe for a nucleic acid fragment encoding survivin, an important anti-apoptotic cancer marker (Altieri, 2003; Stobiecka et al., 2019). We found that the optimized nanoprobe provides a ratiometric response to the target nucleic acid with limit of detection in solution of 3 pM. Remarkably, our nanoprobe, immobilized on glass surface, enabled detection of nucleic acids at the single-particle level, using RGB microscopy camera as well as a smartphone camera. We show that our biosensor system can work with an inexpensive consumer-grade RGB camera, using low excitation power densities. These results open the route to very simple smartphone-based biosensing devices for point-of-care detection of nucleic acid markers of diseases.

2. Results and discussions

2.1. Design of RGB compatible FRET-based nanoprobe

The design of the nanoparticle probe is based on DNA-functionalized nanoantenna, which serves as a FRET donor for a FRET acceptor

conjugated to a short oligonucleotide hybridized at the particles surface (Fig. 1A and B). Then, hybridization with the target nucleotide displaces the acceptor leading to FRET turn off and thus a color switch (Melnychuk and Klymchenko, 2018; Melnychuk et al., 2020). To obtain a system compatible with RGB detection, it is necessary to select a FRET pair where emission of the donor and the acceptor is compatible with two distinct RGB channels with minimal crosstalk (Fig. 1C and D). To this end, we designed as the FRET donors the green-emitting octadecyl ester of Rhodamine 110 (R110-C18) and the yellow-emitting octadecyl ester of Rhodamine 6G (R6G-C18). Both of them emit in the green channel region of the RGB systems (Figs. 1D and 2A). They were synthesized by esterification of corresponding acid form of the dyes with octadecanol in acidic conditions. ATTO 647N (Fig. 3B) was chosen as the FRET acceptor because its absorption overlaps well with the emission of the donor dyes, thus ensuring an efficient FRET, and its emission is compatible with the RGB red channel (Fig. 1D).

2.2. Donor NPs preparation

Polymeric NPs were prepared based on a polymer derivative of poly (methyl methacrylate-co-methacrylic acid (PMMA-MA, 1.6% methacrylic acid) (Fig. 2A) bearing azide groups (PMMA-AspN3) as was previously described (Melnychuk and Klymchenko, 2018) and loaded with donor dye paired with a bulky hydrophobic counterion. The role of the counterion is to insulate the dye molecules in order to prevent their aggregation-caused quenching (ACQ) (Reisch et al., 2014) and to ensure their efficient encapsulation without dye leakage in biological environment (Andreiuk et al., 2017b). Moreover, the presence of counterion creates a supramolecular organization of dyes and counterions which produce an ultrafast excitation energy migration allow efficient FRET from thousands of donor dyes to few acceptors (Trofymchuk et al., 2017). We chose to test two different counterions: one based on a fluorinated tetraphenylborate (F12) and tetrakis(perfluoro-tert-butoxy) aluminate (F9-Al) (Krossing, 2001), because of their already established effectiveness (Andreiuk et al., 2017a, 2017b) (Fig. 2A).

The two donor dyes were paired with the two counterions, using ion exchange method (Reisch et al., 2014), for a total of four ion pairs. Then, NPs were prepared by nanoprecipitation of the polymer with these four pairs at three different loadings (10, 120 and 250 mM with respect to the polymer). Charged carboxylate group in the polymer ensures controlled formation of the small particles during nanoprecipitation due to electrostatic repulsion (Reisch et al., 2018, 2017). The as-prepared samples were characterized by dynamic light scattering (DLS) and optical spectroscopy. Hydrodynamic diameters of NPs remained relatively stable, in the range of 35–50 nm, independently of dye loading and ion pair (Table S1 of the Supplementary Materials). The increase in the dye loading resulted in some broadening of the absorption and emission spectra, indicating the effect of dye aggregation in the polymer matrix. These changes were accompanied by blue shifts in the absorption spectra and red shifts in the emission spectra, which were more pronounced for the R6G-C18 dyes (Fig. S1 of the Supplementary Materials). For all ion pairs the fluorescence quantum yields (QY) decreased with the loading due to some ACQ. Nevertheless, R6G-C18/F12 loaded NPs displayed relatively high QY (Fig. 2C), around 20% at 250 mM dye loading (i.e. ~ 6000 dyes per particle) and the emission band for all dye salts remained relatively narrow (Fig. 2D).

2.3. FRET-based DNA nanoprobe preparation

Ion pair R110-C18/F12 was excluded from FRET studies, because of its too low quantum yield (Fig. 2C). For the remaining ion pairs, NPs loaded with 250 mM and different quantities of FRET acceptor (DiD, Fig. S3, Supplementary Material) were prepared by co-precipitating donor and acceptor dyes together and their FRET properties were studied (Figs. S4–S6, Supplementary Material). It was found that both R6G-C18/F12 and R6G-C18/F9-Al performed better in terms of FRET

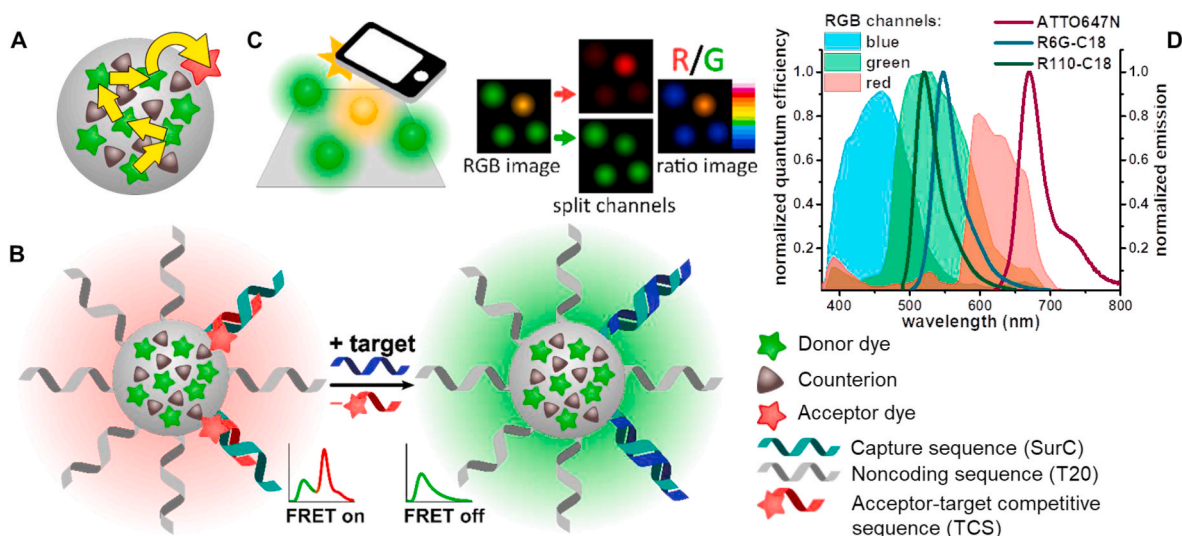


Fig. 1. DNA nanoprobe for smartphone-based RGB detection of nucleic acids. (A) Light-harvesting in the nanoantenna particles: donor-donor excitation energy transfer inside NPs is followed by FRET to the acceptor at the NP surface. (B) Nanoprobe design: the green donors inside the NP transfer part of their excitation energy towards FRET acceptor at the surface, making the fluorescence from the nanoprobe yellow-orange. In presence of the target sequence bearing the FRET acceptor is displaced, turning off FRET and switching the emission color to green. (C) Smartphone-based data analysis workflow: an RGB image is taken and the ratio between the red and green channel is evaluated; this ratio is a function of target concentration. (D) Comparison between the spectral response (quantum efficiency) of the RGB channels of the color camera (Nikon DS-Fi3) with the emission spectra in ethanol of the dyes selected for the nanoprobe design. (For interpretation of the references to color in this figure legend, the reader is referred to the Web version of this article.)

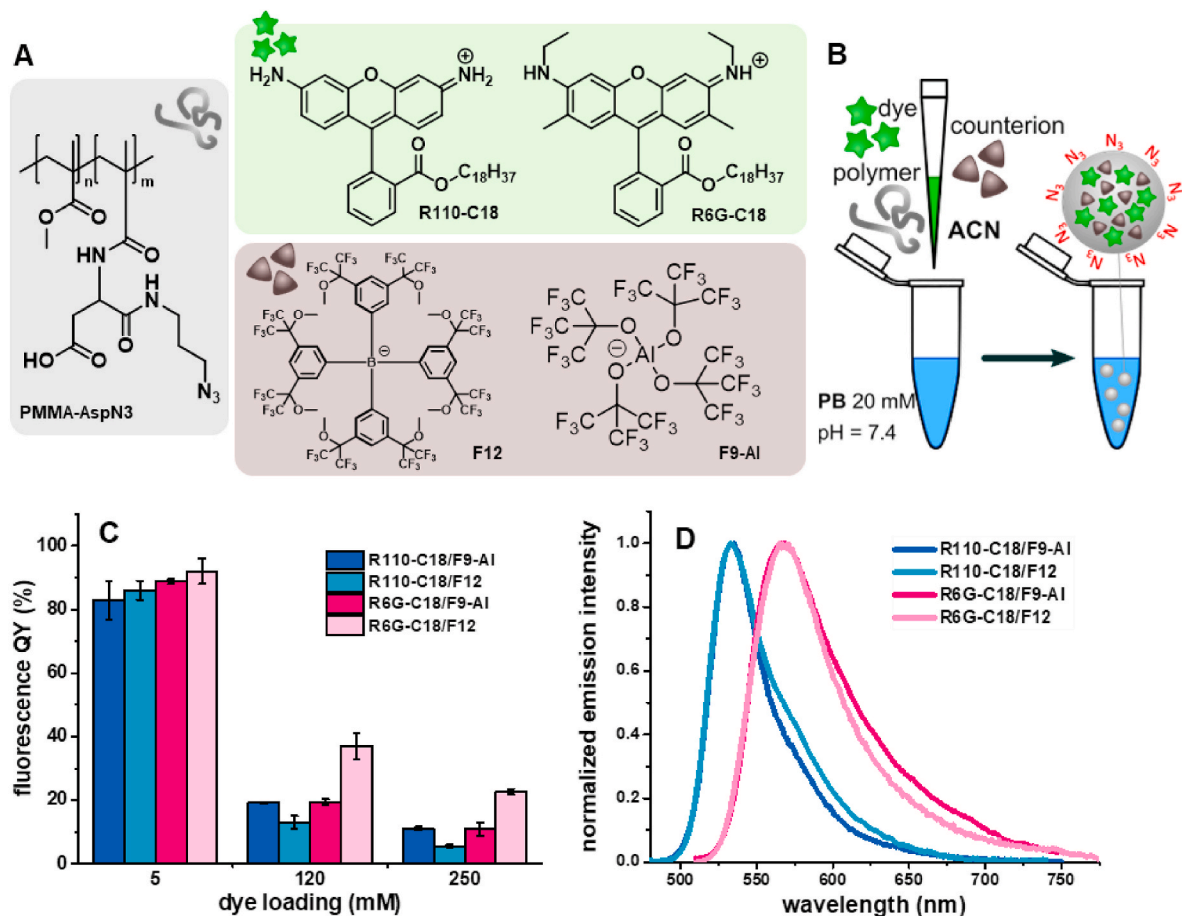


Fig. 2. Design and fluorescence properties of light-harvesting nanoantenna particles (donor NPs). (A) Azide-modified polymer PMMA-AspN3 (left), dyes (upper row) and counterions (lower row) used for the nanoparticles preparation. (B) Nanoparticles preparation scheme: nanoprecipitation from acetonitrile (ACN) to phosphate buffer (PB). (C) Quantum yields of NPs prepared with different dye salts at different loadings. Error bars are standard deviation ($n = 3$). (D) Fluorescence spectra for the NPs formulated with the four different dye salts at 250 mM loading.

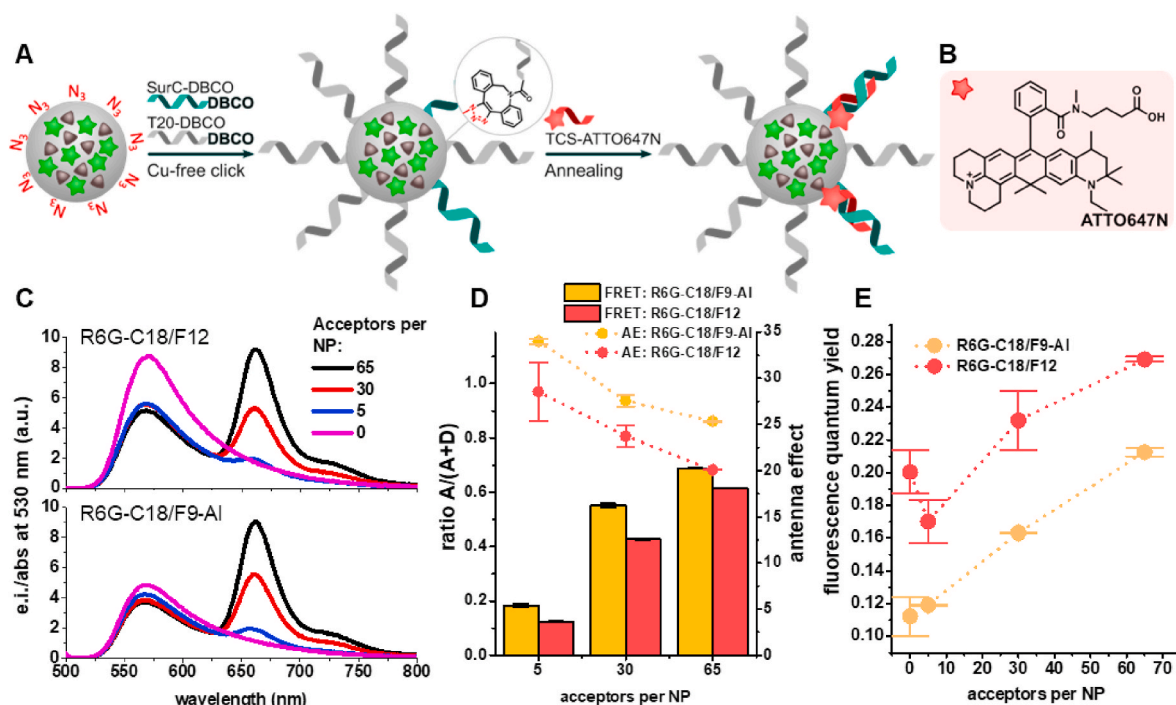


Fig. 3. Preparation, optical properties and antenna effect of DNA nanoprobe. (A) Preparation of nanoprobe: functionalization of dye-loaded nanoparticles with DNA and subsequent annealing with the FRET acceptor bearing oligonucleotide. (B) Structure of the FRET acceptor ATTO647N. (C) Fluorescence spectra, (D) FRET ratio (semi-quantitative FRET efficiency), antenna effect, and (E) quantum yield of NPs loaded at 250 mM of R6G-C18 with two different counterions (F12 and F9–Al) with increasing number of ATTO647N acceptors per NP. Error bars are standard deviation ($n = 3$).

efficiency than R110-C18/F9–Al (Fig. S7, Supplementary Material). Moreover, antenna effect (AE), which is a value indicating the magnitude of acceptor amplification by the nanoantenna particle measured by the excitation spectrum (Trofymchuk et al., 2017; Woller et al., 2013), was much higher for R6G-C18/F12 and R6G-C18/F9–Al NPs compared to R110-C18/F9–Al NPs. Therefore, we selected R6G-C18 salts for fabrication of FRET-based DNA nanoprobe, bearing the hybridized FRET acceptor (TCS-ATTO647N, which has similar spectral properties to DiD) at the NP surface. After nanoprecipitation (Fig. 2B) azide-bearing NPs were functionalized by clicking oligonucleotide sequences bearing dibenzocyclooctyne (DBCO) reactive group, and subsequently annealed with an acceptor-bearing complementary sequence (TCS-ATTO647N) (Fig. 3A), following a previously described methodology (Melnychuk and Klymchenko, 2018). To control the amount of capture sequence (SurC) on NPs surface, SurC-DBCO was added to NPs at different concentrations (0.5 μM , 1.5 μM and 3 μM) together with a non-coding DNA-DBCO (T20), while keeping constant the total amount of added DNA-DBCO (23 μM). Then, the obtained DNA-functionalized NPs were hybridized with TCS-ATTO647N and purified by ultrafiltration. The amount of hybridized TCS-ATTO647N on the surface of the nanoparticles was quantified by absorption spectroscopy (Fig. S8 of the Supplementary Materials). For each SurC concentration the number of TCS-ATTO647N acceptors per NP was, respectively, 5, 30 and 65 acceptors per particle.

For both tested donor dye salts, the increase in the number of acceptors per NP increased relative intensity of the acceptor emission, accompanied by a small decrease in the donor emission (Figs. 3C and S9A, Supplementary Material). These spectral changes indicate that FRET takes place from donor NPs to ATTO647N acceptor at the surface. FRET efficiency, expressed as the empirical FRET ratio $A/(A + D)$, increased with the increase of the number of acceptors. The FRET ratio was slightly higher for R6G-C18/F9–Al (Fig. 3D). The total QY value of donor and acceptor also increased in the presence of acceptor, especially in the case R6G-C18/F9–Al NPs, where QY increased from 0.11 ± 0.01 for NPs without acceptor, to 0.212 ± 0.002 for those with 65 acceptors

per particle (Fig. 3E). This QY enhancement could be due to the fact that a part of the excitation energy transferred to the acceptor derives from the non-emissive self-quenched donor dyes, thus producing a de-quenching effect on the whole system, as shown for other NPs (Genovese et al., 2013). For both donor dye salts (R6G-C18/F12 and R6G-C18/F9–Al) the antenna effect increased with decrease in the number of acceptors per NP. R6G-C18/F9–Al NPs performed slightly better than R6G-C18/F12 NPs, with its AE ranging from 25 till 34 for number of acceptors per NP varied from 65 till 5. The latter means that the signal of the acceptor is amplified 25–34 times due to the light-harvesting effect of the nanoantenna, where a large number of donor dyes inside nanoparticle (~ 6000 per 43-nm particle) undergo efficient FRET to a few acceptors at the surface. R6G-C18/F9–Al NPs were selected for the experiments on the DNA target detection. Taking into account the number of encapsulated dyes (n), extinction coefficient of Rhodamine 6G ($116,000 \text{ M}^{-1} \text{ cm}^{-1}$) and their quantum yield (QY), we can estimate the brightness of R6G-C18/F9–Al nanoprobe: $B = n \times \epsilon \times \text{QY} = 6000 \times 116,000 \text{ cm}^{-1} \text{ M}^{-1} \times 0.212 = 1.48 \times 10^8 \text{ M}^{-1} \text{ cm}^{-1}$. This value is equivalent of ~ 2000 high-performance dyes with typical extinction coefficient of $150,000 \text{ M}^{-1} \text{ cm}^{-1}$ and QY of 0.5 ($B = 7.5 \times 10^4 \text{ M}^{-1} \text{ cm}^{-1}$) and of ~ 135 Qdots-605 ($B = 1.1 \times 10^6 \text{ M}^{-1} \text{ cm}^{-1}$, excitation at 488 nm, assuming QY = 1).

2.4. Detection of target DNA sequence

All the following experiments were performed on the R6G-C18/F9–Al-loaded NP-probe with 65 acceptors per NP (NP-probe-65). In the nanoprobe design, DNA target sequence, encoding survivin fragment (20mer ssDNA), displaces the TCS-ATTO647N acceptor from NP surface, thus turning off the FRET signal (Fig. 1B). Indeed, after incubation with the target, the signal corresponding to the acceptor at 662 nm decreased. This confirmed that the FRET acceptor was hybridized at the NP surface instead of just being nonspecifically absorbed, so that the target effectively displaced the TCS-ATTO647N and turned off the FRET. This result is in line with our previous FRET-based probes operating in the red

region (Melnychuk et al., 2020; Melnychuk and Klymchenko, 2018). To optimize sensitivity of our assay, we diluted the NPs suspension to 10 pM of the acceptor (corresponding to ~ 0.15 pM of NPs) and incubated it (6 h, rt) with the DNA target at different concentrations (3–200 pM). We observed that, with increase in the target concentration, the acceptor relative intensity decreased gradually with some recovery of donor fluorescence (Fig. S11), showing almost linear change of the FRET ratio vs target concentration (Fig. 4). The limit of detection and the limit of quantitation (LOD and LOQ, defined as, respectively, 3 and 10 times the ratio between the standard error of the control without target and the slope of the linear regression (Analytical Methods Committee, 1987) (see Table S2, Supplementary Material) for this assay were 3 and 9 pM, respectively.

To study the response of NP-probe-65 at the single-particle level, it was immobilized on the glass surface using a sandwich of biotinylated BSA, neutravidin and biotinylated A20, followed by a hybridization of the nanoprobe (Fig. 5A) (Melnychuk and Klymchenko, 2018). Immobilized NP-probe-65 was visualized via fluorescence microscopy using both a sCMOS (Hamamatsu Orca Flash 4.0) camera equipped with a beam splitter (W-VIEW GEMINI) and an RGB camera (Nikon, DS-Fi3). The beam splitter at 640 nm allowed us to separately detect donor and acceptor channels and then to construct merged and ratio images. The increase in the target concentration decreased gradually the intensity in the acceptor channel, so that on the merged images the particles turned from orange to green (Fig. 5B). In the ratio images drastic change of NPs color towards blue (low acceptor/donor ratio) was observed, in line with the spectroscopic data in solution (Fig. 4). A histogram of the ratio distribution shows that ratio of the NP-probe-65 initially centered at ~ 0.6 shifted gradually to ~ 0.4 and ~ 0.2 for 10 and 1000 pM of the

target, respectively (Fig. 5D), indicating that this method could in principle allow quantification of the target. On the other hand, for RGB color camera, merged images showed only small color change from orange to yellow with addition of the 1000 pM DNA target. The differences in performance between the sCMOS camera and the RGB camera could be due to two reasons: (i) sCMOS has a higher sensitivity and dynamic range to the RGB sensor and (ii) the use of the beam splitter with a dichroic at 640 nm provides efficient separation of donor and acceptor signals of NP-probe-65 than green and red channels of the RGB sensor. Nevertheless, the ratio images for the RGB camera (Fig. 5C) showed clear changes in the red/green ratio in response to the target (color change from orange to blue), which was confirmed by the ratio histogram (Fig. 5D).

Finally, we challenged our NP-probe-65 biosensor by imaging it on glass surface using a cellphone camera (iPhone SE, Backlit Sony Exmor RS 12 MP, 1.22 μm , f/2.2 aperture). The detection setup was simply constructed by replacing the Nikon RGB camera with a smartphone together with an eyepiece (10x) at the exit of the microscope (Fig. 6A). The estimated pixel size in our images was 0.526 $\mu\text{m}/\text{px}$ (see Supplementary Materials 1.3.8). Using a special smartphone application that allows controlling key camera parameters (ISO, exposure time, aperture), we acquired images where individual particles could be readily identified. Remarkably, the true-color images recorded with a smartphone could directly show the change in the color of NP-probe-65 in the presence of 10 pM target. The color change from orange to yellow-green corresponded to loss of FRET in NP-probe-65, expected for the strand displacement induced by the DNA target (Fig. 6B). Red/green channel ratio images revealed drastic changes in the ratio from red pseudo-color to green-yellow, green-blue and blue for 10, 100 and 1000 pM target, respectively (Fig. 6C). The ratio histograms confirmed the gradual change in the red/green ratio, and distribution histograms looked better separated compared to Nikon RGB camera (Fig. 6D vs 5D). The major response was observed already at 10 pM target, probably because at this concentration corresponded to ~ 10 -fold excess with respect to the FRET acceptor (TCS-ATTO647N). Thus, the ratiometric response of FRET-based nanoprobe to target DNA can be readily recorded with a smartphone camera using a standard epi-fluorescence optical microscope.

3. Conclusion

In this work, a FRET-based DNA nanoprobe was developed for detection with a smartphone camera. To this end, we designed 40-nm PMMA-based polymeric NPs encapsulating green emitting fluorescent dyes, octadecyl Rhodamines 110 and 6G, paired with bulky counterions for preventing aggregation-caused quenching in the polymer matrix. Their surface was functionalized with DNA complementary to the sequence encoding cancer marker survivin, which is hybridized with the target competitive sequence bearing red emitting FRET acceptor ATTO647N. Among tested dye salts, octadecyl Rhodamine 6G with aluminum-based bulky counterion, showed best FRET characteristics, while the optimal acceptor concentration was 65 molecules per NP. The obtained nanoprobe displayed fluorescence quantum yield $>20\%$ and antenna effect of 25. The nanoprobe showed ratiometric response to the target DNA in solution with a limit of detection of 3 pM. Single-particle fluorescence microscopy of immobilized nanoprobe revealed that both sCMOS camera with a beam splitter and RGB camera can detect the color switch of the FRET nanoprobe in presence of varying concentrations of the DNA target. Finally, our nanoprobe enabled detection of 10-pM DNA target using RGB camera of a smartphone in true color or ratio (red-to-green) imaging at the single-particle level. Thus, high brightness of NPs and signal amplification through light harvesting allowed DNA sensing by a smartphone sensor coupled to an appropriate optical setup. We foresee that the optical part could be greatly simplified, which would open the way to simple and inexpensive smartphone-based point-of-care assays for detection of biomolecular markers of diseases.

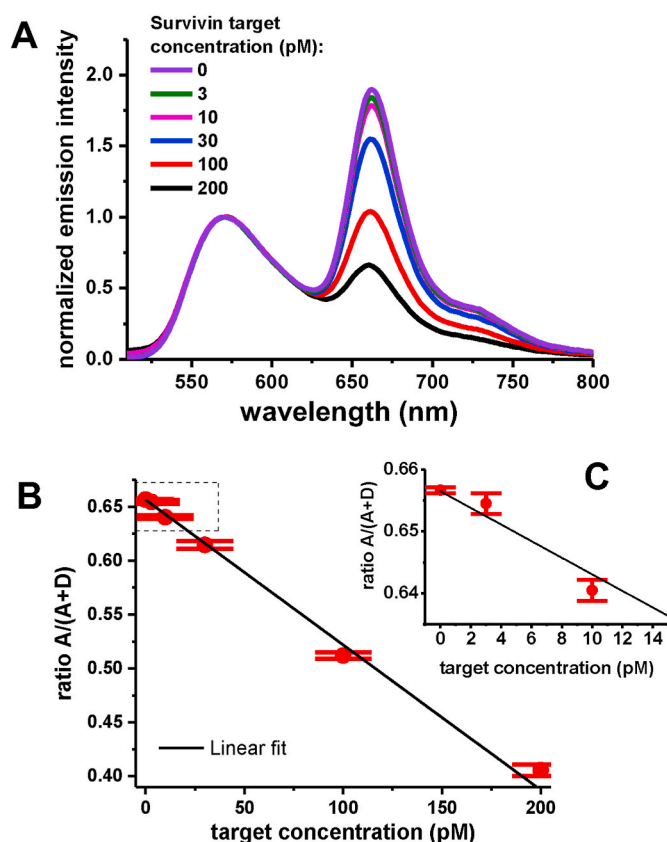


Fig. 4. Ratiometric detection of the DNA target. (A) Fluorescence spectra of NP-probe-65 incubated with increasing concentrations of the DNA target sequence. The spectra were normalized at the donor intensity. (B) FRET ratio as a function of target concentration. (C) Data points in the square shown in (B). Error bars are standard deviation ($n = 3$).

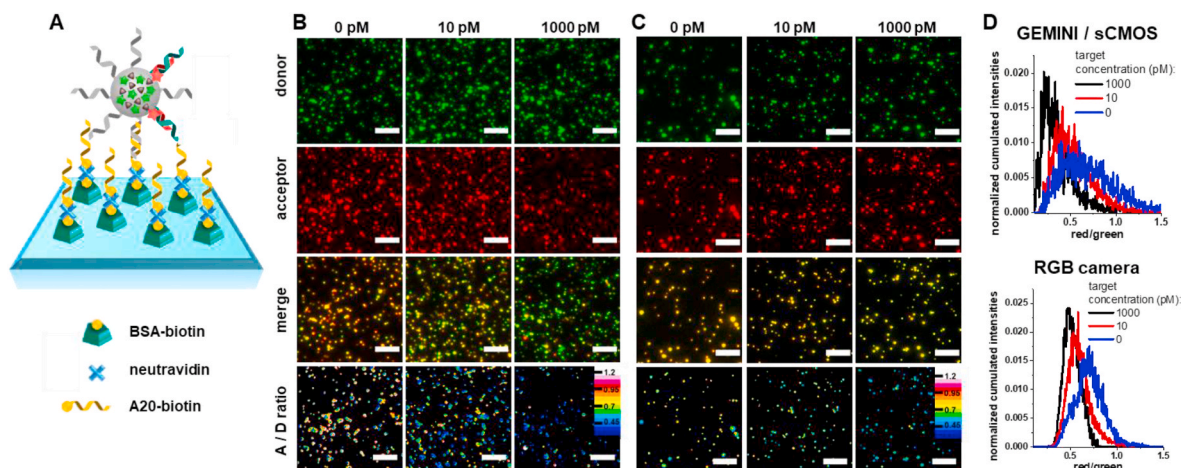


Fig. 5. Nucleic acid detection by NP-probe-65 on glass surfaces using scientific-grade sCMOS with image splitting (GEMINI) and RGB camera. (A) Surface immobilization of nanoprobe for microscopy experiments. (B) and (C): Detection of DNA target (survivin) at the single-particle level using sCMOS (Hamamatsu Orca Flash 4) with image splitter (B) and RGB (Nikon DS-Fi3) camera (C). Samples were incubated for 3 h (rt) with nucleic acid target at different concentrations. From up to down, fluorescence microscopy images: donor channel, acceptor channel, donor + acceptor merged image, and ratiometric image of the acceptor (red) over the donor (green) channel. Excitation was at 488 nm with irradiance of 2 W cm^{-2} . (D) Ratio distribution histograms for the corresponding ratiometric images using the two camera types. Scale bars: 5 μm . (For interpretation of the references to color in this figure legend, the reader is referred to the Web version of this article.)

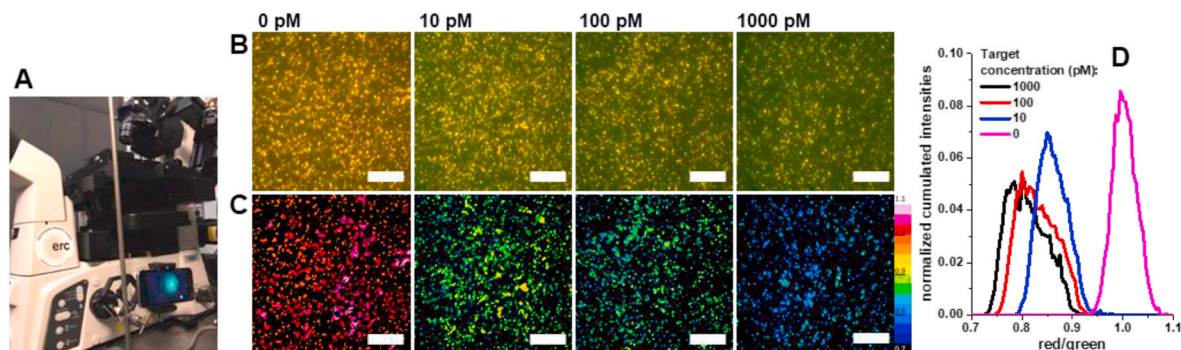


Fig. 6. Smartphone-based detection of nucleic acids by NP-probe-65 on glass surface. (A) Smartphone-based detection setup. (B) RGB true-color images acquired with a smartphone (iPhone SE). Images were acquired after 3 h of incubation (rt) with DNA target (survivin) at different concentrations. (C) Ratiometric images of the red over the green channel from the images shown in (B). Excitation was at 488 nm with irradiance of 2 W cm^{-2} . (D) Ratio distribution histograms for the images shown in (C). Scale bars: 25 μm . (For interpretation of the references to color in this figure legend, the reader is referred to the Web version of this article.)

CRediT authorship contribution statement

Caterina Severi: Data curation, Formal analysis, Investigation, Methodology, Software, Validation, Visualization, Writing - original draft. **Nina Melnychuk:** Investigation, Methodology, Writing - review & editing. **Andrey S. Klymchenko:** Conceptualization, Funding acquisition, Investigation, Methodology, Project administration, Resources, Supervision, Visualization, Writing - review & editing.

Declaration of competing interest

The authors declare the following financial interests/personal relationships which may be considered as potential competing interests:

Acknowledgments

This work, CS and NM were supported from European Research Council ERC Consolidator grant BrightSens 648528 and SATT Conectus Alsace grant Nanoantenna. We thank I. Krossing for providing sample of lithium tetrakis(perfluoro-tert-butoxy)aluminate.

Appendix A. Supplementary data

Supplementary data to this article can be found online at <https://doi.org/10.1016/j.bios.2020.112515>.

References

- Acuna, G.P., Möller, F.M., Holzmeister, P., Beater, S., Lalkens, B., Tinnefeld, P., 2012. *Science* 338, 506–510.
- Ali, M.M., Li, F., Zhang, Z., Zhang, K., Kang, D.-K., Ankrum, J.A., Le, X.C., Zhao, W., 2014. *Chem. Soc. Rev.* 43, 3324.
- Altieri, D.C., 2003. *Oncogene* 22, 8581–8589.
- Analytical Methods Committee, 1987. *The Analyst* 112, 199.
- Andreiuk, B., Reisch, A., Bernhardt, E., Klymchenko, A.S., 2019. *Chem. Asian J.* 14, 836–846.
- Andreiuk, B., Reisch, A., Lindecker, M., Follain, G., Peyri ras, N., Goetz, J.G., Klymchenko, A.S., 2017a. *Small* 13, 1701582.
- Andreiuk, B., Reisch, A., Pivovarenko, V.G., Klymchenko, A.S., 2017b. *Mater. Chem. Front.* 1, 2309–2316.
- Breslauer, D.N., Maamari, R.N., Switz, N.A., Lam, W.A., Fletcher, D.A., 2009. *PLoS One* 4, e6320.
- Chen, A., Chatterjee, S., 2013. *Chem. Soc. Rev.* 42, 5425.
- Choi, H.M.T., Chang, J.Y., Trinh, L.A., Padilla, J.E., Fraser, S.E., Pierce, N.A., 2010. *Nat. Biotechnol.* 28, 1208–1212.
- Coskun, A.F., Nagi, R., Sadeghi, K., Phillips, S., Ozcan, A., 2013. *Lab Chip* 13, 4231–4238.
- Dakshayini, B.S., Reddy, K.R., Mishra, A., Shetti, N.P., Malode, S.J., Basu, S., Naveen, S., Raghu, A.V., 2019. *Microchem. J.* 147, 7–24.

- Genovese, D., Bonacchi, S., Juris, R., Montalti, M., Prodi, L., Rampazzo, E., Zaccheroni, N., 2013. *Angew. Chem. Int. Ed.* 52, 5965–5968.
- Grimm, J.B., English, B.P., Chen, J., Slaughter, J.P., Zhang, Z., Revyakin, A., Patel, R., Macklin, J.J., Normanno, D., Singer, R.H., Lionnet, T., Lavis, L.D., 2015. *Nat. Methods* 12, 244–250.
- Jiang, Y., McNeill, J., 2017. *Chem. Rev.* 117, 838–859.
- Kanchi, S., Sabela, M.L., Mdluli, P.S., Inamuddin Bisetty, K., 2018. *Biosens. Bioelectron.* 102, 136–149.
- Krossing, I., 2001. *Chem. Eur. J.* 7, 490–502.
- Kühnemund, M., Wei, Q., Darai, E., Wang, Y., Hernández-Neuta, I., Yang, Z., Tseng, D., Ahlford, A., Mathot, L., Sjöblom, T., Ozcan, A., Nilsson, M., 2017. *Nat. Commun.* 8.
- Melnychuk, N., Eglhoff, S., Runser, A., Reisch, A., Klymchenko, A.S., 2020. *Angew. Chem. Int. Ed.*, 13913.
- Melnychuk, N., Klymchenko, A.S., 2018. *J. Am. Chem. Soc.* 140, 10856–10865.
- Noor, M.O., Krull, U.J., 2014. *Anal. Chem.* 86, 10331–10339.
- Petryayeva, E., Algar, W.R., 2015. *The Analyst* 140, 4037–4045.
- Reisch, A., Didier, P., Richert, L., Oncul, S., Arntz, Y., Mély, Y., Klymchenko, A.S., 2014. *Nat. Commun.* 5, 4089.
- Reisch, A., Heimbürger, D., Ernst, P., Runser, A., Didier, P., Dujardin, D., Klymchenko, A. S., 2018. *Adv. Funct. Mater.* 28, 1805157.
- Reisch, A., Klymchenko, A.S., 2016. *Small* 12, 1968–1992.
- Reisch, A., Trofymchuk, K., Runser, A., Fleith, G., Rawiso, M., Klymchenko, A.S., 2017. *ACS Appl. Mater. Interfaces* 9, 43030–43042.
- Rochat, S., Swager, T.M., 2013. *ACS Appl. Mater. Interfaces* 5, 4488–4502.
- Roy, R., Hohng, S., Ha, T., 2008. *Nat. Methods* 5, 507–516.
- Roy, S., Malode, S.J., Shetti, N.P., Chandra, P., 2019. Modernization of biosensing strategies for the development of lab-on-chip integrated systems. In: Krishnaraj, R., Sani, R.K. (Eds.), *Bioelectrochemical Interface Engineering*. John Wiley & Sons, Hoboken, NJ, pp. 325–342.
- Scrimin, P., Prins, L.J., 2011. *Chem. Soc. Rev.* 40, 4488–4505.
- Shetti, N.P., Bukkitgar, S.D., Reddy, K.R., Reddy, ChV., Aminabhavi, T.M., 2019. *Biosens. Bioelectron.* 141, 111417.
- Stobiecka, M., Ratajczak, K., Jakiela, S., 2019. *Biosens. Bioelectron.* 137, 58–71.
- Takayanagi, I., 2006. CMOS image sensor. In: Nakamura, J. (Ed.), 2006. *Image Sensors and Signal Processing for Digital Still Cameras*. Taylor & Francis, Boca Raton, FL, pp. 143–178.
- Trofymchuk, K., Reisch, A., Didier, P., Fras, F., Gilliot, P., Mely, Y., Klymchenko, A.S., 2017. *Nat. Photon.* 11, 657–663.
- Wang, X., Gorris, H.H., Stolwijk, J.A., Meier, R.J., Groegel, D.B.M., Wegener, J., Wolfbeis, O.S., 2011. *Chem. Sci.* 2, 901.
- Wei, Q., Acuna, G., Kim, S., Vietz, C., Tseng, D., Chae, J., Shir, D., Luo, W., Tinnfeld, P., Ozcan, A., 2017. *Sci. Rep.* 7, 1–10.
- Wei, Q., Luo, W., Chiang, S., Kappel, T., Mejia, C., Tseng, D., Chan, R.Y.L., Yan, E., Qi, H., Shabbir, F., Ozcan, H., Feng, S., Ozcan, A., 2014. *ACS Nano* 8, 12725–12733.
- Wei, Q., Qi, H., Luo, W., Tseng, D., Ki, S.J., Wan, Z., Göröcs, Z., Bentolila, L.A., Wu, T.-T., Sun, R., Ozcan, A., 2013. *ACS Nano* 7, 9147–9155.
- Woller, J.G., Hannestad, J.K., Albinsson, B., 2013. *J. Am. Chem. Soc.* 135, 2759–2768.
- Xu, H., Xia, A., Wang, D., Zhang, Y., Deng, S., Lu, W., Luo, J., Zhong, Q., Zhang, F., Zhou, L., Zhang, W., Wang, Y., Yang, C., Chang, K., Fu, W., Cui, J., Gan, M., Luo, D., Chen, M., 2020. *Sci. Adv.* 6, eaaz7445.
- Yan, Q., Chen, Z.-H., Xue, S.-F., Han, X.-Y., Lin, Z.-Y., Zhang, S., Shi, G., Zhang, M., 2018. *Sensor. Actuator. B Chem.* 268, 108–114.
- Yang, M., Liu, Y., Jiang, X., 2019. *Chem. Soc. Rev.* 48, 850–884.
- Zhang, D., Liu, Q., 2016. *Biosens. Bioelectron.* 75, 273–284.
- Zhu, H., Sikora, U., Ozcan, A., 2012. *The Analyst* 137, 2541–2544.

Supplementary material

Smartphone-assisted detection of nucleic acids by light-harvesting FRET-based nanoprobe

Caterina Severi, Nina Melnychuk, and Andrey S. Klymchenko*

Laboratoire de Bioimagerie et Pathologies, UMR 7021 CNRS, Faculté de Pharmacie, Université de Strasbourg, France

*e-mail: andrey.klymchenko@unistra.fr

Table of Contents

<u>1. Experimental section</u>	3
<u>1.1. Chemical compounds</u>	3
<u>1.1.1. Oligonucleotides</u>	3
<u>1.2. Protocols of synthesis</u>	4
<u>1.2.1. Synthesis of PMMA-AspN3</u>	4
<u>1.2.2. Synthesis of F9-Al counterion</u>	4
<u>1.2.3. Synthesis of Rhodamine 110 octadecyl ester</u>	4
<u>1.2.4. Synthesis of Rhodamine 6G octadecyl ester</u>	5
<u>1.2.5. Synthesis of dye salts</u>	6
<u>1.3. Nanoparticle preparation and characterization</u>	8
<u>1.3.1. Nanoparticles preparation</u>	8
<u>1.3.2. DNA nanoprobe preparation</u>	8
<u>1.3.3. Nanoparticles characterization</u>	8
<u>1.3.4. Estimation of number of dyes per nanoparticle</u>	9
<u>1.3.5. Fluorescence microscopy</u>	9
<u>1.3.6. Detection of survivin oligonucleotide target</u>	10
<u>1.3.7. Calculation of limit of detection (LOD) and limit of quantification (LOQ)</u>	10
<u>1.3.8. Calculation of area smartphone detector</u>	11
<u>2. Supporting figures and tables</u>	12
<u>2.1. DLS measurements</u>	12
<u>2.2. Fluorescence and absorption spectroscopy</u>	13
<u>2.2.1. Donor nanoparticles</u>	13
<u>2.2.2. FRET studies with acceptor inside the NPs</u>	15
<u>2.2.3. FRET studies with acceptor on the surface of the NPs</u>	20
<u>3. References</u>	26

1. Experimental section

1.1. Chemical compounds

Poly (methyl methacrylate-co-methacrylic acid) (PMMA-MA, 1.6% methacrylic acid, $M_n \sim 15000$, $M_w \sim 34000$), 3-chloropropylamine hydrochloride (98%), Rhodamine 6G (95.0%), Rhodamine 110 (>99.0%), 1-octadecanol (95%), 4-(Dimethylamino)pyridine ($\geq 99\%$), N-(3-Dimethylaminopropyl)-N'-ethylcarbodiimide hydrochloride ($\geq 98\%$), sodium tetrakis[3,5-bis(1,1,1,3,3,3-hexafluoro-2-methoxy-2-propyl)phenyl]borate trihydrate (Selectophore™), N,N-Diisopropylethylamine ($\geq 99\%$), acetonitrile (anhydrous, 99.8%), dichloromethane (anhydrous, $\geq 99.8\%$), 1-Hydroxybenzotriazole ($\geq 97\%$), 3- azido-1-propamine ($\geq 95\%$), BSA-biotin, Amicon Centrifugal filters (0.5mL, 100K) were purchased from Sigma-Aldrich. Citric acid monohydrate ($\geq 99.5\%$), sodium azide (99%), sodium iodide ($\geq 99.5\%$) and trifluoroacetic acid (99%) were purchased from Alfa Aesar. FmocAsp(OtBu)-OH was purchased from Activotec. HBTU was purchased from ChemPep Inc. Neutravidin, LabTek chambers (Borosilicate cover glass, eight wells) and MultiSpeck™ Multispectral Fluorescence Microscopy Standards

Kit (M-7901) were purchased from ThermoFisher Scientific. Sodium phosphate monobasic (>99.0%, Sigma-Aldrich) and sodium phosphate dibasic dihydrate (>99.0%, Sigma- Aldrich) were used to prepare 20 mM phosphate buffers at pH 7.4. For saline buffer sodium chloride ($\geq 99\%$, Sigma Aldrich) 30 mM and magnesium chloride ($\geq 98\%$, Sigma Aldrich) 12 mM was added to 20 mM phosphate buffer and pH was adjusted with sodium hydroxide 1N solution. Milli-Q water (Millipore) was used in all experiments. For immobilization protocol PBS (without Ca^{2+} and Mg^{2+}) was purchased from Lonza.

1.1.1. Oligonucleotides

Single stranded lyophilized DNA sequences were purchased from IBA, then dissolved in MilliQ water and stored at -20 °C. The sequences used in this work are the following.

SurC-DBCO: 5'-CCC AGC CTT CCA GCT CCT TGA-(DBCO)-3'

T20-DBCO: 5'-TTT TTT TTT TTT TTT TTT TT-(DBCO)-3'

TCS-ATTO647N: 5'-(ATTO647N)- TCA AGG AGC TGG-3'

Target: 5'-CAA GGA GCT GGA AGG CTG GG-3'

A20-Biotin: 5'-(Biotin)-AAA AAA AAA AAA AAA AAA AA-3'

1.2. Protocols of synthesis

1.2.1. Synthesis of PMMA-AspN3

PMMA-AspN3 was synthesized following a previously described procedure (Melnychuk and Klymchenko, 2018).

1.2.2. Synthesis of F9-Al counterion

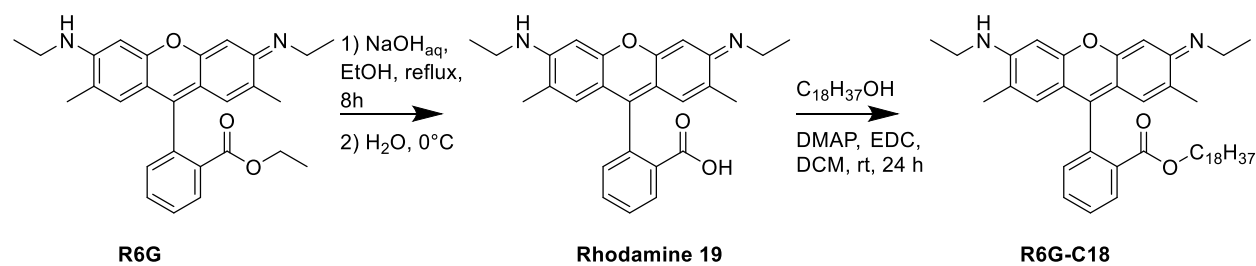
F9-Al counterion was synthesized following previously described procedures (Krossing, 2001; Andreiuk et al., 2017).

1.2.3. Synthesis of Rhodamine 110 octadecyl ester

Green-emitting dye Rhodamine 110 octadecyl ester (R110-C18) was synthesized according to a previously described procedure (Floyd et al., 2008).

Rhodamine 110 (80 mg, 0.21 mmol) and 1-octadecanol (2 g, 7.40 mmol) were mixed together and heated at 80 °C, when the octadecanol dissolved completely concentrated sulfuric acid (0.1 mL) was added. The system was stirred for 48 hours, then 0.6 mL of triethylamine were slowly added. Then the reaction was cooled down at room temperature and to the resulting red solid 200 mL of diethyl ether were added, the system stirred for one hour. The reaction mixture was filtrated and a red solid was obtained. Crude product was purified over preparative TLC using 9:1 DCM/MeOH as an eluent. 72 mg of R110-C18 were obtained (59% yield).

1.2.4. Synthesis of Rhodamine 6G octadecyl ester



Scheme S1 Synthesis of R6G-C18

Rhodamine 19 was prepared according to an already described procedure (Yang et al., 2009).

To a solution of Rhodamine 6G (1 g, 2.1 mmol) in ethanol (20 mL) aqueous sodium hydroxide was added (250 mg, 6.3 mmol in 6 mL). System was refluxed for 8 hours, then the solution was allowed to cool at room temperature and distilled water (10 mL) was added. System was cooled at 0 °C and a red-purple solid started precipitating. The as-obtained precipitate was filtered and dried to obtain 563 mg (1.25 mmol, 59% yield) of Rhodamine 19.

To a solution of Rhodamine 19 (200 mg, 0.44 mmol), 1-octadecanol (360 mg, 1.33 mmol) and 1-Ethyl-3-(3-dimethylaminopropyl)carbodiimide hydrochloride (425 mg, 2.22 mmol) in dichloromethane (5 mL), DMAP (11 mg, 0.09 mmol) was added. Reaction was left stirring at room temperature under argon for 24 hours. Then the reaction was washed three times with HCl 1M and one time with brine. Organic fraction was gathered and solvent evaporated, finally the crude product was purified via silica chromatography using DCM/MeOH 95/5 as eluent. 230 mg of Rhodamine 6G octadecyl ester (R6G-C18) were obtained (78% yield). ¹H NMR (400 MHz, CD₃OD) δ ppm 0.91 (3 H, t, *J*=7.9 Hz) 1.03-1.36 (34H, m) 1.40 (6H, t, *J*=7.17 Hz) 2.16 (6H, s) 3.56 (4H, q, *J*=7.17) 3.93 (2H, t, *J*=6.16 Hz) 6.92 (2H, d, *J*=1.05 Hz) 6.97 (2H, s) 7.43 (1H, dd, *J*=7.31 Hz *J*=1.34 Hz) 7.82-7.91 (2H, m) 8.32 (1H, dd, *J*=7.61 Hz *J*=1.44). ¹³C NMR (126 MHz, CD₃OD) δ ppm 169.58 (s) 161.92 (s) 161.50 (s) 160.28 (s) 137.28 (s) 136.51 (s) 134.90 (s) 134.81 (s) 134.56 (s) 134.12 (s) 134.00 (s) 132.63 (s) 129.50 (s) 117.36 (s) 97.42 (s) 69.24 (s) 42.02 (s) 35.61 (s) 33.31 (s) 33.29 (s) 33.28 (s) 33.24 (s) 33.05 (s) 33.01 (s) 32.81 (s) 31.92 (s) 29.49 (s) 26.27 (s) 20.14 (s) 16.98 (s) 16.63 (s). HRMS (m/z): [M]⁺ calcd. for C₄₄H₆₃N₂O₃ 667.4839; found 667.4833.

1.2.5. Synthesis of dye salts

The salts of octadecyl rhodamine 110 and octadecyl rhodamine 6G with different counterions were prepared by ion exchange followed by purification over silica chromatography.

R110-C18/F9-Al. R110-C18/Cl (1 eq, 3 mg, 0.0048 mmol) and lithium tetrakis(perfluoro-tertbutoxy)aluminate (F9-Al) (3 eq, 14 mg, 0.015 mmol) were mixed in 1 mL of dichloromethane. TLC analysis showed instant conversion. The final product was then purified over silica column using DCM/MeOH 9/1 as eluent. Evaporation of solvent yielded 6 mg of product (corresponding to 81% yield). ¹H NMR (400 MHz, CD₃OD) δ ppm 0.88 (3 H, t, *J*=7.09 Hz) 1.05-1.36 (34H, m) 6.79-6.82 (4H, m) 7.05 (2H, d, *J*=9.28 Hz) 7.40 (1H, dd, *J*=7.26 Hz, *J*=1.36 Hz) 7.75-7.89 (2H, m) 8.28 (1H, dd, *J*=7.65 Hz

$J=1.36$). ^{19}F NMR (376 MHz, CDCl_3) δ ppm -76.15 (36 F, s). ^{27}Al NMR (130 MHz, CD_3OD) δ ppm 38.2 (1 Al, s). ^{13}C NMR (126 MHz, CD_3OD) δ ppm 212.63 (s) 169.46 (s) 163.92 (s) 163.88 (s) 162.23 (s) 137.11 (s) 136.45 (s) 135.48 (s) 134.46 (s) 134.04 (s) 123.10 (q, $J=292.30$ Hz) 120.52 (s) 117.48 (s) 100.97 (s) 69.37 (s) 35.59 (s) 33.29 (s) 33.27 (s) 33.24 (s) 33.22 (s) 33.19 (s) 33.03 (s) 32.99 (s) 23.84 (s) 31.94 (s) 29.55 (s) 26.25 (s) 16.94 (s) 3.28 (s). HRMS (m/z): $[\text{M}]^+$ calcd. for $\text{C}_{38}\text{H}_{51}\text{N}_2\text{O}_3$ 583.3900; found 583.3911; $[\text{M}]^-$ calcd. for $\text{C}_{16}\text{AlF}_3\text{O}_4$ 966.9037; found 966.9039.

R110-C18/F12. R110-C18/Cl (1 eq, 3 mg, 0.0048 mmol) and sodium tetrakis[3,5-bis(1,1,1,3,3,3-hexafluoro-2-methoxy-2-propyl)phenyl]borate trihydrate (F12) (3 eq, 28 mg, 0.015 mmol) were mixed in 1 mL of dichloromethane. TLC analysis showed instant conversion. The final product was then purified over silica column using DCM/MeOH 9/1 as eluent. Evaporation of solvent yielded 9 mg of product (corresponding to 82% yield). ^1H NMR (400 MHz, CD_3OD) δ ppm 0.86 (3 H, m) 1.12-1.41 (34H, m) 3.30 (24H, s), 6.85-6.60 (4H, m) 7.11 (2H, d, $J=9.27$ Hz), 7.42 (4H, bs) 7.47 (1H, dd, $J=7.37$ Hz, $J=1.42$ Hz), 7.58 (8H, bs), 7.83-7.92 (2H, m) 8.26 (1H, dd, $J=7.63$ Hz $J=1.56$). ^{19}F NMR (376 MHz, CDCl_3) δ ppm -71.29 (48 F, s). ^{11}B NMR (128 MHz, CD_3OD) δ ppm -5.95 (1 B, s). ^{13}C NMR (126 MHz, CD_3OD) δ ppm 212.62 (s) 169.45 (s) 163.92 (s) 163.88 (s) 162.23 (s) 161.39 (s) 137.84 (s) 137.11 (s) 136.45 (s) 135.47 (s) 134.45 (s) 134.03 (s) 126.51 (s) 123.61 (s) 122.23 (q, $J=289$ Hz) 120.52 (s) 117.48 (s) 100.97 (s) 69.36 (s) 35.58 (s) 33.28 (s) 33.27 (s) 33.24 (s) 33.22 (s) 33.18 (s) 33.03 (s) 32.99 (s) 23.84 (s) 31.93 (s) 29.54 (s) 26.24 (s) 16.94 (s) 3.27 (s). HRMS (m/z): $[\text{M}]^+$ calcd. for $\text{C}_{38}\text{H}_{51}\text{N}_2\text{O}_3$ 583.3900; found 583.3873; $[\text{M}]^-$ calcd. for $\text{C}_{56}\text{H}_{36}\text{BF}_{48}\text{O}_8$ 1759.1737; found 1759.1770.

R6G-C18/F9-Al. R6G-C18/Cl (1 eq, 3 mg, 0.0043 mmol) and lithium tetrakis(perfluoro-tert-butoxy)aluminate (F9-Al) (3 eq, 12 mg, 0.013 mmol) were mixed in 1 mL of dichloromethane. TLC analysis showed instant conversion. The final product was then purified over silica column using DCM/MeOH 95/5 as eluent. Evaporation of solvent yielded 5 mg of product (corresponding to 71% yield). ^1H NMR (400 MHz, CD_3OD) δ ppm 0.88 (3 H, t, $J=6.76$ Hz) 0.99-1.33 (34H, m) 1.37 (6H, t, $J=7.24$ Hz) 2.13 (6H, s) 3.53 (4H, q, $J=7.24$) 3.90 (2H, t, $J=6.20$ Hz) 6.89 (2H, s) 6.94 (2H, s) 7.40 (1H, d, $J=7.01$ Hz) 7.77-7.88 (2H, m) 8.30 (1H, dd, $J=7.67$ Hz $J=1.22$). ^{19}F NMR (376 MHz, CDCl_3) δ ppm -75.50 (36 F, s). ^{27}Al NMR (130 MHz, CD_3OD) δ ppm 34.0 (1 Al, s). ^{13}C NMR (126 MHz, CD_3OD) δ ppm 165.67 (s) 158.02 (s) 157.57 (s) 156.35 (s) 133.32 (s) 132.53 (s) 130.91 (s) 130.63 (s) 130.16 (s) 130.05 (s) 128.69 (s) 122.16 (q, $J=293$ Hz) 113.43 (s) 93.46 (s) 65.30 (s) 38.07 (s) 31.66 (s) 29.35 (s) 29.34 (s) 29.32 (s) 29.28 (s) 29.10 (s) 29.05 (s) 28.86 (s) 27.96 (s) 25.54 (s) 22.31 (s) 16.14 (s) 13.01 (s) 12.65 (s). HRMS (m/z): $[\text{M}]^+$ calcd. for $\text{C}_{44}\text{H}_{63}\text{N}_2\text{O}_3$ 667.4839; found 667.4828; $[\text{M}]^-$ calcd. for $\text{C}_{16}\text{AlF}_3\text{O}_4$ 966.9037; found 966.9062.

R6G-C18/F12. R6G -C18/Cl (1 eq, 3 mg, 0.0043 mmol) and sodium tetrakis[3,5-bis(1,1,1,3,3,3-hexafluoro-2-methoxy-2-propyl)phenyl]borate trihydrate (F12) (3 eq, 24 mg, 0.013 mmol) were mixed in 1 mL of dichloromethane. TLC analysis showed instant conversion. The final product was then purified over silica column using DCM/MeOH 95/5 as eluent. Evaporation of solvent yielded 9 mg of product (corresponding to 88% yield). ¹H NMR (400 MHz, CD₃OD) δ ppm 0.65 (3 H, t, *J*=6.84 Hz) 1.07-1.40 (34H, m) 1.43 (6H, t, *J*=7.20 Hz) 2.20 (6H, s) 3.30 (24H, s) 3.60 (4H, q, *J*=7.20) 3.96 (2H, t, *J*=6.20 Hz) 6.95 (2H, s) 7.00 (2H, s) 7.42 (4H, bs) 7.45 (1H, dd, *J*=7.45 Hz *J*=1.37 Hz) 7.58 (8H, bs) 7.84-7.94 (2H, m) 8.36 (1H, dd, *J*=7.60 Hz *J*=1.37). ¹⁹F NMR (376 MHz, CDCl₃) δ ppm -71.35. (48 F, s). ¹¹B NMR (128 MHz, CD₃OD) δ ppm -5.95 (1 B, s). ¹³C NMR (126 MHz, CD₃OD) δ ppm 165.67 (s) 162.59 (s) 161.39 (s) 158.02 (s) 157.58 (s) 156.36 (s) 136.93 (s) 133.32 (s) 132.54 (s) 130.92 (s) 130.64 (s) 130.16 (s) 130.05 (s) 128.70 (s) 125.56 (s) 125.20 (s) 122.70 (s) 122.54 (q, *J*=288.18 Hz) 113.43 (s) 93.46 (s) 83.29 (sept., *J*= 28.5 Hz) 65.30 (s) 52.84 (s) 38.07 (s) 31.66 (s) 29.36 (s) 29.33 (s) 29.29 (s) 29.10 (s) 29.05 (s) 28.87 (s) 27.97 (s) 25.54 (s) 22.32 (s) 16.15 (s) 13.01 (s) 12.66 (s). HRMS (m/z): [M]⁺ calcd. for C₄₄H₆₃N₂O₃ 667.4839; found 667.4818; [M]⁻ calcd. for C₅₆H₃₆BF₄₈O₈ 1759.1737; found 1759.1781.

1.3. Nanoparticle preparation and characterization

1.3.1. Nanoparticles preparation

PMMA-AspN3 and different amounts of dye were dissolved in acetonitrile at polymer concentration of 2 mg/mL. This stock solution was quickly diluted in a ten-fold excess of phosphate buffer (20 mM, pH = 7.4) under shaking. Afterwards the acetonitrile was gently evaporated under vacuum.

1.3.2. DNA nanoprobe preparation

SurC-DBCO (at concentrations ranging from 0.5 μ M to 3 μ M) and T20-DBCO (at concentrations ranging from 20 μ M to 21.5 μ M) were added to a freshly prepared nanoparticles solution. The mixture was kept for 20 h at 40 °C without any stirring and protected from light. The mixture was then allowed to cool at room temperature. Annealing with TCS-ATTO647N was performed by adding the flare (at the same concentration of SurC-DBCO) to the DNA-nanoparticle mixture, then heating to 70 °C for 3 minutes. The mixture was cooled down to room temperature again and kept in the dark for 1 h. Purification from unreacted DNA strands was performed by diluting the mixture with 20 mM phosphate buffer containing 12 mM MgCl₂ and 30 mM NaCl, then centrifuging using centrifuge filter (Amicon, 0.5 mL, 100 kDa) at 1000 G for 2 min. The ultra-filtration was repeated 5 times. The as-prepared DNA nanoprobe were then stored at 4 °C in the dark.

1.3.3. Nanoparticles characterization

Nanoparticle size was determined *via* DLS on a Zetasizer Nano ZSP (Malvern Instruments S.A.). For the analysis the mean value of the size distribution per volume was taken. For spectroscopic characterization all solvents used were of spectroscopic grade and MilliQ water was used. Absorption spectra were recorded on a Cary-4000 scan UV-visible spectrophotometer (Varian). Excitation and emission spectra were recorded on a Spectrofluorometer FS5 (Edinburgh Instruments). The fluorescence spectra were recorded setting the excitation wavelength at 470 nm for R110-C18 and 488 nm for R6G-C18. Moreover, fluorescence spectra were corrected both for lamp fluctuations and detector response. Fluorescence quantum yield of nanoparticles loaded with donor dye were calculated using Fluorescein for R110-C18 (QY = 0.91 in NaOH 0.1 M (Brouwer, 2011)) with an absorbance <0.1 at 470 nm, and Rhodamine 6G for R6G-C18 (QY = 0.94 in EtOH (Brouwer, 2011)) with absorbance <0.1 at 488 nm. FRET efficiency was expressed as the semi-quantitative FRET ratio:

$$E_{FRET} = \frac{A}{A + D}$$

Where D is the donor intensity at the maximum and A is the acceptor intensity. Antenna effect (AE), which represents the amplification factor of the acceptor emission was calculated as the ratio of the excitation intensity at the maximum of the donor and the excitation intensity at the maximum of the acceptor, correcting it by the emission of the donor dyes at 680 nm (Trofymchuk et al., 2017):

$$AE = \frac{I_{D-FRET}^{ex} - I_D^{ex} * \frac{I_{D-FRET}^{em}}{I_D^{em}}}{I_{A-FRET}^{ex} - I_A^{ex}}$$

Where I_{D-FRET}^{ex} and I_{A-FRET}^{ex} represent the excitation intensity of donor and acceptor at their respective maxima. I_D^{ex} and I_A^{ex} are the excitation intensities at the maximum wavelengths of donor and acceptor in the sample without acceptor. I_{D-FRET}^{em} and I_D^{em} are the maximum emission intensities of the donor in the samples with and without acceptor.

1.3.4. Estimation of number of dyes per nanoparticle

Using the diameter of the nanoparticles measured by DLS we calculated the volume of a nanoparticle assuming a spherical shape. Then, we calculated the approximate amount of dye molecules encapsulated in each nanoparticle of a given volume: the number of moles of the dye per unit of volume of a single particle is calculated from the dye loading inside the polymer matrix (250 mM), and multiplying this value by the Avogadro constant yields an approximate number of donor dye molecules per nanoparticle (~6000). We estimated the number of FRET acceptor molecules on the surface of the nanoparticles based on the absorption spectra of the DNA probes (Figure S7) by calculating the concentration of the acceptor and the donor at their respective absorption maxima, then the number of TCS-ATTO647N per NPs were estimated to be $6000 \times c(\text{acceptor})/c(\text{donor})$.

1.3.5. Fluorescence microscopy

NPs were immobilized in LabTek following a previously described protocol (Schmied et al., 2014). The LabTek chamber was washed three times with PBS, then incubated with a solution of BSA-Biotin (0.5 mg/mL in PBS) for 10 min. Then the BSA-biotin solution was removed, and the chamber washed with PBS 3 times. The chamber then was incubated with a solution of neutravidin (0.5 mg/mL in PBS) for 10 minutes and washed again 3 times with PBS. Then, a solution of A20-biotin (1 μ M in PBS) was added and left incubating for another 10 min, afterwards the chamber was washed 3 times with 20 mM phosphate buffer pH = 7.4 containing 12 mM MgCl₂ 30 mM and NaCl. Finally, the NPs solution at the appropriate concentration to obtain the desired density on the surface was incubated for 15 minutes in the dark. Chamber was then washed two more times with 20 mM phosphate buffer (pH = 7.4) containing

12 mM MgCl₂ and 30 mM NaCl, the same buffer for the measurements. Single-particle measurements were performed with a Nikon Ti-E inverted microscope with a 60x objective (Apo TIRF, oil, NA 1.49, Nikon) in the epifluorescence mode. Excitation source was a laser (Oxxius) at 488 nm and the power density was set at 2 W·cm⁻² throughout all the experiments. For monochrome microscopy the fluorescence signal was recorded with Hamamatsu Orca Flash 4 camera and the exposure time was set to 200 ms per image frame. To enable a two-channel detection, corresponding to the donor and acceptor channel, W-VIEW GEMINI image splitting system (Hamamatsu) was used with dichroic 640 nm (Semrock FF640-FDi01-25x36). For RGB microscopy measurements the signal was recorded with a Nikon DS-Fi3 camera, the exposure time was set at 500 ms per image frame. For data acquired with both the monochrome camera and the RGB camera the ratiometric images were obtained by summing 10 image frames and then using an ImageJ plugin (developed by Roman Vauchelles, available upon request). The plugin divides the red channel image by the green channel image; for each pixel a pseudo-color scale is employed for coding the ratio, while the intensity corresponds to the integral intensity recorded for both channels at the corresponding image. For smartphone-based measurements an iPhone SE was used with an app (Halide developed by Ben Sandofsky) which allowed acquiring RAW images and controlling camera parameters. The images were recorded with a shutter exposure of 1/3 of a second and an ISO of 2000. Data analysis of the as-acquired images was performed as described above.

1.3.6. Detection of survivin oligonucleotide target

Detection in solution was performed by diluting the DNA probe in 20 mM phosphate buffer containing 30 mM NaCl and 12 mM MgCl₂ to a concentration of 10 pM (corresponding to TCS-ATTO647N) and an aliquot of survivin oligonucleotide target was added. The solution was then incubated in the dark at 25 °C for 6 h. Detection of the target on a glass surface was done by adding the target oligonucleotide to the LabTek chamber containing the immobilized DNA probes; the system was then kept in the dark at room temperature when the incubation time was 3 h.

1.3.7. Calculation of limit of detection (LOD) and limit of quantification (LOQ)

LOD and LOQ were calculated by performing a linear fit on all the data points shown in Figure 4B and then using the following equations (“Recommendations for the definition, estimation and use of the detection limit,” 1987):

$$LOD = 3 \cdot \frac{\sigma_B}{S}, LOQ = 10 \cdot \frac{\sigma_B}{S}$$

Where σ_B is the standard error of the intercept of the linear regression (corresponding to the noise of the control sample without the target) and S is the slope of the linear regression (corresponding to the sensitivity of the method). The parameters of the linear regression of the data shown in Figure 4B are reported in Table S2.

1.3.8. Calculation of the detection area by smartphone camera

To calculate the area of detection with the smartphone camera a calibration experiment where the same field of fluorescent beads (MultiSpeck™, Thermo Fisher) absorbed on a surface was imaged with both a scientific grade sCMOS camera and the smartphone RGB camera (Figure S12). The two as-acquired images were then overlaid and it was found that the pixel dimension of the smartphone images was 0.526 $\mu\text{m}/\text{px}$. The size of the images analyzed for smartphone-based DNA detection experiments was of 200px \times 200px, meaning that the area of detection is 105 $\mu\text{m} \times$ 105 μm .

2. Supporting figures and tables

2.1. DLS measurements

Table S1. Nanoparticle diameters measured via dynamic light scattering for each ion pair and loading.^a

	diameter (nm)			
	dye/counterion pair			
loading (mM)	R110/F9-Al	R110-C18/F12	R6G-C18/F9-Al	R6G-C18/F12
5	44 ± 2	39 ± 5	45 ± 1	45 ± 1
120	42 ± 1	37 ± 2	48 ± 5	43 ± 5
250	39 ± 1	42 ± 1	43 ± 2	44 ± 1

^a Errors are standard deviation (n = 3).

2.2. Fluorescence and absorption spectroscopy

2.2.1. Donor nanoparticles

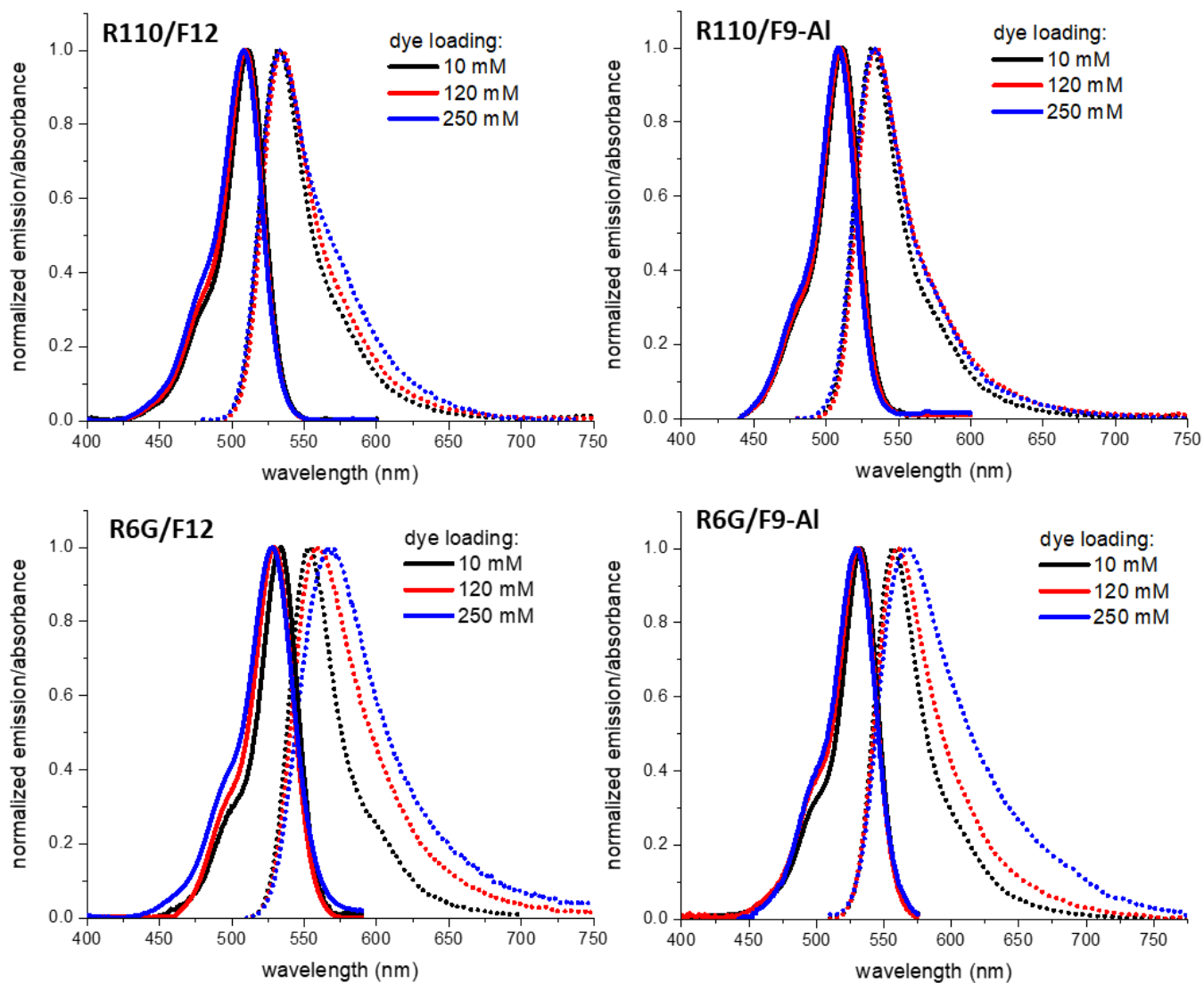


Figure S1. Normalized absorption and emission spectra of the polymeric NPs prepared with the four ion pairs at increasing dye loadings.

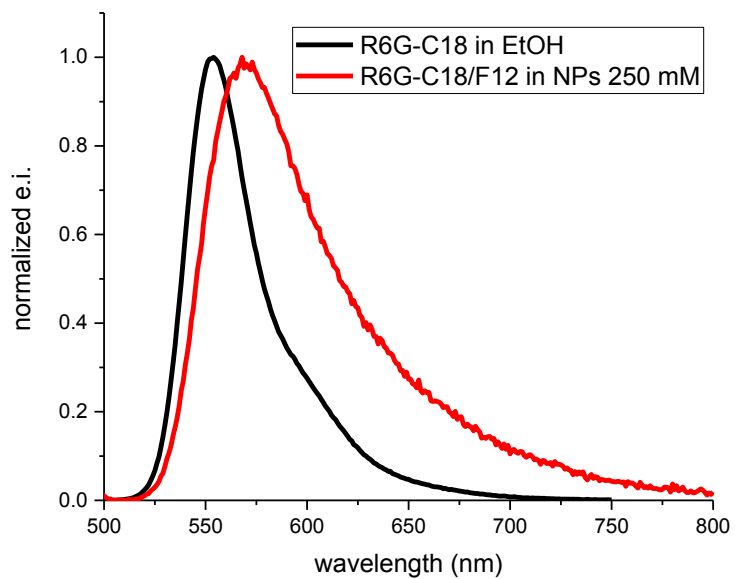


Figure S2. Emission of R6G-C18 in EtOH and in polymeric NPs loaded with R6G-C18 250 mM. A bathochromic shift and an increase of the bandwidth due to partial aggregation of the dye inside the polymeric matrix is evident.

2.2.2. FRET studies with acceptor inside the NPs

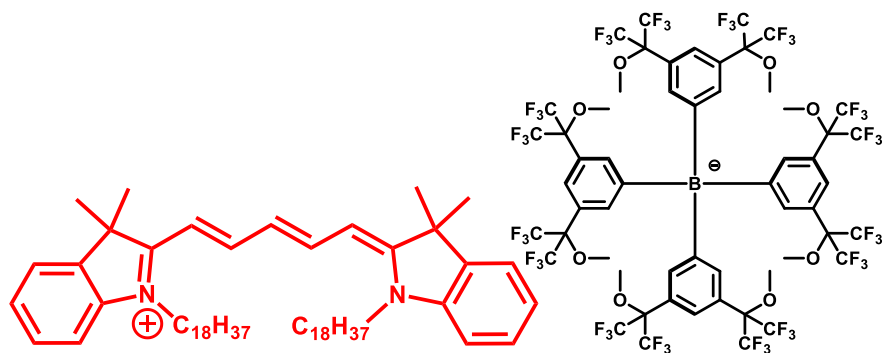


Figure S3. Structure of DID (with its counterion, F12), the FRET acceptor used in FRET studies with the acceptor inside the nanoparticles.

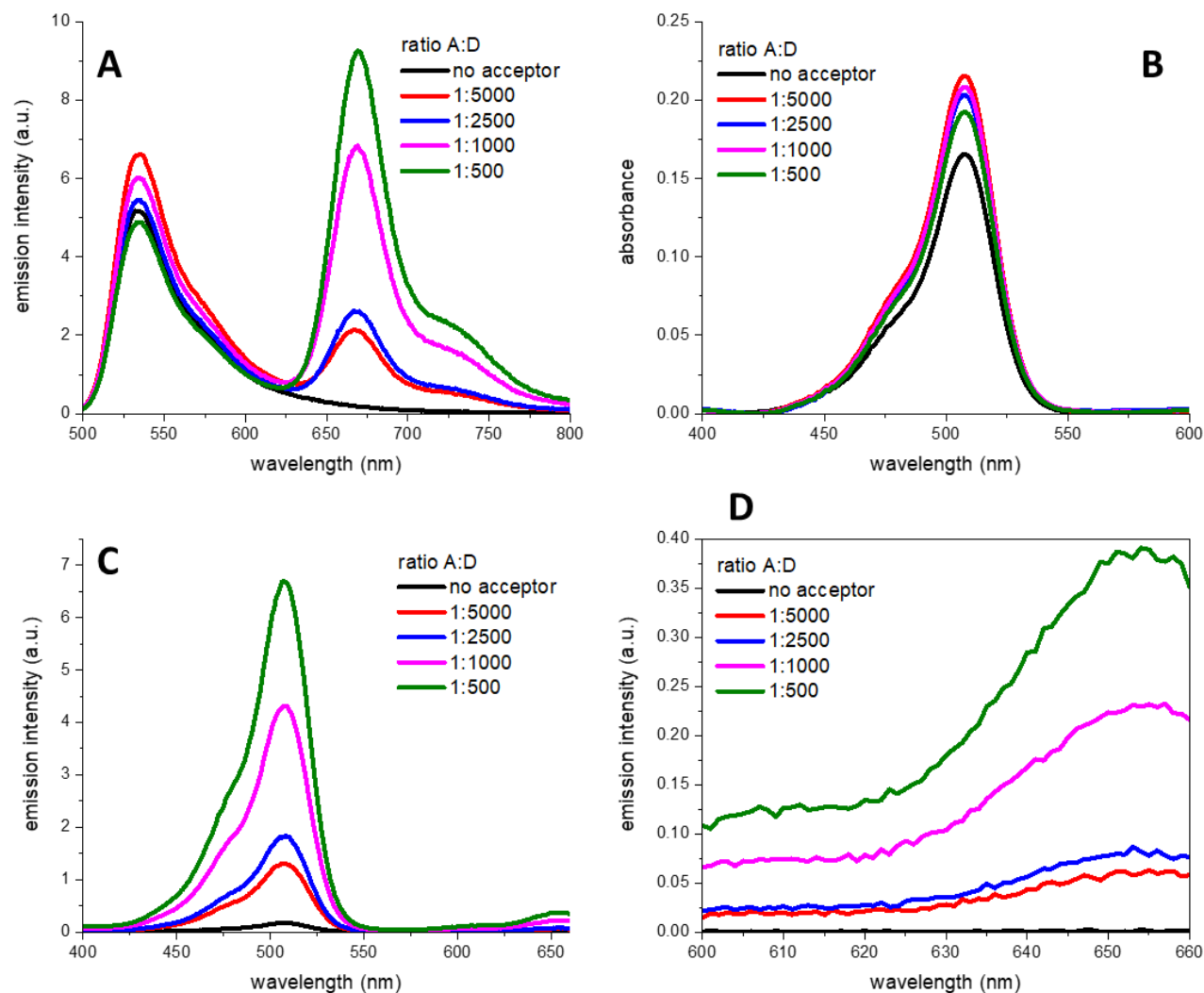


Figure S4. FRET studies: polymeric NPs encapsulating R110-C18/F9-AI at a 250 mM loading as a donor and a small quantity of DiD as an acceptor were prepared, and their FRET properties were tested, different acceptor/donor ratio were tested. (A) Emission spectra ($\lambda_{exc} = 488$ nm), (B) absorption spectra, (C) excitation spectra ($\lambda_{em} = 670$ nm), (D) zoom of the excitation spectra shown in (C).

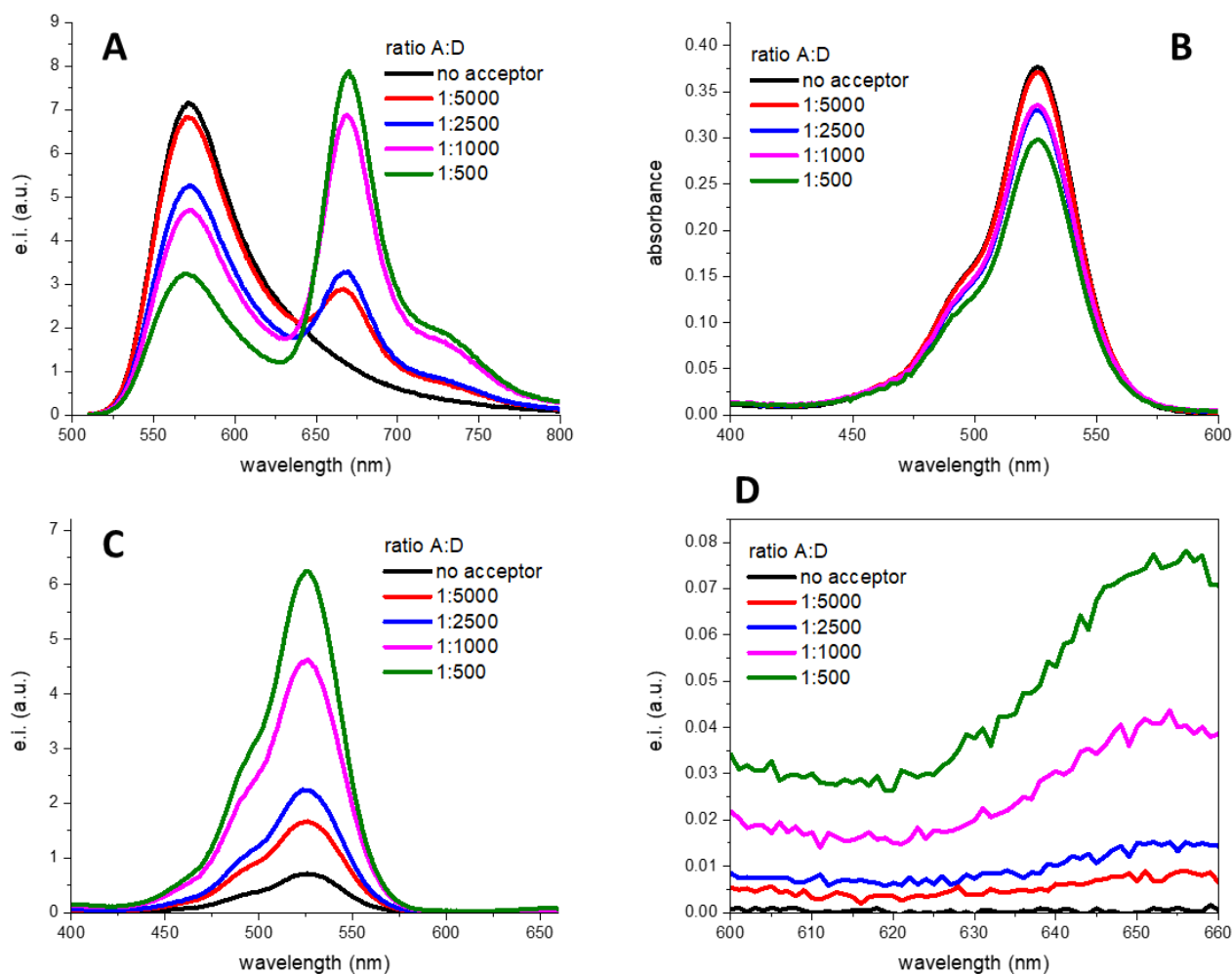


Figure S5. FRET studies: polymeric NPs encapsulating R6G-C18/F12 at a 250 mM loading as a donor and a small quantity of DiD as an acceptor were prepared, and their FRET properties were tested, different acceptor/donor ratio were tested. (A) Emission spectra ($\lambda_{exc} = 488$ nm), (B) absorption spectra, (C) excitation spectra ($\lambda_{em} = 670$ nm), (D) zoom of the excitation spectra shown in (C).

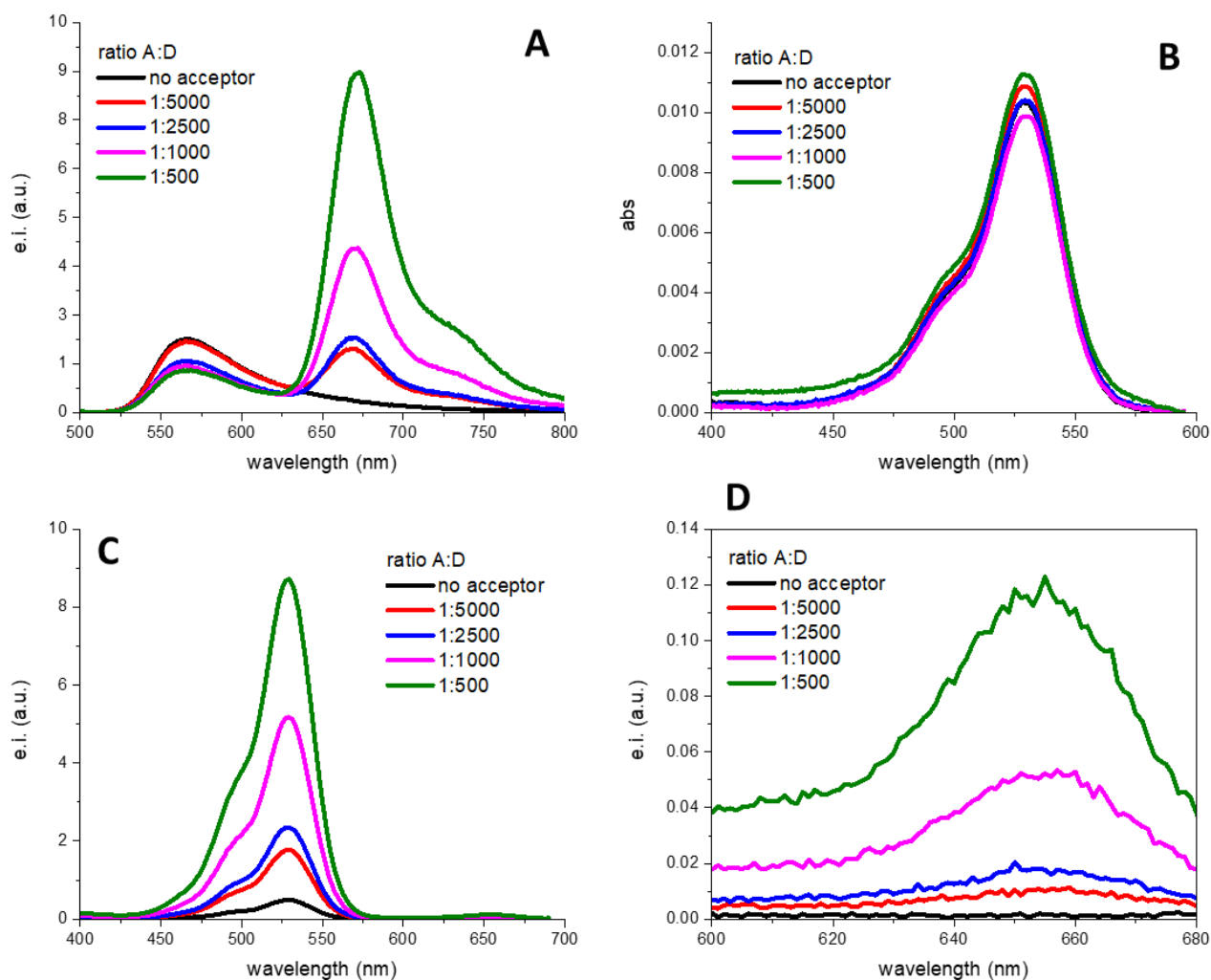


Figure S6. FRET studies: polymeric NPs encapsulating R110-C18/F9-AI at a 250 mM loading as a donor and a small quantity of DiD as an acceptor were prepared, and their FRET properties were tested, different acceptor/donor ratio were tested. (A) Emission spectra ($\lambda_{exc} = 488$ nm), (B) absorption spectra, (C) excitation spectra ($\lambda_{em} = 690$ nm), (D) zoom of the excitation spectra shown in (C).

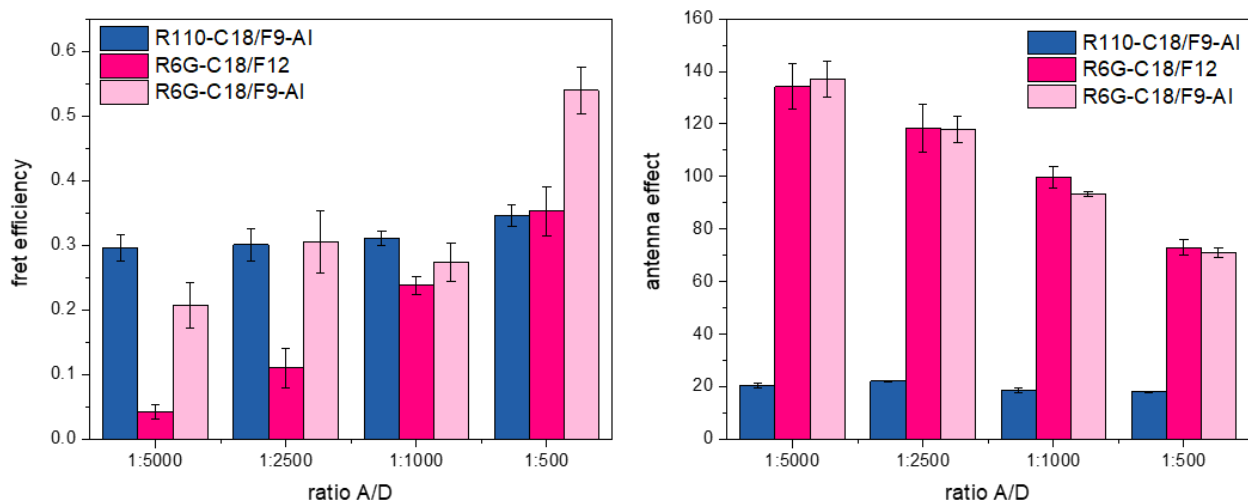


Figure S7. FRET efficiency (left) and antenna effect (right) of the three ion pairs as FRET donors inside NPs, previously shown as a function of acceptor to donor ratio based on the data in Figures S4-S6. Error bars are standard deviation ($n = 3$).

2.2.3. FRET studies with acceptor on the surface of the NPs

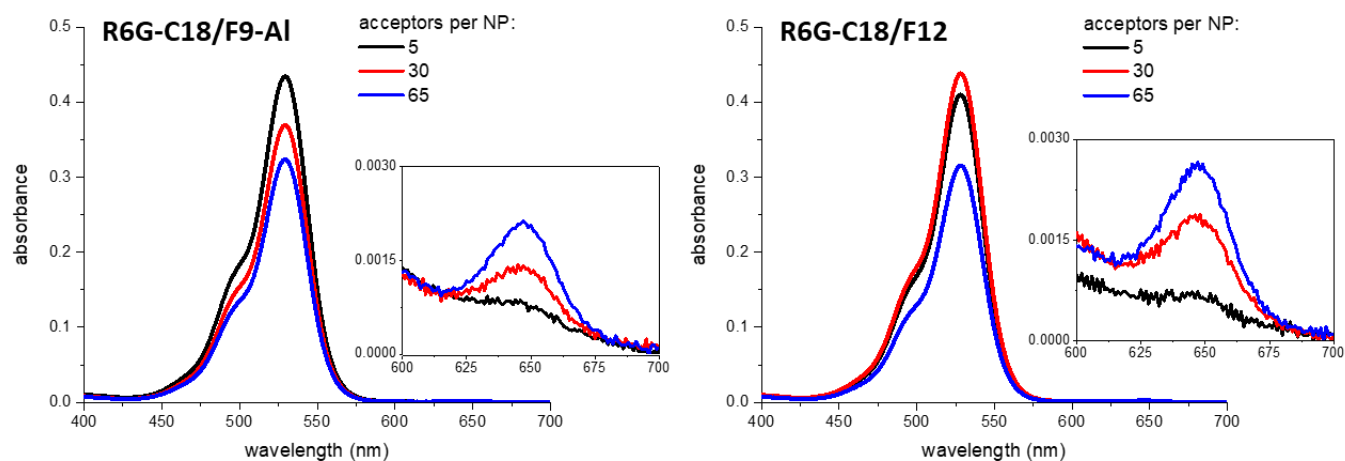


Figure S8. Absorption spectra of DNA-functionalized NPs encapsulating R6G-C18/F9-AI (left) and R6G-C18/F12 (right) with increasing quantities of acceptor (ATTO647N) at the surface, which allows calculation of the number of acceptors as described previously (Melnychuk and Klymchenko, 2018).

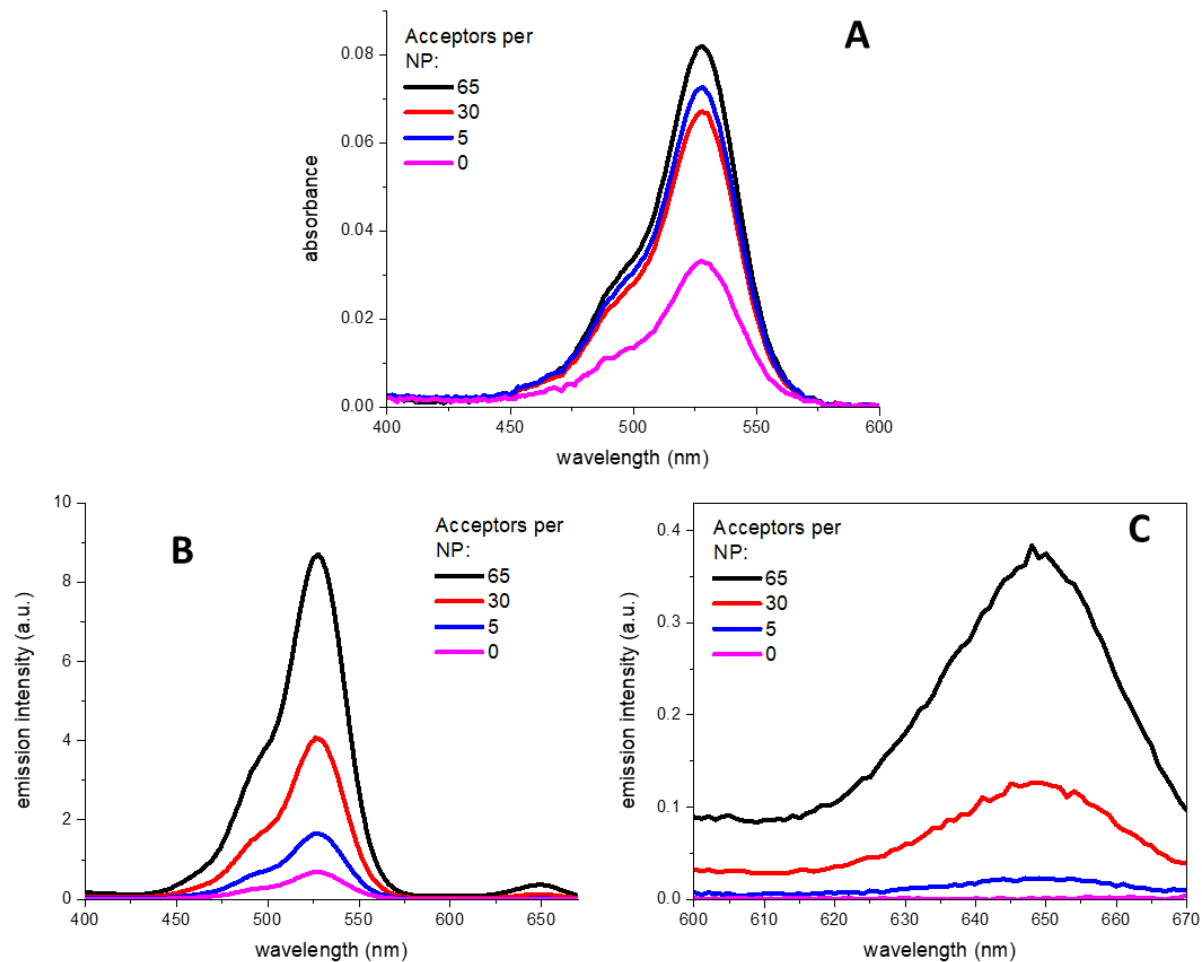


Figure S9. FRET studies on DNA-functionalized NPs encapsulating R6G-C18/F12 with a loading of 250 mM with the acceptor (ATTO647N) on the surface of the NPs with increasing quantity of acceptor. (A) absorption spectra, (B) excitation spectra ($\lambda_{em} = 680$ nm), (C) zoom on the acceptor part of the spectra shown in (C).

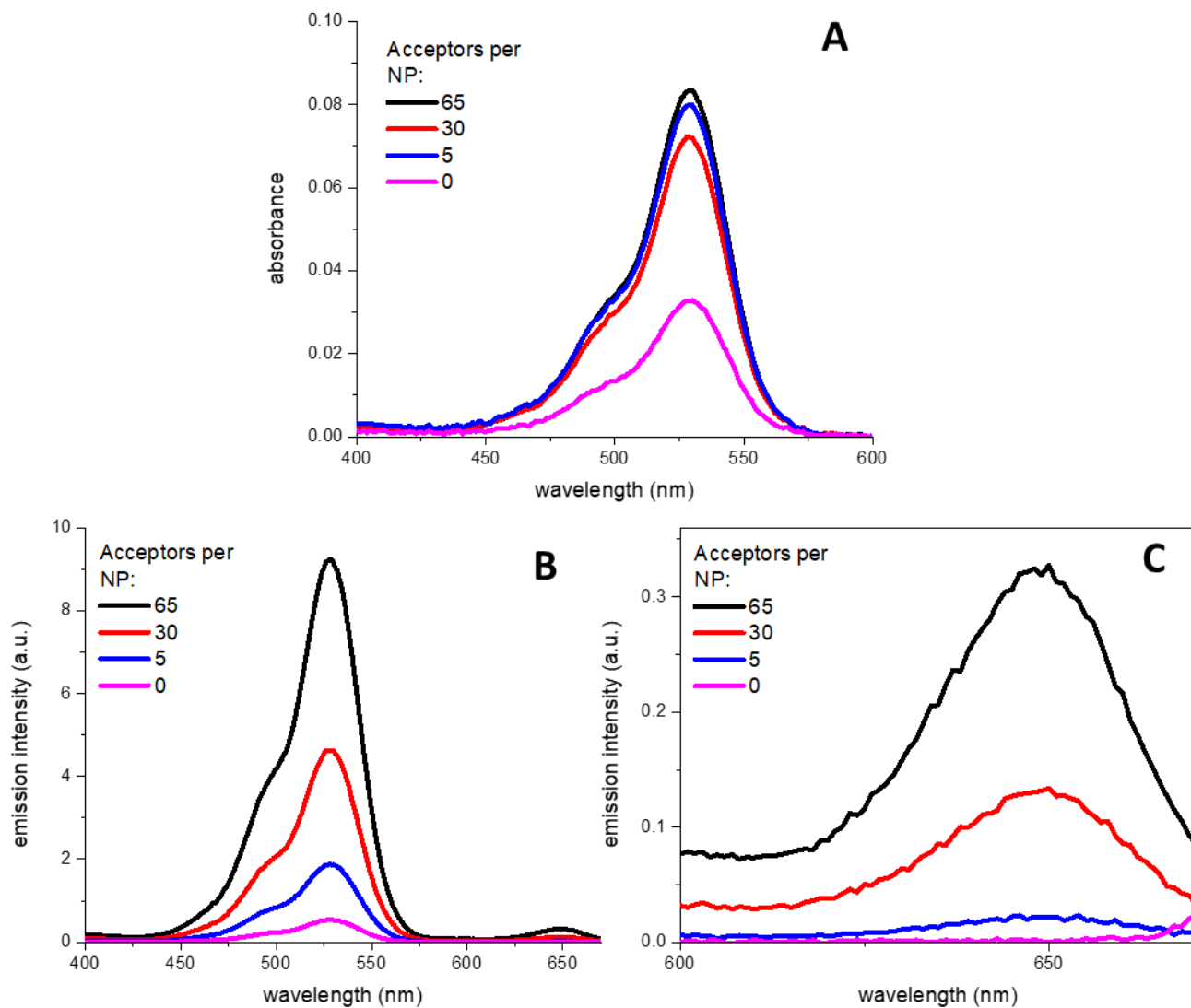


Figure S10. FRET studies on DNA-functionalized NPs encapsulating R6G-C18/F9-AI with a loading of 250 mM with the acceptor (ATTO647N) on the surface of the NPs with increasing quantity of acceptor. (A) absorption spectra, (B) excitation spectra ($\lambda_{em} = 680$ nm), (C) zoom on the acceptor part of the spectra shown in (C).

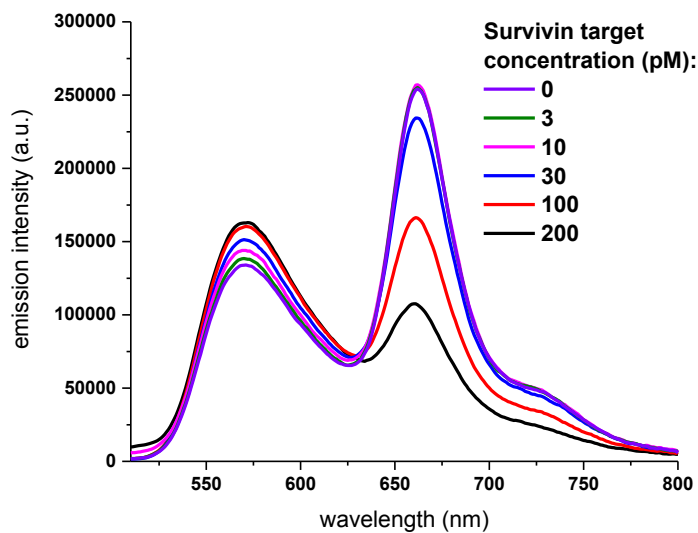


Figure S11. Non-normalized fluorescence spectra of NP-probe-65 incubated with increasing concentrations of the DNA target sequence. Data from Figure 4A.

Table S2 Parameters of the linear regression shown in Figure 3B,C.

Equation	$y = a + b*x$	
Residual Sum of Squares	28.0	
Pearson's r	-0.9971	
Adj. R-Square	0.9927	
	Value	Standard Error
Intercept	0.657	0.00115
Slope	-0.00135	5.17E-05

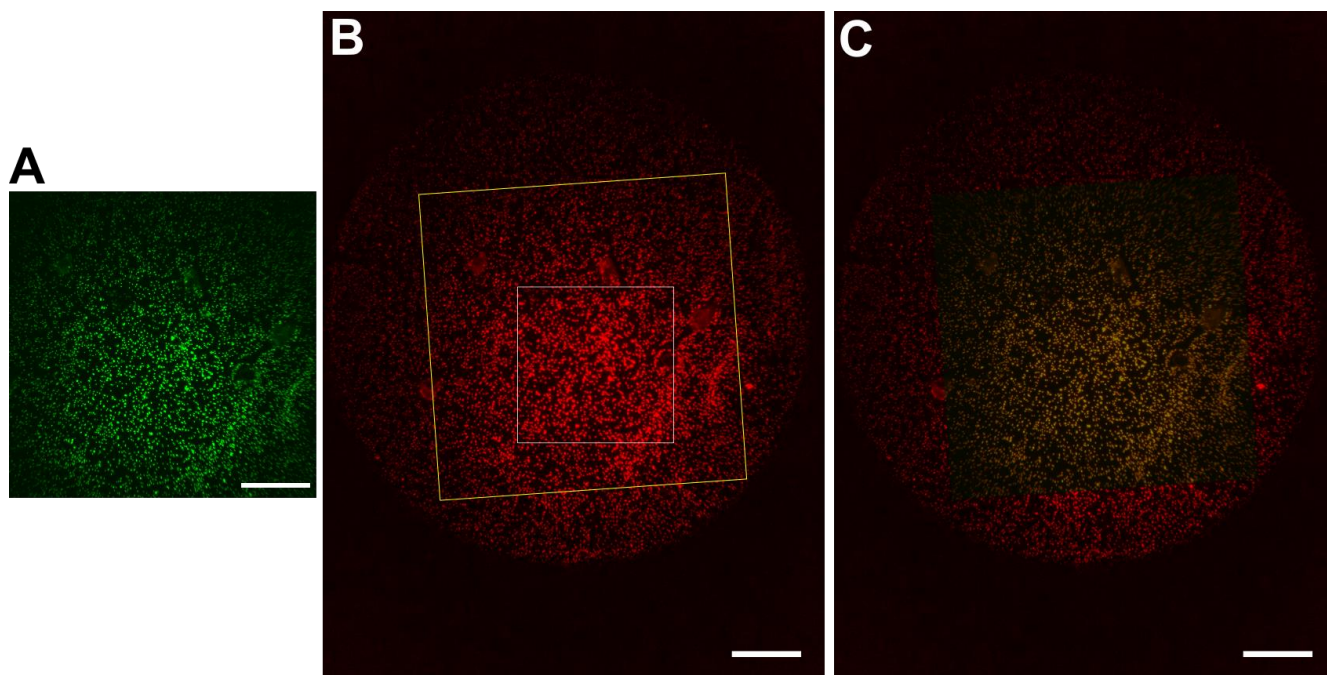


Figure S12. Estimation of the detection area of by the cellphone camera. (A) Microscopy image of fluorescent beads (MultiSpeck™, Thermo Fisher) acquired with sCMOS camera (Hamamatsu Orca Flash 4). (B) The same area of beads shown in (A) but acquired with the cellphone camera; yellow square represents the field captured in image (A), white square represents the area analyzed for DNA detection experiments. (C) Overlay between (A) and (B). Scale bars: 50 μm .

3. References

- Andreiuk, B., Reisch, A., Pivovarenko, V.G., Klymchenko, A.S., 2017. *Mater. Chem. Front.* 1, 2309–2316.
- Brouwer, A.M., 2011. *Pure Appl. Chem.* 83, 2213–2228.
- Floyd, D.L., Ragains, J.R., Skehel, J.J., Harrison, S.C., van Oijen, A.M., 2008. *Proc. Natl. Acad. Sci.* 105, 15382–15387.
- Krossing, I., 2001, *Chem. – Eur. J.*, 7, 490–502.
- Melnychuk, N., Klymchenko, A.S., 2018. *J. Am. Chem. Soc.* 140, 10856–10865.
- Schmied, J.J., Raab, M., Forthmann, C., Pibiri, E., Wunsch, B., Dammeyer, T., Tinnefeld, P., 2014. *Nat. Protoc.* 9, 1367–1391.
- Trofymchuk, K., Reisch, A., Didier, P., Frasc, F., Gilliot, P., Mely, Y., Klymchenko, A.S., 2017. *Nat. Photonics* 11, 657–663.
- Yang, Y.-K., Cho, H.J., Lee, J., Shin, I., Tae, J., 2009. *Org. Lett.* 11, 859–861.
1987. *The Analyst* 112, 199.

2.2. New counterions inside NPs: Synthesis of dye-loaded nanoparticles using a family of lanthanide-based counterions

Our second research direction –much like the first project presented in section 2.1– was focused on tuning the properties of the core of dye-loaded polymeric nanoparticles. While in the previous section we tested new fluorophores in the preparation of nanoparticles, in the present section we turned our attention towards counterions, which can also greatly modulate the photophysical properties of dye-loaded polymeric nanoparticles.

As previously discussed, dye-loaded polymeric nanoparticles are potentially very bright platforms, due to the high numbers of encapsulated dyes. However, when excessively increasing the dye loading, the fluorophores tend to self-quench due to close proximity, limiting the overall brightness of the system. Several strategies to counter this phenomenon have been developed, like employing AIE fluorophores, covalently binding the dyes to the polymeric chains, or employing bulky spacers to reduce dye aggregation.

In the approach developed in our team, a cationic fluorescent dye is paired with a bulky hydrophobic counterion (CI) for encapsulation into polymeric NPs. The presence of the counterion ensures that the fluorophores are well encapsulated and not self-quenched, thus yielding small and bright particles (Figure 2.3B). This approach has been validated so far on few compounds such as tetraphenylborates (Andreiuk et al., 2019; Reisch et al., 2014) and alkoxyaluminates (Andreiuk et al., 2017b). However, two important points are not yet addressed: (i) whether the counterion approach is extensible to anionic complexes of other metals on the periodic table, and (ii) whether it is possible to prepare a system where the anion provides nanoparticles with new properties for other imaging modalities.

With these two questions in mind we prepared NPs using several gadolinium and europium complexes as counterions (provided by a collaborator, Prof. Tero Soukka, University of Turku, Finland) with varied bulkiness, hydrophobicity and fluorination level (Figure 2.3A). Gadolinium complexes were chosen because they can provide a contrast in Transmission Electron Microscopy (TEM), which would enable preparation of NPs for multi-modal imaging. Europium complexes on the other hand can be excited in the ultraviolet (UV – where the ligands absorb) and transfer their energy to energy acceptor (e.g. Cy5), which emits in the far-red, generating ultra-long Stokes shift

2. Results and discussion

nanoparticles. Nanoparticles were prepared by nanoprecipitating polymer and the perchlorate salt of R18 with varied amount of Gd-based counterions (Figure 2.3A).

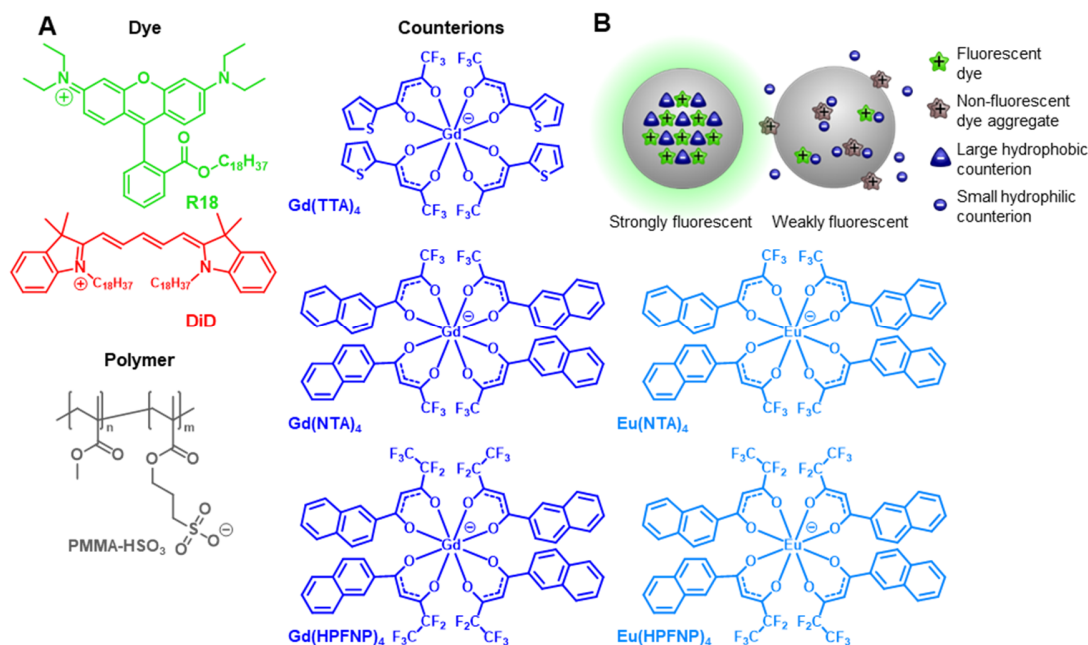


Figure 2.3 (A) Cationic fluorescent dyes (in green and red), lanthanide-based anions (in blue and light blue) and sulfonate bearing polymer (in grey) used for nanoparticle preparation. (B) Hypothetic models of fluorescent dye distribution inside polymeric NPs when prepared with small hydrophilic counterions (left) and bulky hydrophobic counterions (right).

It was found that NPs prepared perchlorate salt of R18 were generally larger, more polydisperse and poorly non-emissive at higher dye loadings, whereas those prepared with the Gd-based counterion were smaller, showing higher quantum yields (Figure 2.3B) and narrower emission bands (Figure 2.4A-B). When compared to quantum dots, all the NPs formulated with the three different Gd-based counterions were significantly brighter. Importantly NPs encapsulating Gd(HPFNP)₄ were the brightest (Figure 2.4C), indicating the importance of size and fluorination of Gd-complex for preventing ACQ. Moreover, when incubated with HeLa cells, the NPs formulated with an excess of Gd-based counterion were readily internalized by endocytosis with no signs of dye leaching, while NPs formulated with the chloride salt of R18 showed strong leaching behaviour, staining both the plasma membrane and the cytoplasm (Figure 2.4D). Moreover, NPs formulated with a Gd-based counterion displayed limited cytotoxicity at the concentrations used habitually for imaging (Figure 2.4E). An article is currently being prepared based on the results reported in this section. Moreover, DiD and Eu-complexes were co-

2.2. Manuscript: Preparation of lanthanide-based nanoparticles

precipitated and the FRET properties of the as-obtained NPs were measured, finding that Eu-CIs were able to transfer almost the totality of their excitation energy towards DiD.

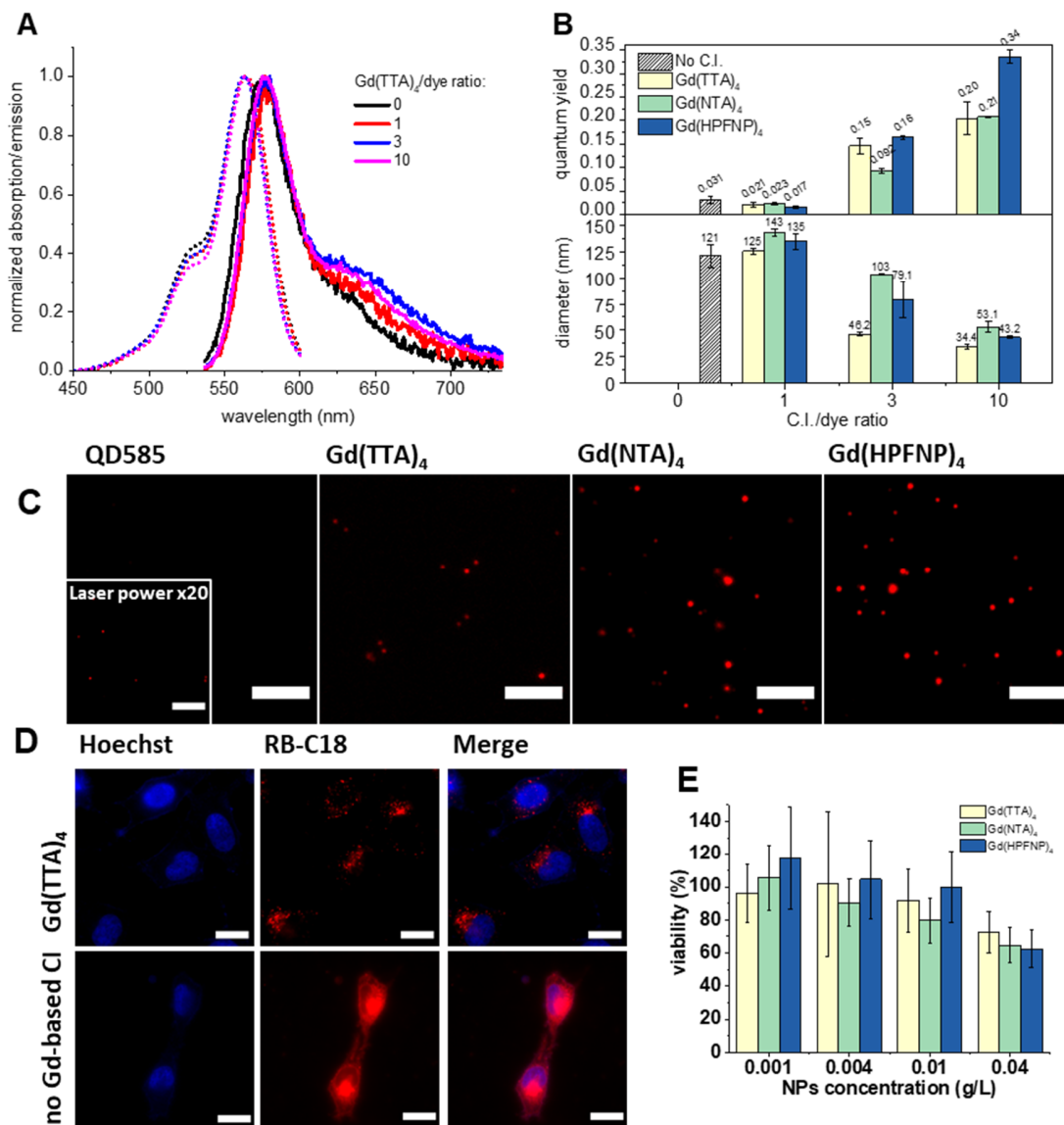


Figure 2.4 (A) Normalized absorption and emission spectra of NPs loaded with R18 (250 mM with respect to the polymer) with increasing quantities of Gd-based counterions. (B) Fluorescence quantum yield (top) and particle size (bottom) as a function of Gd-counterion/R18 dye molar ratio at 250 mM dye loading for three studied Gd-counterions. (C) Single-particle fluorescence images of polymeric NPs prepared with a 10-fold excess of Gd-based counterion with a dye loading of 250 mM compared to reference quantum dots QD585. Scale bars: 5 μ m. (D) Epifluorescence microscopy images of HeLa cells incubated with polymeric NPs (250 mM R18 dye loading with and without a ten-fold excess of Gd(TTA)₄). (E) Cytotoxicity experiments for polymeric NPs loaded with 250 mM R18 and Gd-based counterion. Scale bars: 20 μ m.

2. Results and discussion

2.2.1. Article 2 (manuscript). Lanthanide-based bulky counterions for preparation of highly fluorescent dye-loaded polymeric nanoparticles

Lanthanide-based bulky counterions for enhanced encapsulation and emission of dyes in polymeric nanoparticles

Caterina Severi,^a Satu Lahtinen,^b Jaana Rosenberg,^b Andreas Reisch,^a Tero Soukka,^{b,*} Andrey S. Klymchenko^{a,*}

^a Laboratoire de Biophotonique et Pathologies, Faculté de Pharmacie, UMR 7021 CNRS, Université de Strasbourg, 74, Route du Rhin, 67401 Cedex, Illkirch, France

^b Department of Biotechnology, University of Turku, Kiinamylynkatu 10, 20520 Turku, Finland

*Corresponding authors. E-mail addresses: andrey.klymchenko@unistra.fr (A. S. Klymchenko); tejoso@utu.fi (T. Soukka).

Abstract

Fluorescent nanoparticles are promising bioimaging contrast agents. Dye-loaded polymeric nanoparticles are of particular interest because of their available surface chemistry, high brightness and tunable optical properties. However, high dye loadings can cause the aggregation-caused quenching (ACQ) of the encapsulated fluorophores. Previously, we proposed a way to mitigate the ACQ by insulating cationic dyes with bulky hydrophobic counterions. In the present work, we extend the concept of bulky counterions to lanthanide-based complexes. We show that by employing Gd-based counterions with rhodamine B loaded NPs at 30 wt% loading with respect to polymer, we increase the quantum yield from 0.03 with small inorganic counterion to 0.34. Moreover, Gd-loaded NPs strongly scatter electrons, and appear dark on TEM images even in absence of contrast agent. Finally, luminescent Eu-based complexes were used as counterions in the formulation with a far-red cationic cyanine 5 dye (DiD), yielding FRET NPs where the UV-excited Eu-based counterion transfers energy to DiD, generating an ultra-long Stokes shift of ~340 nm. Our findings will help developing multifunctional nanomaterials presenting high fluorescence brightness.

2. Results and discussion

Introduction

Fluorescent nanoparticles (NPs) have emerged as a powerful bioimaging tool (Wolfbeis, 2015) due to their superior brightness in respect to organic dyes, while their available surface chemistry allows combining different functionalities in one theranostic platform. There are several different types of fluorescent NPs, with the most famous being: quantum dots (QDs) (Michalet, 2005), dye-doped silica nanoparticles (Montalti et al., 2014) and carbon dots (CDs) (Luo et al., 2013; Mochalin et al., 2012). However, recently "all-organic" NPs have started to gain interest as well, with system such as lipid (Klymchenko et al., 2021), conjugated polymer (Wu and Chiu, 2013) and dye-loaded polymeric nanoparticles (Li and Liu, 2014; Reisch and Klymchenko, 2016b), progressively becoming more popular and widespread.

Among all the previously mentioned nanoparticle types, dye-loaded polymeric nanoparticles are attractive systems for various reasons: the polymeric matrix can be designed to be biodegradable and biocompatible; it is possible to co-encapsulate dyes with other contrast agents and/or drugs; the wide variety of organic dyes available makes it possible to prepare fluorescent NPs with virtually any spectroscopic characteristic (Andreiuk et al., 2017a; Reisch et al., 2014; Trofymchuk et al., 2014). However, at high concentrations fluorophores tend to aggregate, giving rise to the aggregation-caused quenching phenomenon (ACQ), limiting the overall brightness of the system (Reisch and Klymchenko, 2016b). This issue has been tackled with different approaches: the most popular and straightforward being the use of aggregation induced emission (AIE) molecules (Li and Liu, 2014; Zhang et al., 2015). Moreover, it was also demonstrated that the incorporation of long hydrocarbon chains and/or bulky side groups can mitigate the ACQ phenomenon (Grazon et al., 2013; Tian et al., 2009; Wagh et al., 2012). In addition, when dealing with charged dyes another powerful approach is the use of bulky hydrophobic counterions (CIs) (Andreiuk et al., 2019; Reisch et al., 2014), which insulate the fluorophores effectively to avoid ACQ and at the same time improve the dye encapsulation inside the polymeric matrix and prevent dye leaching in biological media.

These counterions generally belong to the class of weakly coordinating anions due to their large size and delocalization of charge (Krossing and Raabe, 2004). Notable examples are tetraphenyl borates (TPBs), tetraalkoxyaluminates, bis(alkylsulfonyl)-imides, *etc.* Weakly coordinating ions found a broad range of applications ranging from catalysis (Jia and Bandini, 2015), electrochemistry (Geiger and Barrière, 2010), ionic liquids (Raabe et al., 2009; Rupp and Krossing, 2015), lithium batteries (Rupp et al., 2014), ion sensors (Xie et al., 2015) and organic light-emitting diodes (Ma et al., 2016). This class of compounds found yet another application in the formulation of dye-loaded polymeric nanoparticles (Reisch et al., 2014), ultra-small fluorescent micelles (Shulov et al., 2016a, 2016b) and ultra-bright dye-counterion aggregates (Aparin et al., 2020; Bwambok et al., 2009; Shulov et al., 2015; Yao and Ashiba, 2011).

Originally, the concept of bulky counterions for preventing ACQ in polymer NPs was developed based on fluorinated tetraphenyl borate (Reisch et al., 2014). Later studies showed that these

2.2. Manuscript: Preparation of lanthanide-based nanoparticles

counterions can be replaced by other bulky, hydrophobic, and especially fluorinated counterions based on boron and aluminum (Andreiuk et al., 2019, 2017b). However, in these previous works, the counterion did not add any further functionality to the system besides preventing ACQ and dye leaching; while theoretically it could be possible to tailor the structure of the counterion in order to transform the system into a multifunctional platform.

In this work we further extended the library of bulky counterions by testing a family of lanthanide (specifically gadolinium and europium) chelated counterions with increasing hydrophobicity (Figure 1A). The reasons behind this choice are two: (i) lanthanides are heavy atoms routinely used as contrast agents in transmission electron microscopy (TEM), therefore dye-loaded fluorescent nanoparticles encapsulating a lanthanide-based counterion can function as multifunctional platforms for fluorescence microscopy and TEM; (ii) europium complexes are attractive luminescent reporters due to their long-lived emission, allowing background-free time-gated detection (Cardoso Dos Santos et al., 2019); (iii) emission bands of the UV-excited europium complexes fall in the visible, making it a potential FRET donor for the cationic fluorescent dyes coupled with such counterion, generating ultra-long Stokes shift systems. We tested these lanthanide-based counterions by formulating NPs loaded with two cationic dyes: an octadecyl ester of rhodamine B and a dioctadecyl derivative of cyanine 5 (DiD) (Figure 1A).

We found that NPs prepared with Gd-based counterions featured superior quantum yields, smaller sizes and narrower emission bands in respect to NPs prepared with Rhodamine B perchlorate and DiD perchlorate. Moreover, when imaged by TEM they displayed a strong contrast in respect to NPs formulated without heavy atom-based counterions. When an ion pair of cationic DiD with anionic europium complexes were used for encapsulation, we obtained an efficient FRET from the lanthanide anion to the cationic dye generating delayed fluorescence with ~340 nm Stokes shift. Cellular studies showed that the dye/Gd-anion loaded NPs readily internalized by endocytosis with little to no leaching of the fluorescent dye, while NPs prepared in absence of the bulky counterion displayed a marked dye leaching behavior. Finally, the NPs loaded with dye paired with the lanthanide anion displayed minimal cytotoxicity at concentrations habitually used for cellular imaging.

Materials and methods

Materials

Methyl methacrylate (99%), 3-sulfopropyl methacrylate potassium salt (98%), acetonitrile (anhydrous, 99.8%), rhodamine B octadecyl ester perchlorate (>98.0%), polyethylenimine (branched), potassium hydroxide ($\geq 85\%$, pellets), Tris(hydroxymethyl)aminomethane (ACS reagent, $\geq 99.8\%$), 2-Acetonaphthone (99%), sodium hydride (90%, dry), THF ($\geq 99.9\%$, anhydrous), Ethyl pentafluoropropionate (98%), 4,4,4-Trifluoro-1-(2-naphthyl)-1,3-butanedione (99%), 2-Thenoyltrifluoroacetone (99%), Europium(III) chloride (99.99%), Gadolinium(III) chloride (99.99%) were purchased from Sigma-Aldrich. MilliQ-water (Millipore) was used in all

2. Results and discussion

experiments. 1,1'-Dioctadecyl-3,3,3',3'-Tetramethylindodicarbocyanine Perchlorate (DiD' oil) and Qdot585 streptavidin conjugate were purchased from Thermo-Fisher Scientific.

Synthesis

The polymer PMMA-HSO₃ was synthesized following a previously described procedure (Reisch et al., 2018). HPFNP was synthesized according to a previously described procedure (Raj et al., 2008). The ligand, either 2-thenoyltrifluoroacetone (TTA), 4,4,4-trifluoro-1-(2-naphthyl)-1,3-butanedione (NTA) or HPFNP was dissolved in ethanol and combined with EtOH solution of KOH. Then aqueous lanthanide(III) chloride solution was added dropwise to reach the molar ratio to ligand of 1:4 in case of Gd(III), and 1:3.2 in case of Eu(III). The product was precipitated with water, the precipitate was then filtered, washed twice with cold water and dried.

Nanoparticles preparation and characterization

PMMA-HSO₃ (at a concentration of 2 mg/mL), different amounts of dye ranging from 5 mM to 250 mM (with respect to the polymer) and Gd-based counterions (where specified) were dissolved in acetonitrile. This as-prepared organic stock solution was then diluted initially in a ten-fold excess of milliQ water under shaking and then rapidly diluted a second time in a five-fold excess of milliQ water.

Nanoparticle diameter was determined by DLS using a Zetasizer Nano ZSP (Malvern Instruments S.A.). For the data analysis the mean value of the size distribution per volume was taken. For the spectroscopic characterization all the solvents used were of spectroscopic grade and MilliQ water was used in all experiments. Absorption spectra were recorded on a Cary-4000 scan UV-visible spectrophotometer (Varian), while emission spectra were recorded with a Spectrofluorometer FS5 (Edinburgh Instruments). Fluorescence spectra were corrected both for lamp fluctuations and detector response. The emission spectra were recorded setting the excitation wavelength to 535 nm for R18-based NPs and at 340 nm for Eu-based NPs. Fluorescence quantum yields of nanoparticles loaded with rhodamine B octadecyl ester perchlorate were calculated using Rhodamine 101 (QY = 1.0 in MeOH) as a standard (Würth et al., 2013); for nanoparticles loaded with Eu complexes (with and without FRET acceptor), Quinine sulfate (QY = 0.52 in H₂SO₄ 0.05 M) was taken as reference; while for nanoparticles loaded exclusively with DiD, Nile blue (QY = 0.27 in EtOH) was taken as a reference (Brouwer, 2011).

Fluorescence decays of nanoparticles loaded with Eu complexes (with and without FRET acceptor) were recorded on a Cary Varian Eclipse Spectrofluorometer using the lifetime mode with excitation wavelength of 337 nm (20 nm slit) and emission wavelength 612 nm (20 nm slit). Lifetimes were obtained by fitting the data to single or biexponential decay function.

FRET efficiency was calculated both from donor fluorescence intensity and lifetime using the following formulas:

2.2. Manuscript: Preparation of lanthanide-based nanoparticles

$$E = 1 - \frac{I_D^A}{I_D} \quad (1)$$

$$E = 1 - \frac{\tau_D^A}{\tau_D} \quad (2)$$

where I_D^A and I_D are the donor fluorescence intensity in presence and absence of acceptor respectively, τ_D^A and τ_D are the donor fluorescence lifetime in presence and absence of acceptor respectively.

Single-particle fluorescence microscopy

For single-particle fluorescence microscopy experiments, the NPs were adsorbed on a glass surface (LabTek 8-well plate) according to a previously described procedure (Reisch et al., 2014). The glass surface was first treated with KOH solution 1 M, and subsequently incubated with a solution of polyethylenimine (PEI) 1 g/L in TRIS 10 mM, pH 7.4. The NP suspensions were diluted 100 times and they were incubated on the PEI-covered glass for 15 min before washing and measuring with a layer of milliQ water above the sample. QD585 (10 pM) were immobilized on the glass surface with the same protocol.

Single-particle measurements were performed in the wide-field epi-fluorescence mode with a Nikon Ti-E inverted microscope with a 60x objective (Apo TIRF, oil, NA 1.49, Nikon). The excitation was provided by light-emitting diodes (SpectraX, Lumencor). Sample was excited at 550 nm with a LED at a power of 6.75 mW. Images were recorded with an integration time of 200 ms and the single particle analysis was performed on the FIJI software.

Particles were detected using a FIJI macro (available upon request) applied to a projection (average intensity) of 10 frames using an appropriate threshold: after automatic background subtraction the mean intensities of circular region of interest with a diameter of 6 pixels around the as-found intensity maximum were measured. Then the intensity in the circular regions of interest was integrated over the first 5 frames and it was used to generate the particle intensity histograms.

Transmission electron microscopy

5 μ L of NPs suspension were deposited on carbon-coated copper-rhodium TEM grids previously treated *via* amylamine glow-discharge. The prepared grids were imaged using a Tecnai F20 Twin transmission electron microscope (FEI Eindhoven Holland) operating at 200 kV. Images of areas of interest were acquired with a US1000 camera (Gatan). Image analysis was performed in FIJI.

Cellular studies

HeLa cells were cultured in DMEM (Gibco-Invitrogen) supplemented with 10% FBS (Lonza), 5% L-glutamine (Gibco-Invitrogen) and 1% antibiotic solution (penicillin-streptomycin, Gibco-Invitrogen) at 37 °C in a humidified atmosphere containing 5% of CO₂. Cells were seeded in a μ -

2. Results and discussion

dish (glass bottom, 35 mm, IBiDi) at a density of 100k cells per well 24 h before the microscopy measurement.

For imaging, the culture medium was removed and the cells were washed with Opti-MEM (Gibco-Invitrogen). Cells were stained with Hoechst dye with a concentration of 5 $\mu\text{g}/\text{mL}$ for 15 min at 37 $^{\circ}\text{C}$. Then cells were washed again with Opti-MEM and a freshly prepared suspension of NPs (with a concentration of 0.004 g/L) in Opti-MEM was added to the cells and incubated for 30 min at 37 $^{\circ}\text{C}$. Finally, cells were washed once again with Opti-MEM and imaged.

Cytotoxicity studies were performed by seeding HeLa cells in 96-well plates with a concentration of $\sim 10\text{k}$ cells/well in 100 μL of the DMEM growth medium and incubating them overnight. Then NPs were added by replacing the DMEM with the same culture medium containing increasing quantities of nanoparticles. Cells were incubated for 24 hours in presence of NPs, then the culture medium was removed and the wells washed with PBS. The wells were filled with DMEM containing MTT (3-(4,5-dimethylthiazol-2-yl)-2,5-diphenyltetrazolium bromide) and the cells were again incubated at 37 $^{\circ}\text{C}$ for 4 h. The formazan crystals were re-dissolved by adding 100 μL of DMSO and shaking gently for 10 min. Then the absorbance at 570 nm on each well was read with a microplate reader. Experiments were carried out in triplicates and the viability of the cells is expressed as a percentage of viable cells compared to the control group.

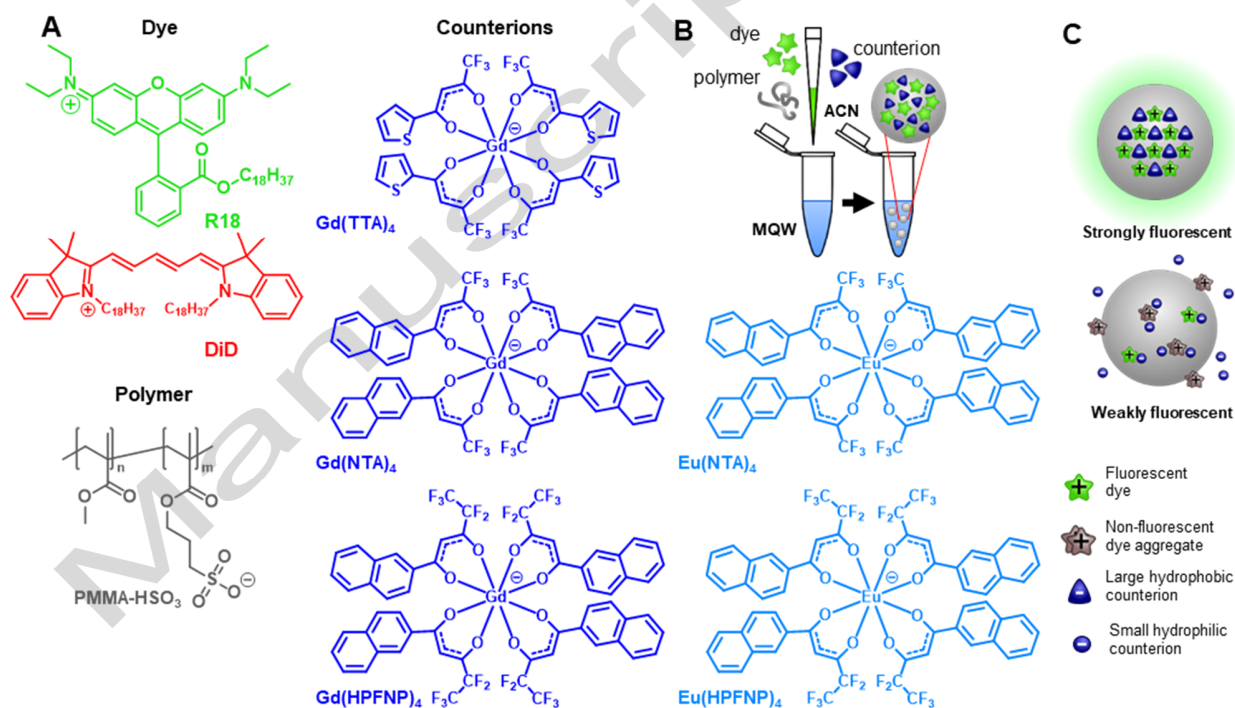


Figure 1. (A) Cationic fluorescent dyes: R18 (in green), DiD (in red); sulfonate bearing polymer (in grey), and lanthanide-based anions (in blue and light blue) used for nanoparticle preparation. (B) Preparation of NPs via nanoprecipitation scheme. (C) Hypothetic models of fluorescent dye distribution inside polymeric NPs when prepared with small hydrophilic counterions (left) and bulky hydrophobic counterions (right).

Results and discussion

Preparation and characterization of NPs based on lanthanide counterions

To design the lanthanide counterions, we used Gd and Eu salts, known to yield optically transparent and emissive complexes, respectively. For the Gd ion, we prepared three complexes characterized by increasing size and/or fluorination level in the following order: $\text{Gd}(\text{TTA})_4 < \text{Gd}(\text{NTA})_4 < \text{Gd}(\text{HPFNP})$ (Figure 1A). For the Eu ion, the two largest complexes were prepared: $\text{Eu}(\text{NTA})_4$ and $\text{Eu}(\text{HPFNP})$. First, we attempted to prepare pure salts of R18 dye with corresponding lanthanide-based counterions (Figure 1A) by ion exchange followed by silica gel chromatography as previously reported (Andreiuk et al., 2017a). However, the dye salts showed tendency to decompose on silica. We suspect that lanthanide-based counterions are not as hydrophobic as fluorinated TPB, so that they undergo an ion exchange on the silica. Therefore, we mixed the dye perchlorate salt solution with the lanthanide-based counterion potassium salt solution directly in the organic stock to be nanoprecipitated.

First, we investigated the optimal ratio between the dye and the counterion in the formulation of NPs. To this end, NPs loaded with 250 mM of R18 with respect to the polymer and increasing quantities of Gd-based CIs (Figure 1A) were prepared, their sizes and spectroscopic properties measured, and their quantum yields calculated (Figure 2). It was immediately clear that NPs formulated in absence of a bulky hydrophobic counterion tended to yield poorly emissive particles due to ACQ. Moreover, we observed that fluorophores did not get properly encapsulated either, resulting in larger particles (Figure 1C), in line with previous studies (Andreiuk et al., 2019; Reisch et al., 2014).

Preparing NPs with a molar ratio 1:1 of dye/counterion improved neither the quantum yield, nor their size (Figure 2B). A three-fold excess of CI marginally increased the QY of the NPs and yielded smaller sizes, while NPs formulated with a 10-fold excess of CI yielded NPs with very high quantum yields (up to 0.34) and the smallest size. Furthermore, we observed that the presence of higher quantities of counterion in the polymeric matrix also had an effect on absorption and emission spectra (Figure 2A and C), with bands getting narrower with the increase in Gd-CI loading: an indication of a lower degree of the dye aggregation in presence of the counterion.

After establishing that the optimal counterion molar excess in respect to R18 was 10-fold, we proceeded to test lower loadings of R18 with and without the 10-fold excess of different Gd-CIs. At the lowest loading (5 mM), there was no any marked effect of counterion on particle size because the dye concentration was too low to influence the particle formation process (Figure 2D). However, there was a strong effect on fluorescence quantum yields, with an increase from 0.4 to >0.9 in presence of Gd-CIs. At the intermediate loading of R18 (75 mM) there was a marked effect on both particle size and fluorescence quantum yield, where $\text{Gd}(\text{TTA})_4$ performed best, both in terms of QY and size (0.48 and 22 nm). However, at the highest loading (250 mM), the trend inverted, and the highest QY was obtained by employing the largest counterion $\text{Gd}(\text{HPFNP})_4$ (Figure 2D).

2. Results and discussion

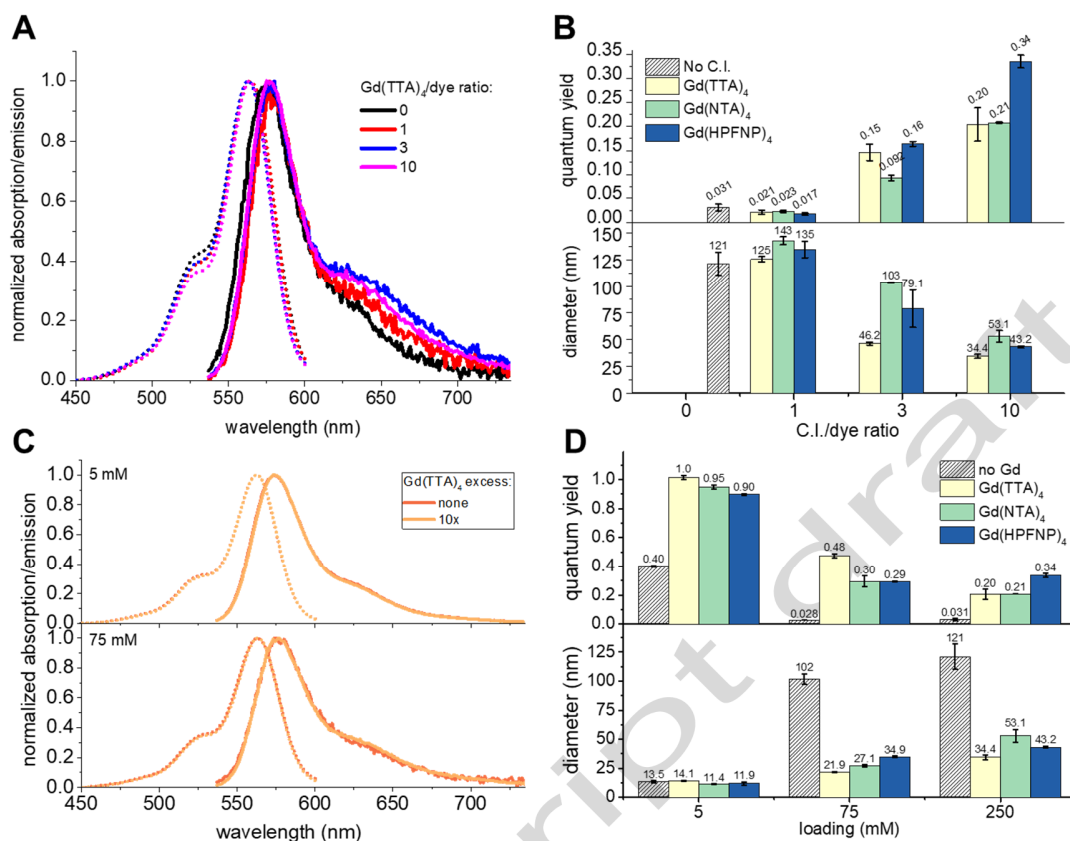


Figure 2. NPs loaded with R18 (250 mM) with increasing quantities of Gd-based counterions: (A) Normalized absorption and emission spectra for increasing quantities of Gd(TTA)₄ and (B) fluorescence quantum yield (top) and particle size (bottom) as a function of counterion/dye molar ratio for each counterion. (C) Normalized absorption and emission spectra of NPs loaded with R18 (5 mM and 75 mM) with and without a ten-fold excess of Gd(TTA)₄. (D) Fluorescence quantum yield (top) and particle size (bottom) for R18-loaded NPs as a function of dye loading with and without a ten-fold excess of each Gd-based counterion.

Taking into account the number of encapsulated dyes (n), the extinction coefficient of each dye (ϵ) and the quantum yield (ϕ), we can estimate the brightness (B) of each dye loaded NP sample using the equation $B = n \times \epsilon \times \phi$. The number of encapsulated dyes can be calculated from the volume of the NPs (obtained from the DLS diameters assuming spherical shape) and the loading of dye in the polymeric matrix. For NPs loaded with R18/Gd(TTA)₄ (250 mM): $B = 2800 \times 125,000 \text{ M}^{-1} \text{ cm}^{-1} \times 0.20 = 7 \times 10^7 \text{ M}^{-1} \text{ cm}^{-1}$, which is roughly equivalent to ~ 226 Qdots 585 ($B = 3.1 \times 10^5 \text{ M}^{-1} \text{ cm}^{-1}$, with excitation at 532 nm, assuming that $\phi = 1$). For R18/Gd(NTA)₄ $B = 10200 \times 125,000 \text{ M}^{-1} \text{ cm}^{-1} \times 0.21 = 2.5 \times 10^8 \text{ M}^{-1} \text{ cm}^{-1}$, roughly equivalent to ~ 800 Qdots 585. While for NPs R18/Gd(HPFNP)₄ (250 mM) $B = 5500 \times 125,000 \text{ M}^{-1} \text{ cm}^{-1} \times 0.43 = 3 \times 10^8 \text{ M}^{-1} \text{ cm}^{-1}$, roughly equivalent to ~ 1000 Qdots 585. We should note that the differences would be less dramatic if Qdots 585 are excited in the violet region (e.g. 405 nm), where it is expected to show 10-fold higher absorption coefficient.

2.2. Manuscript: Preparation of lanthanide-based nanoparticles

Furthermore, these Gd-loaded nanoparticles were studied also *via* TEM imaging of R18 NPs at the three different loadings (5, 75 and 250 mM) formulated with a ten-fold excess of Gd(TTA)₄, and R18 NPs with the 250 mM loading of the other two counterions Gd(NTA)₄ and Gd(HPFNP)₄ (Figure 3). It should be noted that TEM size analysis mostly reproduced the results obtained with DLS, with the only exception of R18/ Gd(TTA)₄ (250 mM). The reason for the latter is unclear, but it might be due to the process of immobilization on the TEM grid, which can compromise the stability of NPs. Moreover, it should be noted that the Gd-loaded NPs were all quite strongly visible *via* TEM without the use of any contrast agent, while control NPs without Gd-Cl were noticeably less visible (Figure 3). This implies that heavy Gd-atoms could improve TEM contrast, so that this system could potentially be developed as a multi-imaging platform in approaches combining TEM and fluorescence techniques.

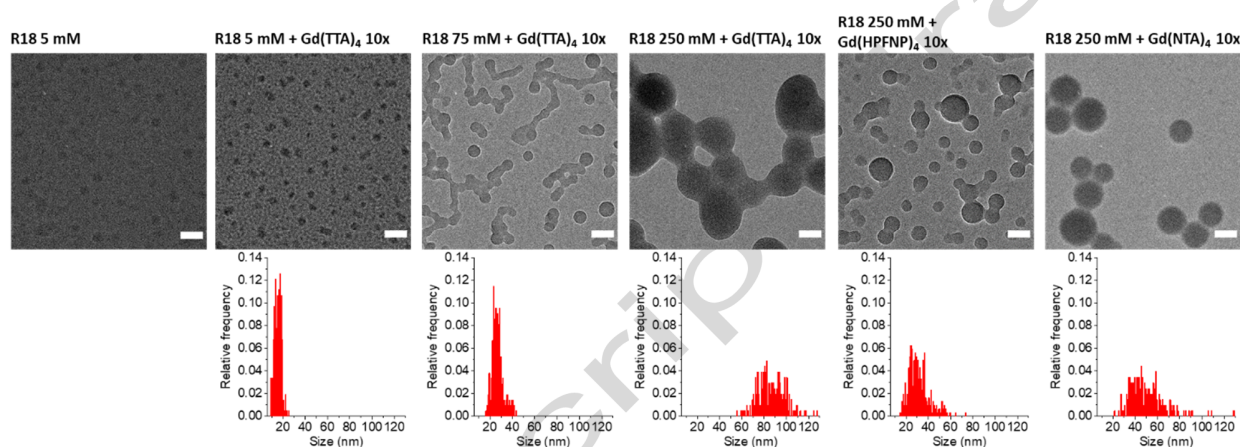


Figure 3. TEM images of R18 loaded NPs with different Gd-based counterions (top) and relative size distributions (bottom). Scale bars: 50 nm.

Next, we tested the influence on fluorescence quantum yield of a ten-fold molar excess of Gd-Cl in NP formulated with another cationic dye: cyanine 5 derivative DiD (Figure 1A). At low loading (5 mM) the same trend of R18 was reproduced, with a strong increase in quantum yield (from 0.49 to 0.85), Gd(TTA)₄ performing the best and Gd(HPFNP)₄ performing the worst (Figure 4A). At the highest loading investigated with DiD (75 mM) again the trend inverted, with Gd(TTA)₄ yielding the lowest QY (0.13) among the Gd-Cl and Gd(HPFNP)₄ the highest (0.21). Thus, for two cationic dyes R18 and DiD of different color and dye class, we found that at the highest loading the bulkiest counterion Gd(HPFNP)₄ provides the best dye insulation against ACQ.

However, the most interesting aspect of formulating DiD-loaded NPs was in constructing a FRET system where Eu-based counterions function as donors and DiD as acceptor. Europium displays many narrow emission bands in the visible, its strongest one overlapping very well with DiD absorption. Moreover, owing to its aromatic ligands the Eu complexes strongly absorb in the UV. Therefore, the ion pair with DiD could undergo FRET, yielding a system with a quite large Stokes shift, absorbing in the UV to emit in the NIR.

2. Results and discussion

We formulated FRET NPs comprising DiD/Eu-CIs with a loading of 75 mM for DiD (acceptor) and a ten-fold molar excess (*i.e.* 750 mM) for the Eu-CIs (donor). Control nanoparticles loaded with only donor or only acceptor were also formulated. We found that when exciting the Eu-CIs (at 340 nm) the FRET NPs displayed a strong acceptor emission and relatively weak donor bands, while at the same concentration donor only nanoparticles had much stronger donor emission (Figure 4B). Acceptor only NPs, when excited at 340 nm, showed a negligible emission, three orders of magnitude weaker than that of the FRET NPs, meaning that the contribution of direct excitation of the acceptor is negligible in the FRET NPs. In terms of quantum yields Eu(HPFNP)₄ only nanoparticles had a higher quantum yield in respect to Eu(NTA)₄ nanoparticles. When introducing the acceptor, the total QY of the system improved for both CIs, but more drastically for Eu(NTA)₄, almost doubling in value (Figure 4C).

Moreover, we recorded the time-resolved fluorescence decay curves of donor-only NPs and FRET NPs at emission wavelength of Eu (Figure 4E) and calculated their lifetimes. We found that donor only NPs displayed a single exponential decay, with NPs loaded with Eu(NTA)₄ having a lifetime of $281 \pm 1 \mu\text{s}$ and NPs loaded with Eu(HPFNP)₄ having a lifetime of $295.5 \pm 0.3 \mu\text{s}$. On the other hand, FRET NPs displayed a biexponential decay, meaning that the system has two different lifetimes ($18.0 \pm 0.3 \mu\text{s}$ and $127 \pm 2 \mu\text{s}$ for NPs with Eu(NTA)₄ as donor $9.2 \pm 0.1 \mu\text{s}$ and $61 \pm 1 \mu\text{s}$ for NPs with Eu(HPFNP)₄ as donor) the lifetime with the largest amplitude was the shortest. This means that not all Eu-CIs transfer efficiently their excitation energy, with only a minor fraction of Eu-based complexes having a longer lifetime.

We further measured FRET efficiency using both fluorescence emission and lifetime of the donor. For NPs with Eu(HPFNP)₄ as donor the two values were in good agreement, being close to unity. The short lifetimes of the FRET NPs confirmed also that the energy-transfer between the Eu-CIs and DiD is non-radiative resonance-energy transfer and not based on reabsorption of the donor emission. For Eu(NTA)₄ as donor, the FRET efficiency calculated from the lifetime was higher than the value calculated from intensity. This overestimation is probably due to the presence of a fraction of CI that has a longer lifetime. Aside from this, both counterions produced high FRET efficiency, with Eu(HPFNP)₄ being the best performing (Figure 4D).

2.2. Manuscript: Preparation of lanthanide-based nanoparticles

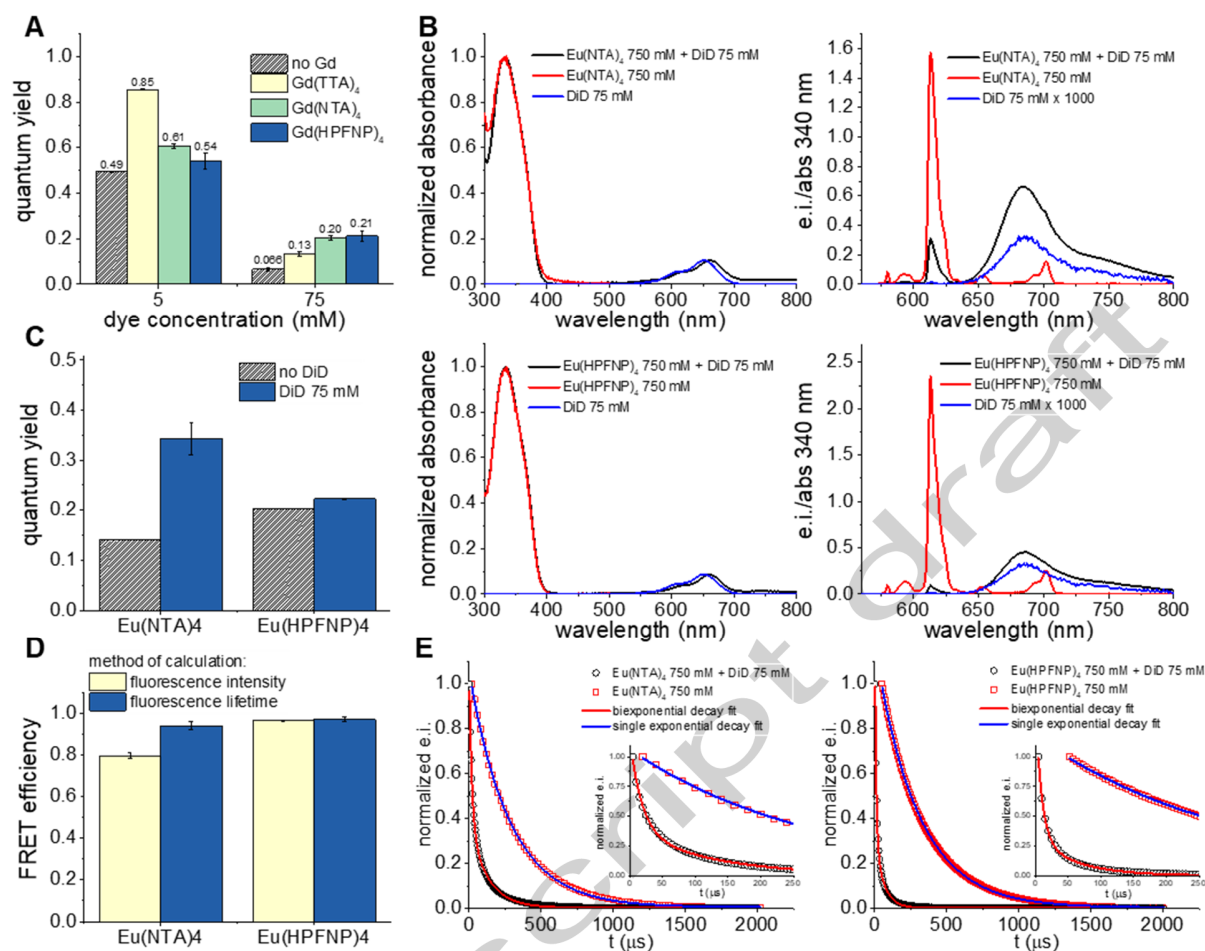


Figure 4. Preparation of nanoparticles loaded with DiD. (A) Fluorescence quantum yields for NPs at different DiD loadings formulated with and without a ten-fold excess of each Gd-based counterion. (B) Absorption (left) and emission (right) spectra for FRET and control nanoparticles formulated with DiD at a loading of 75 mM and a ten-fold excess of Eu(NTA)₄ (top) and Eu(HPFNP)₄ (bottom). (C) Quantum yields of Eu(NTA)₄ and Eu(HPFNP)₄ nanoparticles with and without acceptor. (D) FRET efficiency of FRET NPs calculated from fluorescence intensity and fluorescence lifetime. (E) Fluorescence decay curves for Eu(NTA)₄ NPs (left) and Eu(HPFNP)₄ NPs (right) with and without DiD.

Next, we studied the fluorescence properties of the prepared NPs *via* fluorescence microscopy. We selected the NPs with the highest R18 loading (250 mM) and 10-fold excess of each Gd-based counterion. Their brightness was compared with quantum dots emitting in the same spectral window, QD585. The polymeric NPs and QDs were immobilized on a polyethyleneimine (PEI) covered glass surface and imaged with a wide-field fluorescence microscope. What we observed was in line with the spectroscopic data recorded in cuvette. All polymeric NP samples were brighter than the reference QDs (Figure 5), with the brightest samples being R18/Gd(NTA)₄ and R18/Gd(HPFNP)₄. According to single-particle microscopy analysis, R18/Gd(TTA)₄ NPs were as bright as ~375 QD585, while R18/Gd(NTA)₄ and R18/Gd(HPFNP)₄ displayed a brightness of ~1300 QD585, in accordance with our theoretical estimations. Thus, our single-particle analysis

2. Results and discussion

data confirms that the largest counterions yields the brightest NPs, probably due to the best dye insulation inside NPs.

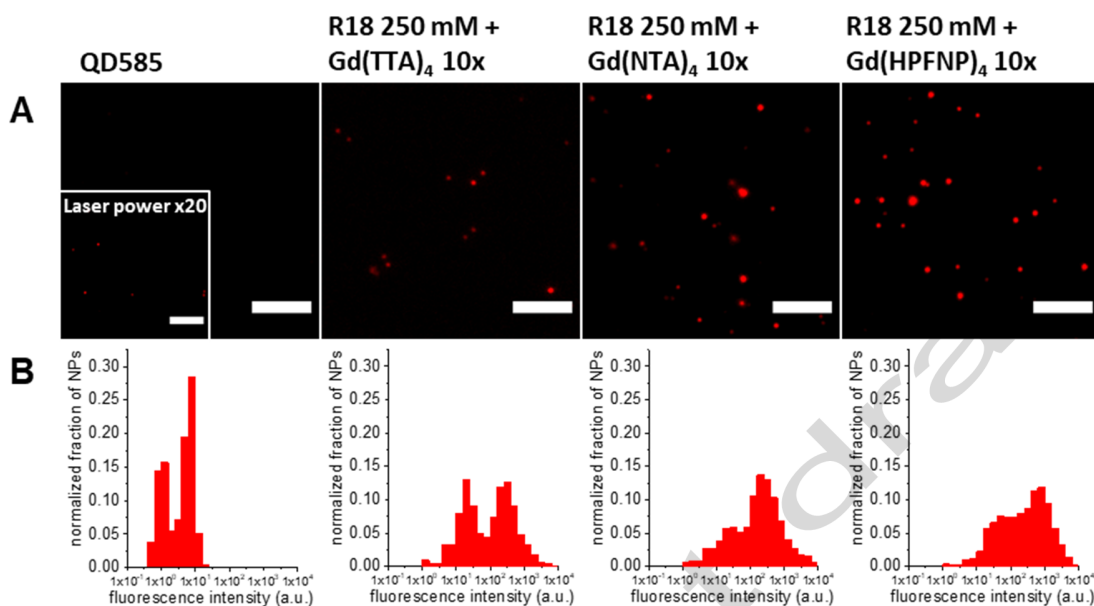


Figure 5. Single-particle characterization of Gd-based NPs. (A) Single particle fluorescence images of polymeric NPs prepared with a 10-fold excess of Gd-based counterion with a dye loading of 250 mM compared to reference quantum dots QD585. (B) Brightness histograms of the images shown in (A). Wide field microscopy was performed with excitation at 550 nm. Scale bars: 5 μ m.

Cellular experiments

Finally, we tested our new NPs for cellular imaging experiments. NPs formulated with 10-fold excess of each of the three Gd-CIs and without were incubated with HeLa cells for 3 hours at 37 °C and then imaged with a fluorescence microscope in an epi-fluorescence mode. While NPs formulated in presence of Gd-CIs were internalized by endocytosis (observed as dots in the perinuclear region) with no sign of dye leaching, R18/CI NPs showed a marked leaching behavior with the dye staining the whole cell. This is in line with previous observations, where in absence of a bulky hydrophobic counterion in the NPs the fluorescent dye was not well encapsulated in the particle and therefore tended to leach in the cellular context (Andreiuk et al., 2019). Interestingly, NPs loaded with Gd(HPFNP)₄ —despite yielding the brightest particles in all the previous experiments— were barely visible, while Gd(TTA)₄ and Gd(NTA)₄ performed better (Figure 6A). Finally, we tested the cytotoxicity of NPs formulated with Gd-based counterions *via* MTT assay and found no cytotoxic effect at concentrations habitually used for cellular imaging (up to 0.004 g/L). However, cell viability began to decline at higher concentrations (Figure 6B).

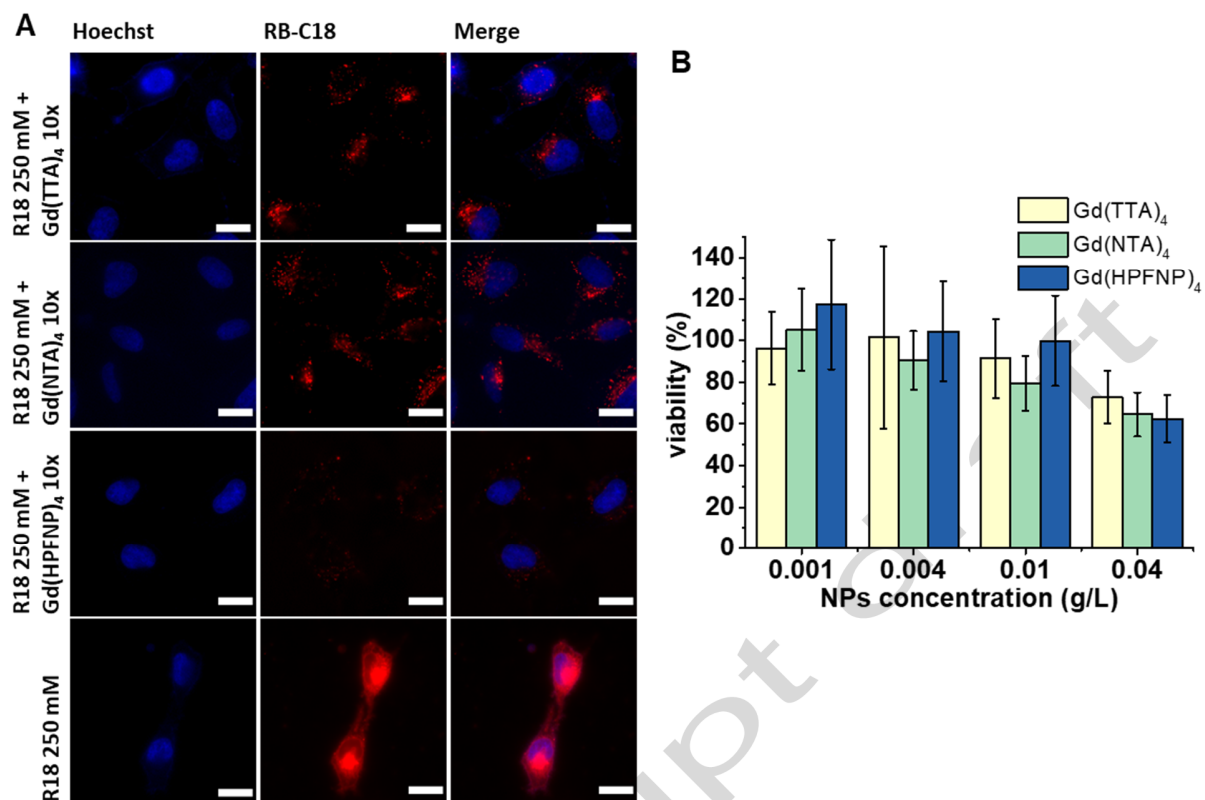


Figure 6. Cellular studies of nanoparticles. (A) Epifluorescence microscopy images of HeLa cells incubated with polymeric NPs loaded with 250 mM R18 with and without a ten-fold excess of Gd-CIs. In presence of Gd-CIs NPs get internalized by endocytosis without any dye leaching, while without the Gd-counterion there is a strong leaching of the fluorescent dye. (B) Cytotoxicity experiments for polymeric NPs loaded with 250 mM R18 + Gd-CIs 10x. Scale bars: 50 μ m.

2. Results and discussion

Conclusions

Bulky hydrophobic counterions enable preparation of bright dye-loaded polymeric nanoparticles due to the dye insulation effect minimizing aggregation-caused quenching. Previously, this approach was validated on tetra-arylborates and on tetra-alkoxyaluminates. In this work we further extend this approach to yet another class of bulky anions: lanthanide complexes. NPs were prepared with three different Gd-based counterions and two different Eu-based counterions, with increasing bulkiness, hydrophobicity and fluorination level. We found that NPs loaded with Gd-based counterions showed superior quantum yields and smaller diameters in respect to their counterparts based on small hydrophilic counterion. These positive effects were observed for both, a rhodamine dye R18 and a cyanine dye DiD, showing that lanthanide-based counterions can be applied to different dye families. Moreover, the encapsulation of Gd-CIs provided a stronger TEM contrast in respect to control nanoparticles. The as-prepared NPs have been incubated with cells and it was found that they readily internalize via endocytosis without leaching due to the action of Gd-based counterions. MTT assays revealed the NPs to be non-toxic at the concentration used for imaging. Moreover, counterions based on europium complexes were encapsulated with DiD and employed as FRET donors, obtaining very efficient FRET with emission in the NIR upon UV excitation, generating an ultra-large Stokes shift systems. Our findings show that the anionic complexes of lanthanides can be used to light up dyes in polymeric nanomaterials and potentially allow implementing additional functions due to unique properties of lanthanides.

Bibliography

- Andreiuk, B., Reisch, A., Bernhardt, E., Klymchenko, A.S., 2019. Fighting Aggregation-Caused Quenching and Leakage of Dyes in Fluorescent Polymer Nanoparticles: Universal Role of Counterion. *Chem. – Asian J.* 14, 836–846. <https://doi.org/10.1002/asia.201801592>
- Andreiuk, B., Reisch, A., Lindecker, M., Follain, G., Peyri ras, N., Goetz, J.G., Klymchenko, A.S., 2017a. Fluorescent Polymer Nanoparticles for Cell Barcoding In Vitro and In Vivo. *Small* 13, 1701582. <https://doi.org/10.1002/smll.201701582>
- Andreiuk, B., Reisch, A., Pivovarenko, V.G., Klymchenko, A.S., 2017b. An aluminium-based fluorinated counterion for enhanced encapsulation and emission of dyes in biodegradable polymer nanoparticles. *Mater. Chem. Front.* 1, 2309–2316. <https://doi.org/10.1039/C7QM00248C>
- Aparin, I.O., Melnychuk, N., Klymchenko, A.S., 2020. Ionic Aggregation-Induced Emission: Bulky Hydrophobic Counterions Light Up Dyes in Polymeric Nanoparticles. *Adv. Opt. Mater.* 8, 2000027. <https://doi.org/10.1002/adom.202000027>
- Brouwer, A.M., 2011. Standards for photoluminescence quantum yield measurements in solution (IUPAC Technical Report). *Pure Appl. Chem.* 83, 2213–2228. <https://doi.org/10.1351/PAC-REP-10-09-31>

2.2. Manuscript: Preparation of lanthanide-based nanoparticles

Bwambok, D.K., El-Zahab, B., Challa, S.K., Li, M., Chandler, L., Baker, G.A., Warner, I.M., 2009. Near-Infrared Fluorescent NanoGUMBOS for Biomedical Imaging. *ACS Nano* 3, 3854–3860. <https://doi.org/10.1021/nn9010126>

Cardoso Dos Santos, M., Runser, A., Bartenlian, H., Nonat, A.M., Charbonnière, L.J., Klymchenko, A.S., Hildebrandt, N., Reisch, A., 2019. Lanthanide-Complex-Loaded Polymer Nanoparticles for Background-Free Single-Particle and Live-Cell Imaging. *Chem. Mater.* 31, 4034–4041. <https://doi.org/10.1021/acs.chemmater.9b00576>

Geiger, W.E., Barrière, F., 2010. Organometallic Electrochemistry Based on Electrolytes Containing Weakly-Coordinating Fluoroarylborate Anions. *Acc. Chem. Res.* 43, 1030–1039. <https://doi.org/10.1021/ar1000023>

Grazon, C., Rieger, J., Méallet-Renault, R., Charleux, B., Clavier, G., 2013. Ultrabright Fluorescent Polymeric Nanoparticles Made from a New Family of BODIPY Monomers. *Macromolecules* 46, 5167–5176. <https://doi.org/10.1021/ma400590q>

Jia, M., Bandini, M., 2015. Counterion Effects in Homogeneous Gold Catalysis. *ACS Catal.* 5, 1638–1652. <https://doi.org/10.1021/cs501902v>

Klymchenko, A.S., Liu, F., Collot, M., Anton, N., 2021. Dye-Loaded Nanoemulsions: Biomimetic Fluorescent Nanocarriers for Bioimaging and Nanomedicine. *Adv. Healthc. Mater.* 10, 2001289. <https://doi.org/10.1002/adhm.202001289>

Krossing, I., Raabe, I., 2004. Noncoordinating Anions—Fact or Fiction? A Survey of Likely Candidates. *Angew. Chem. Int. Ed.* 43, 2066–2090. <https://doi.org/10.1002/anie.200300620>

Li, K., Liu, B., 2014. Polymer-encapsulated organic nanoparticles for fluorescence and photoacoustic imaging. *Chem Soc Rev* 43, 6570–6597. <https://doi.org/10.1039/C4CS00014E>

Luo, P.G., Sahu, S., Yang, S.-T., Sonkar, S.K., Wang, J., Wang, H., LeCroy, G.E., Cao, L., Sun, Y.-P., 2013. Carbon “quantum” dots for optical bioimaging. *J. Mater. Chem. B* 1, 2116. <https://doi.org/10.1039/c3tb00018d>

Ma, D., Duan, L., Qiu, Y., 2016. Orange-red- and white-emitting diodes fabricated by vacuum evaporation deposition of sublimable cationic iridium complexes. *J. Mater. Chem. C* 4, 5051–5058. <https://doi.org/10.1039/C6TC00738D>

Michalet, X., 2005. Quantum Dots for Live Cells, in Vivo Imaging, and Diagnostics. *Science* 307, 538–544. <https://doi.org/10.1126/science.1104274>

Mochalin, V.N., Shenderova, O., Ho, D., Gogotsi, Y., 2012. The properties and applications of nanodiamonds. *Nat. Nanotechnol.* 7, 11–23. <https://doi.org/10.1038/nnano.2011.209>

2. Results and discussion

Montalti, M., Prodi, L., Rampazzo, E., Zaccheroni, N., 2014. Dye-doped silica nanoparticles as luminescent organized systems for nanomedicine. *Chem Soc Rev* 43, 4243–4268. <https://doi.org/10.1039/C3CS60433K>

Raabe, I., Wagner, K., Guttsche, K., Wang, M., Grätzel, M., Santiso-Quiñones, G., Krossing, I., 2009. Tetraalkylammonium Salts of Weakly Coordinating Aluminates: Ionic Liquids, Materials for Electrochemical Applications and Useful Compounds for Anion Investigation. *Chem. - Eur. J.* 15, 1966–1976. <https://doi.org/10.1002/chem.200800417>

Raj, D.B.A., Biju, S., Reddy, M.L.P., 2008. One-, Two-, and Three-Dimensional Arrays of Eu 3+ -4,4,5,5,5-pentafluoro-1-(naphthalen-2-yl)pentane-1,3-dione complexes: Synthesis, Crystal Structure and Photophysical Properties. *Inorg. Chem.* 47, 8091–8100. <https://doi.org/10.1021/ic8004757>

Reisch, A., Didier, P., Richert, L., Oncul, S., Arntz, Y., Mély, Y., Klymchenko, A.S., 2014. Collective fluorescence switching of counterion-assembled dyes in polymer nanoparticles. *Nat. Commun.* 5. <https://doi.org/10.1038/ncomms5089>

Reisch, A., Heimbürger, D., Ernst, P., Runser, A., Didier, P., Dujardin, D., Klymchenko, A.S., 2018. Protein-Sized Dye-Loaded Polymer Nanoparticles for Free Particle Diffusion in Cytosol. *Adv. Funct. Mater.* 28, 1805157. <https://doi.org/10.1002/adfm.201805157>

Reisch, A., Klymchenko, A.S., 2016. Fluorescent Polymer Nanoparticles Based on Dyes: Seeking Brighter Tools for Bioimaging. *Small* 12, 1968–1992. <https://doi.org/10.1002/smll.201503396>

Rupp, A., Roznyatovskaya, N., Scherer, H., Beichel, W., Klose, P., Sturm, C., Hoffmann, A., Tübke, J., Koslowski, T., Krossing, I., 2014. Size Matters! On the Way to Ionic Liquid Systems without Ion Pairing. *Chem. - Eur. J.* 20, 9794–9804. <https://doi.org/10.1002/chem.201400168>

Rupp, A.B.A., Krossing, I., 2015. Ionic Liquids with Weakly Coordinating [M III (OR F) 4] – Anions. *Acc. Chem. Res.* 48, 2537–2546. <https://doi.org/10.1021/acs.accounts.5b00247>

Shulov, I., Arntz, Y., Mély, Y., Pivovarenko, V.G., Klymchenko, A.S., 2016a. Non-coordinating anions assemble cyanine amphiphiles into ultra-small fluorescent nanoparticles. *Chem. Commun.* 52, 7962–7965. <https://doi.org/10.1039/C6CC03716J>

Shulov, I., Oncul, S., Reisch, A., Arntz, Y., Collot, M., Mely, Y., Klymchenko, A.S., 2015. Fluorinated counterion-enhanced emission of rhodamine aggregates: ultrabright nanoparticles for bioimaging and light-harvesting. *Nanoscale* 7, 18198–18210. <https://doi.org/10.1039/C5NR04955E>

Shulov, I., Rodik, R.V., Arntz, Y., Reisch, A., Kalchenko, V.I., Klymchenko, A.S., 2016b. Protein-Sized Bright Fluorogenic Nanoparticles Based on Cross-Linked Calixarene Micelles with Cyanine Corona. *Angew. Chem. Int. Ed.* 55, 15884–15888. <https://doi.org/10.1002/anie.201609138>

2.2. Manuscript: Preparation of lanthanide-based nanoparticles

Tian, Z., Shaller, A.D., Li, A.D.Q., 2009. Twisted perylenedyes enable highly fluorescent and photostable nanoparticles. *Chem Commun* 180–182. <https://doi.org/10.1039/B815507K>

Trofymchuk, K., Reisch, A., Shulov, I., Mély, Y., Klymchenko, A.S., 2014. Tuning the color and photostability of perylene diimides inside polymer nanoparticles: towards biodegradable substitutes of quantum dots. *Nanoscale* 6, 12934–12942. <https://doi.org/10.1039/C4NR03718A>

Wagh, A., Qian, S.Y., Law, B., 2012. Development of Biocompatible Polymeric Nanoparticles for in Vivo NIR and FRET Imaging. *Bioconjug. Chem.* 23, 981–992. <https://doi.org/10.1021/bc200637h>

Wolfbeis, O.S., 2015. An overview of nanoparticles commonly used in fluorescent bioimaging. *Chem. Soc. Rev.* 44, 4743–4768. <https://doi.org/10.1039/C4CS00392F>

Wu, C., Chiu, D.T., 2013. Highly Fluorescent Semiconducting Polymer Dots for Biology and Medicine. *Angew. Chem. Int. Ed.* 52, 3086–3109. <https://doi.org/10.1002/anie.201205133>

Würth, C., Grabolle, M., Pauli, J., Spieles, M., Resch-Genger, U., 2013. Relative and absolute determination of fluorescence quantum yields of transparent samples. *Nat. Protoc.* 8, 1535–1550. <https://doi.org/10.1038/nprot.2013.087>

Xie, X., Gutiérrez, A., Trofimov, V., Szilagy, I., Soldati, T., Bakker, E., 2015. Charged Solvatochromic Dyes as Signal Transducers in pH Independent Fluorescent and Colorimetric Ion Selective Nanosensors. *Anal. Chem.* 87, 9954–9959. <https://doi.org/10.1021/acs.analchem.5b02566>

Yao, H., Ashiba, K., 2011. Highly fluorescent organic nanoparticles of thiocyanine dye: A synergetic effect of intermolecular H-aggregation and restricted intramolecular rotation. *RSC Adv.* 1, 834. <https://doi.org/10.1039/c1ra00497b>

Zhang, Xiaoyong, Wang, K., Liu, M., Zhang, Xiqi, Tao, L., Chen, Y., Wei, Y., 2015. Polymeric AIE-based nanoprobe for biomedical applications: recent advances and perspectives. *Nanoscale* 7, 11486–11508. <https://doi.org/10.1039/C5NR01444A>

2. Results and discussion

2.3. *Design of NPs surface for specific targeting*

The second research direction on dye-loaded polymeric nanoparticles was focused on their surface functionalization to obtain systems with targeting properties. Our group previously demonstrated that dye-loaded polymeric nanoparticles are readily internalized by endocytosis and the presence of the bulky hydrophobic counterion ensures negligible dye leaching (Andreiuk et al., 2017b; Reisch et al., 2014). Being non-cytotoxic and not readily degraded, they were also successfully applied in barcoding applications. By preparing PLGA-based nanoparticles in three different colors (encapsulating DiO, DiI and DiD) and mixing them in different proportions allowed to distinguish up to 13 color codes for >2 weeks (Andreiuk et al., 2017a).

Important progress was also made in terms of coating of NPs, previous work demonstrated that postmodification coatings with amphiphiles such as Tween 80 and pluronic F-127 imparts stealth characteristics to the nanoparticles (Reisch et al., 2015), allowing their usage *in vivo* (Khalin et al., 2020) and, if small enough, free diffusion in the cytosol when microinjected (Reisch et al., 2018). Moreover, our group reported also the synthesis of zwitterionic polymers which possess the same stealth properties of amphiphiles-coated nanoparticles alike, but with a much smaller stealth shell and eliminating the necessity of performing a postmodification coating (Runser et al., 2020). In addition, our group also reported the development of a reliable and quick method for functionalizing covalently the surface of nanoparticles by employing an azide-bearing polymer in NPs formulation and clicking DBCO groups *via* copper-free click chemistry (Melnychuk and Klymchenko, 2018).

It is therefore clear that our dye-loaded polymeric nanoparticles are promising contrast agents for live-cell imaging. However, targeted imaging still has to be achieved with these systems; the two next sections of this work will be dedicated to this question.

2.3.1. *Synthesis of PEGylated nanoparticles for the targeting of lipids and proteins*

As previously mentioned, receptors have been extensively studied both as imaging and therapeutic targets. In particular G-protein coupled receptors (GPCRs) represent the biggest and most varied group of membrane receptors in eukaryotes (Rosenbaum et al., 2009), being the therapeutic target of over 30% of the drugs on the market.

2. Results and discussion

The present section reports the preparation of targeting nanoparticles for lipids and proteins. First, stealth nanoparticles were synthesized by clicking multiple DBCO-functionalized PEGs on the surface of azide-bearing NPs. Then PEG2000-DBCO were functionalized with targeting ligands: (i) a phenylboronic acid derivative, which is able to bind selectively to phosphatidylethanolamine (a lipid present on the outer leaflet of plasma membrane in bacteria and apoptotic eukaryotic cells); (ii) carbetocin, an oxytocin analogue, which binds to the G-protein coupled receptor of oxytocin (OTR).

2.3.1.1. Synthesis of stealth nanoparticles

Polymeric nanoparticles loaded with R18/F5-TPB (with loading 10% in weight in respect to the polymer) were prepared by nanoprecipitation employing an azide-bearing polymer (Figure 2.5A), developed previously (Melnychuk and Klymchenko, 2018).

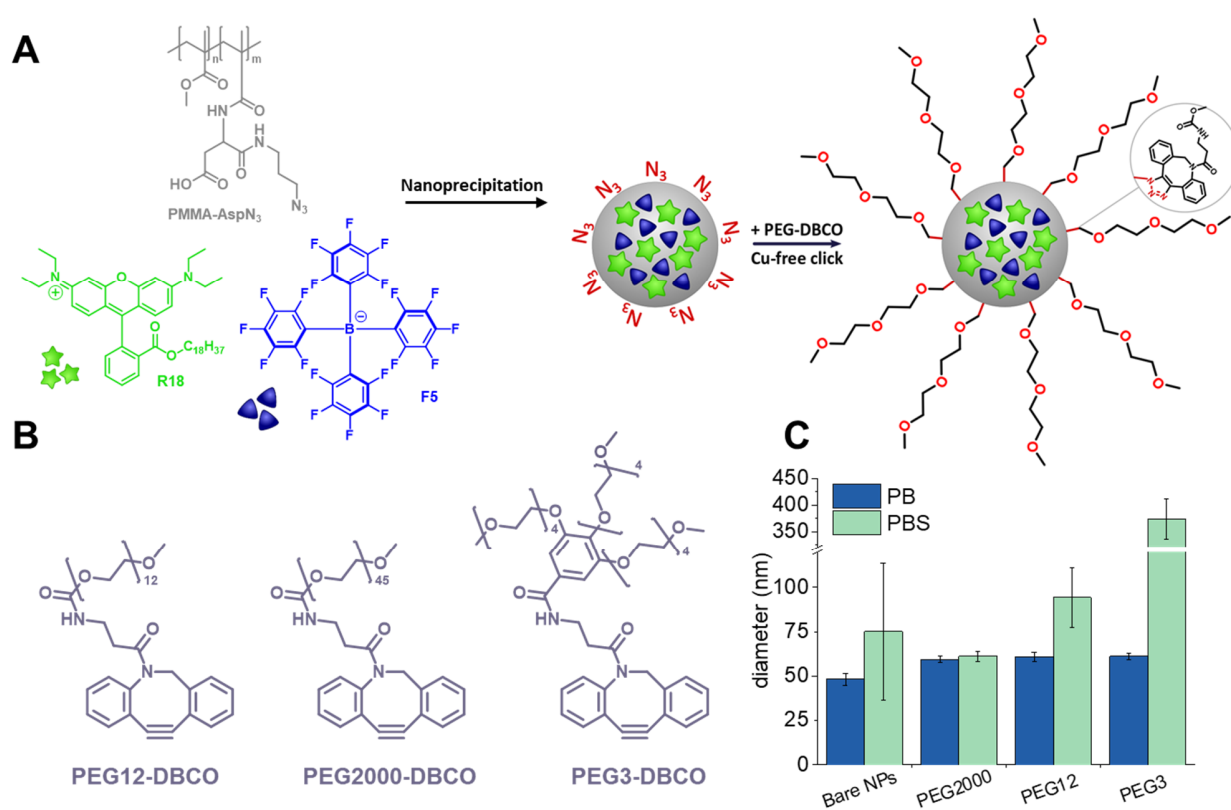


Figure 2.5 (A) Nanoprecipitation and copper-free click chemistry schemes. (B) Structures of the three DBCO-PEG tested for the synthesis of stealth nanoparticles. (C) Resistance to aggregation in high salinity conditions of stealth nanoparticles.

2.3. Design of NPs surface for specific targeting

Then three clickable PEGs at variable length and branching degree were selected to produce stealth nanoparticles (Figure 2.5B). First their capability to resist to high salinity conditions was tested, finding that only the NPs coated with the longest PEG (PEG2000) did not aggregate when incubated in PBS (Figure 2.5C). Therefore, only PEG2000-DBCO was employed in the following experiments, while the two shorter clickable PEGs were discarded. Next, NPs covered with PEG2000 were incubated with HeLa cells and subsequently imaged *via* fluorescence microscopy. We found that, while bare non-functionalized NPs quickly absorbed on the surface of cells, PEGylated NPs did not interact with cells at all (Figure 2.6A). This qualitative observation was later confirmed by flow cytometry too (Figure 2.6B), with cells incubated with bare NPs displaying a strong fluorescence, while cells incubated with nanoparticles grafted with PEG2000 are nearly indistinguishable from HeLa cells alone.

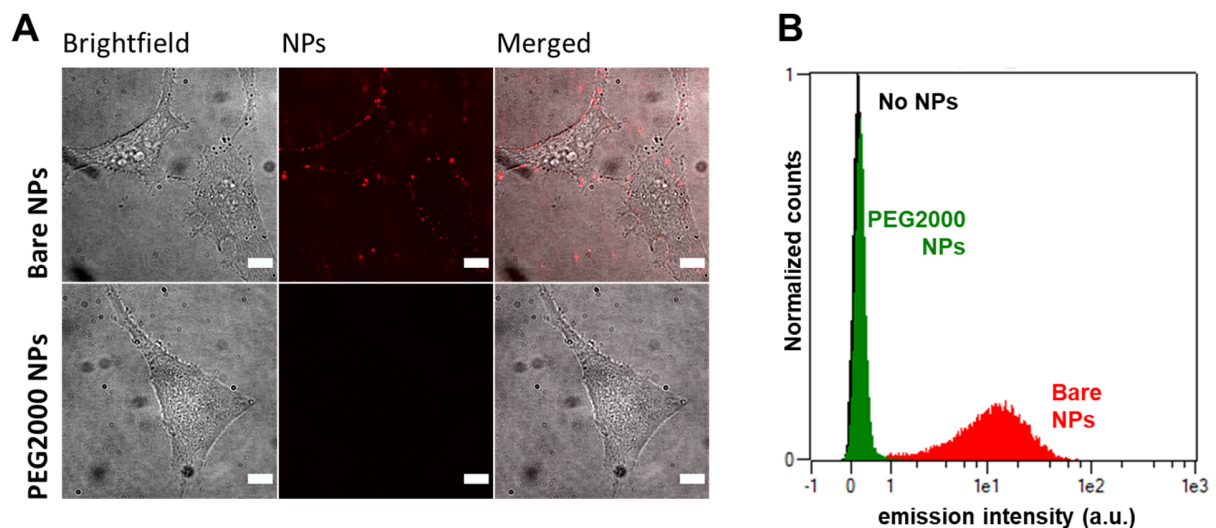


Figure 2.6 Stealth PEGylated NPs. (A) Confocal microscopy image of HeLa cells incubated with non-functionalized NPs (top row) and PEGylated NPs (bottom row). (B) Flow cytometry fluorescence intensity histograms of HeLa cells: (i) without NPs, (ii) incubated with PEGylated NPs, (iii) incubated with nonfunctionalized NPs. Scale bars: 10 μm .

2.3.1.2. *Synthesis of targeting nanoparticles*

Encouraged by the results on the conception of stealth nanoparticles, we dedicated our efforts in designing targeting nanoparticles. To this end we synthesized two clickable targeting ligands, linked by a PEG2000 chain, said ligands targeted (i) phosphatidylethanolamine (Figure

2. Results and discussion

2.8A) and (ii) the oxytocin receptor (Figure 2.9) . Then we clicked on the surface of NPs both PEG2000-DBCO and PEG2000-DBCO bearing the targeting ligand (Figure 2.7).

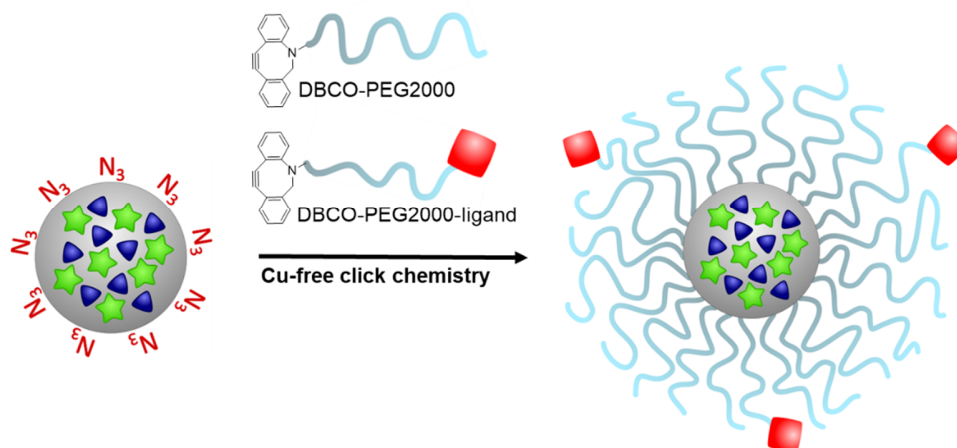


Figure 2.7 Scheme of synthesis of targeting NPs, PEG2000-DBCO and ligand-PEG2000-DBCO are mixed in a set ratio and then clicked on the surface of azide bearing NPs. The resulting NPs ideally should selectively target only the desired biological functionality.

2.3.1.1.1. *Synthesis of nanoparticles targeting phosphatidylethanolamine*

We synthesized a clickable PEG2000 conjugated with an acetyl phenylboronic acid derivative, APBA-PEG2000-DBCO. This class of compounds was previously demonstrated to bind selectively to phosphatidylethanolamine (Bandyopadhyay et al., 2015), a phospholipid present on the outer leaflet of plasma membrane of bacteria and apoptotic eukaryotic cells. We performed fluorescence microscopy on apoptotic HeLa cells incubated with APBA-bearing NPs, and we found only a limited degree of binding on the surface of cells (Figure 2.8A). Later flow cytometry experiments confirmed the previous results, with APBA-bearing NPs weakly binding to apoptotic cells (Figure 2.8B-C).

2.3. Design of NPs surface for specific targeting

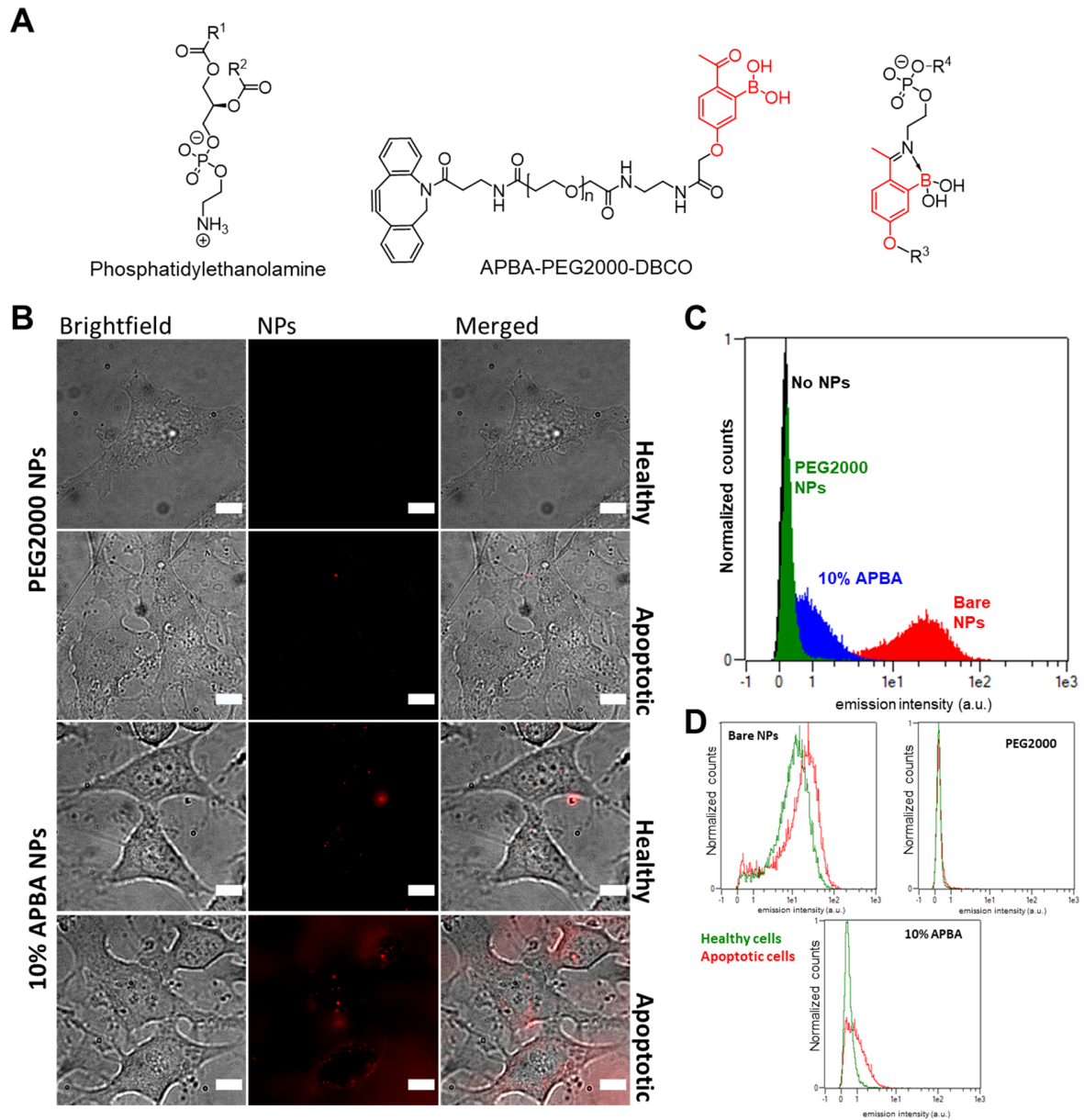


Figure 2.8 Apoptosis-targeting NPs. (A) Structure of phosphatidylethanolamine and the clickable APBA derivative, and the mechanism of covalent binding of APBA with PE. (B) Fluorescence microscopy images of normal and apoptotic HeLa cells incubated with PEGylated NPs (top rows) and APBA-bearing NPs (bottom rows). (C) Flow cytometry of apoptotic HeLa cells: (i) without NPs, (ii) with PEG2000 NPs, (iii) with NPs bearing 10% of APBA-PEG2000, (iv) with non-functionalized NPs. (D) Flow cytometry of normal cells vs apoptotic cells with: (i) non-functionalized NPs (top left), (ii) PEG2000 NPs (top right), (iii) NPs bearing 10% of APBA-PEG2000. Scale bars: 10 μm .

2. Results and discussion

2.3.1.1.2. Synthesis of nanoparticles targeting the oxytocin receptor

Next, we devoted our efforts to produce nanoparticles capable to target receptors. To this end we selected the oxytocin receptor and we targeted it using carbetocin (CBT), an oxytocin analogue stable *in vivo*. We synthesized a clickable PEG2000-DBCO ligand functionalized on the other end with carbetocin (Figure 2.9). Finally, we clicked it on the surface of azide-bearing NPs. To avoid excessive exposure of carbetocin on the NPs surface, NPs were functionalized with 25% of CBT-PEG2000-DBCO and 75% of PEG2000-DBCO without the ligand.

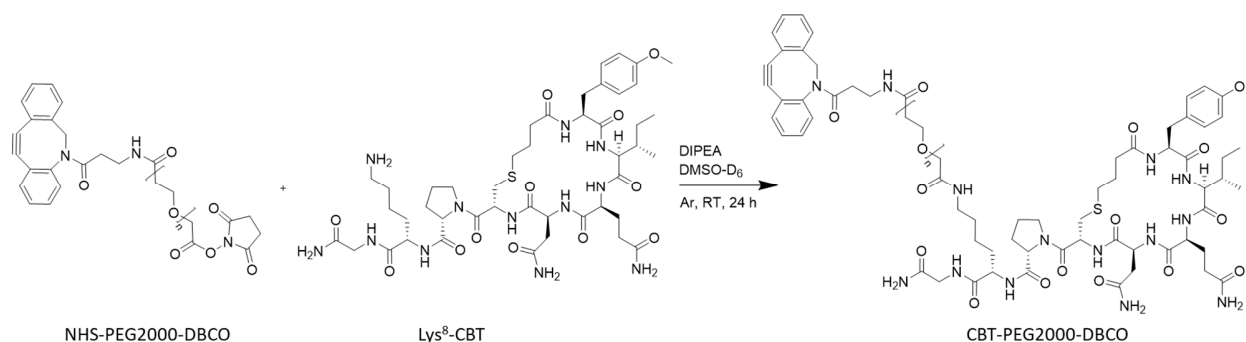


Figure 2.9 Synthesis scheme of CBT-PEG2000-DBCO.

The NPs bearing or not CBT ligand were incubated with HEK293 cells expressing or not the OTR fused to the green fluorescent protein. We found that some fluorescence intensity from nanoparticles can be observed for each of the four experiments. In control cell samples without OTR, the signal from NPs remained weak, with somewhat higher intensity for the control, supposedly stealthy, NPs without the ligand (Figure 2.10). In case of OTR-expressing cells, the fluorescence signal was stronger for NPs bearing CBT ligand, although a significant signal was still observed for the control NPs (Figure 2.10). Although we observe a slightly stronger particle internalization in the case of CBT-bearing NPs, these results alone do not provide sufficient evidence for receptor-specific targeting of cells by NPs.

In conclusion to this section, we produced PEGylated NPs *via* copper-free click chemistry. NPs covered exclusively with PEG2000 showed stealth behaviour, not interacting with cells, while NPs featuring bioactive groups on their surface showed a limited targeting ability, which should be further explored and tested.

2.3. Design of NPs surface for specific targeting

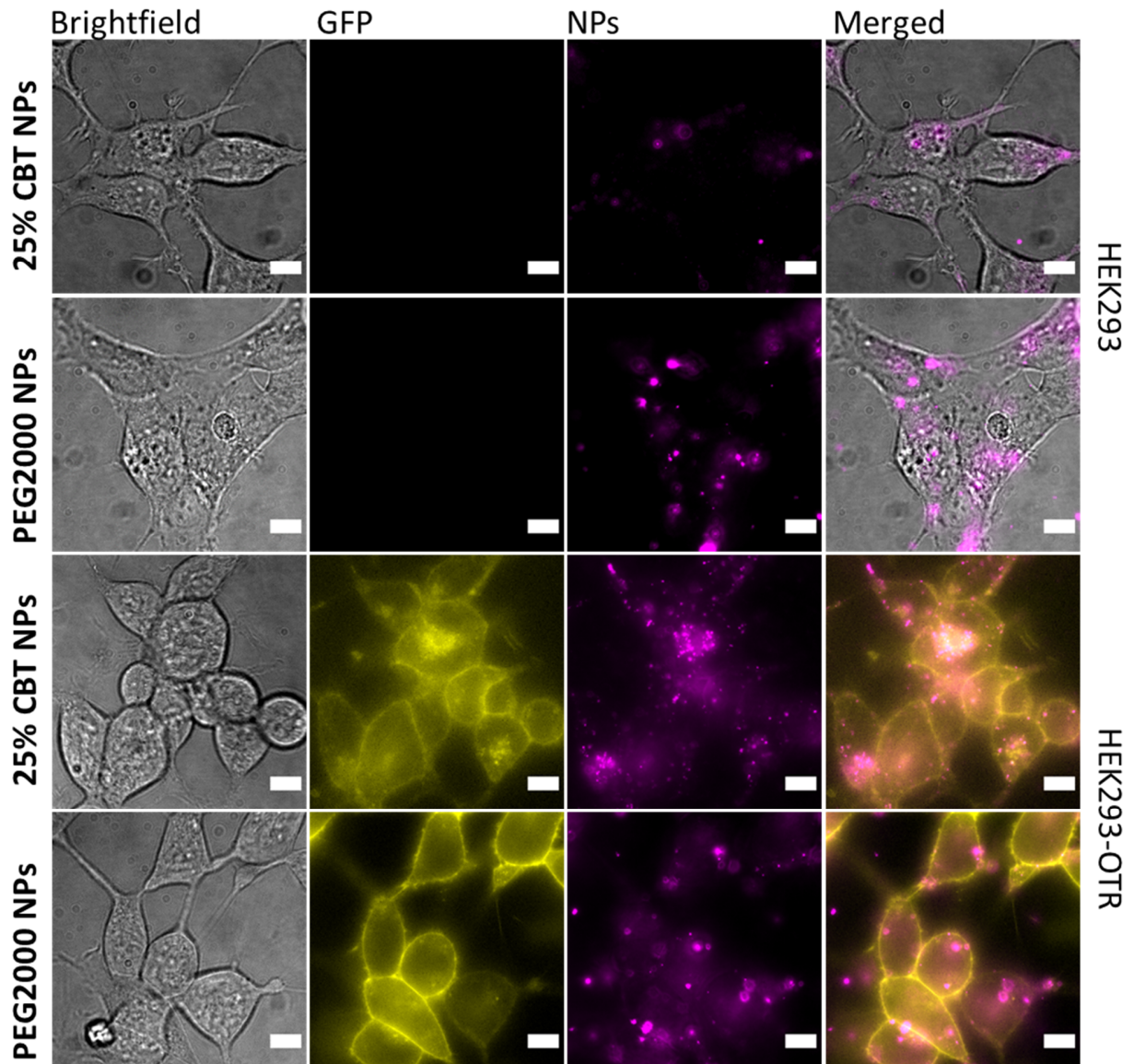


Figure 2.10 OTR-targeting NPs. (A) Structure of the clickable carbetocin derivative. (B) Fluorescence microscopy images of HEK293 cells expressing the OTR fused with the GFP (bottom rows) and control HEK293 cells (top rows), incubated with PEG2000 NPs and CBT-bearing NPs. Epifluorescence microscopy was done using green channel (excitation at 470 nm) and red channel (550 nm excitation). Scale bars: 10 μ m.

2. Results and discussion

2.3.2. *Synthesis of nanoparticles with a protein like surface and investigation of their potential targeting abilities*

Being interested in the question of employing dye-loaded polymeric nanoparticles as a targeting platform, we devoted our efforts in designing NPs with a protein-like surface. We hypothesize that certain biological functionalities can emerge from a complex enough surface. To this end we selected eight amino-acids (AAs) with different properties to impart variety to the resulting NPs. Each amino-acid was grafted on both poly(methyl methacrylate)-co methacrylic acid (1.6 %) (PMMA-MA) and poly(ethyl methacrylate)-co methacrylic acid (5 %) (PEMA-MA). We tested these polymers by using them in the formulation of nanoparticles, we measured their sizes, spectroscopic properties and interaction with cells. Moreover, we tested (i) their capability to survive in harsh conditions (namely high salt concentrations) and (ii) their capability to adapt in response to environmental conditions, for the latter point we tested how nanoparticles behaved when formulated in PBS. The idea behind the latter point would be to produce further down the line, NPs that could be “imprinted” on species of biological interest.

Nanoparticles prepared with AA grafted PMMA (PMMA-AA NPs) showed generally large diameters and readily aggregated in high salt conditions, while PEMA-AA NPs were generally smaller and resisted well in high salt conditions. Encouraged by these preliminary positive results we studied their spectroscopic characteristics both in suspension and at the single-particle level, and then evaluated their interactions with cells. Finally, we tested how the system responded when formulated in high salt conditions, and we found that when PEMA-AA NPs were nanoprecipitated in phosphate buffered saline (PBS) they featured bigger diameters in respect than nanoparticles nanoprecipitated in phosphate buffer (PB) and were generally stable over time, meaning that the system is capable to evolve and “imprint” itself when exposed to different conditions.

2.3.2.2. *Synthesis of polymers grafted with amino acids*

Among the 20 fundamental amino acids, we have chosen 8 with different characteristic functionalities (Figure 2.11B): (i) positively charged AAs: histidine (His), arginine (Arg), lysine (Lys); (ii) negatively charged AAs: aspartic acid (Asp); (iii) polar AAs with a neutral side chain: serine (Ser) and asparagine (Asn); (iv) and hydrophobic AAs: tyrosine (Tyr) and leucine (Leu). In this way, we aimed to finely tune the surface properties of the nanoparticles composed of these AA-bearing polymers.

2.3. Design of NPs surface for specific targeting

Amino acid-functionalized PMMAs and PEMAs were synthesized by grafting AAs on PMMA-MA and PEMA-MA *via* peptide coupling reaction following deprotection to remove the tert-butyloxycarbonyl protecting group (Boc) on the carboxylic acid and other protecting groups on the side chain if present (Figure 2.11A).

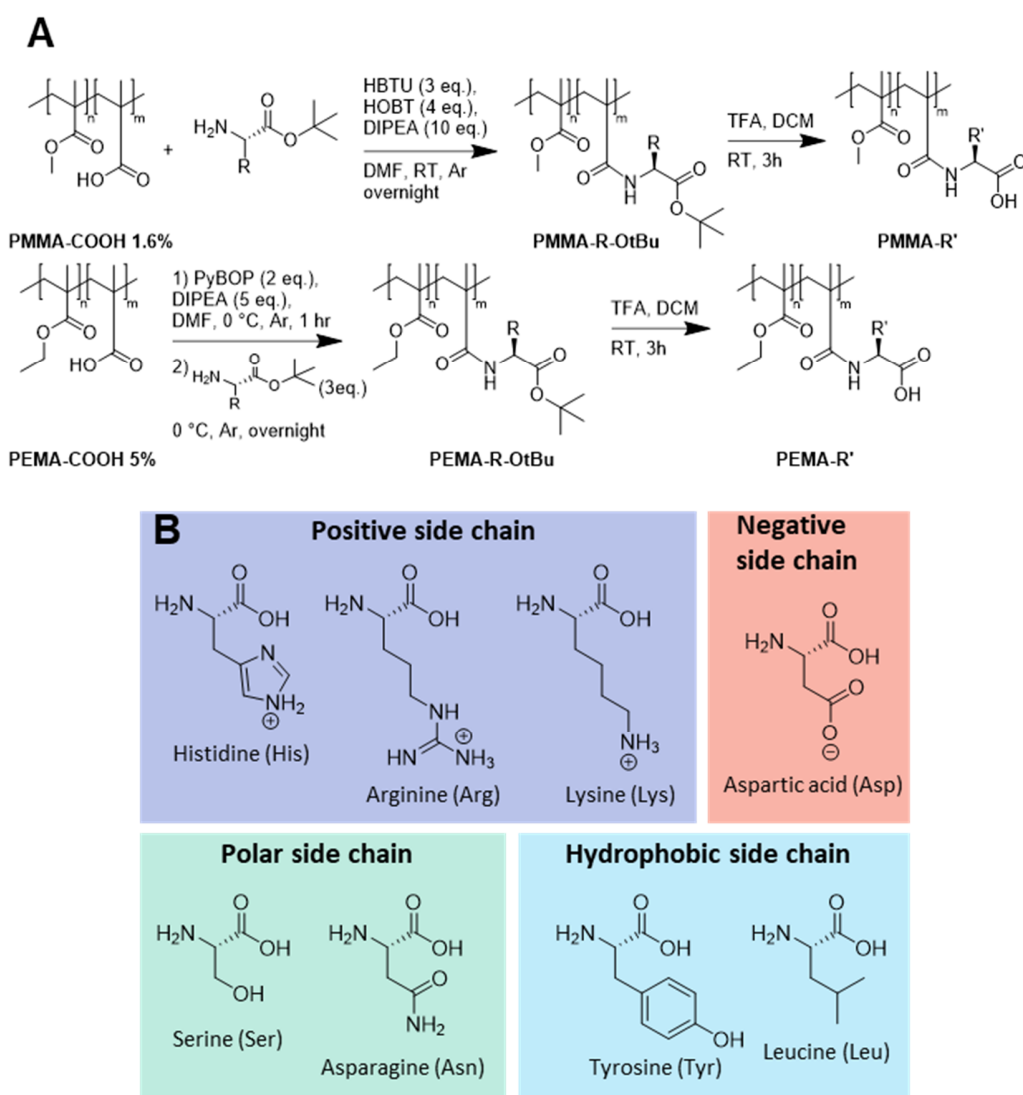


Figure 2.11 (A) Synthesis scheme of AA-bearing PMMAs (top) and PEMAs (bottom). (B) The 8 amino acids chosen based on their different properties.

The functionalization yields were measured *via* ^1H NMR by quantifying the signal of the *tert*-butyl protecting group on the amino-acid carboxylic moiety (and on the side chain when present, see section 4.1.1.3.). Moreover, for grafting reactions with Tyr and His, the

2. Results and discussion

functionalization yield obtained by integrating the *tert*-butyl group was validated by quantification of the aromatic signals. All functionalization yields were relatively high for all AAs with both PEMA and PMMA, PEMA having slightly higher values in respect to PMMA in most of the cases (Figure 2.9). The only exception was the low yield (8%) for coupling of tyrosine and PMMA, which can be explained by steric hindrance effects.

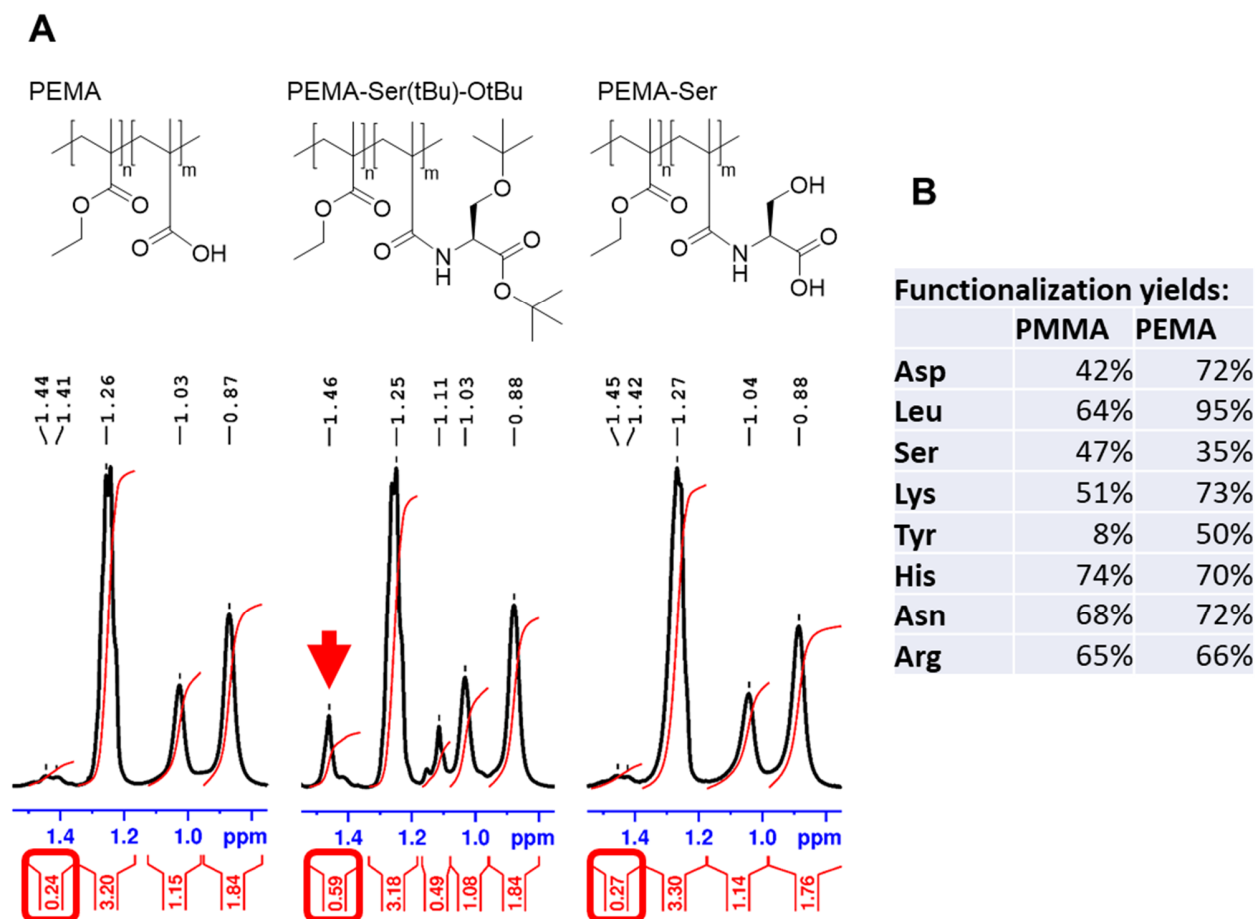


Figure 2.12 Estimation of the functionalization yields for polymer conjugates with amino acids. (A) Chemical structures and corresponding ^1H NMR spectra in CDCl_3 the area of 1.55-1.75 ppm of PEMA, PEMA grafted with protected Ser, and PEMA grafted with deprotected Ser. The peak characteristic of *tert*-butyl (highlighted by the red arrow) is clearly visible in the in the **PEMA-Ser(tBu)-OtBu** sample. Comparing the integral of the signals of the three samples allows to (i) estimate the functionalization yield, (ii) confirm that the deprotection reaction proceeds to completion. (B) Functionalization reaction yields for both types of polymers conjugated to different protected AA. The functionalization yields were calculated *via* NMR by integrating the *tert*-butyl protecting group on the amino-acid carboxylic moiety.

Based on number average molar mass (M_n) of PMMA-MA 1.6% of 15000 g/mol, we estimated that 2-3 carboxylic acid moieties are present per chain. In case of reaction yield of 50%,

2.3. Design of NPs surface for specific targeting

at least one amino-acid is grafted per chain. In case of PEMA-MA 5% $M_n \approx 127000$ g/mol (according to size exclusion chromatography measurements), meaning that on average per chain there are ~60 reactive sites, which allows a much higher number of amino acids grafted per chain for similar reaction yields.

The amino acids functionalized polymers feature a carboxylic group, like the starting polymers, and the lateral side chain characteristic of the amino acid (Figure 2.13A). At the pH used for nanoprecipitation (pH = 7.4) the carboxylate is deprotonated, and its presence is fundamental for two reasons: (i) it allows to obtain small nanoparticles during nanoprecipitation because it reduces the rate at which nucleating nanoparticles grow thanks to electrostatic repulsion, (ii) being a hydrophilic group it ensures that the AA lateral chain are exposed to the aqueous environment and not embedded in the hydrophobic polymeric matrix.

2.3.2.3. *Preparation and characterization of AA-decorated NPs*

Nanoparticles constituted of AA-polymers were formulated by nanoprecipitation (Figure 2.13A) and their diameters were measured by DLS. PMMAs functionalized with Arg, Lys, His and Tyr did not yield nanoparticles but large aggregates (Figure 2.13B). For the first three polymers this is probably due to their zwitterionic nature with net neutral charge that prevents the charge-based control of the size of nucleating particles. In the case of PMMA-Tyr the reason is less clear, since, as mentioned above, its degree of functionalization is not very high; an increased hydrophobicity of the polymer and a tendency to π -stack of the aromatic moiety might be the reasons. The other PMMA-AA yield nanoparticles with diameters between 25 and 80 nm, with PMMA-Asp giving the smallest size, probably because of the increased quantity of negatively charged groups. Interestingly, when formulating NPs by mixing PMMA-Asp with other PMMA-AA at a 1:1 molar ratio, it was possible to obtain nanoparticles for every PMMA-AA with sizes consistently smaller than the NPs formulated without PMMA-Asp (Figure 2.13B). These observations are in line with previous studies on how the quantity of charge in polymers influences the size of NPs obtained by nanoprecipitation (Reisch et al., 2015).

Most of PEMAs functionalized with AA yielded small nanoparticles after nanoprecipitation, with the exception of PEMA-Lys and PEMA-His forming big aggregates (Figure 2.13C). Again, mixing PEMA-Asp and each PEMA-AA in a ratio 1:1 yielded consistently smaller NPs compared to those exclusively constituted by PEMA-AA (Figure 2.13C). Moreover,

2. Results and discussion

PEMA-AAs yielded smaller NPs in respect to PMMA-AAs, probably because of the higher quantity of charged groups on the polymeric chains.

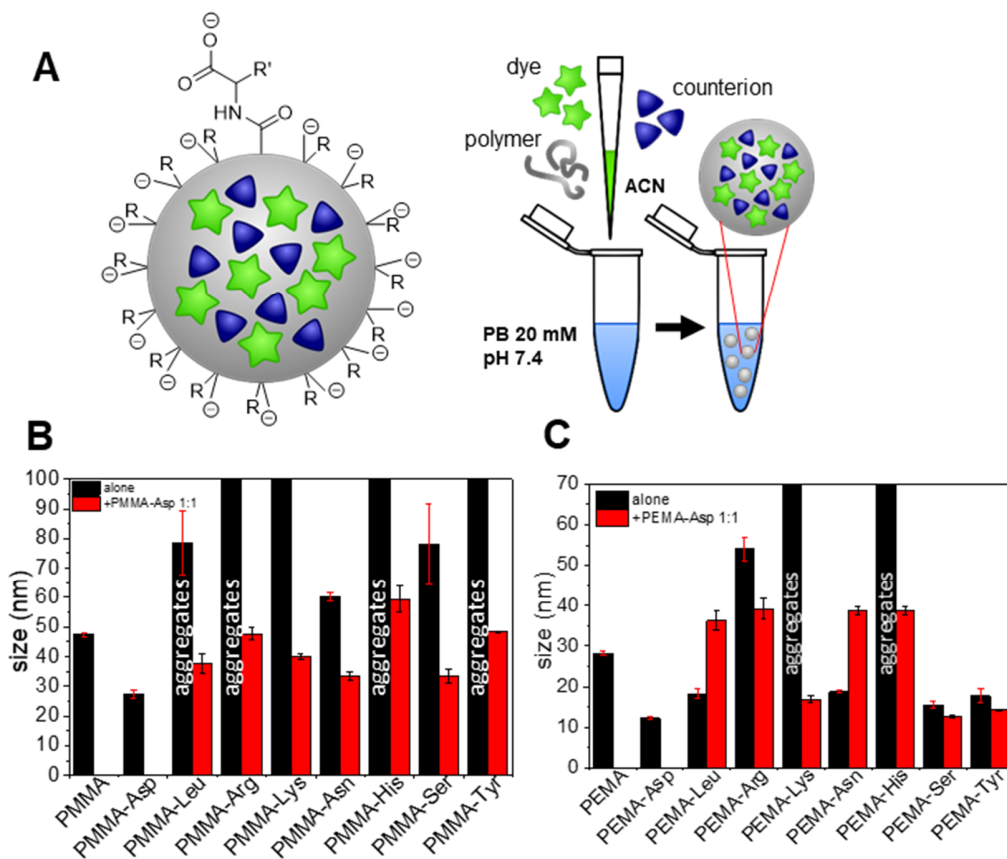


Figure 2.13 (A) Schematic structure of the surface of AA-decorated nanoparticles (left) and nanoprecipitation scheme (right). DLS diameters of NPs formulated with AA-functionalized polymers: (B) PMMA-AA and (C) PEMA-AA.

Another important point to evaluate when designing an imaging agent is its spectroscopic properties. Quantum yield measurements on NPs loaded with 10% of R18/F5-TPB showed that most of the amino acid grafted did not decrease the dye quantum yield and the values were mostly close to the QY of nanoparticles formulated with the unmodified polymer. However, quantum yield of NPs constituted of PEMA-Tyr and PEMA-His were lower in respect to the rest of the samples, probably due to the quenching action of the aromatic moieties (Figure 2.14).

2.3. Design of NPs surface for specific targeting

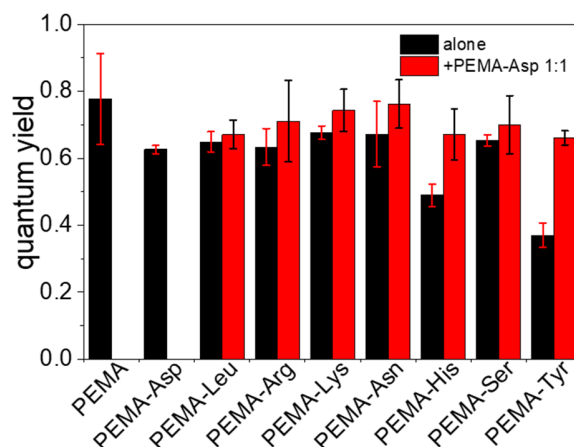


Figure 2.14 Quantum yields for nanoparticles formulated with PEMA-AAs and 10 wt% of R18/F5-TPB.

At the single-particle level all AA-decorated NPs were several orders of magnitude brighter than the reference quantum dots (QD585). Moreover, fluorescence microscopy experiments confirmed some observations already remarked in previous experiments: *i.e.* PEMA-Tyr NPs were dimmer than the rest and nanoparticles decorated with cationic side chains AA showed large aggregates. On the other hand, PEMA-Asp NPs were slightly less bright due to their small size, which resulted in a smaller number of encapsulated fluorophores. We also formulated dye-loaded NPs by mixing polymers bearing all 8 amino acids (NPs-AA) and found that their single particle brightens was similar to other NPs.

2. Results and discussion

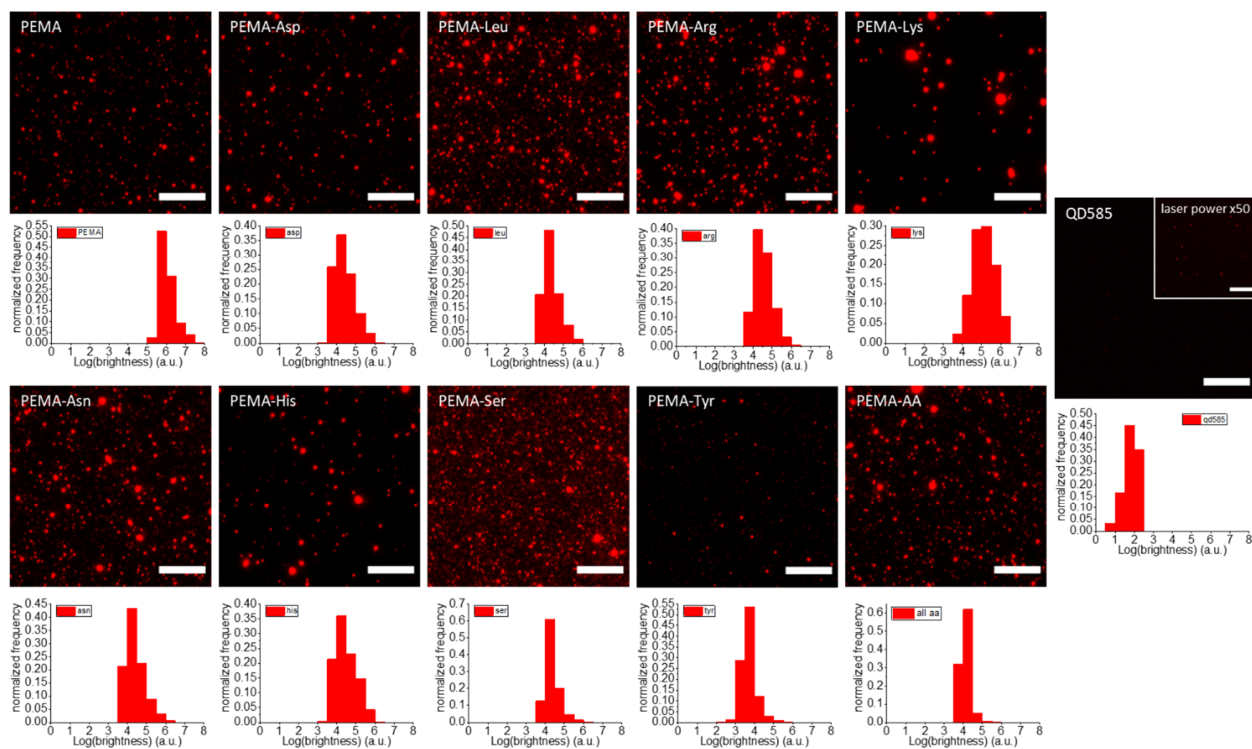


Figure 2.15 Single-particle images with the corresponding fluorescence intensity histograms for nanoparticles formulated with different PEMA-AAs and comparison with QD585 at the same conditions. Epifluorescence microscopy was done using 550 nm excitation. Scale bars: 10 μm

2.3. Design of NPs surface for specific targeting

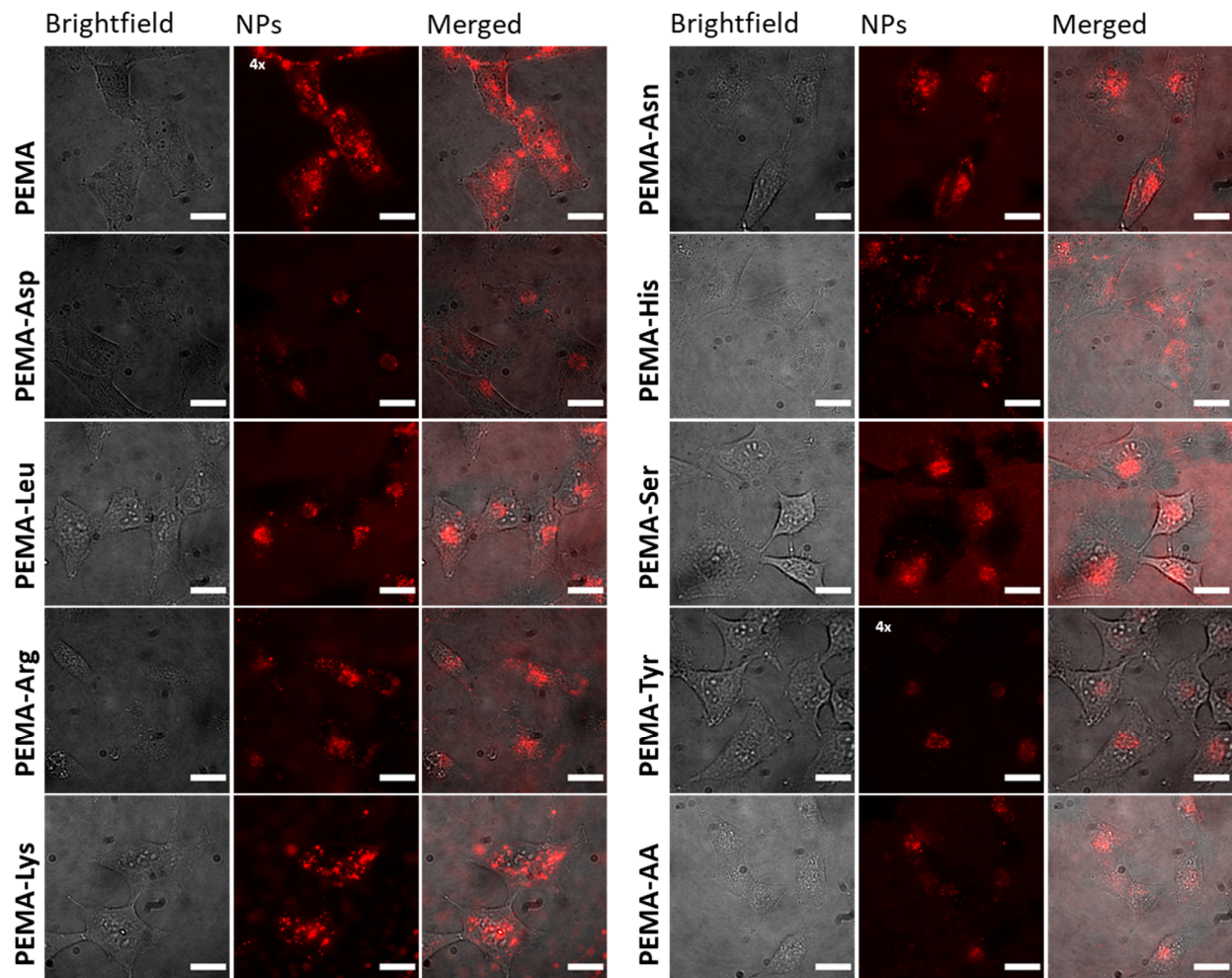


Figure 2.16 Cellular experiments with AA-functionalized NPs. HeLa cells were incubated for three hours with nanoparticles, washed and then imaged. Epifluorescence microscopy was done using 550 nm excitation. Scale bars: 25 μ m.

The interaction with cells was then studied for AA-functionalized nanoparticles. HeLa cells were incubated with NPs for 3 h and fluorescence microscopy imaging showed that all samples readily internalized presenting dotted fluorescence in the perinuclear region, typical for endocytosis. Some variation among different samples was observed, but overall there was not a clear-cut correlation between the nature of amino acids of these NPs and their behaviour when incubated with cells. The NPs presenting all amino acids (NPs-AA) also showed similar internalization profile. The only exception was the sample of PEMA-Tyr NPs, showing much lower fluorescence, which is probably related to its lower fluorescence brightness.

2. Results and discussion

2.3.2.4. Investigation of the effects of high salinity in nanoparticle formation

Next we studied the capability of the AA-decorated NPs to resist to high salinity conditions. To this end, our first step consisted of incubating in phosphate buffered saline (PBS) NPs that were previously prepared in phosphate buffer (PB) and measuring their sizes after 3 and 24 hours. PMMA-based NPs systematically aggregated after 3 h incubation in PBS (Figure 2.17A), therefore, they were discarded from all the following experiments. Conversely, PEMA-based NPs displayed a good resistance to salt, the only two samples aggregating being PEMA-Asp and PEMA-Asp+Lys (Figure 2.17B). The reason PEMA-Asp aggregates so readily might lie in its very small particle size, since it is known that smaller particles have a stronger tendency to aggregate. On the other hand, for PEMA-Asp+Lys the reason is less obvious.

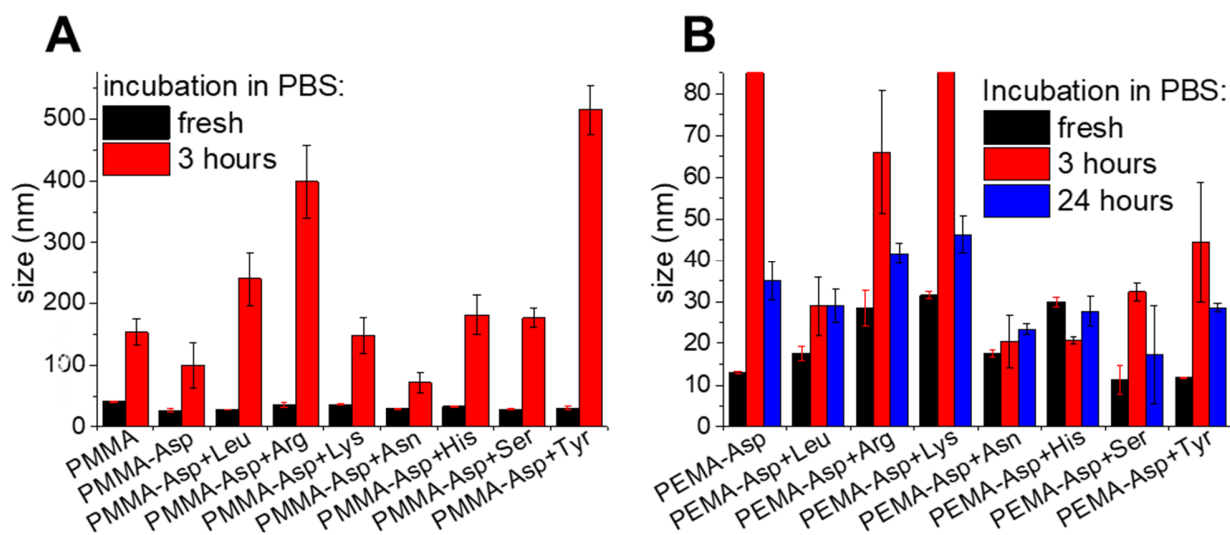


Figure 2.17 (A, B) Resistance to high salinity conditions: NPs, after being prepared in PB, were incubated in PB and PBS and their sizes measured by DLS after 3 and 24 h. (A) Sizes of PMMA-AA NPs, (B) sizes of PEMA-AA NPs.

At the next step, we tested whether our NPs decorated with AA are capable to adapt in response to external stimuli. To this end, we introduced the high salinity condition during the nanoprecipitation process of nanoparticles, then measured their size immediately and after 24 h. NPs were produced by nanoprecipitation from an organic phase, which contains polymer and dye, in an aqueous phase by two successive dilutions (see paragraph 4.2.1.). We tested a nanoprecipitation condition in which both of the dilutions were performed in PBS (*preparation 1* conditions, Figure 2.18A). In the second approach, the first step of nanoprecipitation was performed in a low salt phosphate buffer, followed by a second dilution in PBS (*preparation 2*

2.3. Design of NPs surface for specific targeting

conditions, Figure 2.18B). The preparation 1 conditions gave particles of a bit larger size than those in preparation 2, which is in line with the previous works on the effect of salt on the nanoprecipitation processes (Reisch et al., 2018). Remarkably, in preparation 1 conditions most of the polymers formed nanoparticles stable over time.

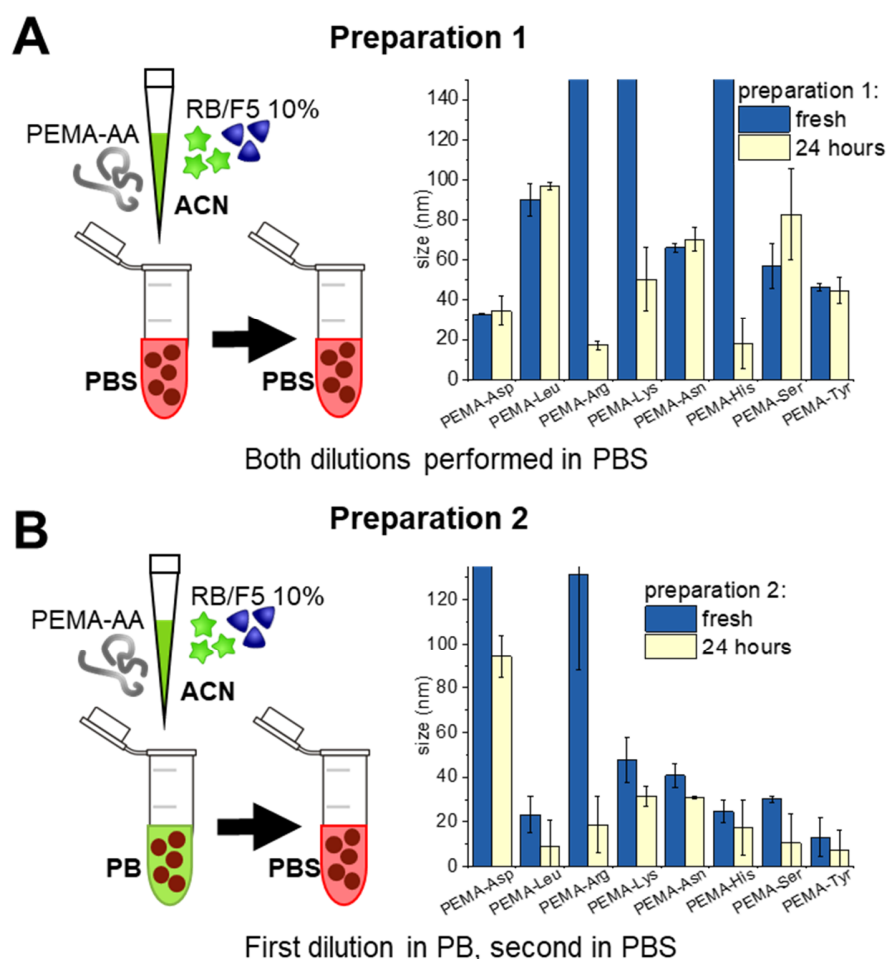


Figure 2.18 Testing the capability of AA-bearing nanoparticles to adapt to different salinity conditions using dynamic light scattering (size) measurements. (A) Scheme of Preparation 1 (left), NPs are formulated by nanoprecipitation with both dilutions performed in PBS. DLS diameters of freshly prepared nanoparticles and after a 24-hour incubation time (right). (B) Scheme of Preparation 2 (left), NPs are formulated by nanoprecipitation with the first dilution in PB and the second in PBS. DLS diameters of freshly prepared nanoparticles and after a 24-hour incubation time (right).

The loss of material over time was relatively small, as demonstrated by absorption spectra (Figure 2.19), with NPs constituted of PEMA-Asp being the most stable over time. The only exceptions were PEMAs grafted with cationic AAs, which already proved themselves as not charged enough to form NPs *via* charge-controlled nanoprecipitation.

2. Results and discussion

On the other hand, for preparation 2 conditions, the absorbance values were extremely low even for the freshly prepared samples (Figure 2.19), suggesting that nanoparticles quickly aggregated and precipitated. In this case, the sizes measured *via* DLS do not provide meaningful information, since according to absorption measurement the concentration of NPs is extremely low.

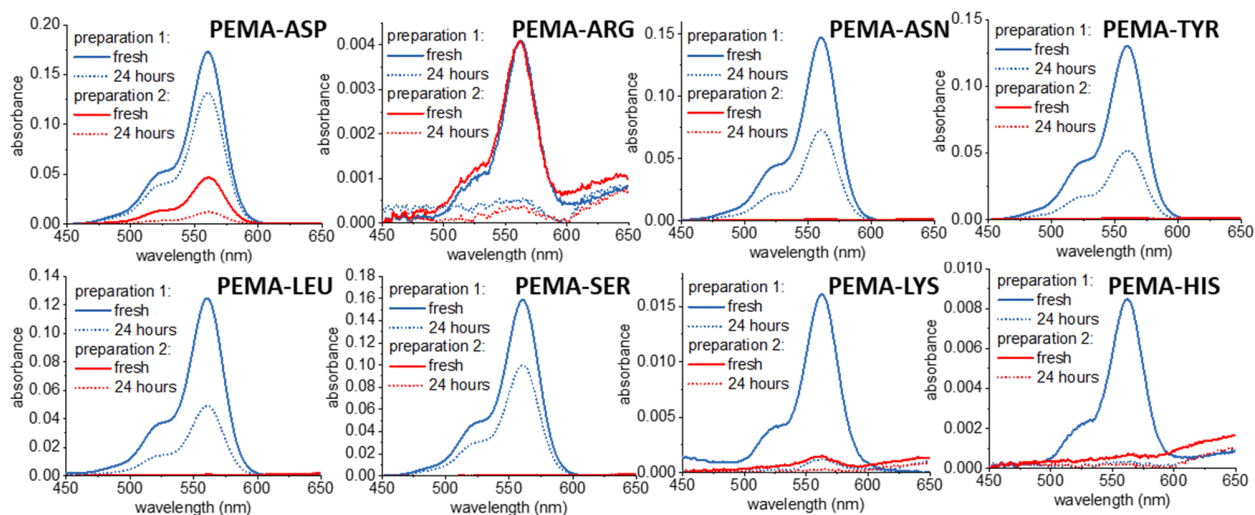


Figure 2.19 Testing the capability of AA-bearing nanoparticles to adapt to different salinity conditions using optical absorption measurements. Absorption spectra of the samples presented in Figure 2.18. It is clear that the loss of material for nanoparticles prepared with preparation 1 is less pronounced in respect to nanoparticles prepared with preparation 2, where most of nanoparticles aggregate and precipitate immediately.

Thus, we can conclude that preparation of NPs in high salt buffer (preparation 1) generates particles stable to these conditions. It is therefore clear, that our amino acid decorated NPs are capable to adapt to the external stimuli during the nanoprecipitation. We expect that in the future we will be able to stimulate NPs to adapt to other conditions than high salts. In particular, we are interested to use specific molecules that could “imprint” certain patterns on the NPs surface, in order to obtain NPs with specific targeting properties.

Chapter 3. Conclusions and perspectives

The aim of this PhD research work consisted in the rational design of dye-loaded polymeric nanoparticles at the level of their core (dyes and counterions) and surface chemistry in order to obtain new properties and functions for bioimaging and biosensing applications. Indeed, as extensively discussed, dye-loaded polymeric nanoparticles are complex system composed of multiple parts which can be individually addressed to obtain new functionalities.

The objective of this work was to implement new functionalities into dye-loaded polymeric nanoparticles through a rational design of their core and shell. This was attained through different routes. We tested new dyes for the preparation of nanoparticles, in order to obtain NPs emitting in different colors and we formulated nanoparticles loaded with new counterions with the aim to synthesize multi-functional platforms. These research topics are fundamental when interested in finding new sensing applications for dye-loaded polymeric nanoparticles, since the fine-tuning of photophysical properties is vital in this context. However, the sensing and imaging functionalities arise from some kind of interaction of the nanoparticle probe with the target, meaning that the surface properties of nanoparticles employed in a sensing context cannot be overlooked. Therefore, we also dedicated ourselves to the study functionalization of the surface of dye-loaded polymeric nanoparticles, with the intent to produce targeted imaging agents. We pursued both a ligand-based approach, by grafting on the surface of nanoparticles groups to selectively target lipids and proteins; and a molecularly imprinting approach, by preparing nanoparticles with their surface covered in amino-acids, resulting in a complex, protein-like surface. These research topics are particularly important when the interest is to adapt dye-loaded polymeric nanoparticles for targeting applications, since the fine-tuning and strict control of the surface properties is fundamental to achieve the desired biological activity and reduce to a minimum non-specific interactions.

In the first part of this work we focused on the properties of the core of nanoparticles by varying the nature of the encapsulated dyes and counterions to produce systems with new photophysical properties. In this context, a new green-emitting antenna nanoparticles, based on rhodamine 6G and rhodamine 110 analogues were synthesized. These green-emitting nanoparticles were used to construct a FRET-based DNA sensor. The FRET acceptor chosen (ATTO647N) emits in the red, meaning that a change in the FRET ratio upon addition of the target could be easily

3. Conclusions and perspectives

detected by RGB camera of a smartphone. Indeed, we succeeded to detect *via* smartphone-enabled fluorescence microscopy oligonucleotides encoding survivin cancer marker down to concentrations of 10 pM. This is an important milestone, because it represents the first step towards the application of our dye-loaded polymeric nanoparticles in point-of-care diagnostics, potentially enabling smartphone-based detection of single strands and/or in complex biological matrices.

Another research direction explored in the context of fine tuning the core properties of NPs, was on the nature of the counterions. Since in all the past works of our team on the CIs do not explore any additional functionality besides acting as bulky hydrophobic spacers, we decided to test a class of counterions which could transform our dye-loaded polymeric nanoparticles into multi-imaging platforms: lanthanide-based complexes, in particular based on gadolinium and europium. Lanthanides are heavy atoms and in particular gadolinium is used as a contrast agent in transmission electron microscopy. Moreover, europium absorbs in UV but emits in the visible, therefore, dyes paired with this lanthanide counterion could generate NPs with an ultra-long Stokes shift based on FRET. We found that NPs formulated with dyes paired with Gd-CIs featured higher quantum yields and smaller sizes than NPs without the counterion. Moreover, when Gd-loaded NPs were imaged *via* TEM, they displayed a stronger contrast in respect to NPs without Gd-CI. On the other hand, Eu-based counterions showed remarkably efficient FRET to their paired cyanine dye, so that the obtained NPs emitted in near-infrared while being excited in the UV. These results could open the way to the conception of new materials featuring multi-modal imaging capabilities and unique optical properties. Moreover, our counterion concept for preventing aggregation-caused quenching of dyes is now extended to different anionic complexes of metals, which makes this approach more generic.

In the second part of this work we focused on the surface properties of the nanoparticles, with the intent to modify their surface to obtain biological activity. On one front, we followed a ligand-based approach, by functionalizing the surface of NPs with bioactive molecules. The important step here was development of PEGylation strategy based on copper-free click chemistry. Testing PEGs of different size revealed that only relatively long PEGs of 2000 Da could minimize non-specific interactions with the cells. Then, we chose two different targeting ligands: (i) an acetyl phenylboronic acid derivative, which targets selectively phosphatidylethanolamine, a phospholipid present on the outer leaflet of the plasma membrane in bacteria and apoptotic eukaryotic cells, (ii)

carbetocin, an oxytocin analogue, which targets oxytocin membrane receptors. The obtained ligand functionalized NPs displayed some targeting ability, which was nevertheless quite limited and some further optimization of these systems should be further performed. However, this work still is important because it demonstrated that it is possible to quickly and reliably functionalize NPs with PEG shell and targeting ligands *via* copper-free click chemistry. These results will allow preparation of NPs for specific targeting and detection of biomolecules at the level of cells and small animals.

Another viable front we explored to produce targeting systems relied on applying a bio-mimicking approach, where we decorated NPs with nine different amino acids to obtain “artificial proteins”. To this end PMMA-MA and PEMA-MA were amino acid functionalized with polymers and then nanoparticles were formulated by nanoprecipitation with the idea to generate complex protein-like surface. We studied the properties of AA-decorated nanoparticles and concluded that only PEMA-AAs were the most suitable for further studies. In terms of spectroscopic properties, all nanoparticles loaded with R18/F5-TPB dye featured good quantum yields, being several orders of magnitude brighter than quantum dots. When nanoprecipitated in buffers of different salt concentration, we found that they have a capacity to “adapt” to their environment, showing good stability in the corresponding buffer. When incubated with HeLa cells NPs were readily internalized *via* endocytosis, regardless of their surface. In our ongoing studies, we test whether it was possible to imprint these protein-like nanoparticles a molecular template. However, for the moment the results presented are not convincing and require further dedicated studies. Overall, we showed a proof of concept for preparation of NPs decorated with amino acids, which constitute an interesting bio-mimicking platform for specific targeting applications.

4. Materials and methods

Chapter 4. Materials and methods

4.1. *Materials*

4.1.1. *Chemicals*

All chemicals and solvents employed were purchased either from Alfa Aesar or Sigma Aldrich and used as received unless noted otherwise.

Poly-(methylmethacrylate-co-methacrylic acid) (PMMA-MA, 1.6% methacrylic acid), Rhodamine 6G (95.0%), Rhodamine 110 (>99.0%), rhodamine B octadecyl ester perchlorate (>98.0%), 1-octadecanol (95%), 4-(Dimethylamino)pyridine ($\geq 99\%$), N-(3-Dimethylaminopropyl)-N'-ethylcarbodiimide hydrochloride ($\geq 98\%$), sodium tetrakis[3,5-bis(1,1,1,3,3,3-hexafluoro-2-methoxy-2-propyl)phenyl]borate trihydrate (Selectophore™), N,N-Diisopropylethylamine ($\geq 99\%$), acetonitrile (anhydrous, 99.8%), dichloromethane (anhydrous, $\geq 99.8\%$), sodium hydroxide ($\geq 97.0\%$), polyethylenimine (branched), potassium hydroxide ($\geq 85\%$, pellets), BSA-biotin, Amicon Centrifugal filters (0.5mL, 100K), PD-10 desalting columns (Sephadex™ G-25 M) were purchased from Sigma-Aldrich. HBTU was purchased from ChemPep Inc. Trifluoroacetic acid (99%) was purchased from Alfa Aesar. 1,1'-Dioctadecyl-3,3,3',3'-Tetramethylindodicarbocyanine Perchlorate, Neutravidin, LabTek chambers (Borosilicate cover glass, eight wells), MultiSpeck™ Multispectral Fluorescence Microscopy Standards Kit (M-7901) and Qdot™ 585 Streptavidin Conjugate were purchased from ThermoFisher Scientific. H-Tyr(tBu)-OtBu · HCl, H-Asn-OtBu · HCl, H-Asp(OtBu)-OtBu · HCl, H-Ser(tBu)-OtBu, H-His(1-Trt)-OtBu, H-Arg(Pbf)-OtBu · HCl, H-Leu-OtBu · HCl, H-Lys(Boc)-OtBu · HCl were purchased from Bachem.

Sodium phosphate monobasic (>99.0%, Sigma-Aldrich) and sodium phosphate dibasic dihydrate (>99.0%, Sigma-Aldrich) were used to prepare 20 mM phosphate buffers at pH 7.4. For saline buffer sodium chloride ($\geq 99\%$, Sigma Aldrich) 30 mM and magnesium chloride ($\geq 98\%$, Sigma Aldrich) 12 mM was added to 20 mM phosphate buffer and pH was adjusted with sodium hydroxide 1N solution. Milli-Q water (Millipore) was used in all experiments. For immobilization protocol PBS (without Ca^{2+} and Mg^{2+}) was purchased from Lonza.

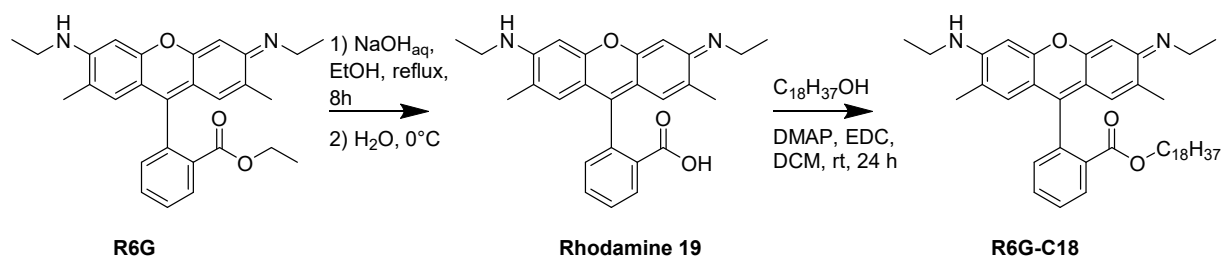
4.1.1.1. *Dyes*

Figure 4.1 Synthesis scheme of R6G-C18

Rhodamine 19 was prepared following a previously described procedure (Yang et al., 2009).

To a solution of **Rhodamine 19** (200 mg, 0.44 mmol), 1-octadecanol (360 mg, 1.33 mmol) and 1-Ethyl-3-(3-dimethylaminopropyl)carbodiimide hydrochloride (425 mg, 2.22 mmol) in dichloromethane (5 mL), DMAP (11 mg, 0.09 mmol) was added. Reaction was left stirring at room temperature under argon for 24 hours. Then the reaction was washed three times with HCl 1M and one time with brine. Organic fraction was gathered and solvent evaporated, finally the crude product was purified via silica chromatography using DCM/MeOH 95/5 as eluent. 230 mg of **Rhodamine 6G octadecyl ester (R6G-C18)** were obtained (78% yield). ^1H NMR (400 MHz, CD_3OD) δ ppm 0.91 (3 H, t, $J=7.9$ Hz) 1.03-1.36 (34H, m) 1.40 (6H, t, $J=7.17$ Hz) 2.16 (6H, s) 3.56 (4H, q, $J=7.17$) 3.93 (2H, t, $J=6.16$ Hz) 6.92 (2H, d, $J=1.05$ Hz) 6.97 (2H, s) 7.43 (1H, dd, $J=7.31$ Hz $J=1.34$ Hz) 7.82-7.91 (2H, m) 8.32 (1H, dd, $J=7.61$ Hz $J=1.44$). ^{13}C NMR (126 MHz, CD_3OD) δ ppm 169.58, 161.92, 161.50, 160.28, 137.28, 136.51, 134.90, 134.81, 134.56, 134.12, 134.00, 132.63, 129.50, 117.36, 97.42, 69.24, 42.02, 35.61, 33.31, 33.29, 33.28, 33.24, 33.05, 33.01, 32.81, 31.92, 29.49, 26.27, 20.14, 16.98, 16.63. HRMS (m/z): $[\text{M}]^+$ calcd. for $\text{C}_{44}\text{H}_{63}\text{N}_2\text{O}_3$ 667.4839; found 667.4833.

Rhodamine 110 octadecyl ester (R110-C18), was synthesized following a previously described procedure (Floyd et al., 2008).

4. Materials and methods

4.1.1.2. Counterions

Gd(TTA)₄, Gd(NTA)₄, Gd(HPFNP)₄, Eu(NTA)₄, Eu(HPFNP)₄ were provided by Prof. Tero Soukka (University of Turku, Finland) and synthesized according to a previously described procedure (Fratini et al., 2008).

F9-Al was provided by Prof. Ingo Krossing (University of Freiburg, Germany) and synthesized according to a previously described procedure (Krossing, 2001).

4.1.1.3. Polymers

PMMA-AspN₃ was provided by Dr. Nina Melnychuk and synthesized according to a previously described procedure (Melnychuk and Klymchenko, 2018).

Poly-(methylmethacrylate-co-3-sulfopropyl methacrylate) (PMMA-HSO₃, 1% 3-sulfopropyl methacrylate) was provided by Mr. Antoine Combes and synthesized following a previously described procedure (Reisch et al., 2018).

Poly-(ethyl methacrylate-co-methacrylic acid) (PEMA-MA, 5% methacrylic acid) was provided by Mr. Antoine Combes and synthesized according to a previously described procedure (Melnychuk et al., 2020).

PMMA-AAs and **PEMA-AAs** were synthesized by peptide coupling as described below, functionalization yields were calculated by integrating the Boc signal in the NMR spectra of the protected polymers and the aromatic signals when present.

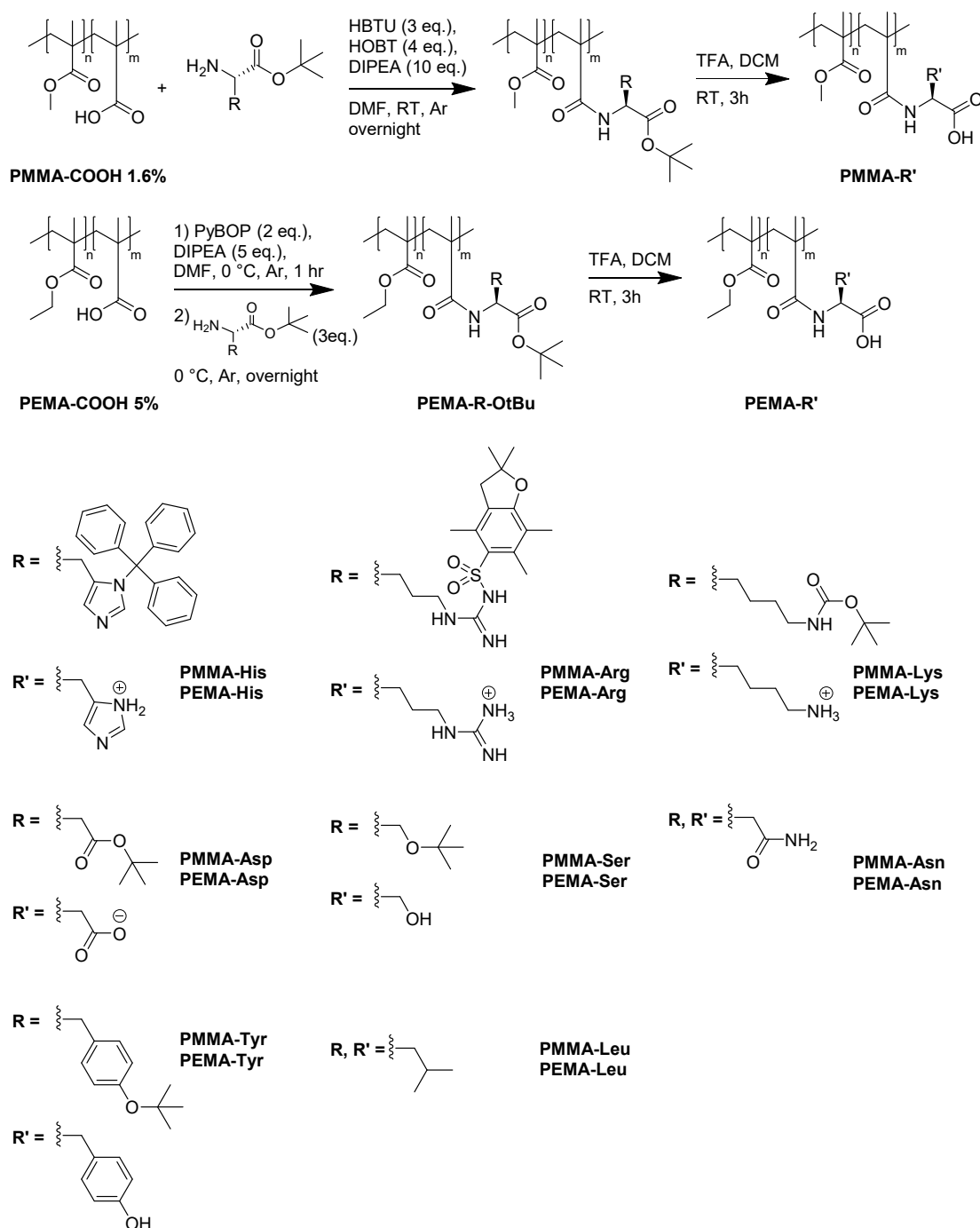


Figure 4.2 Synthesis scheme for amino acid-functionalized PMMAs and PEMAs.

PMMA-MA 1.6% (1 eq of COOH, 0.15 mmol, 1g) was dissolved into 12.5 mL of anhydrous DMF. HBTU (3 eq, 0.45 mmol, 171 mg), HOBT (4 eq, 0.6 mmol, 81 mg) and N,N-diisopropylethylamine (10 eq, 1.5 mmol, 0.26 mL) were added. The mixture was stirred for 15

4. Materials and methods

minutes, and then the protected AA of choice (3 eq, 0.45 mmol) was added. The system was then allowed to stir under argon at room temperature overnight. Solvent was then evaporated under vacuum and the residue was dissolved in the smallest amount possible of ACN and precipitated in cold MeOH. The residue was then washed with MeOH and redissolved in ACN and reprecipitated in cold MeOH two additional times. Finally, the product was dried under vacuum. Functionalization yields were calculated *via* ^1H NMR by integrating the signal corresponding to the tert-butyl protecting group of the AA carboxylic moiety (and on the side chain when present), said signal is expected around 1.5 ppm.

The as-synthesized polymer was deprotected by dissolving 200 mg of it in 5 mL of DCM and 2 mL of TFA and stirring at room temperature for 3 hours. The solvent was evaporated under vacuum and ACN was added and re-evaporated several times until TFA was completely removed. The product was then again reprecipitated in cold MeOH and dried under vacuum.

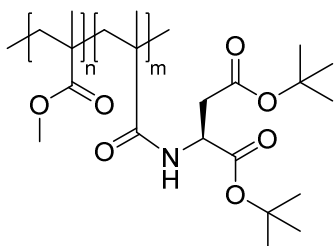
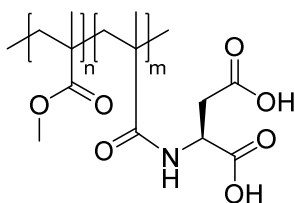
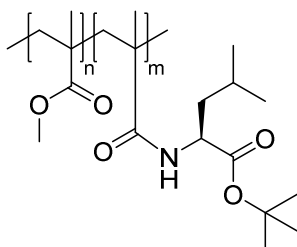


Figure 4.3 Structure of **PMMA-Asp(OtBu)-OtBu**.

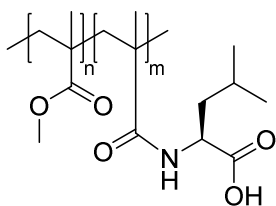
PMMA-Asp(OtBu)-OtBu: functionalization yield 42%. ^1H NMR (400 MHz, CDCl_3) δ ppm 0.83 (br s, 1.70 H), 1.01 (br s, 1.25 H), 1.17 – 1.26 (m, 0.27 H), 1.40 – 1.48 (m, 0.25 H), 1.79 – 2.04 (m, 1.85 H), 3.59 (br s, 3H).

Figure 4.4 Structure of **PMMA-Asp**.

PMMA-Asp: yield 80%. ^1H NMR (400 MHz, CDCl_3) δ ppm 0.82 (br s, 1.59 H), 0.99 (br s, 1.21 H), 1.17 – 1.26 (m, 0.34 H), 1.40 – 1.48 (m, 0.37 H), 1.79 – 2.04 (m, 1.82 H), 3.57 (br s, 3H).

Figure 4.5 Structure of **PMMA-Leu-OtBu**.

PMMA-Leu-OtBu: functionalization yield 64%. ^1H NMR (400 MHz, CDCl_3) δ ppm 0.82 (br s, 1.66 H), 1.00 (br s, 1.17 H), 1.17 – 1.27 (m, 0.26 H), 1.41 – 1.48 (m, 0.33 H), 1.69 – 2.04 (m, 1.84 H), 3.58 (br s, 3H).

Figure 4.6 Structure of **PMMA-Leu**.

PMMA-Leu: yield 85%. ^1H NMR (400 MHz, CDCl_3) δ ppm 0.82 (br s, 1.73 H), 1.00 (br s, 1.31 H), 1.17 – 1.27 (m, 0.29 H), 1.41 – 1.48 (m, 0.26 H), 1.55 (br s, 0.41 H), 1.71 – 2.04 (m, 2.03 H), 3.59 (br s, 3H).

4. Materials and methods

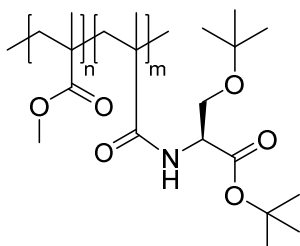


Figure 4.7 Structure of **PMMA-Ser(tBu)-OtBu**.

PMMA-Ser(tBu)-OtBu: functionalization yield 47%. $^1\text{H NMR}$ (400 MHz, CDCl_3) δ ppm 0.83 (br s, 1.64 H), 1.01 (br s, 1.16 H), 1.18 – 1.27 (m, 0.26 H), 1.32 – 1.52 (m, 0.38 H), 1.71 – 2.09 (m, 1.72 H), 3.59 (br s, 3H).

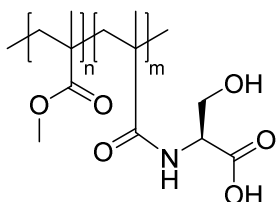


Figure 4.8 Structure of **PMMA-Ser**.

PMMA-Ser: yield 86%. $^1\text{H NMR}$ (400 MHz, CDCl_3) δ ppm 0.83 (br s, 1.70 H), 1.01 (br s, 1.17 H), 1.15 – 1.29 (m, 0.24 H), 1.34 – 1.50 (m, 0.26 H), 1.69 – 2.09 (m, 1.88 H), 3.59 (br s, 3H).

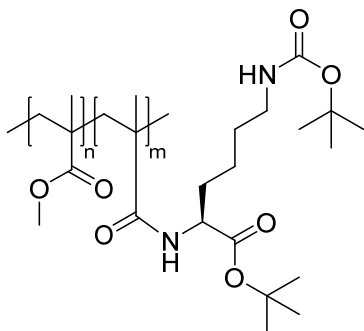
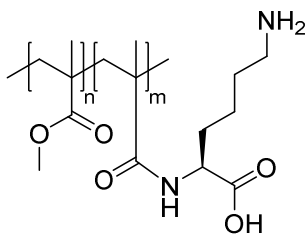
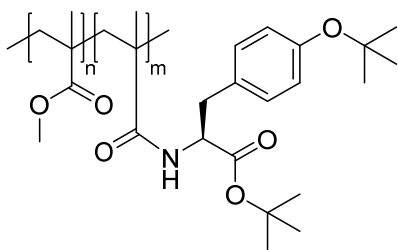


Figure 4.9 Structure of **PMMA-Lys(Boc)-OtBu**.

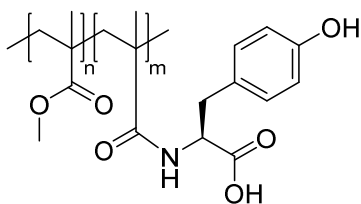
PMMA-Lys(Boc)-OtBu: functionalization yield 51%. $^1\text{H NMR}$ (400 MHz, CDCl_3) δ ppm 0.83 (br s, 1.66 H), 1.01 (br s, 1.18 H), 1.14 – 1.32 (m, 0.31 H), 1.34 – 1.52 (m, 0.39 H), 1.63 (br s, 0.12 H), 1.71 – 1.98 (m, 1.74 H), 3.58 (br s, 3H).

Figure 4.10 Structure of **PMMA-Lys**.

PMMA-Lys: yield 87%. $^1\text{H NMR}$ (400 MHz, CDCl_3) δ ppm 0.83 (br s, 1.66 H), 1.01 (br s, 1.09 H), 1.16 – 1.28 (m, 0.24 H), 1.35 – 1.52 (m, 0.26 H), 1.74 – 2.10 (m, 1.75 H), 3.59 (br s, 3H).

Figure 4.11 Structure of **PMMA-Tyr(tBu)-OtBu**.

PMMA-Tyr(tBu)-OtBu: functionalization yield 8%. $^1\text{H NMR}$ (400 MHz, CDCl_3) δ ppm 0.82 (br s, 1.66 H), 1.00 (br s, 1.15 H), 1.14 – 1.29 (m, 0.27 H), 1.31 (br s, 0.14 H), 1.41 (br s, 0.27), 1.58 (br s, 0.09 H), 1.71 – 1.99 (m, 1.77 H), 3.58 (br s, 3H), 6.89 (m, 0.01 H), 7.08 (m, 0.01 H).

Figure 4.12 Structure of **PMMA-Tyr**.

PMMA-Tyr: yield 83%. $^1\text{H NMR}$ (400 MHz, CDCl_3) δ ppm 0.82 (br s, 1.65 H), 1.00 (br s, 1.20 H), 1.16 – 1.31 (m, 0.27 H), 1.32 – 1.50 (m, 0.28 H), 1.72 – 2.01 (m, 1.77 H), 3.58 (br s, 3H), 6.83 (m, 0.01 H), 7.10 (m, 0.01 H).

4. Materials and methods

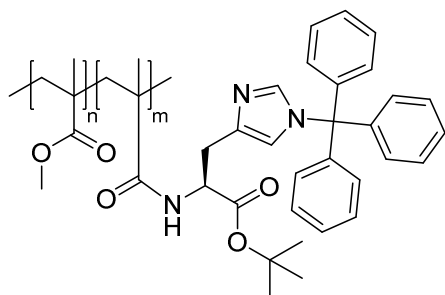


Figure 4.13 Structure of **PMMA-His(1-Trt)-OtBu**.

PMMA-His(1-Trt)-OtBu: functionalization yield 74%. ^1H NMR (400 MHz, CDCl_3) δ ppm 0.82 (br s, 1.62H), 1.00 (br s, 1.22 H), 1.13 – 1.28 (m, 0.29 H), 1.31 – 1.51 (m, 0.35 H), 1.69 – 1.99 (m, 1.82 H), 3.58 (br s, 3H), 7.10 (s, 0.05 H), 7.32 (m, 0.08 H), 7.41 (br s, 0.01 H).

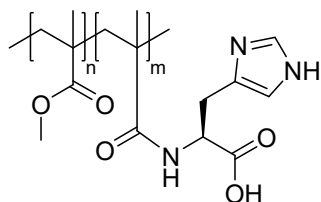


Figure 4.14 Structure of **PMMA-His**.

PMMA-His: yield 79%. ^1H NMR (400 MHz, CDCl_3) δ ppm 0.84 (br s, 1.71 H), 1.02 (br s, 1.21 H), 1.15 – 1.31 (m, 0.30 H), 1.34 – 1.55 (m, 0.29 H), 1.67 – 2.10 (m, 1.85 H), 3.60 (br s, 3H), 7.28 (m, 0.04 H), 7.30 (m, 0.03 H), 7.31 (m, 0.02 H)

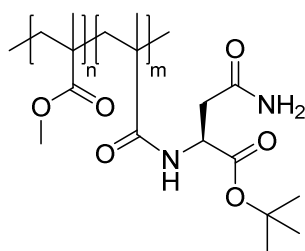
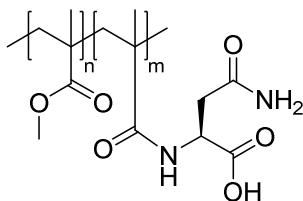
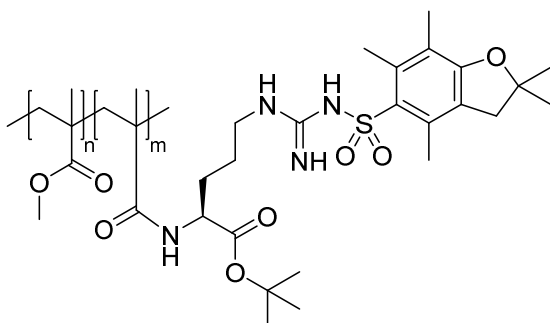


Figure 4.15 Structure of **PMMA-Asn-OtBu**.

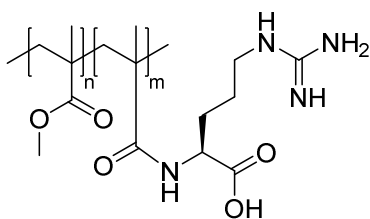
PMMA-Asn-OtBu: functionalization yield 68%. ^1H NMR (400 MHz, CDCl_3) δ ppm 0.83 (br s, 1.66 H), 1.00 (br s, 1.18 H), 1.18 – 1.31 (m, 0.28 H), 1.33 – 1.54 (m, 0.34 H), 1.66 (br s, 0.12 H), 1.70 – 2.09 (m, 1.61 H), 3.58 (br s, 3H).

Figure 4.16 Structure of **PMMA-Asn**.

PMMA-Asn: yield 88%. $^1\text{H NMR}$ (400 MHz, CDCl_3) δ ppm 0.83 (br s, 1.62 H), 1.01 (br s, 1.20 H), 1.16 – 1.30 (m, 0.27 H), 1.33 – 1.53 (m, 0.29 H), 1.71 – 2.09 (m, 1.80 H), 3.59 (br s, 3H).

Figure 4.17 Structure of **PMMA-Arg(Pbf)-OtBu**.

PMMA-Arg(Pbf)-OtBu: functionalization yield 65%. $^1\text{H NMR}$ (400 MHz, CDCl_3) δ ppm 0.82 (br s, 1.65 H), 1.00 (br s, 1.16 H), 1.13 – 1.30 (m, 0.32 H), 1.32 – 1.51 (m, 0.34 H), 1.67 – 1.99 (m, 1.79 H), 3.58 (br s, 3H).

Figure 4.18 Structure of **PMMA-Arg**.

PMMA-Arg: yield 78%. $^1\text{H NMR}$ (400 MHz, CDCl_3) δ ppm 0.83 (br s, 1.64 H), 1.01 (br s, 1.23 H), 1.13 – 1.27 (m, 0.26 H), 1.34 – 1.51 (m, 0.27 H), 1.71 – 2.07 (m, 1.80 H), 3.59 (br s, 3H).

4. Materials and methods

PEMA-MA 5% (1 eq of COOH, 0.05 mmol, 100 mg) was dissolved into 1.25 mL of anhydrous DMF. The system was kept under argon and cooled down in an ice bath, then PyBOP (2 eq, 0.1 mmol, 52 mg) and DIPEA (5 eq, 0.25 mmol, 43 μ L) were added. One hour after the protected AA of choice (3 eq, 0.15 mmol) was added and the reaction was left to stir overnight. Then the crude was dried over vacuum and precipitated three times in a cold mixture of MeOH/H₂O (1:1), then the product was lyophilized. Deprotection was performed as described above.

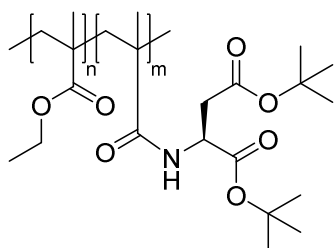


Figure 4.19 Structure of **PEMA-Asp(OtBu)-OtBu**.

PEMA-Asp(OtBu)-OtBu: functionalization yield 72%. ¹H NMR (400 MHz, CDCl₃) δ ppm 0.88 (br s, 1.81 H), 1.03 (br s, 1.26 H), 1.25 (br s, 3.43 H), 1.44 (br s, 0.84 H), 1.62 (br s 0.28 H), 1.76 – 2.04 (m, 2.06 H), 4.03 (s, 2 H).

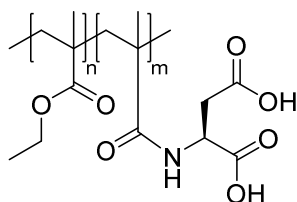
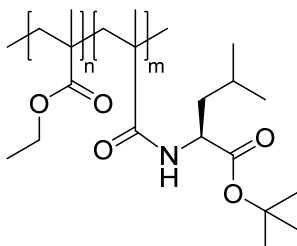
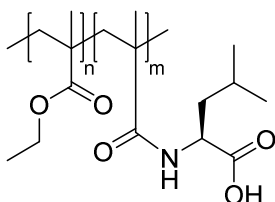


Figure 4.20 Structure of **PEMA-Asp**.

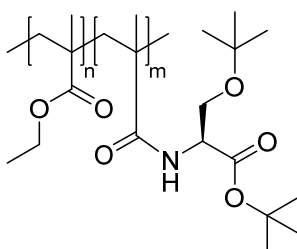
PEMA-Asp: yield 80%. ¹H NMR (400 MHz, CDCl₃) δ ppm 0.88 (br s, 1.80 H), 1.04 (br s, 1.22 H), 1.26 (br s, 3.16 H), 1.43 (m, 0.28 H), 1.70 – 2.08 (m, 1.76 H), 4.04 (s, 2 H).

Figure 4.21 Structure of **PEMA-Leu-OtBu**.

PEMA-Leu-OtBu: functionalization yield 95%. $^1\text{H NMR}$ (400 MHz, CDCl_3) δ ppm 0.88 (br s, 1.98 H), 1.03 (br s, 1.37 H), 1.25 (br s, 3.42 H), 1.45 (br s, 0.85 H), 1.63 (br s 0.52 H), 1.69 – 2.03 (m, 2.19 H), 4.03 (s, 2 H).

Figure 4.22 Structure of **PEMA-Leu**.

PEMA-Leu: yield 89%. $^1\text{H NMR}$ (400 MHz, CDCl_3) δ ppm 0.88 (br s, 1.97 H), 1.04 (br s, 1.31 H), 1.25 (br s, 3.27 H), 1.44 (br s, 0.29 H), 1.65 – 2.14 (m, 2.05 H), 4.04 (s, 2 H).

Figure 4.23 Structure of **PEMA-Ser(tBu)-OtBu**.

PEMA-Ser(tBu)-OtBu: functionalization yield 35%. $^1\text{H NMR}$ (400 MHz, CDCl_3) δ ppm 0.88 (br s, 1.84 H), 1.03 (br s, 1.08 H), 1.11 (m, 0.49 H), 1.25 (br s, 3.18 H), 1.46 (m, 0.59 H), 1.71 – 2.05 (m, 1.87 H), 4.04 (s, 2 H).

4. Materials and methods

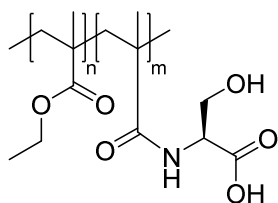


Figure 4.24 Structure of **PEMA-Ser**.

PEMA-Ser: yield 84%. $^1\text{H NMR}$ (400 MHz, CDCl_3) δ ppm 0.88 (br s, 1.76 H), 1.04 (br s, 1.14 H), 1.27 (br s, 3.30 H), 1.43 (m, 0.29 H), 1.71 – 2.12 (m, 1.74 H), 4.04 (s, 2 H).

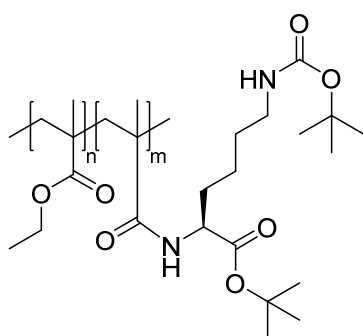


Figure 4.25 Structure of **PEMA-Lys(Boc)-OtBu**.

PEMA-Lys(Boc)-OtBu: functionalization yield 73%. $^1\text{H NMR}$ (400 MHz, CDCl_3) δ ppm 0.88 (br s, 1.85 H), 1.03 (br s, 1.12 H), 1.25 (br s, 3.31 H), 1.50 (m, 0.87 H), 1.54 (m, 0.20 H), 1.69 (br s 0.28 H), 1.75 – 1.95 (m, 1.68 H), 4.03 (s, 2 H).

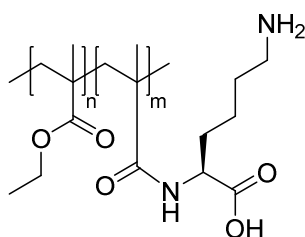
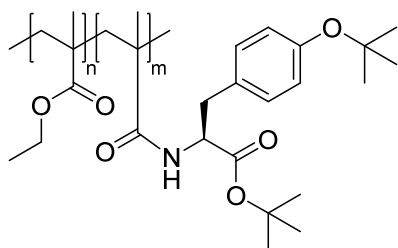
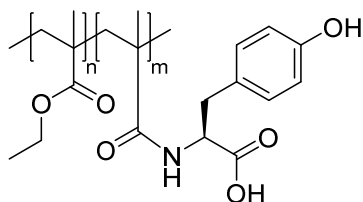


Figure 4.26 Structure of **PEMA-Lys**.

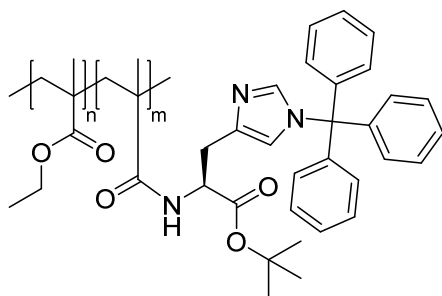
PEMA-Lys: yield 88%. $^1\text{H NMR}$ (400 MHz, CDCl_3) δ ppm 0.88 (br s, 1.91 H), 1.04 (br s, 1.16 H), 1.25 (br s, 3.27 H), 1.44 (m, 0.29 H), 1.71 – 2.1 (m, 1.82 H), 4.04 (s, 2 H).

Figure 4.27 Structure of **PEMA-Tyr(tBu)-OtBu**.

PEMA-Tyr(tBu)-OtBu: functionalization yield 50%. $^1\text{H NMR}$ (400 MHz, CDCl_3) δ ppm 0.88 (br s, 1.83 H), 1.03 (br s, 1.11 H), 1.25 (br s, 3.74 H), 1.43 (m, 0.30 H), 1.56 (br s, 0.73 H), 1.77 – 2.05 (m, 1.94 H), 4.04 (s, 2 H), 6.92 (m, 0.05 H), 7.10 (m, 0.05 H).

Figure 4.28 Structure of **PEMA-Tyr**.

PEMA-Tyr: yield 79%. $^1\text{H NMR}$ (400 MHz, CDCl_3) δ 0.88 (br s, 1.82 H), 1.04 (br s, 1.16 H), 1.26 (br s, 3.10 H), 1.43 (m, 0.21 H), 1.69 – 2.07 (m, 1.72 H), 4.04 (s, 2 H), 6.84 (br s, 0.04 H), 7.11 (br s, 0.04 H).

Figure 4.29 Structure of **PEMA-His(1-Trt)-OtBu**.

PEMA-His(1-Trt)-OtBu: functionalization yield 70%. $^1\text{H NMR}$ (400 MHz, CDCl_3) δ ppm 0.88 (br s, 1.82 H), 1.03 (br s, 1.19 H), 1.25 (br s, 3.56 H), 1.43 (br s, 0.21 H), 1.74 – 2.05 (m, 1.75 H), 4.04 (s, 2 H), 7.11 (br s, 0.21 H), 7.33 (br s, 0.31 H).

4. Materials and methods

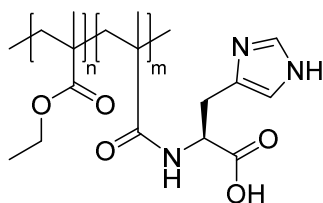


Figure 4.30 Structure of **PEMA-His**.

PEMA-His: yield 82%. $^1\text{H NMR}$ (400 MHz, CDCl_3) δ ppm 0.88 (br s, 1.77 H), 1.04 (br s, 1.25 H), 1.25 (br s, 3.22 H), 1.44 (br s, 0.09 H), 1.75 – 2.01 (m, 2 H), 4.04 (s, 2 H), 7.29 (m, 0.05 H), 7.30 (br s, 0.03 H), 7.31 (br s, 0.02).

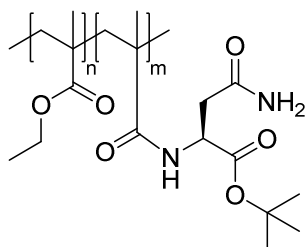


Figure 4.31 Structure of **PEMA-Asn-OtBu**.

PEMA-Asn-OtBu: functionalization yield 72%. $^1\text{H NMR}$ (400 MHz, CDCl_3) δ ppm 0.88 (br s, 1.77 H), 1.03 (br s, 1.15 H), 1.26 (br s, 3.27 H), 1.44 (br s, 0.59 H), 1.63 (br s 0.21 H), 1.77 – 2.05 (m, 1.83 H), 4.03 (s, 2 H).

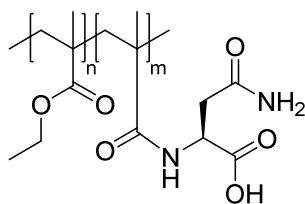
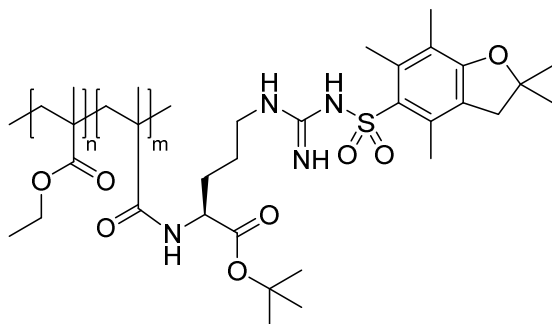
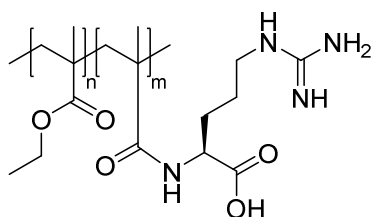


Figure 4.32 Structure of **PEMA-Asn**.

PEMA-Asn: yield 85%. $^1\text{H NMR}$ (400 MHz, CDCl_3) δ ppm 0.88 (br s, 1.79 H), 1.03 (br s, 1.20 H), 1.25 (br s, 3.22 H), 1.43 (br s, 0.26 H), 1.75 – 2.06 (m, 1.78 H), 4.04 (s, 2 H).

Figure 4.33 Structure of **PEMA-Arg(Pbf)-OtBu**.

PEMA-Arg(Pbf)-OtBu: functionalization yield 66%. $^1\text{H NMR}$ (400 MHz, CDCl_3) δ ppm 0.88 (br s, 1.80 H), 1.03 (br s, 1.11 H), 1.26 (br s, 3.36 H), 1.46 (br s, 0.54 H), 1.76 – 2.10 (m, 1.76 H), 4.04 (s, 2 H).

Figure 4.34 Structure of **PEMA-Arg**.

PEMA-Arg: yield 81%. $^1\text{H NMR}$ (400 MHz, CDCl_3) δ 0.88 (br s, 1.88 H), 1.04 (br s, 1.20 H), 1.25 (br s, 3.25 H), 1.43 (m, 0.22 H), 1.70 – 2.08 (m, 1.83 H), 4.04 (s, 2 H).

4.1.1.4. *Dye salts*

Unless otherwise noted, all dye/bulky hydrophobic counterion pairs were synthesised as previously described (Andreiuk et al., 2017a).

R110-C18/F9-Al. **R110-C18/Cl** (1 eq, 3 mg, 0.0048 mmol) and lithium tetrakis(perfluoro-tertbutoxy)aluminate (**F9-Al**) (3 eq, 14 mg, 0.015 mmol) were mixed in 1 mL of dichloromethane. TLC analysis showed instant conversion. The final product was then purified over silica column using DCM/MeOH 9/1 as eluent. Evaporation of solvent yielded 6 mg of product (corresponding to 81% yield). $^1\text{H NMR}$ (400 MHz, CD_3OD) δ ppm 0.88 (3 H, t, $J=7.09$ Hz) 1.05-1.36 (34H, m) 6.79-6.82 (4H, m) 7.05 (2H, d, $J=9.28$ Hz) 7.40 (1H, dd, $J=7.26$ Hz, $J=1.36$ Hz) 7.75-7.89 (2H, m) 8.28 (1H, dd, $J=7.65$ Hz $J=1.36$). $^{19}\text{F NMR}$ (376 MHz, CDCl_3) δ ppm -76.15 (36 F, s). $^{27}\text{Al NMR}$

4. Materials and methods

(130 MHz, CD₃OD) δ ppm 38.2 (1 Al, s). ¹³C NMR (126 MHz, CD₃OD) δ ppm 212.63, 169.46, 163.92, 163.88, 162.23, 137.11, 136.45, 135.48, 134.46, 134.04, 123.10 (q, $J=292.30$ Hz) 120.52, 117.48, 100.97, 69.37, 35.59, 33.29, 33.27, 33.24, 33.22, 33.19, 33.03, 32.99, 23.84, 31.94, 29.55, 26.25, 16.94, 3.28. HRMS (m/z): [M]⁺ calcd. for C₃₈H₅₁N₂O₃ 583.3900; found 583.3911; [M]⁻ calcd. for C₁₆AlF₃₆O₄ 966.9037; found 966.9039.

R110-C18/F12. R110-C18/Cl (1 eq, 3 mg, 0.0048 mmol) and sodium tetrakis[3,5-bis(1,1,1,3,3,3-hexafluoro-2-methoxy-2-propyl)phenyl]borate trihydrate (**F12**) (3 eq, 28 mg, 0.015 mmol) were mixed in 1 mL of dichloromethane. TLC analysis showed instant conversion. The final product was then purified over silica column using DCM/MeOH 9/1 as eluent. Evaporation of solvent yielded 9 mg of product (corresponding to 82% yield). ¹H NMR (400 MHz, CD₃OD) δ ppm 0.86 (3 H, m) 1.12-1.41 (34H, m) 3.30 (24H, s), 6.85-6.60 (4H, m) 7.11 (2H, d, $J=9.27$ Hz), 7.42 (4H, bs) 7.47 (1H, dd, $J=7.37$ Hz, $J=1.42$ Hz), 7.58 (8H, bs), 7.83-7.92 (2H, m) 8.26 (1H, dd, $J=7.63$ Hz $J=1.56$). ¹⁹F NMR (376 MHz, CDCl₃) δ ppm -71.29 (48 F, s). ¹¹B NMR (128 MHz, CD₃OD) δ ppm -5.95 (1 B, s). ¹³C NMR (126 MHz, CD₃OD) δ ppm 212.62, 169.45, 163.92, 163.88, 162.23, 161.39, 137.84, 137.11, 136.45, 135.47, 134.45, 134.03, 126.51, 123.61, 122.23 (q, $J=289$ Hz) 120.52, 117.48, 100.97, 69.36, 35.58, 33.28, 33.27, 33.24, 33.22, 33.18, 33.03, 32.99, 23.84, 31.93, 29.54, 26.24, 16.94, 3.27. HRMS (m/z): [M]⁺ calcd. for C₃₈H₅₁N₂O₃ 583.3900; found 583.3873; [M]⁻ calcd. for C₅₆H₃₆BF₄₈O₈ 1759.1737; found 1759.1770.

R6G-C18/F9-Al. R6G-C18/Cl (1 eq, 3 mg, 0.0043 mmol) and lithium tetrakis(perfluoro-tertbutoxy)aluminate (**F9-Al**) (3 eq, 12 mg, 0.013 mmol) were mixed in 1 mL of dichloromethane. TLC analysis showed instant conversion. The final product was then purified over silica column using DCM/MeOH 95/5 as eluent. Evaporation of solvent yielded 5 mg of product (corresponding to 71% yield). ¹H NMR (400 MHz, CD₃OD) δ ppm 0.88 (3 H, t, $J=6.76$ Hz) 0.99-1.33 (34H, m) 1.37 (6H, t, $J=7.24$ Hz) 2.13 (6H, s) 3.53 (4H, q, $J=7.24$) 3.90 (2H, t, $J=6.20$ Hz) 6.89 (2H, s) 6.94 (2H, s) 7.40 (1H, d, $J=7.01$ Hz) 7.77-7.88 (2H, m) 8.30 (1H, dd, $J=7.67$ Hz $J=1.22$). ¹⁹F NMR (376 MHz, CDCl₃) δ ppm -75.50 (36 F, s). ²⁷Al NMR (130 MHz, CD₃OD) δ ppm 34.0 (1 Al, s). ¹³C NMR (126 MHz, CD₃OD) δ ppm 165.67, 158.02, 157.57, 156.35, 133.32, 132.53, 130.91, 130.63, 130.16, 130.05, 128.69, 122.16 (q, $J=293$ Hz) 113.43, 93.46, 65.30, 38.07, 31.66, 29.35, 29.34, 29.32, 29.28, 29.10, 29.05, 28.86, 27.96, 25.54, 22.31, 16.14, 13.01, 12.65. HRMS (m/z): [M]⁺

calcd. for $C_{44}H_{63}N_2O_3$ 667.4839; found 667.4828; $[M]^-$ calcd. for $C_{16}AlF_{36}O_4$ 966.9037; found 966.9062.

R6G-C18/F12. R6G-C18/Cl (1 eq, 3 mg, 0.0043 mmol) and sodium tetrakis[3,5-bis(1,1,1,3,3,3-hexafluoro-2-methoxy-2-propyl)phenyl]borate trihydrate (**F12**) (3 eq, 24 mg, 0.013 mmol) were mixed in 1 mL of dichloromethane. TLC analysis showed instant conversion. The final product was then purified over silica column using DCM/MeOH 95/5 as eluent. Evaporation of solvent yielded 9 mg of product (corresponding to 88% yield). 1H NMR (400 MHz, CD_3OD) δ ppm 0.65 (3 H, t, $J=6.84$ Hz) 1.07-1.40 (34H, m) 1.43 (6H, t, $J=7.20$ Hz) 2.20 (6H, s) 3.30 (24H, s) 3.60 (4H, q, $J=7.20$) 3.96 (2H, t, $J=6.20$ Hz) 6.95 (2H, s) 7.00 (2H, s) 7.42 (4H, bs) 7.45 (1H, dd, $J=7.45$ Hz $J=1.37$ Hz) 7.58 (8H, bs) 7.84-7.94 (2H, m) 8.36 (1H, dd, $J=7.60$ Hz $J=1.37$). ^{19}F NMR (376 MHz, $CDCl_3$) δ ppm -71.35. (48 F, s). ^{11}B NMR (128 MHz, CD_3OD) δ ppm -5.95 (1 B, s). ^{13}C NMR (126 MHz, CD_3OD) δ ppm 165.67, 162.59, 161.39, 158.02, 157.58, 156.36, 136.93, 133.32, 132.54, 130.92, 130.64, 130.16, 130.05, 128.70, 125.56, 125.20, 122.70, 122.54 (q, $J=288.18$ Hz) 113.43, 93.46, 83.29 (sept., $J=28.5$ Hz) 65.30, 52.84, 38.07, 31.66, 29.36, 29.33, 29.29, 29.10, 29.05, 28.87, 27.97, 25.54, 22.32, 16.15, 13.01, 12.66. HRMS (m/z): $[M]^+$ calcd. for $C_{44}H_{63}N_2O_3$ 667.4839; found 667.4818; $[M]^-$ calcd. for $C_{56}H_{36}BF_{48}O_8$ 1759.1737; found 1759.1781.

4.1.1.5. Clickable PEG derivatives

PEG12-DBCO, **PEG2000-DBCO** and **PEG3-DBCO** were synthesized by Dr. Nina Melnychuk.

APBA-PEG2000-DBCO was synthesized by Dr. Pichandi Ashokkumar according to a previously described procedure (Bandyopadhyay et al., 2015).

CBT-PEG2000-DBCO: Lys⁸-CBT was synthesized by Dr. Julie Karpenko according to a previously described procedure (Karpenko et al., 2014).

4. Materials and methods

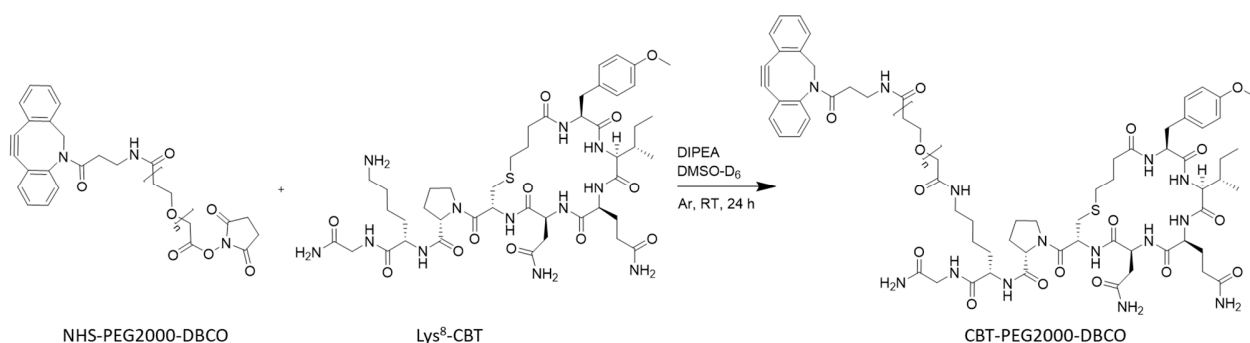


Figure 4.35 Synthesis scheme of CBT-PEG2000-DBCO.

NHS-PEG2000-DBCO (1 eq., 50 mg, 0.020 mmol) and **Lys⁸-CBT** (1 eq., 21 mg, 0.020 mmol) were added to 1 mL of DMSO-D₆, DIPEA (10 eq, 0.2 mmol, 40 μ L) was added and the system was left stirring under argon for 24 h, the product was then purified *via* HPLC and analyzed *via* MALDI-TOF MS.

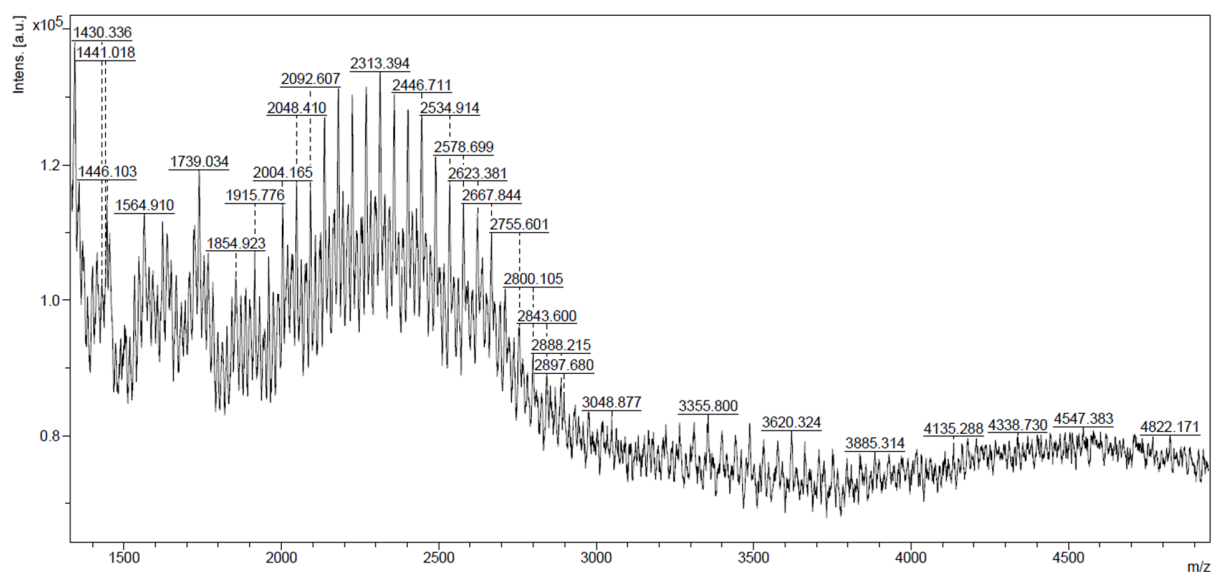


Figure 4.36 MALDI/TOF MS of CBT-PEG2000-DBCO

4.1.2. Oligonucleotides

Single stranded lyophilized DNA sequences were purchased from IBA, then dissolved in MilliQ water and stored at -20 °C. The sequences used in this work are the following.

SurC-DBCO: 5'-CCC AGC CTT CCA GCT CCT TGA-(DBCO)-3'

T20-DBCO: 5'-TTT TTT TTT TTT TTT TTT TT-(DBCO)-3'

TCS-ATTO647N: 5'-(ATTO647N)- TCA AGG AGC TGG-3'

Target: 5'-CAA GGA GCT GGA AGG CTG GG-3'

A20-Biotin: 5'-(Biotin)-AAA AAA AAA AAA AAA AAA AA-3

4.2. *Methods*

4.2.1. *Nanoparticles preparation*

ACN stock solution containing the polymer (at a concentration of 2 g/L) and the dye/counterion pair (at varying concentrations) were prepared. This organic stock was quickly diluted in a ten-fold excess of phosphate buffer (20 mM, pH = 7.4) under shaking. Afterwards, to lower the ACN content of the NPs solution, the as-prepared NPs suspension was either diluted another five times in the same buffer or the ACN was gently evaporated under vacuum.

For the preparation of NPs to be functionalized with carbetocin-PEG2000-DBCO, the ACN stock solution was nanoprecipitated in a ten-fold excess of NaOH 1 mM, followed by a second dilution in a five-fold excess of phosphate buffer 2 mM (pH = 7.4).

4.2.1.1. *DNA nanoprobe preparation*

FRET-based DNA nanoprobe were prepared according to a previously described procedure (Melnychuk and Klymchenko, 2018). Briefly, SurC-DBCO (at concentrations ranging from 0.5 μ M to 3 μ M) and T20-DBCO (at concentrations ranging from 20 μ M to 21.5 μ M) were added to a freshly prepared azide-bearing nanoparticles solution. The mixture was kept for 20 h at 40 °C without any stirring and protected from light. The mixture was then allowed to cool at room temperature. Annealing with TCS-ATTO647N was performed by adding the flare (at the same concentration of SurC-DBCO) to the DNA-nanoparticle mixture, then heating to 70 °C for 3 minutes. The mixture was cooled down at room temperature again and kept in the dark for 1 h. Purification from unreacted DNA strands was performed by diluting the mixture with 20 mM phosphate buffer containing 12 mM MgCl₂ and 30 mM NaCl, then centrifuging using centrifuge filter (Amicon, 0.5 mL, 100 kDa) at 1000 G for 2 min. The ultra-filtration was repeated 5 times. The as-prepared DNA probes were then stored at 4 °C in the dark.

4. Materials and methods

4.2.1.1.1. *Detection of survivin oligonucleotide target*

Detection in solution was performed by diluting the DNA probe in 20 mM phosphate buffer containing 30 mM NaCl and 12 mM MgCl₂ to a concentration of 10 pM (corresponding to TCS-ATTO647N) and an aliquot of survivin oligonucleotide target was added. The solution was then incubated in the dark at 25 °C for 6 h. Detection of the target on a glass surface was done by adding the target oligonucleotide to the LabTek chamber containing the immobilized DNA probes; the system was then kept in the dark at room temperature when the incubation time was 3 h.

4.2.1.2. *Nanoparticle surface functionalization via Cu-free click chemistry*

4.2.1.2.1. *Synthesis of PEGylated and APBA-bearing nanoparticles*

To a freshly prepared suspension of azide-bearing nanoparticles 23 μM of clickable PEG or 21.5 of PEG2000-DBCO plus 2.5 APBA-PEG2000-DBCO were added and the system was kept at for 6 h at 40 °C without any stirring and protected from light. The mixture was then cooled to room temperature and purified *via* size exclusion chromatography using PD-10 desalting columns.

4.2.1.2.2. *Synthesis of carbetocin-bearing nanoparticles*

A freshly prepared suspension of azide-bearing nanoparticles was dialyzed overnight in presence of 1 mM of cyclodextrin, then the suspension was purified from the cyclodextrin *via* size exclusion. Then 50 μM of PEG2000-DBCO or 45 μM of PEG2000-DBCO plus 5 μM of carbetocin-PEG2000-DBCO were added, and the system was kept at for 6 h at 40 °C without any stirring and protected from light. The mixture was then cooled at room temperature and purified *via* size exclusion chromatography using PD-10 desalting columns. Then TWEEN20 was added to the NPs suspension at a concentration of 0.1%.

4.2.2. *Nanoparticles characterization*

Nanoparticle size was determined *via* DLS on a Zetasizer Nano ZSP DTS 1060 (Malvern Instruments S.A.). The instrument is equipped with a laser source at 633 nm, therefore the size analysis of samples emitting and absorbing at this wavelength is not possible. For size analysis the mean value of the size distribution per volume was taken. Three independent measurements were averaged and their standard deviation used as error.

For the spectroscopic characterization spectroscopic grade solvents and MilliQ water were used. Absorption spectra were recorded on a Cary-4000 scan UV-visible spectrophotometer (Agilent Technologies). Excitation and emission spectra were recorded on a Spectrofluorometer FS5 (Edinburgh Instruments), the fluorescence spectra were corrected both for lamp fluctuations and detector response. Fluorescence quantum yields of dye-loaded NPs were measured taking care that both samples and standard had an absorbance <0.1 at the excitation wavelength. Standard used were: quinine sulfate for Eu-complexes NPs (QY = 0.52 in H_2SO_4 0.05 M), fluorescein for R110-C18 NPs (QY = 0.91 in NaOH 0.1 M), rhodamine 6G for R6G-C18 NPs (QY = 0.94 in EtOH),

4. Materials and methods

rhodamine 101 for R18 NPs (QY = 1.0 in MeOH), and Nile blue (QY = 0.27 in EtOH) for DiD NPs (Brouwer, 2011).

FRET efficiency was evaluated as the semiempirical FRET ratio:

$$E_{FRET} = \frac{A}{A + D}$$

Where D is the donor intensity at the maximum and A is the acceptor intensity.

Antenna effect (AE), which represents the amplification of the acceptor fluorescence as a result of FRET between few acceptors and many donors, was calculated as the ratio between the excitation intensity at the maximum of the donor and the excitation intensity at the maximum of the acceptor, correcting it by the emission of the donor dyes at the emission wavelength at which the excitation spectrum was recorded (Trofymchuk et al., 2017):

$$AE = \frac{I_{D-FRET}^{ex} - I_D^{ex} * \frac{I_{D-FRET}^{em}}{I_D^{em}}}{I_{A-FRET}^{ex} - I_A^{ex}}$$

Where I_{D-FRET}^{ex} and I_{A-FRET}^{ex} are the excitation intensity of donor and acceptor at their respective maxima. I_D^{ex} and I_A^{ex} are the excitation intensities at the maximum wavelengths of donor and acceptor in the sample without acceptor. I_{D-FRET}^{em} and I_D^{em} are the maximum emission intensities of the donor in the samples with and without acceptor.

4.2.3. Fluorescence microscopy

Single-particle measurements were performed with a Nikon Ti-E inverted microscope with a 60x objective (Apo TIRF, oil, NA 1.49, Nikon) in the epifluorescence mode. Excitation source was provided either by a laser (Oxxius) or a light-emitting diode (SpectraX, Lumencor). For monochrome imaging, the fluorescence signal was recorded with Hamamatsu Orca Flash 4 camera. Simultaneous two channel-detection was performed using an W-VIEW GEMINI image splitting system (Hamamatsu) equipped with dichroic 640 nm (Semrock FF640-FDi01-25x36). For RGB microscopy imaging the signal was recorded with a Nikon DS-Fi3 camera. For cellphone imaging, an iPhone SE 2016 paired with an app (Halide, developed by Ben Sandowsky) able to acquire RAW images and control the image acquisition parameters were employed. Images were recorded with a shutter exposure of 1/3 of a second and an ISO of 2000.

4.2.3.1. *Immobilization protocols*

Immobilization of samples with DNA. For the results discussed in section 2.1, the DNA nanoprobes were immobilized according to an already published protocol (Schmied et al., 2014). The LabTek chamber was washed three times with PBS, then, it was incubated for 10 minutes with a solution of BSA-biotin (0.5 g/L in PBS). The BSA solution was removed and the surface washed three times with PBS, then, incubated for another 10 minutes with neutravidin (0.5 g/L in PBS). After removing the neutravidin solution and washing again three times with PBS a solution of A20-biotin (1 μ M in PBS) was deposited on the glass surface for another 10 minutes. Afterwards the system was washed three times with phosphate buffer (20 mM, pH = 7.4 containing 12 mM MgCl₂ 30 mM and NaCl). Lastly, the NPs solution at a concentration of approximately 100 pM was incubated for 15 minutes. The glass surface was then washed two other times with phosphate buffer (20 mM, pH = 7.4 containing 12 mM MgCl₂ 30 mM and NaCl), and measurements were performed with a layer of the same buffer above the particles.

Immobilization of samples with PEI. For the results discussed in section 2.2, NPs were immobilized on a glass surface (LabTek 8-well plate) following a previously described procedure (Reisch et al., 2014). The glass surface was first treated by incubating a solution of KOH 1M for 15 minutes, then the chamber was thoroughly rinsed and incubated with a solution of polyethylenimine (PEI, 1 g/L in TRIS 10 mM) for 30 minutes. Lastly, after rinsing the system again, NPs at a concentration of approximately 100 pM were incubated on the PEI-covered glass for 15 minutes. After washing the surface yet another time, the NPs were imaged with a layer of MilliQ water on top.

Immobilization of samples with PB. For the results discussed in section 2.4, the LabTek chamber was washed three times with MilliQ water, then NPs were diluted in phosphate buffer (20 mM, pH = 7.4) at a concentration of approximately 100 pM and incubated on the glass surface for 5 minutes. The chamber was then washed three times with phosphate buffer and measurements were performed with a layer of the same buffer above the NPs.

4.2.3.2. *Data treatment of microscopy images*

For the results discussed in section 2.1, the acquired images were treated with an ImageJ plugin (developed by Dr. Romain Vauchelles). The plugin makes the ratio between the red and the green channels of the image. A new false-color image, coding the calculated ratios, is generated.

4. Materials and methods

Each pixel color corresponding to the red/green ratio of the original image, while its intensity corresponds to the integral intensity recorded for both channels in the original image. Alongside the pseudo-color image, a red/green ratio histogram is generated as well.

For the results discussed in section 2.2, an image projection (average intensity) of the first 10 frames was generated and the background subtracted. Then particles were detected using a FIJI routine which measures the mean intensity of the circular regions of interest with a diameter of 6 pixels around the found intensity maxima. Then the intensity in the circular regions of interest was integrated over the first 5 frames and it was used to generate the particle emission intensity histograms.

4.2.4. *Transmission electron microscopy*

5 μL of NPs suspension were deposited on carbon-coated copper-rhodium TEM grids previously treated via amylamine glow-discharge. The prepared grids were imaged using a Tecnai F20 Twin transmission electron microscope (FEI Eindhoven Holland) operating at 200 kV. Images of areas of interest were acquired with a US1000 camera (Gatan). Image analysis was performed in FIJI.

4.2.5. *Cellular studies*

4.2.5.1. *Cell culture*

HeLa cells were cultured in DMEM (Gibco-Invitrogen) supplemented with 10% FBS (Lonza), 5% L-glutamine (Gibco-Invitrogen) and 1% antibiotic solution (penicillin-streptomycin, Gibco-Invitrogen) at 37 °C in a humidified atmosphere containing 5% of CO₂.

4.2.5.2. *Apoptosis protocol*

Apoptosis was induced with 1 μM Staurosporine for 2 h at 37 °C, the cells were then washed with PBS and annexin-binding buffer (10 mM HEPES, 140 mM NaCl, and 2.5 mM CaCl₂, pH 7.4) containing 5 μL of Annexin V Alexa Fluor 488 conjugate. The cells were then incubated at room temperature for 15 min and washed again twice with PBS.

4.2.5.3. *Cytotoxicity assays*

Cytotoxicity assays were performed by seeding HeLa cells in 96-well plates with a concentration of ~10k cells/well in 100 μL of the DMEM growth medium. Cells were then left to

adhere overnight. Then the growth medium was removed and substituted with the same medium but with different concentration of nanoparticles in suspension. Cells were incubated in presence of polymeric NPs for 24 hours, then the medium was removed and the wells washed with PBS. The cells were incubated with fresh medium containing MTT 3-(4,5-dimethylthiazol-2-yl)-2,5-diphenyltetrazolium bromide) 0.5 g/L for 4 hours. Lastly, the formazan crystals were solubilized by adding 100 μ L of DMSO per well and shaking gently for 10 minutes. The absorbance at 570 nm was read with a microplate reader. Experiments were carried out in triplicates, viability of the cells expressed as a percentage in respect to the control group.

4.2.5.4. *Flow cytometry*

Cells were detached using Accutase. The cell pellet was then washed with PBS and cells were analyzed with MACSQuant® VYB flow cytometer. Alexa Flour 488 was excited with a laser at 488 nm and fluorescence signal was collected in the interval 525/50 nm. R18 was instead excited with a laser at 561 nm and the signal was collected in the interval 615/20 nm.

4.2.5.5. *Fluorescence microscopy on cells*

Cells were seeded in a μ -dish (glass bottom, 35 mm, IBDi) at a density of 100k cells per well 24 h before the microscopy measurement.

4.2.5.5.1. *Incubation of PEGylated and PBA-bearing nanoparticles*

Cells were washed with Opti-MEM and a freshly prepared suspension of NPs (with a concentration of 0.004 g/L) in Opti-MEM was added to the cells and incubated for 30 min at room temperature. Finally, cells were washed again three times with Opti-MEM and imaged.

4.2.5.5.2. *Incubation of carbetocin-bearing nanoparticles*

Cells were washed with Opti-MEM and a freshly prepared suspension of NPs (with a concentration of 0.004 g/L) in Opti-MEM was added to the cells and incubated for 4 h at 37 °C. Then cells were imaged.

4.2.5.5.3. *Incubation of lanthanide-loaded nanoparticles*

For imaging the culture medium was removed and the cells were washed with Opti-MEM (Gibco-Invitrogen). Cells were stained with Hoechst stain with a concentration of 5 μ g/mL for 15 min at 37 °C Then cells were washed again with Opti-MEM and a freshly prepared suspension of

4. Materials and methods

NPs (with a concentration of 0.004 g/L) in Opti-MEM was added to the cells and incubated for 3 h at 37 °C. Finally, cells were washed again three times with Opti-MEM and imaged.

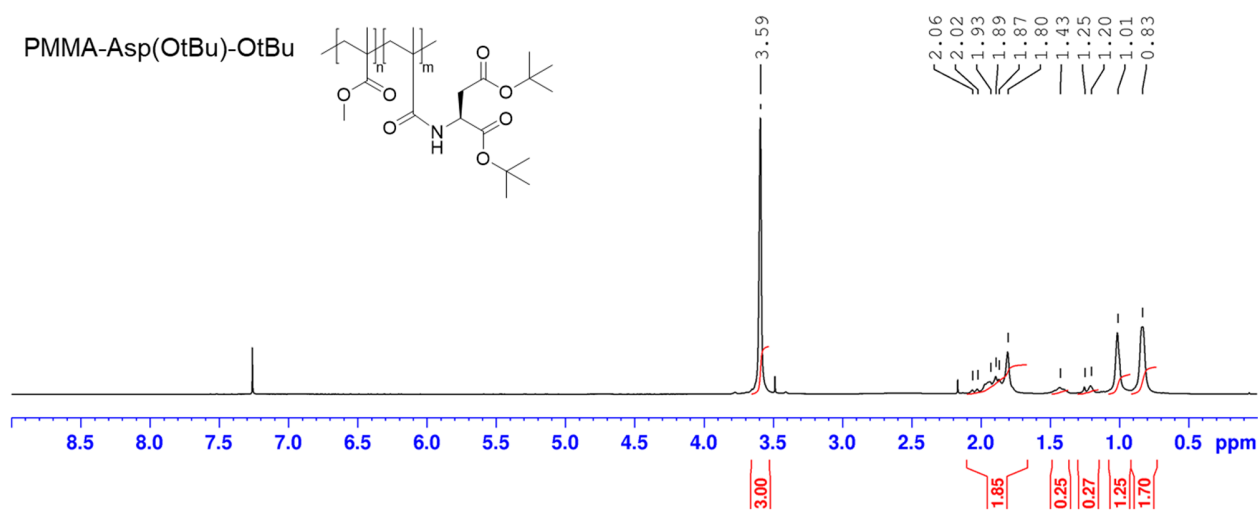
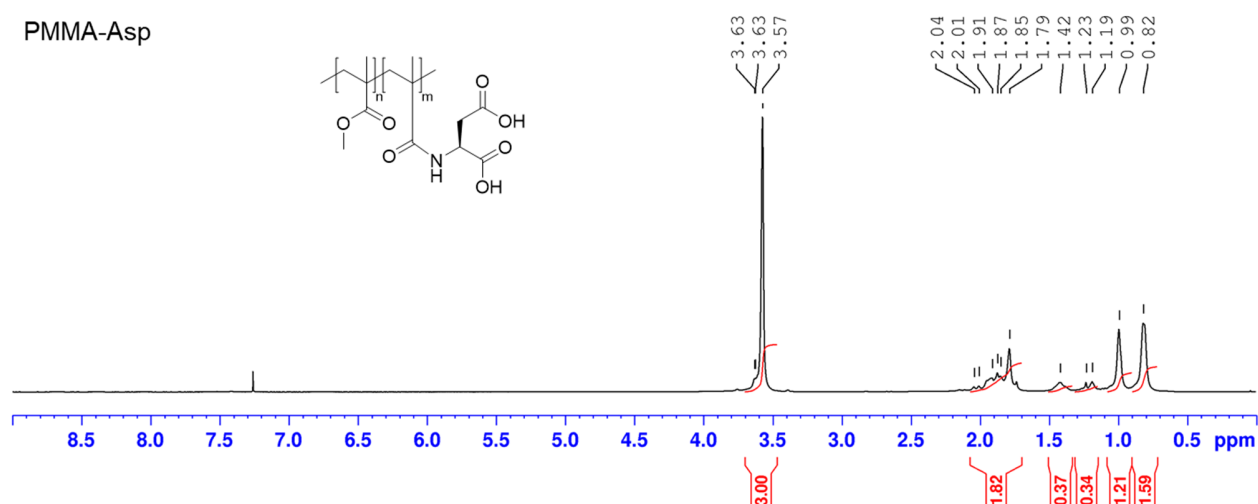
4.2.6. *Calculation of limit of detection (LOD) and limit of quantification (LOQ)*

LOD and LOQ were calculated by performing a linear fit on data points and then using the following equations (“Recommendations for the definition, estimation and use of the detection limit,” 1987):

$$LOD = 3 \cdot \frac{\sigma_B}{S}, LOQ = 10 \cdot \frac{\sigma_B}{S}$$

Where σ_B is the standard error of the intercept of the linear regression (corresponding to the noise of the blank) and S is the slope of the linear regression (corresponding to the sensitivity of the method).

4.3. NMR spectra

Figure 4.37 ^1H NMR spectrum of PMMA-Asp(OtBu)-OtBu in CDCl_3 Figure 4.38 ^1H NMR spectrum of PMMA-Asp in CDCl_3

4. Materials and methods

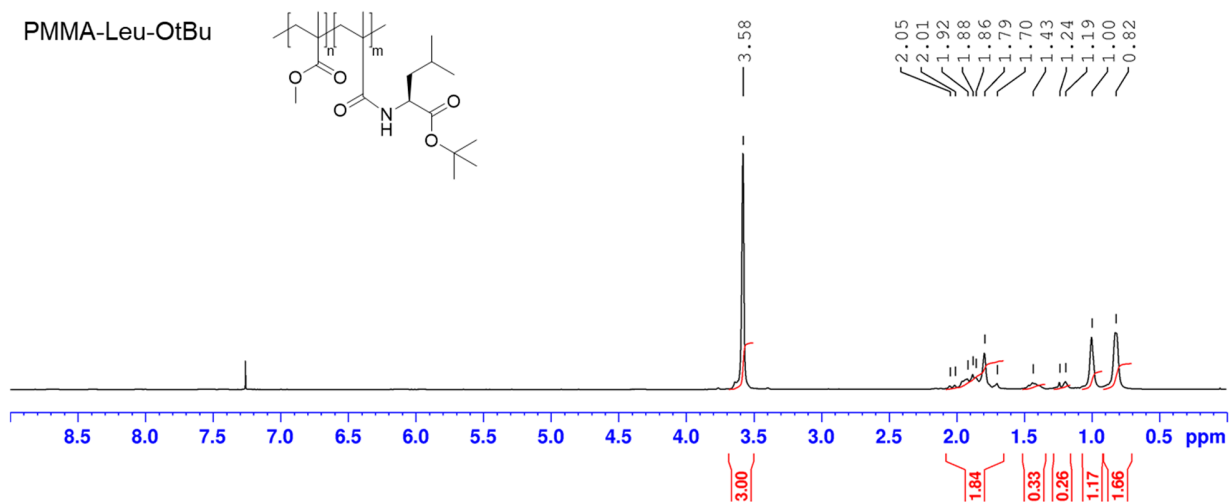


Figure 4.39 ^1H NMR spectrum of **PMMA-Leu-OtBu** in CDCl_3

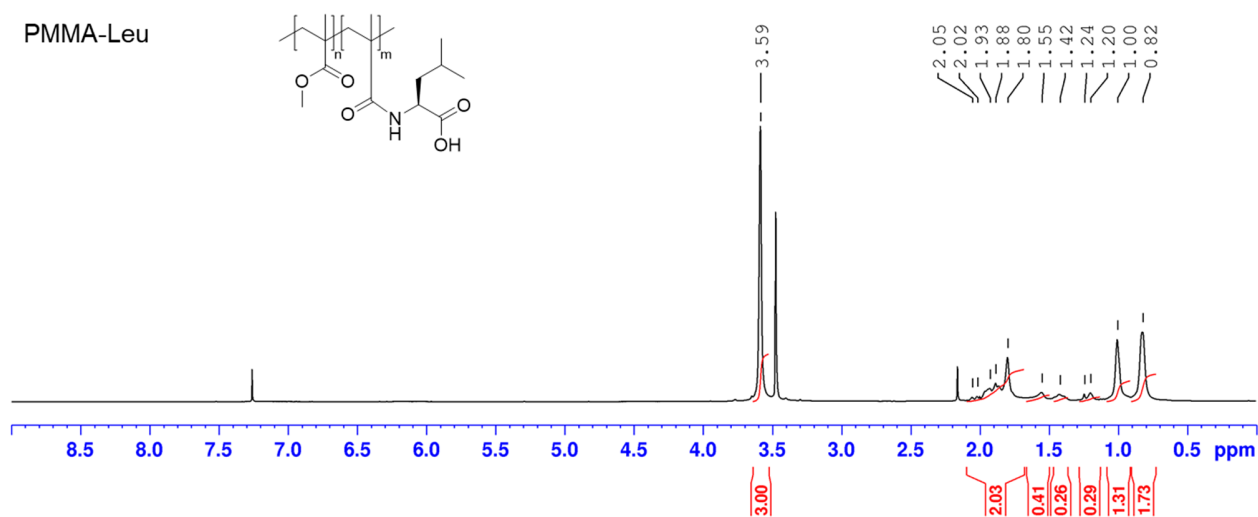


Figure 4.40 ^1H NMR spectrum of **PMMA-Leu** in CDCl_3

4.3. NMR spectra

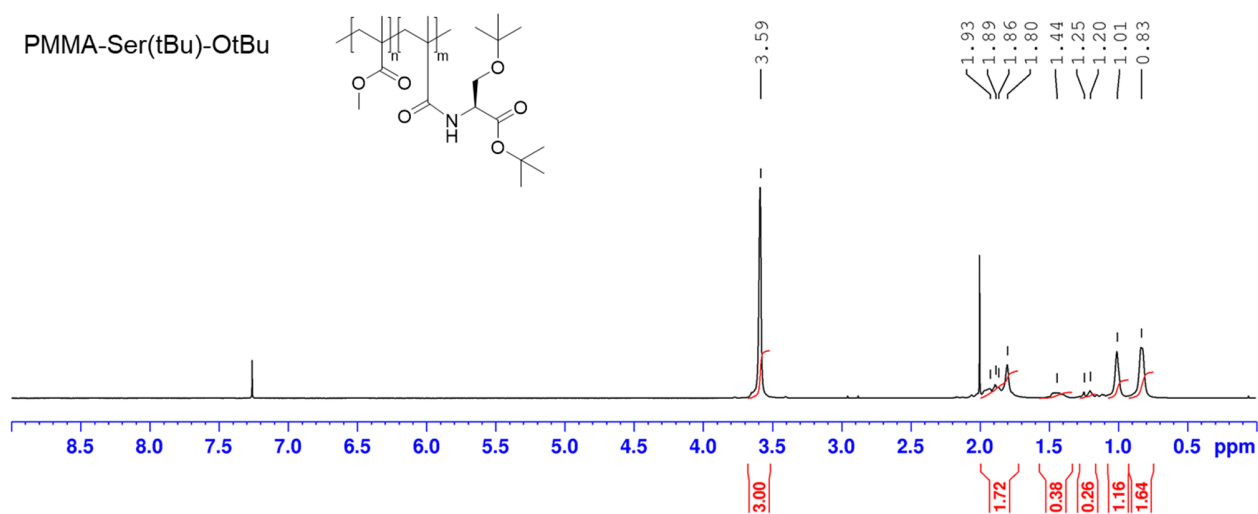


Figure 4.41 ^1H NMR spectrum of **PMMA-Ser(tBu)-OtBu** in CDCl_3

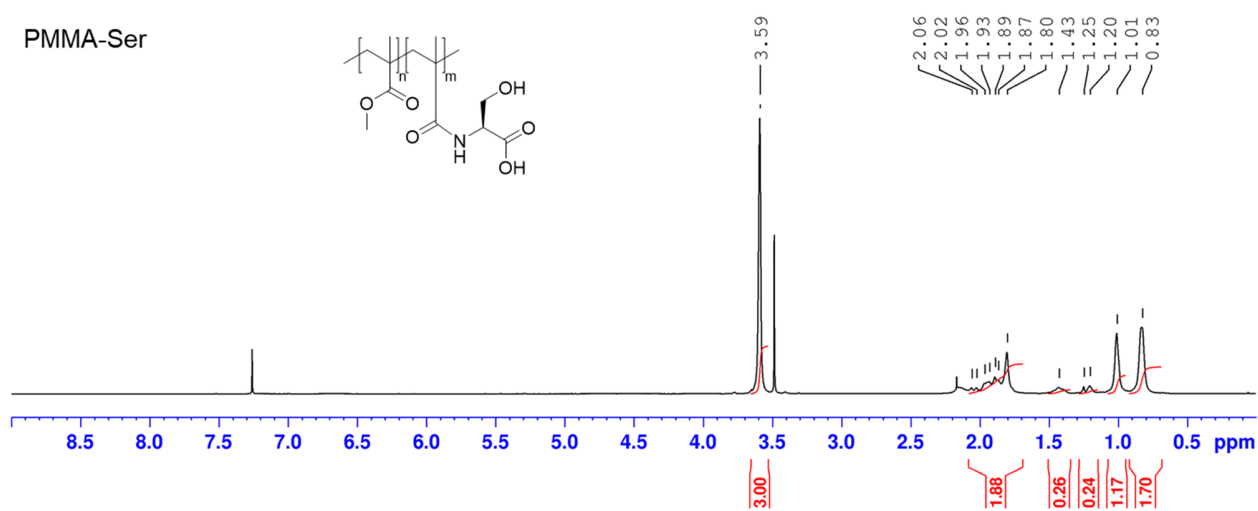


Figure 4.42 ^1H NMR spectrum of **PMMA-Ser** in CDCl_3

4. Materials and methods

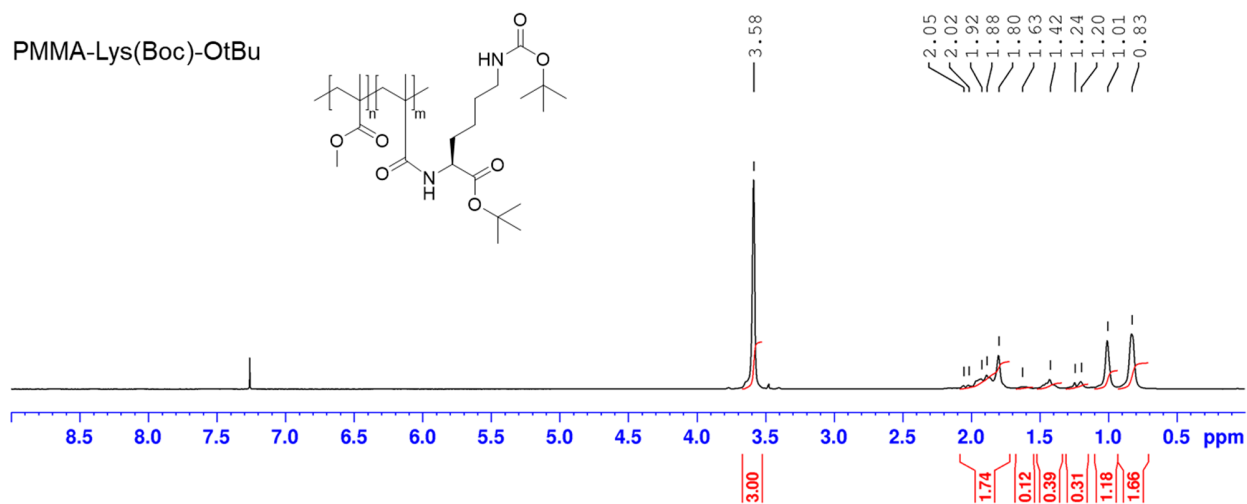


Figure 4.43 ^1H NMR spectrum of **PMMA-Lys(Boc)-OtBu** in CDCl_3

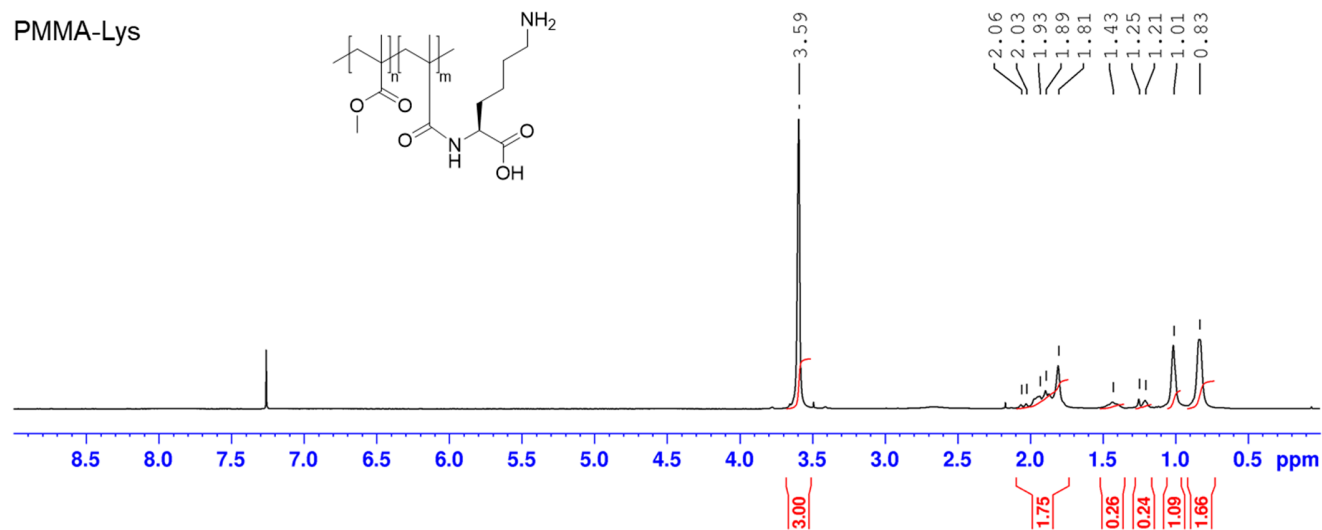


Figure 4.44 ^1H NMR spectrum of **PMMA-Lys** in CDCl_3

4.3. NMR spectra

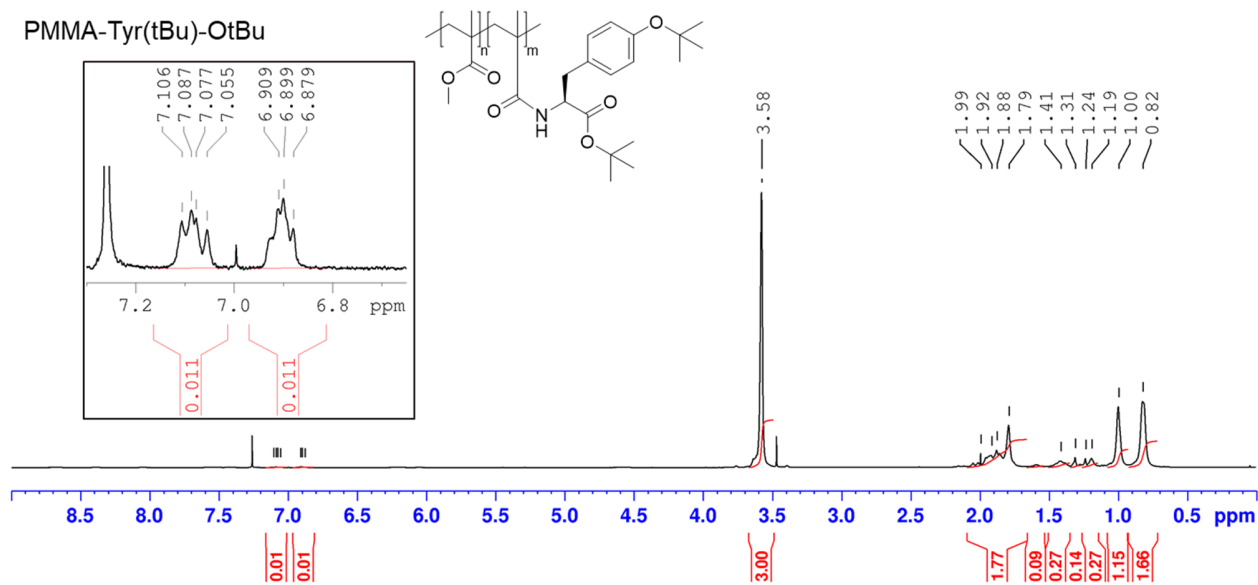


Figure 4.45 ^1H NMR spectrum of **PMMA-Tyr(tBu)-OtBu** in CDCl_3

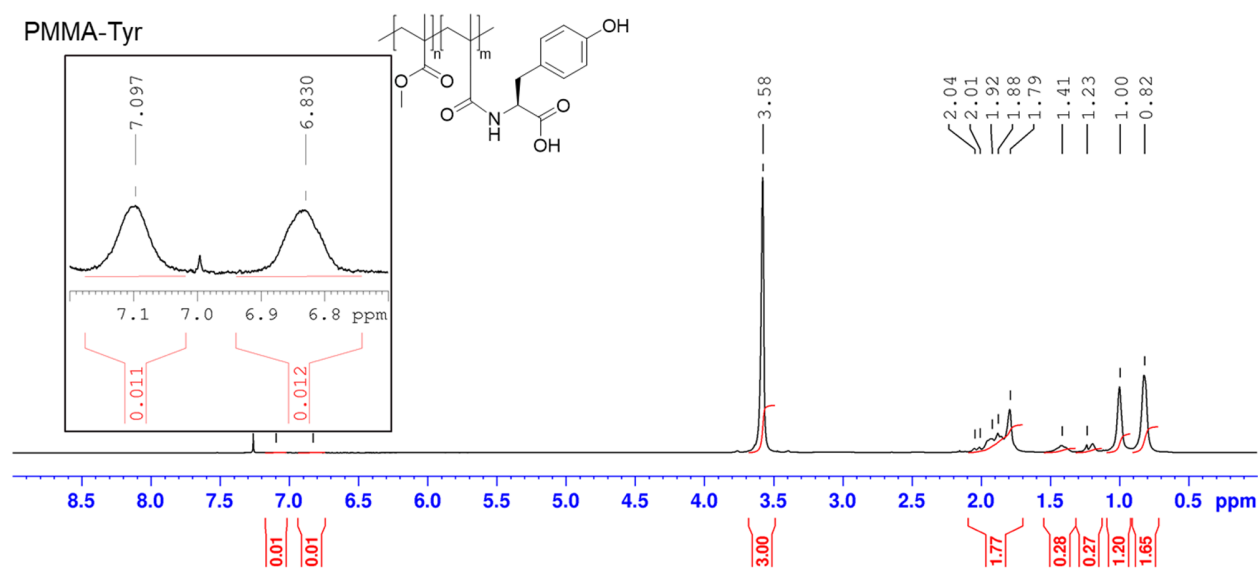


Figure 4.46 ^1H NMR spectrum of **PMMA-Tyr** in CDCl_3

4. Materials and methods

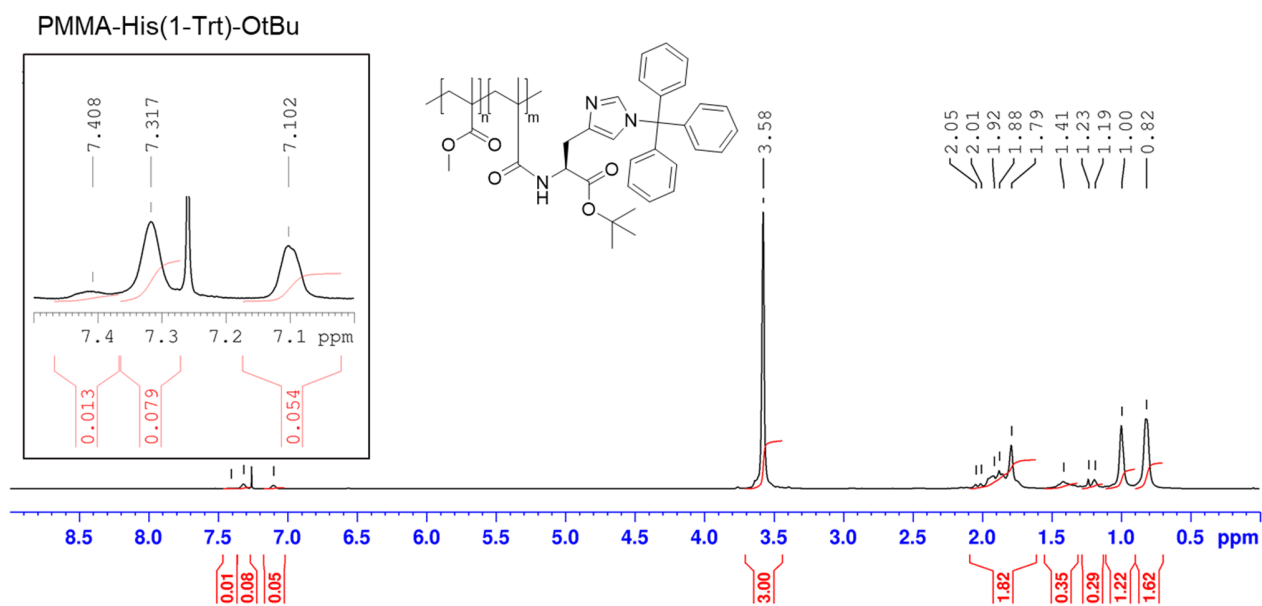


Figure 4.47 ^1H NMR spectrum of **PMMA-His(1-Trt)-OtBu** in CDCl_3

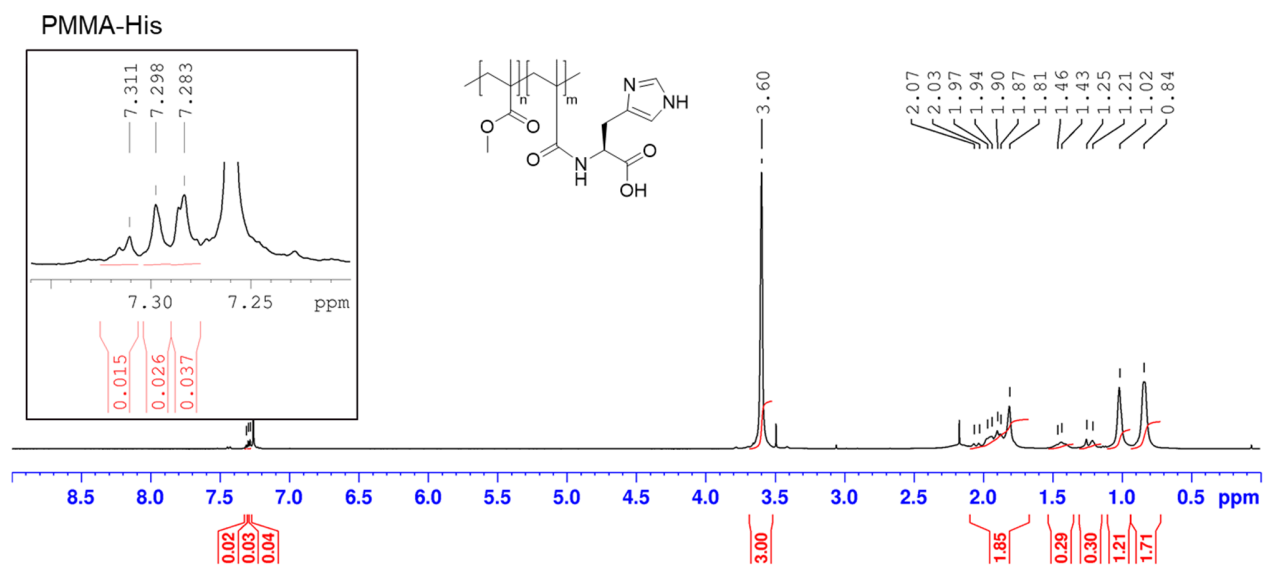


Figure 4.48 ^1H NMR spectrum of **PMMA-His** in CDCl_3

4.3. NMR spectra

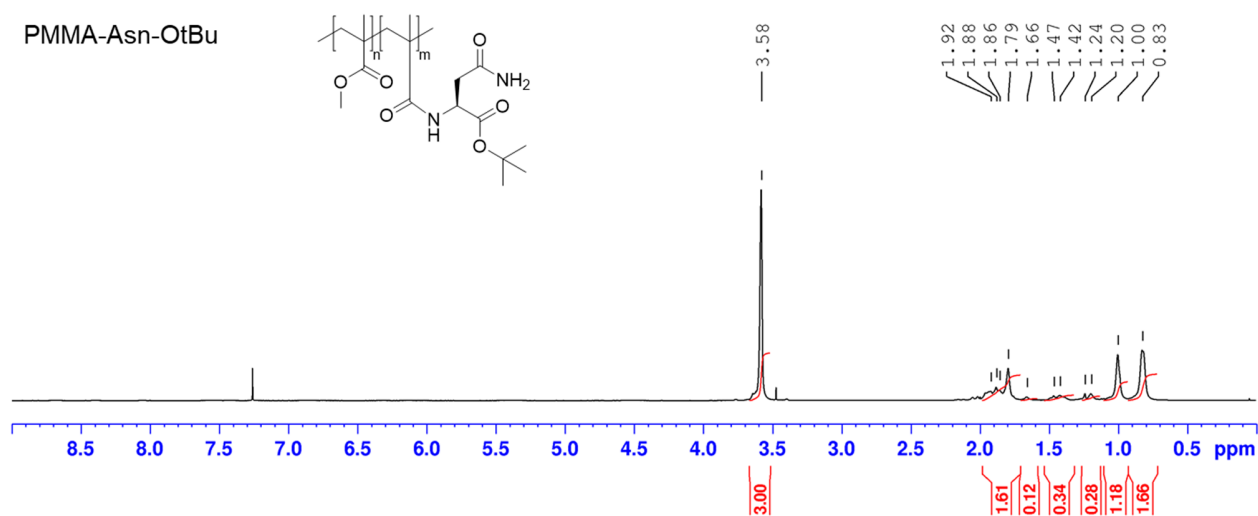


Figure 4.49 ^1H NMR spectrum of **PMMA-Asn-OtBu** in CDCl_3

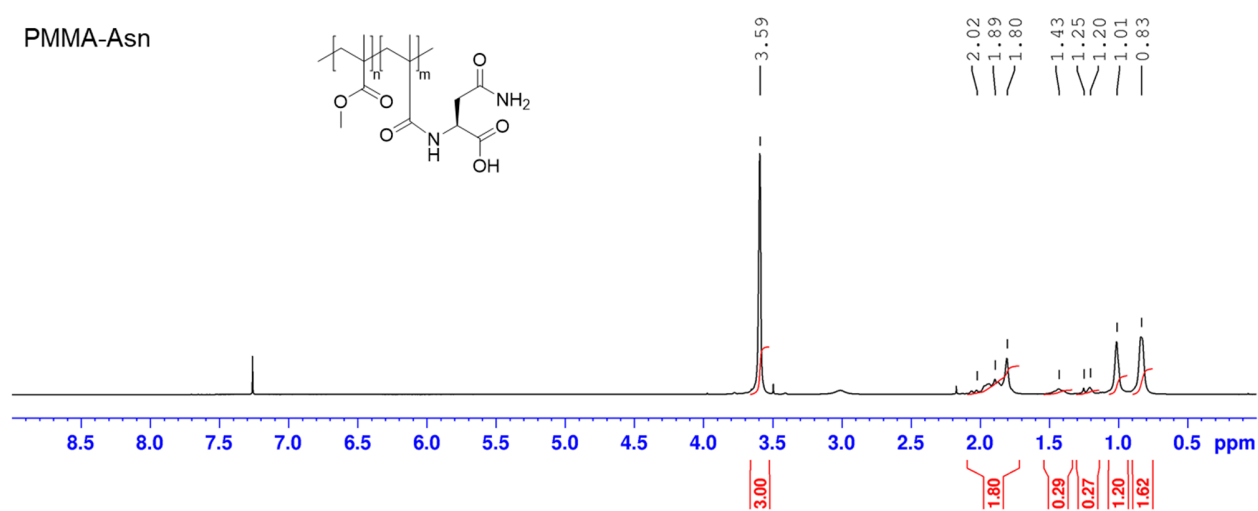


Figure 4.50 ^1H NMR spectrum of **PMMA-Asn** in CDCl_3

4. Materials and methods

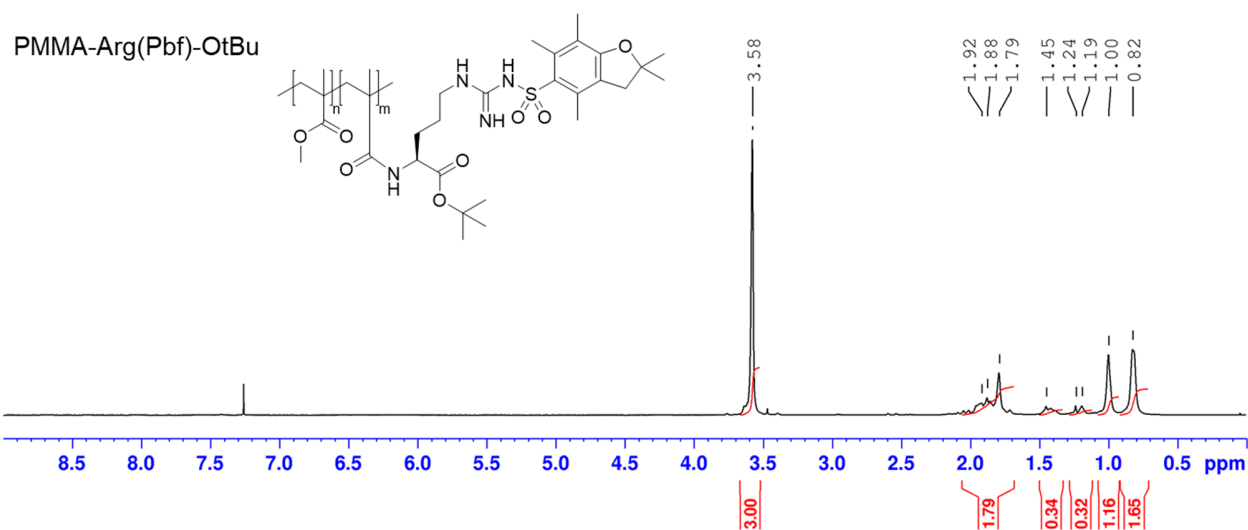


Figure 4.51 ^1H NMR spectrum of **PMMA-Arg(Pbf)-OtBu** in CDCl_3

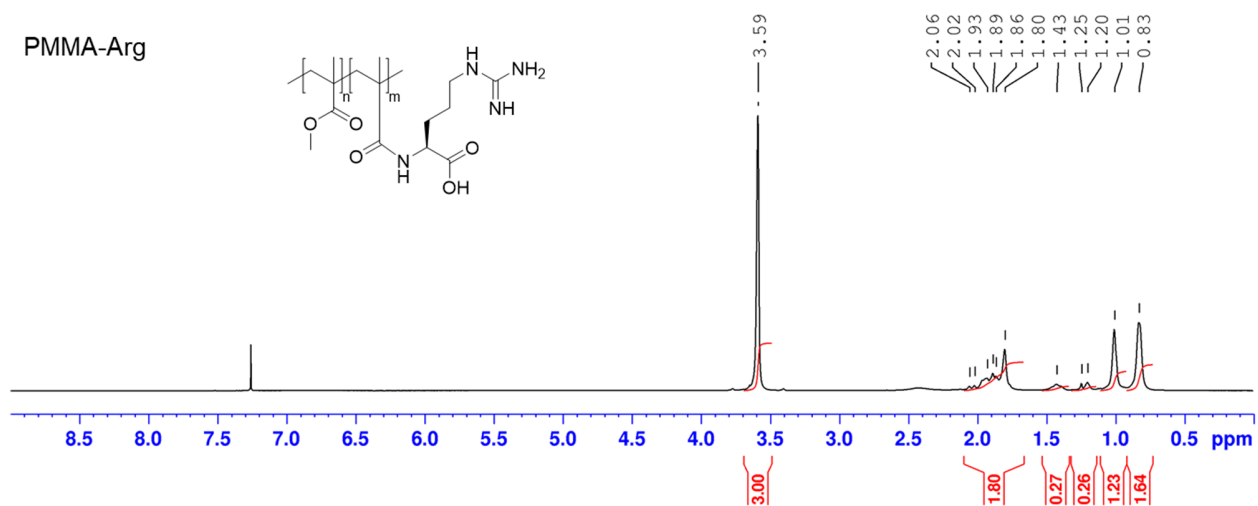


Figure 4.52 ^1H NMR spectrum of **PMMA-Arg** in CDCl_3

4.3. NMR spectra

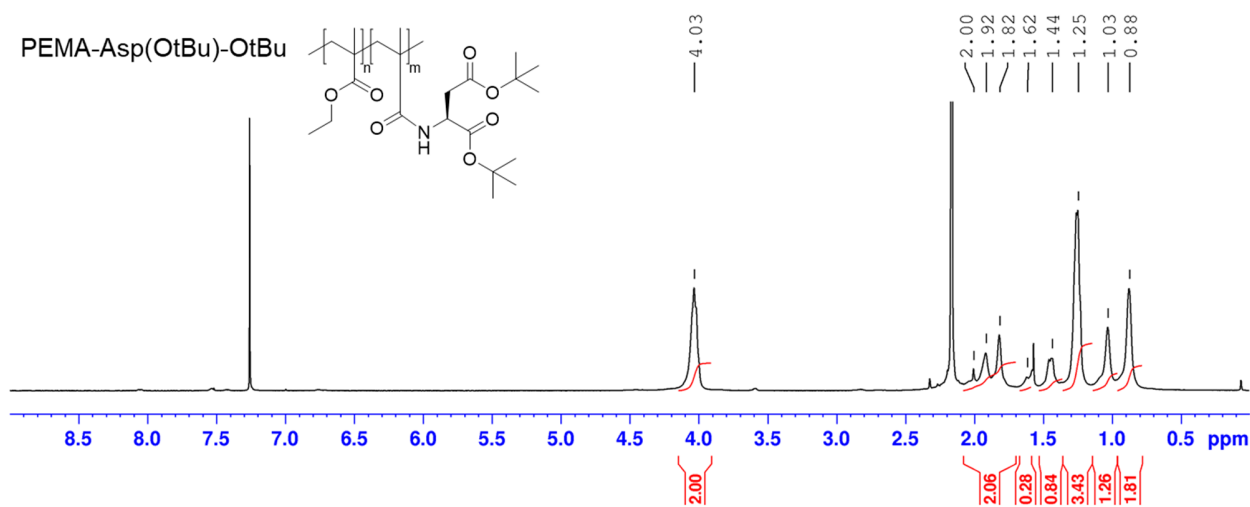


Figure 4.53 ^1H NMR spectrum of **PEMA-Asp(OtBu)-OtBu** in CDCl_3

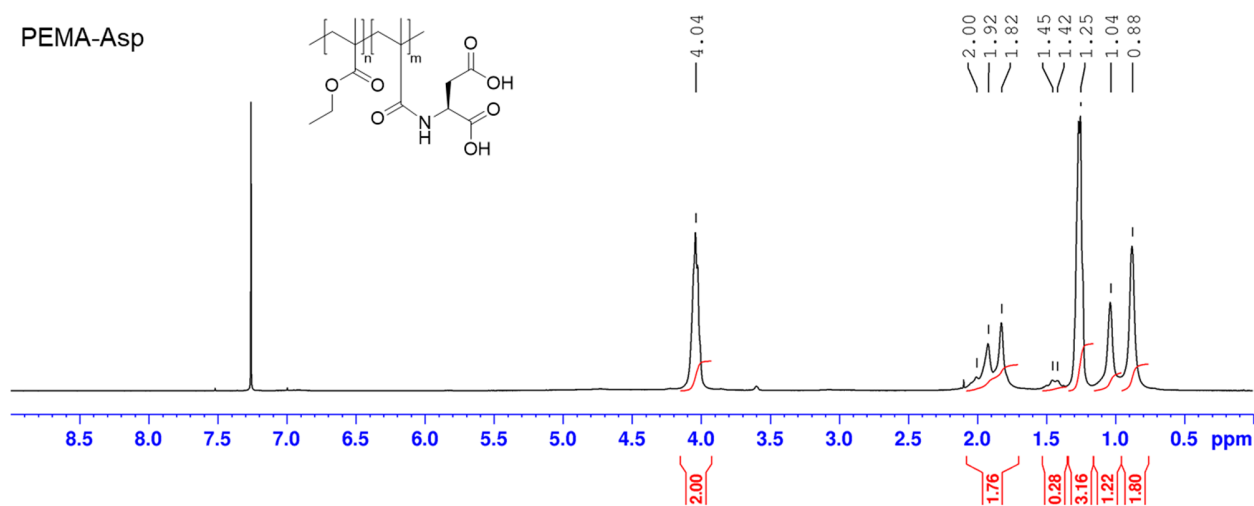


Figure 4.54 ^1H NMR spectrum of **PEMA-Asp** in CDCl_3

4. Materials and methods

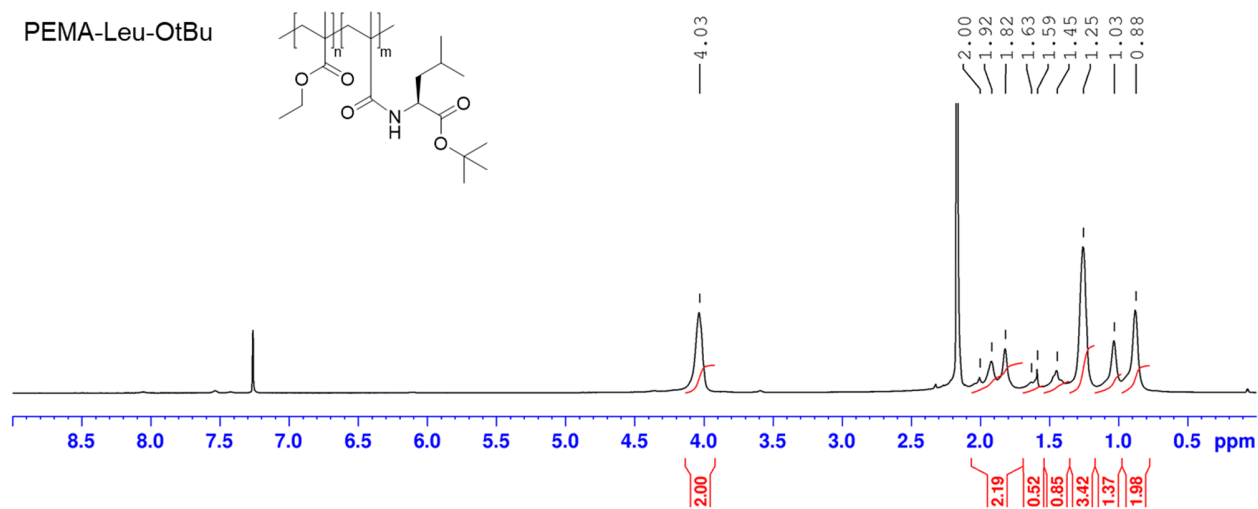


Figure 4.55 ^1H NMR spectrum of **PEMA-Leu-OtBu** in CDCl_3

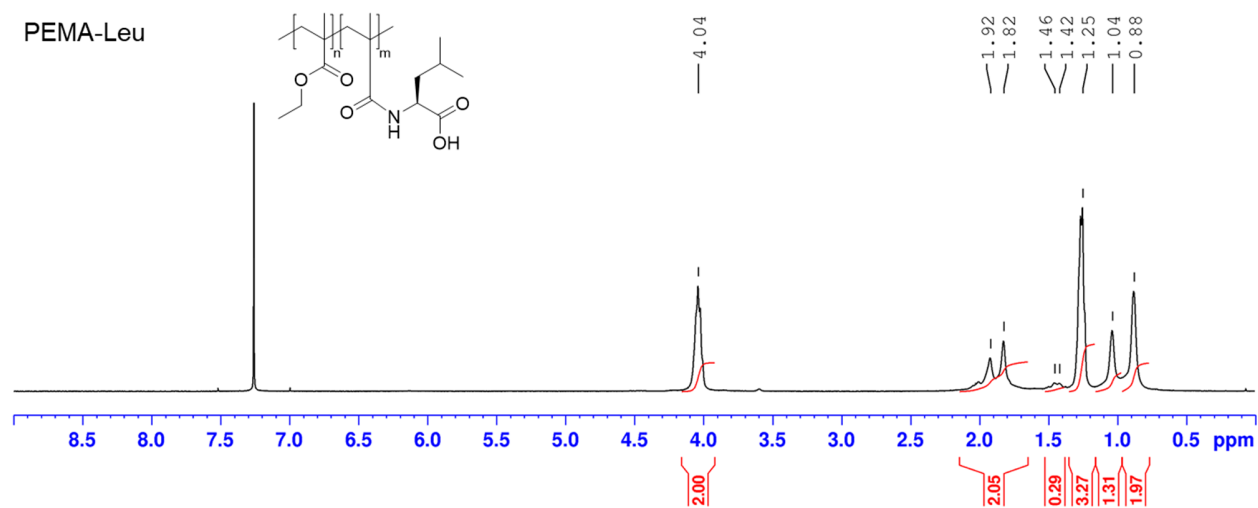


Figure 4.56 ^1H NMR spectrum of **PEMA-Leu** in CDCl_3

4.3. NMR spectra

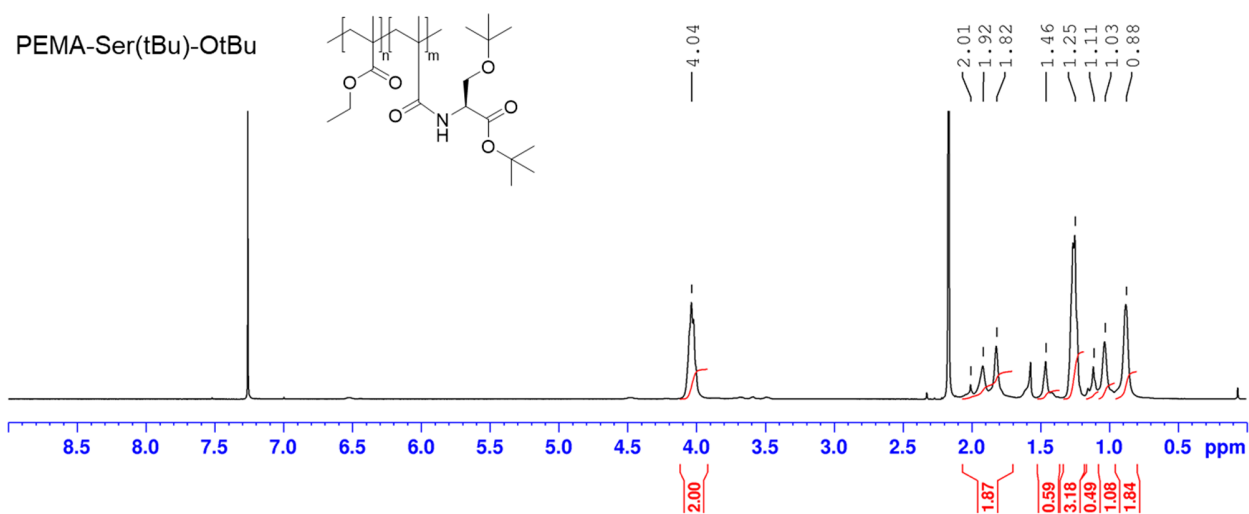


Figure 4.57 ^1H NMR spectrum of **PEMA-Ser(tBu)-OtBu** in CDCl_3

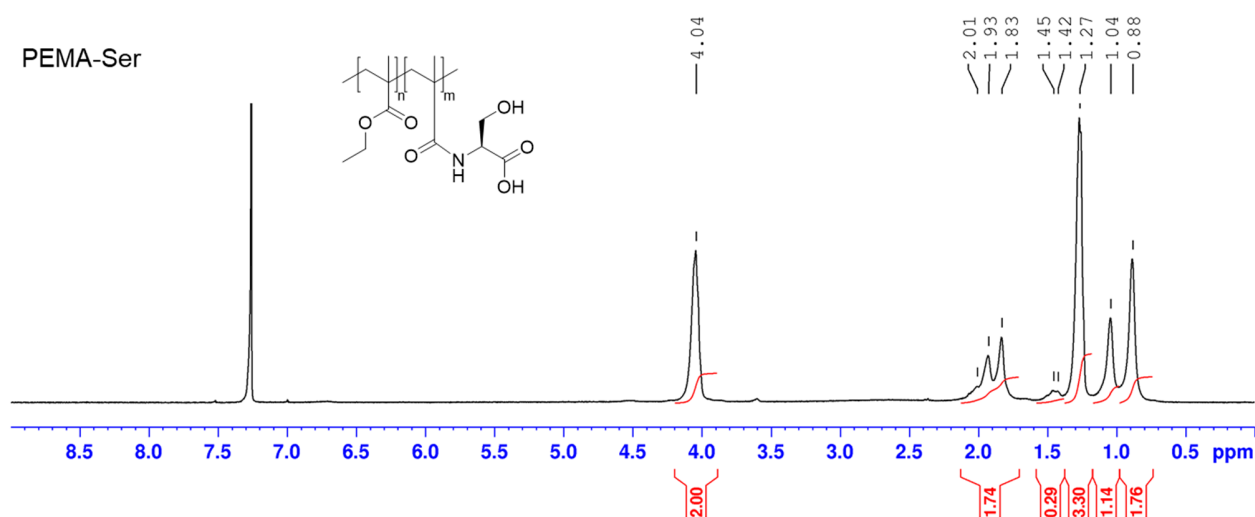


Figure 4.58 ^1H NMR spectrum of **PEMA-Ser** in CDCl_3

4. Materials and methods

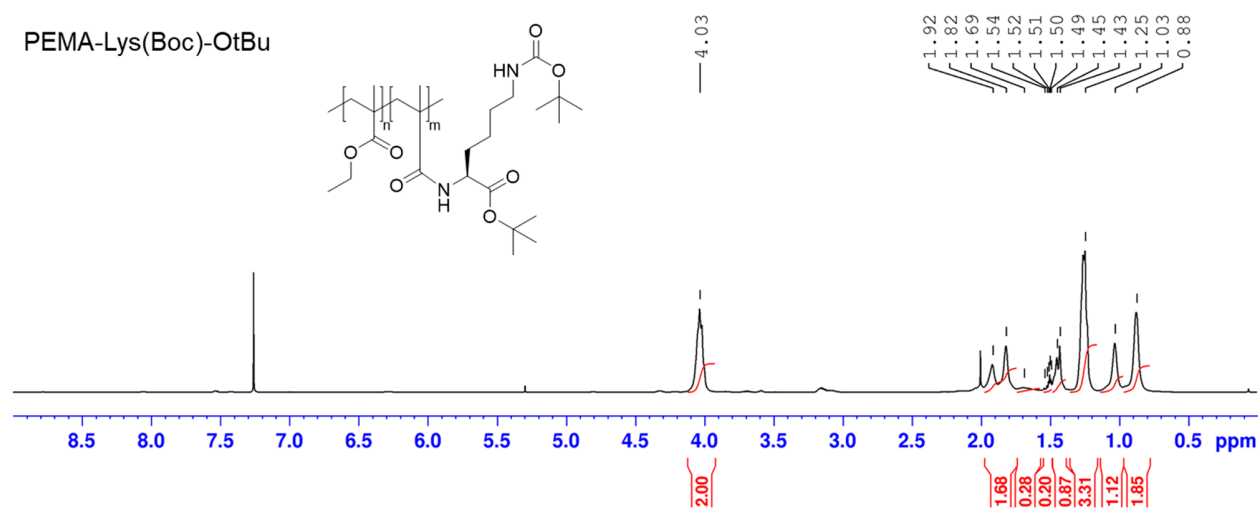


Figure 4.59 ^1H NMR spectrum of **PEMA-Lys(Boc)-OtBu** in CDCl_3

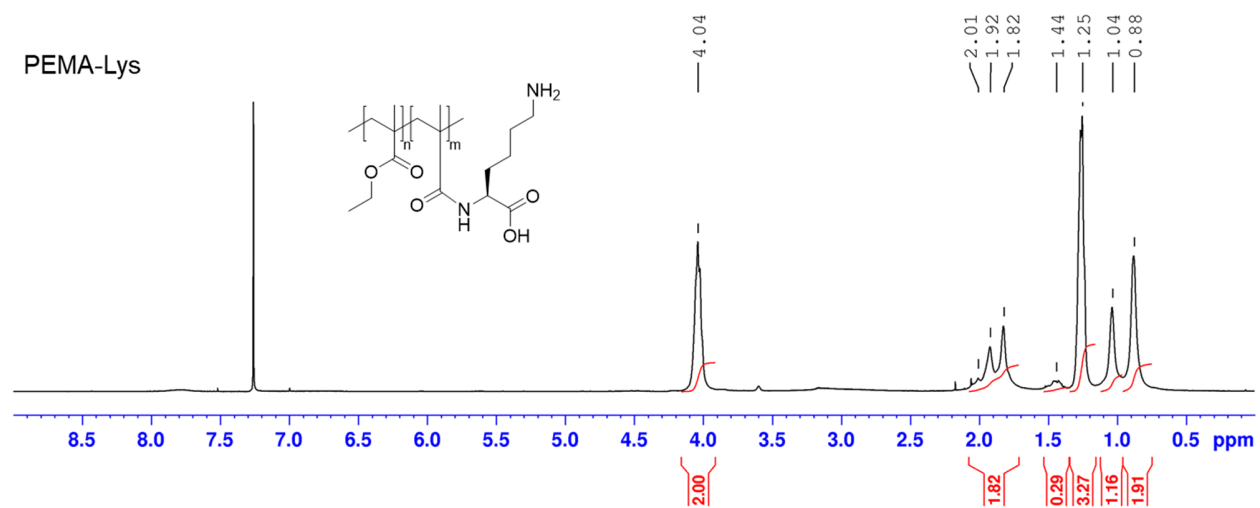


Figure 4.60 ^1H NMR spectrum of **PEMA-Lys** in CDCl_3

4.3. NMR spectra

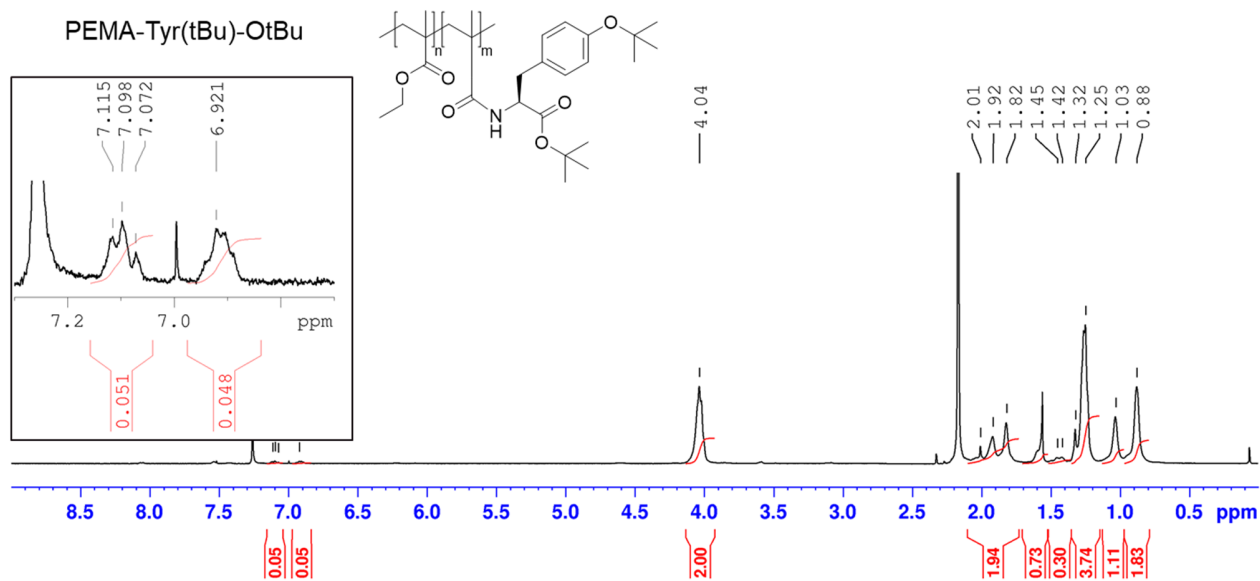


Figure 4.61 ^1H NMR spectrum of **PEMA-Tyr(tBu)-OtBu** in CDCl_3

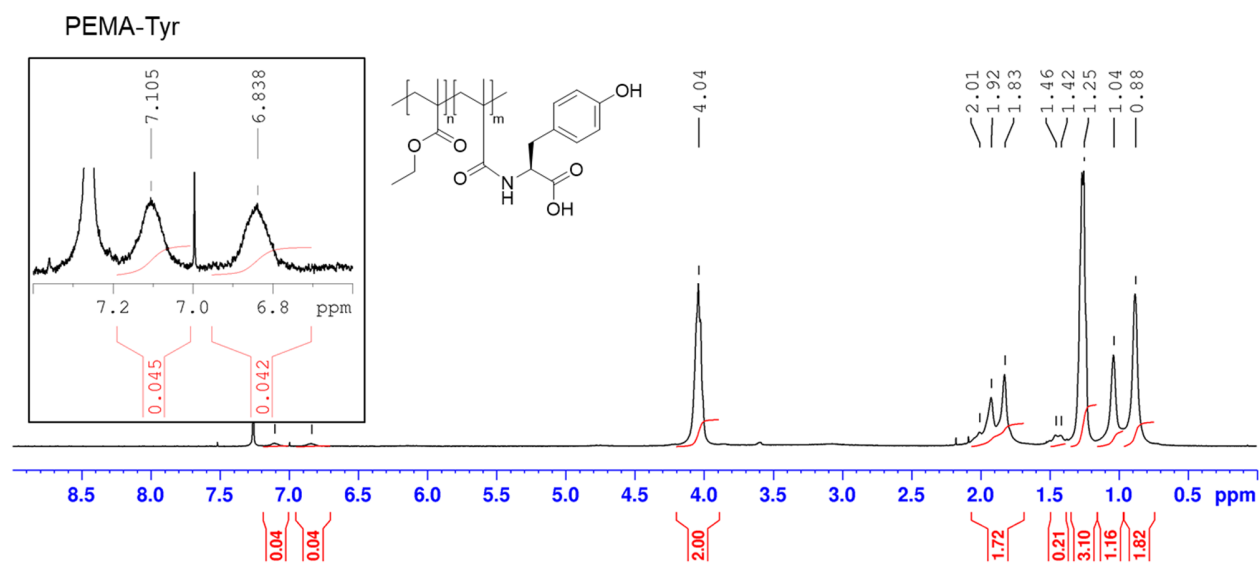


Figure 4.62 ^1H NMR spectrum of **PEMA-Tyr** in CDCl_3

4. Materials and methods

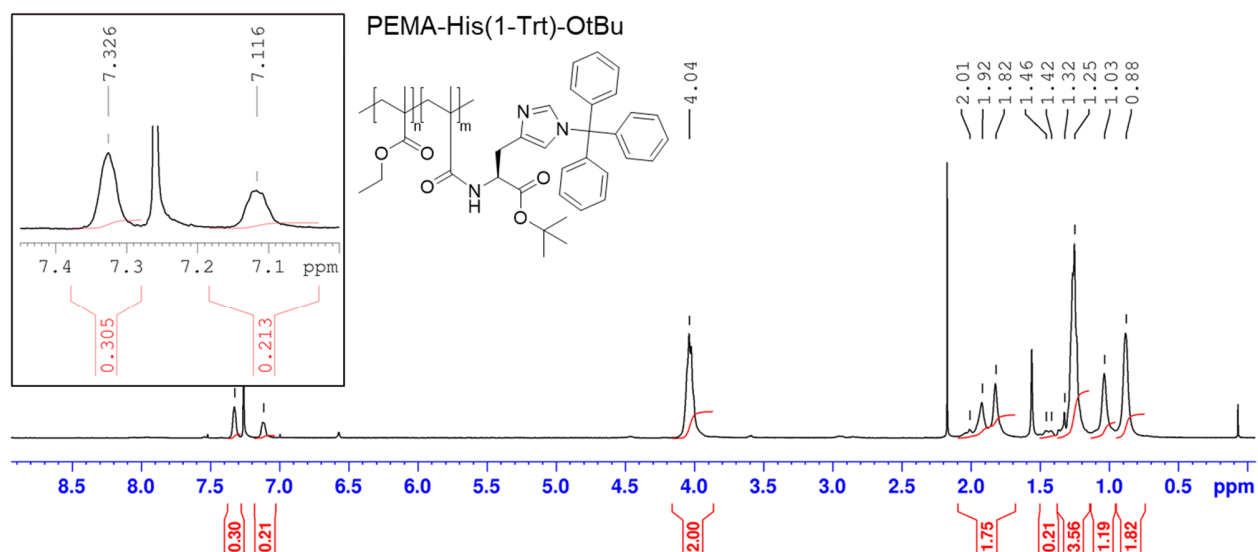


Figure 4.63 ^1H NMR spectrum of **PEMA-His(1-Trt)-OtBu** in CDCl_3

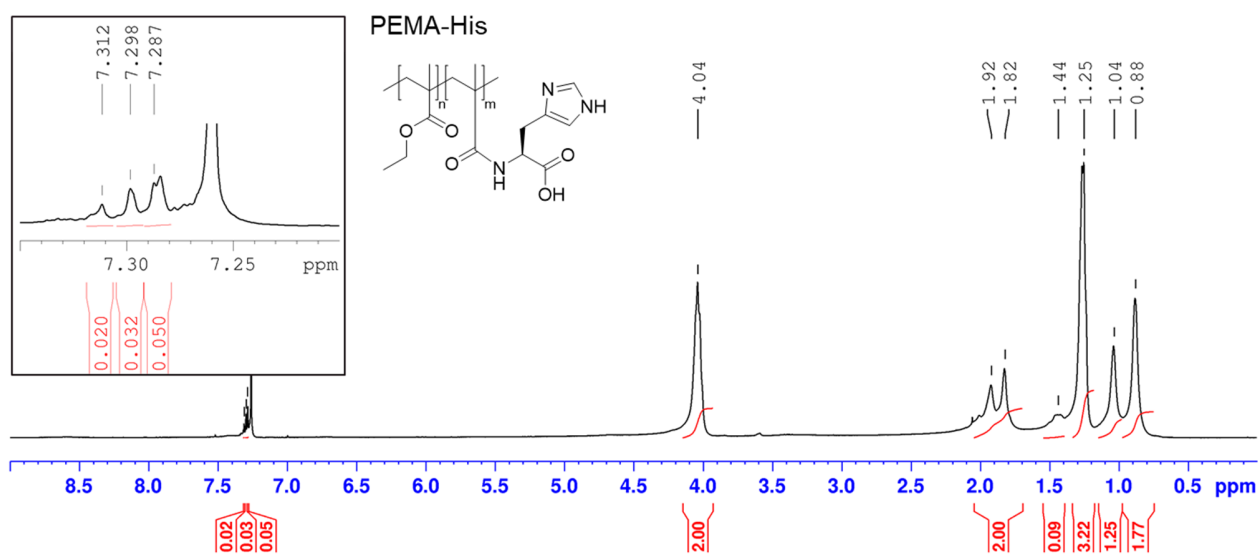


Figure 4.64 ^1H NMR spectrum of **PEMA-His** in CDCl_3

4.3. NMR spectra

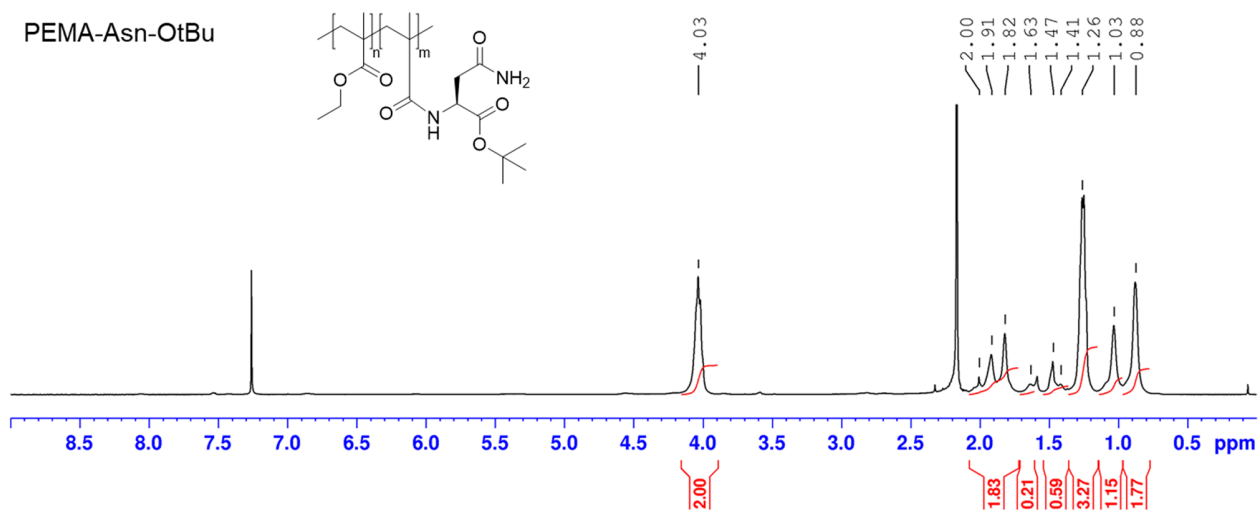


Figure 4.65 ¹H NMR spectrum of **PEMA-Asn-OtBu** in CDCl₃

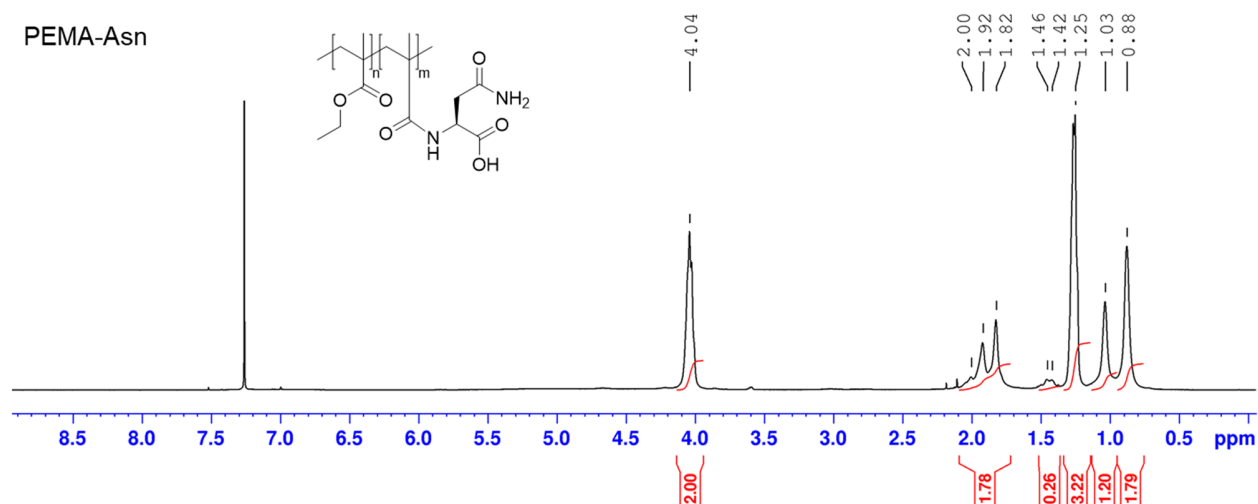


Figure 4.66 ¹H NMR spectrum of **PEMA-Asn** in CDCl₃

4. Materials and methods

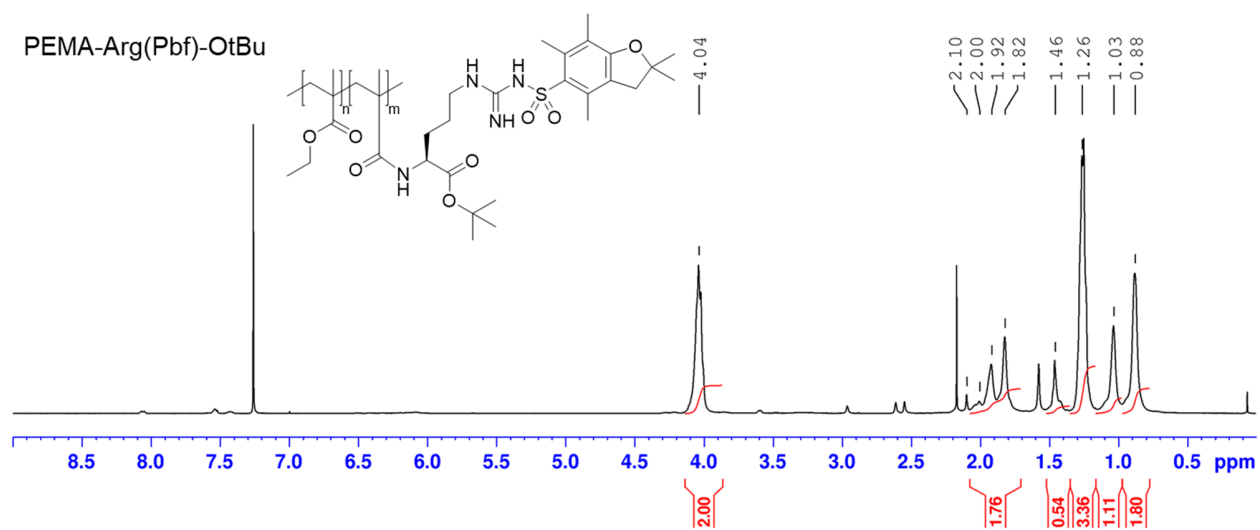


Figure 4.67 ^1H NMR spectrum of **PEMA-Arg(Pbf)-OtBu** in CDCl_3

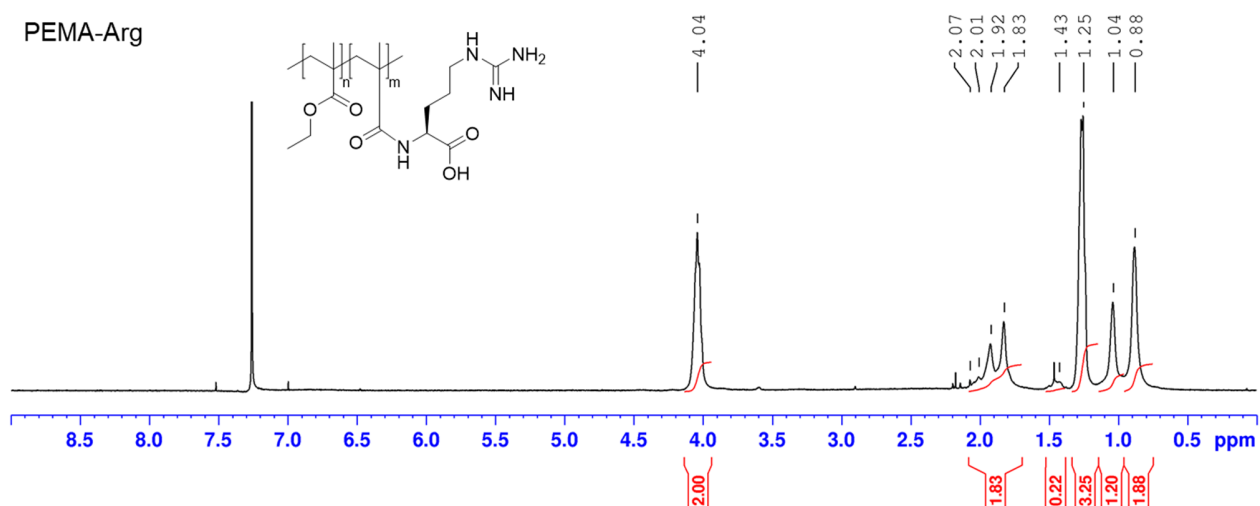


Figure 4.68 ^1H NMR spectrum of **PEMA-Arg** in CDCl_3

Résumé de la thèse en français

1) Introduction

Les nanoparticules (NPs) fluorescentes ont gagné en intérêt dans le domaine de la création d'outils de bioimagerie multifonctionnels et fortement luminescents pour des actions à visée diagnostiques et thérapeutiques (Hildebrandt et al., 2017; Howes et al., 2014; Wolfbeis, 2015). Les NPs polymères chargées en colorant sont une classe intéressante de nanoparticules fluorescentes de par leur grande brillance (une particule peut encapsuler plusieurs centaines de fluorophores), la facilité à fonctionnaliser leur surface et leur biocompatibilité. Cependant, un des défis que ces systèmes posent, est le phénomène d'extinction causé par l'agrégation (ECA) : en augmentant la quantité de fluorophores à l'intérieur de la matrice polymérique, les molécules tendent à s'agréger ce qui inhibe leur fluorescence. Notre groupe a proposé une approche pour surmonter ce problème en employant des fluorophores cationiques associés avec des contre-ions hydrophobes encombrés, qui ont pour rôle d'espacer les fluorophores et par conséquent d'éviter l'ECA (Reisch et al., 2014). En utilisant cette approche, il est possible de formuler des nanoparticules qui sont ~100 fois plus brillantes que les points quantiques (Andreiuk et al., 2017a; Reisch et al., 2014). De plus, la présence de contre-ions crée une organisation supramoléculaire des molécules de colorant permettant le transfert ultra-rapide de l'énergie d'excitation entre tous les fluorophores ce qui engendre un phénomène de commutation collective (Reisch et al., 2014). Sur la base de ce phénomène, notre groupe a récemment publié une nanoantenne géante capteuse de lumière où des milliers de colorants donneurs FRET transfèrent leur énergie d'excitation vers un seul accepteur FRET permettant la détection de molécules uniques en utilisant la lumière ambiante (Trofymchuk et al., 2017). Ce système a par la suite été appliqué à la modélisation de nanosondes ADN de type FRET (Melnichuk et al., 2020; Melnychuk and Klymchenko, 2018).

La présente étude porte sur le développement de nouvelles applications des nanoparticules fluorescentes citées ci-dessus. D'une part, nous ciblons l'amélioration des propriétés photophysiques de ces systèmes : (i) de nouveaux colorants ont été testés sur la formulation des NPs, créant une nouvelle famille de nanoparticules émettrices dans le vert permettant la préparation de capteurs ADN compatibles avec les caméras RGB (rouge, vert, bleu), (ii) de nouveaux contre-ions contenant du gadolinium ont été testés, étendant l'approche des contre-ions à une autre classe de composés créant une potentielle plateforme d'imagerie multiplexe couplant l'utilisation de

Résumé de la thèse en français

fluorophores avec la diffusion d'électrons liée aux atomes lourds. D'autre part, nous avons cherché à obtenir des NPs avec des propriétés de ciblage via les approches suivantes : (i) La greffe de groupes de ciblage à la surface des NPs et (ii) la conjugaison de groupes d'acides aminés aux polymères puis l'utilisation de ces polymères dans la formulation de nanoparticules afin d'obtenir des NPs avec une surface similaire aux protéines et finalement évaluation leurs capacités de ciblage.

2) Résultats et discussion

Synthèse de nanoparticules émettant dans le vert et leur utilisation dans la microscopie assistée par smartphone

Pour obtenir un système qui soit compatible avec la détection RGB, il est nécessaire de sélectionner un couple FRET où l'émission du donneur et celle de l'accepteur sont compatibles avec deux canaux RGB distincts sans chevauchement (Figure 1C-D). Pour y parvenir, nous avons choisi comme donneur FRET émettant dans le vert l'octadécyle ester de Rhodamine 110 (R110-C18) et dans le jaune l'octadécyle ester of Rhodamine 6G (R6G-C18). ATTO 647N (Figure 2A) a été choisi comme accepteur FRET parce que son absorption coïncide bien avec l'émission du colorant donneur, garantissant un FRET efficace. De plus, son émission est compatible avec le canal rouge de la caméra RGB (Figure 1D), couramment utilisé sur les smartphones.

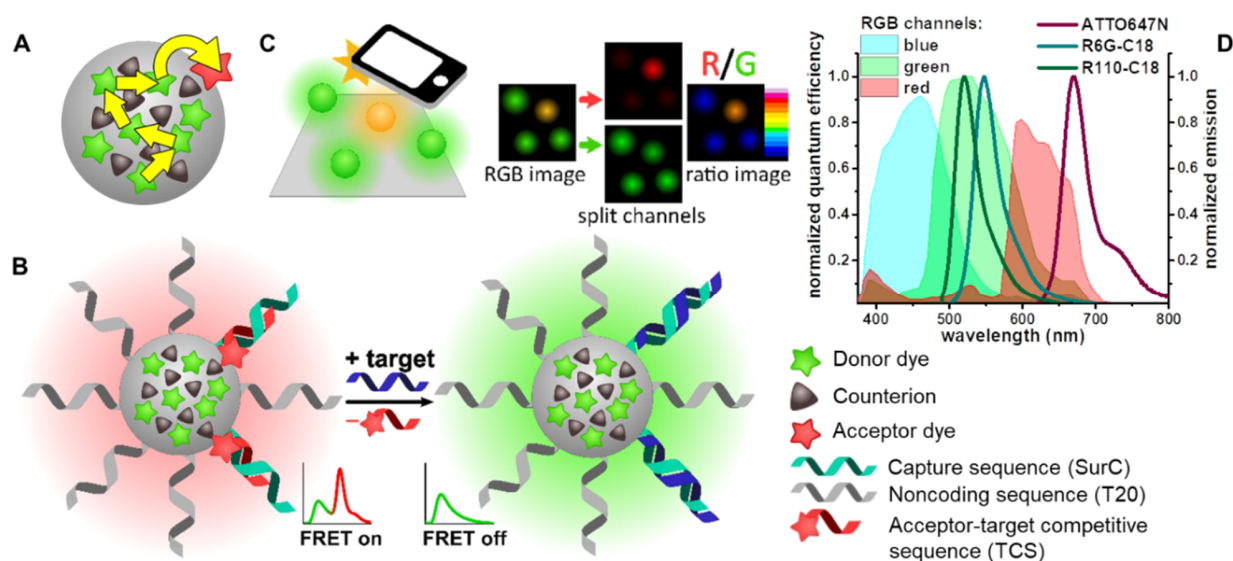


Figure 1. (A) Schéma décrivant le transfert d'énergie intramoléculaire ultrarapide et le captage de lumière par l'accepteur FRET. (B) Création de nanosonde : les donneurs verts à l'intérieur des NPs transfèrent une partie de leur énergie d'excitation vers quelques accepteurs FRET à la surface, générant une fluorescence jaune-orange de la nanosonde. En présence de la séquence cible, l'accepteur FRET portant la séquence est déplacé, inhibant le FRET et changeant la couleur d'émission en vert. (C) Analyses de données par smartphone ; une image RGB est prise et l'on fait le rapport entre l'intensité des signaux rouge et vert ; ce rapport est proportionnel à la concentration en séquence cible. (D) Comparaison entre la réponse spectrale (efficacité quantique) des canaux RGB de la caméra couleur (Nikon DS-Fi3) avec les spectres d'émission dans l'éthanol des colorants donneurs et accepteurs sélectionnés pour la création de nanosonde.

Les NPs polymères sont préparées à base d'un dérivé de poly(méthacrylate de méthyle-co-acide méthacrylique) (PMMA-MA, 1.6% acide méthacrylique) (Figure 2A), portant des groupes azides (PMMA-AspN3) comme décrit précédemment (Melnychuk and Klymchenko, 2018) et chargé d'un colorant donneur portant un contre-ion hydrophobe encombré (Figure 2A-B). Nous avons choisi de tester deux contre-ions différents : un tétraphénylborate fluoré (F12) et un alcoxyaluminate fluoré (F9-Al) (Krossing, 2001), parce qu'ils ont déjà montré leur efficacité (Andreiuk et al., 2017a, 2017b) (Figure 2A).

Les propriétés photophysiques de ces NPs chargées en donneurs ont été étudiées et les deux meilleures paires R6G-C18/F12 and R6G-C18/F9-Al ont été sélectionnées pour préparer une nanosonde ADN de type FRET en utilisant les résultats précédents dans notre groupe (Melnychuk et al., 2020, 2020) (Figure 2C). Succinctement, les NPs chargées en donneurs sont garnies avec des séquences ADN par une réaction click sans cuivre, puis l'accepteur FRET est introduit en hybridant la séquence compétitive cible portant l'accepteur (ATTO647N-TCS) à la surface de la

Résumé de la thèse en français

nanoparticule (Figure 2C). En présence de la séquence cible (dans ce travail, nous avons utilisé un fragment de la séquence qui encode la survivine, un important marqueur du cancer) l'accepteur est déplacé et le FRET inhibé (Figure 1B). Les propriétés spectroscopiques de ces sondes ont été étudiées (Figure 2D) et le meilleur résultat a été obtenu avec le couple R6G-C18/F9-AI.

Les capacités de détection des cibles dans ce système ont été testées à la fois par spectroscopie de fluorescence et par microscopie RGB (Figure 2E-F), la limite de détection (LD) par spectroscopie en solution a été de 3 pM, tandis que pour la microscopie RGB (testée avec un microscope et un smartphone) cette limite était inférieure à 10 pM. Curieusement, le changement de couleur est mieux détecté avec un smartphone qu'avec une caméra de microscope, ouvrant la possibilité de développer des tests rapides avec ce système. Sur la base des résultats de ce paragraphe, un article a été publié : Severi, C., Melnychuk, N. & Klymchenko, A. S. Smartphone-assisted detection of nucleic acids by light-harvesting FRET-based nanoprobe. *Biosensors and Bioelectronics* 168, 112515 (2020).

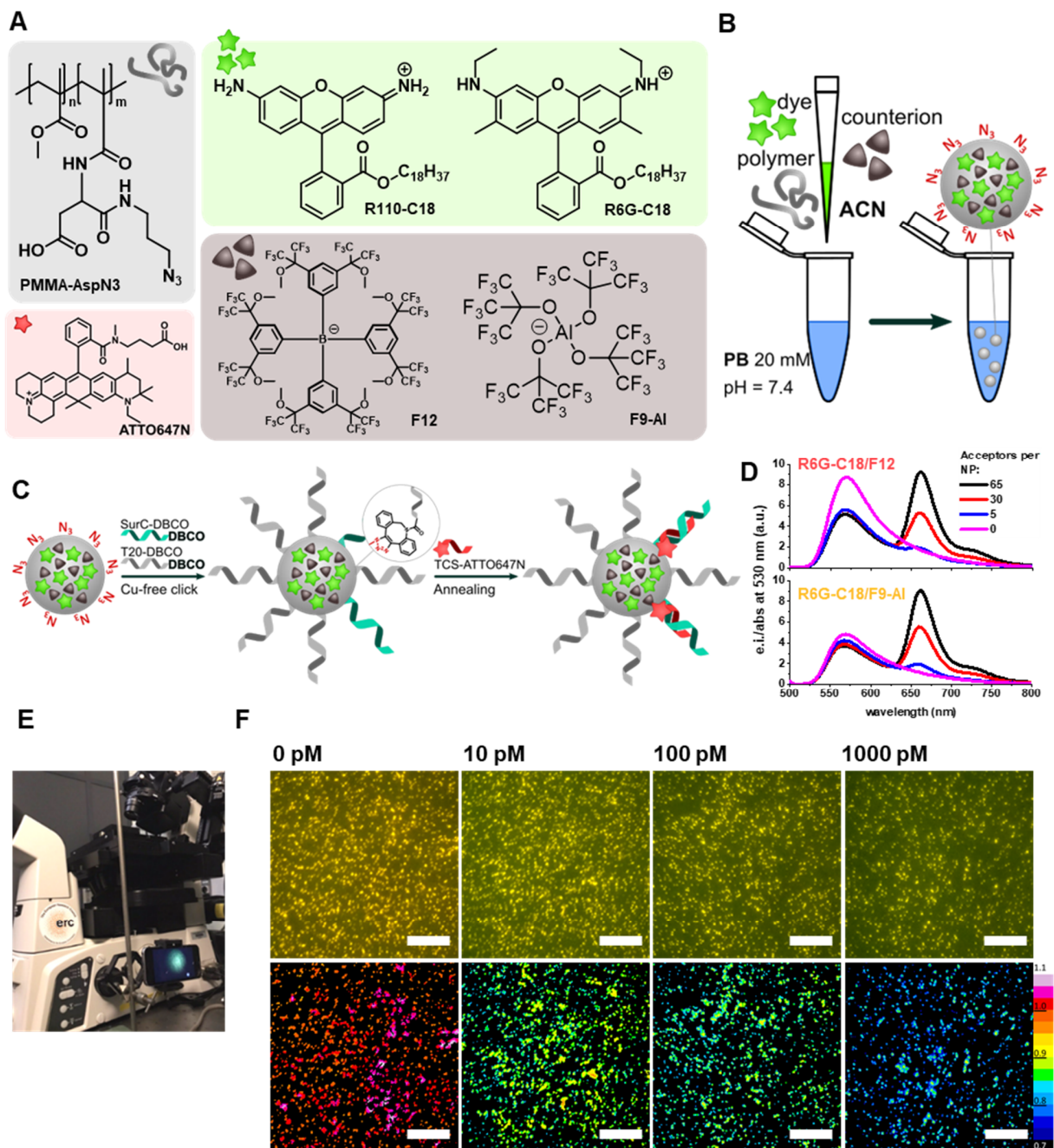


Figure 2. (A) Polymère portant un azoture PMMA-AspN3 (haut gauche), colorants donneurs (haut droite), contre-ions (bas droite) et accepteur (bas gauche) utilisés dans la préparation de nanosondes ADN. (B) Schéma de préparation de NPs chargées en donneur. (C) Schéma de préparation des nanosondes ADN. (D) Spectres de fluorescence de nanosondes FRET chargées avec deux différentes paires d'ions avec concentrations croissantes d'accepteurs. (E) Montage de détection assistée par smartphone pour détecter la séquence cible ADN avec des sondes immobilisées sur une surface en verre. (F) Ligne supérieure : Images RGB brutes acquises avec un smartphone. Ligne inférieure : Images ratiométriques des canaux rouge et vert des images montrés ci-dessus. Images acquises après 3 heures d'incubation à température ambiante avec différentes concentrations cibles. Barre d'échelles : 25 μ m.

Synthèse de nanoparticules fluorescentes utilisant différents contre-ions à base de lanthanides.

Dans cette approche développée au sein de notre équipe, un colorant cationique fluorescent est associé avec un contre-ion hydrophobe encombré pour l'encapsulation dans des NPs polymères. La présence du contre-ion assure que les fluorophores sont bien encapsulés sans ECA, donnant des particules petites et brillantes (Figure 3B). Cette approche a été validée sur quelques composés comme les tétraphénylborates (Andreiuk et al., 2019; Reisch et al., 2014) et les alcoxyaluminates (Andreiuk et al., 2017b). Cependant, deux points importants restent à élucider : (i) Est-ce que l'approche du contre-ion est applicable aux complexes anioniques des autres métaux de la classification périodique, et (ii) s'il est possible de préparer un système où l'anion fournit des nanoparticules avec des nouvelles propriétés pour d'autres modalités d'imagerie.

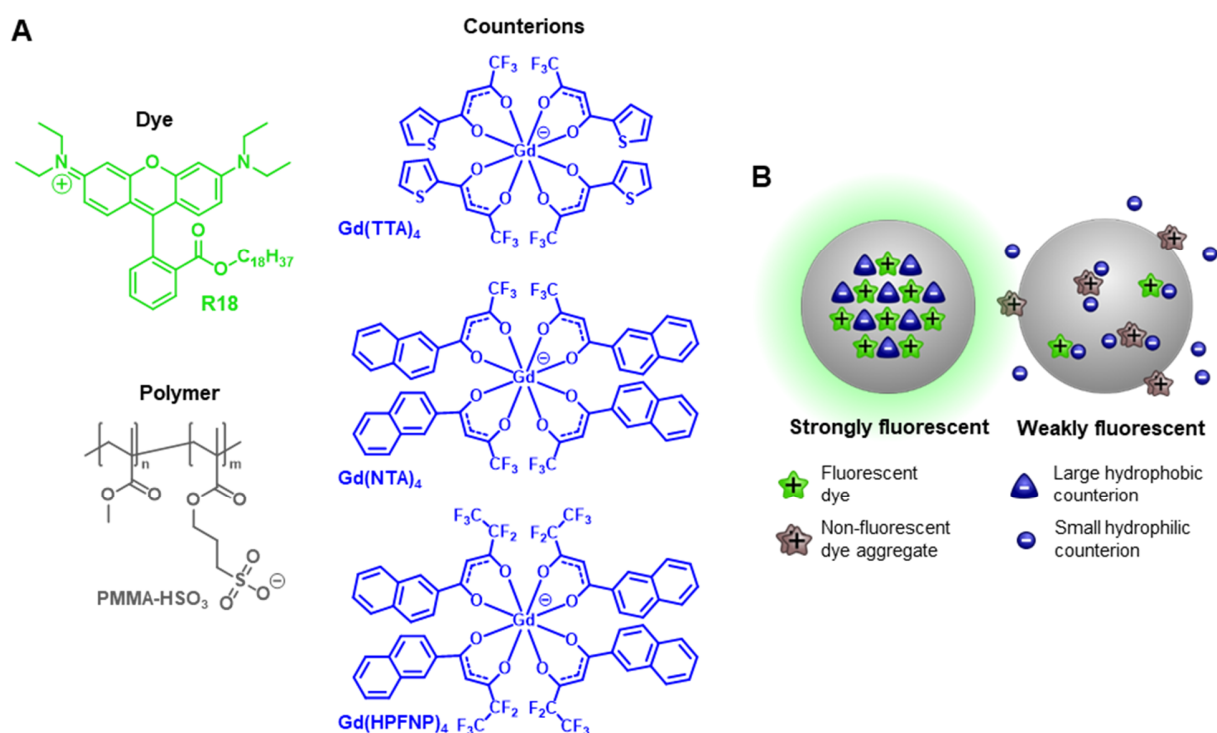


Figure 3. (A) Colorant cationique fluorescent (haut gauche), anions à base de lanthanides (droite) et polymère portant des groupes sulfonates (bas gauche) utilisé pour la préparation des nanoparticules. (B) Modèles théorisés de la distribution des colorants fluorescents à l'intérieur des NPs polymères préparés avec des contre-ions hydrophiles petits (droite) et des contre-ions hydrophobes encombrés (gauche).

Avec ces deux questions en tête, nous avons préparé des NPs utilisant plusieurs complexes de gadolinium comme contre-ions (fourni par un collaborateur, Prof. Tero Soukka, Université de Turku, Finlande) avec différents encombrements, taux d'hydrophobicité et taux de fluorescence (Figure 3A). L'ion gadolinium a été choisi parce qu'il peut fournir un contraste en Microscopie Electronique en Transmission (MET) et en imagerie par résonance magnétique ce qui permettrait la préparation de NPs pour de l'imagerie multimodale.

Les nanoparticules ont été préparées par nanopréciipitation du polymère et du sel de chlorure de R18 avec des quantités variées de contre-ions Gd (Figure 3A). Nous avons trouvé que les NPs préparées sans le contre-ion encombré étaient généralement plus grandes, plus polydisperses et non-émissives pour des charges en colorants plus élevées, tandis que celles préparées avec un complexe à base de Gd étaient plus petites, avaient des rendements quantiques plus élevés (Figure 3B) et des bandes d'émission plus étroites (Figure 4A-B). En comparaison avec les points quantiques, toutes les NPs formulées avec les trois contre-ions à base de Gd étaient significativement plus brillantes. Les NPs encapsulant Gd(HPFNP)₄ étaient notamment les plus brillantes (Figure 4C), indiquant l'importance de la taille et de la fluoration des complexes-Gd pour empêcher l'ECA.

De plus, après incubation avec des cellules HeLa, les NPs formulées avec un excès de contre-ion Gd étaient immédiatement internalisés par endocytose sans signes de lixiviation du colorant, tandis que les NPs formulées avec le sel de chlorure de R18 montraient une forte lixiviation, colorant à la fois la membrane plasmique et le cytoplasme (Figure 4D). De plus, les NPs formulées avec un contre-ion Gd montrent une cytotoxicité limitée aux concentrations habituellement utilisées en imagerie.

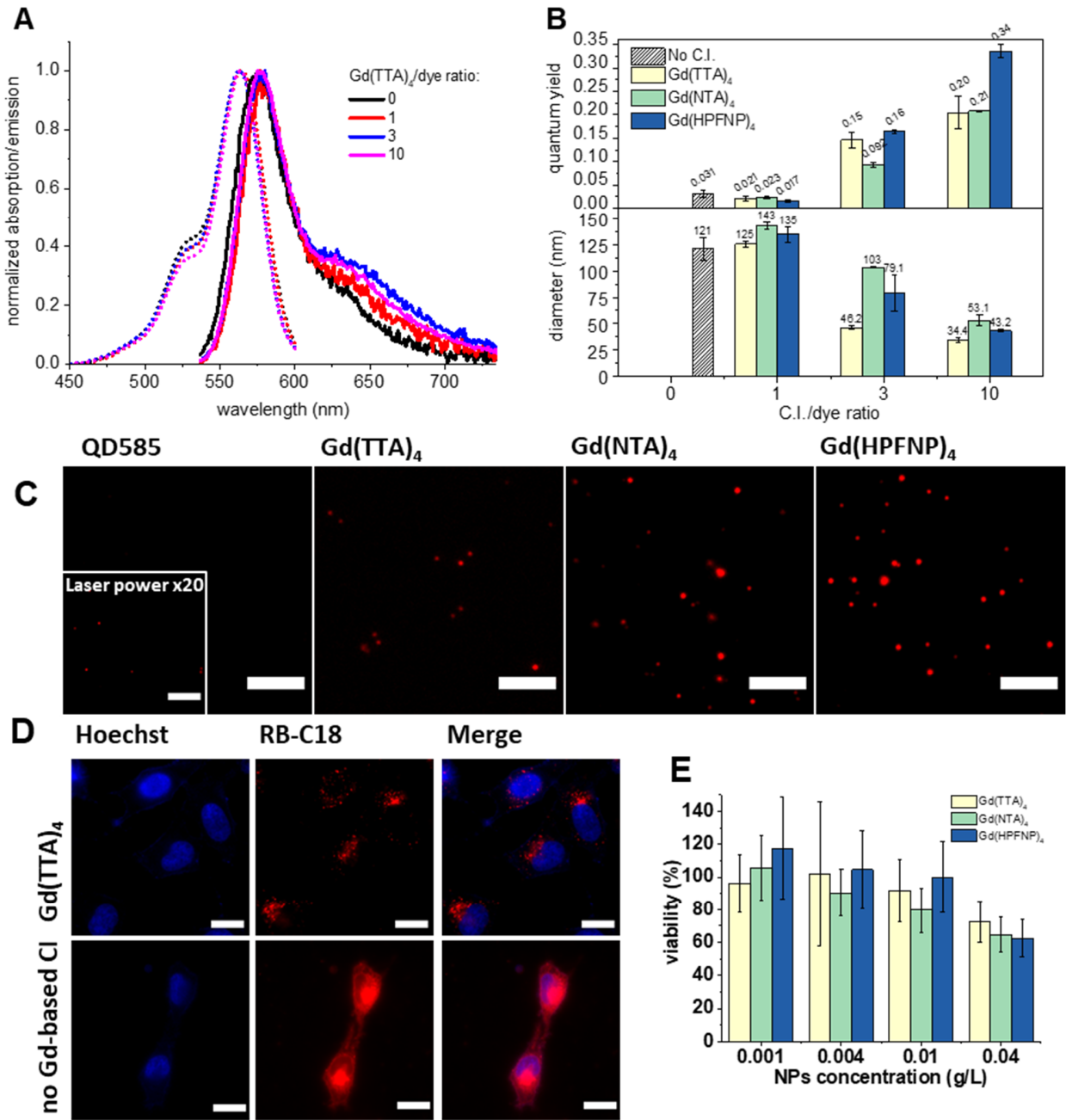


Figure 4. (A) Absorption normalisé et spectre d'émission des NPs chargées avec R18 (250 mM par rapport au polymère) avec des quantités croissantes de contre-ions à base de Gd. (B) Rendement quantique de fluorescence (haut) et taille des particules (bas) en fonction du rapport molaire contre-ion Gd/R18 chargé à 250 mM en colorant pour les trois contre-ions à base de Gd étudiés. (C) Images en fluorescence de particules uniques des NPs polymères préparés avec 10 fois plus de contre-ions à base de Gd chargées à 250 mM en colorant comparées à la référence des points quantiques QD585. Barre d'échelles : 5 μ M. (D) Images de microscopie à épifluorescence de cellules HeLa incubées avec des NPs polymères (chargées avec 250 mM de colorant R18 avec ou sans 10 fois l'excès de Gd(TTA)₄). (E) Tests de cytotoxicité pour les NPs polymères chargées avec 250 mM de colorant R18 et les contre-ions à base de Gd. Barre d'échelles : 20 μ M.

Nanoparticules de ciblage pour lipides et protéines

Le troisième axe de recherche exploré au cours de ce travail porte sur la préparation de NPs de ciblage c'est-à-dire un système qui peut spécifiquement interagir avec des cellules. Un tel système permettrait de distinguer les cellules bactériennes des eucaryotes, les cellules apoptotiques des saines ou détecter l'expression d'un récepteur d'intérêt. Les nanoparticules polymères de type PMMA internalisent aisément par endocytose après incubation sur des cellules HeLa, ce qui représente un problème pour le ciblage spécifique.

C'est pourquoi, la première étape de ce projet a été la production de NPs n'interagissant pas avec les cellules. Cela a été réalisé par « chimie click » avec du PEG2000 fonctionnalisé avec DBCO et des nanoparticules composées d'un polymère portant des groupements azotures (Figure 5A).

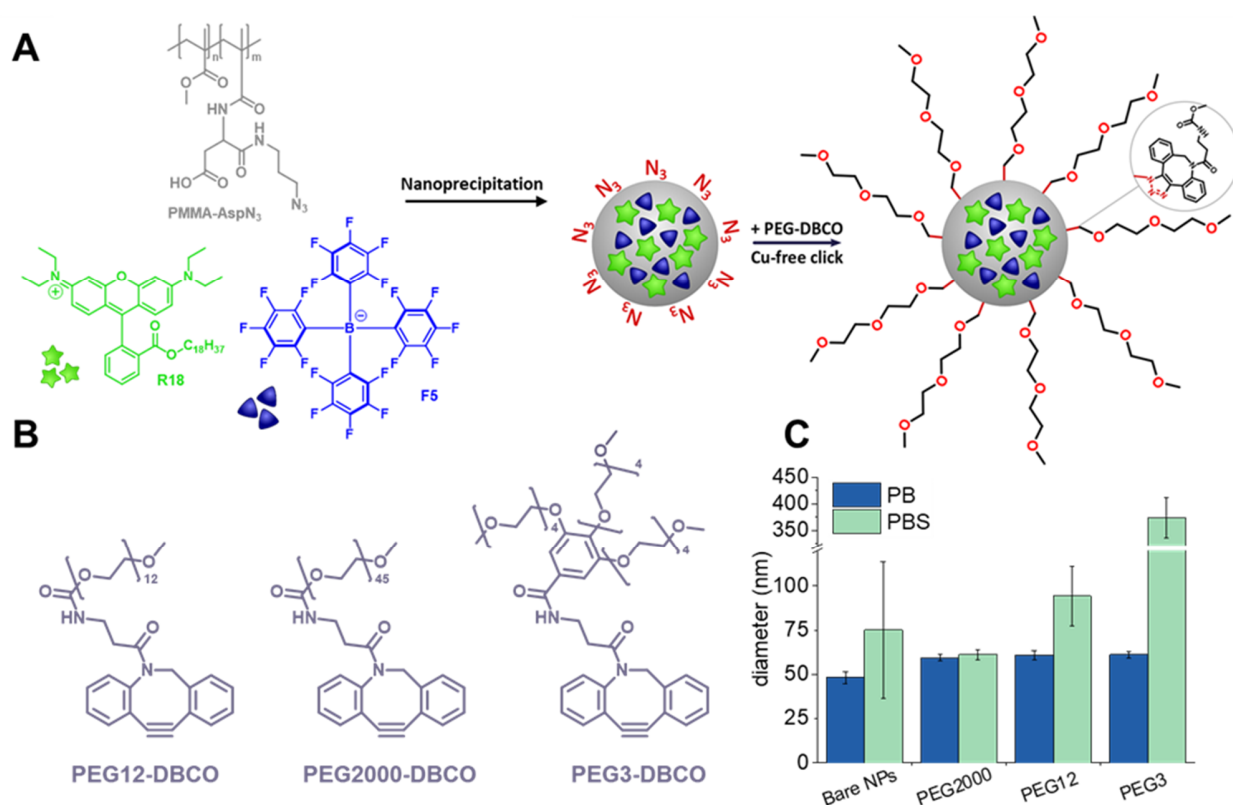


Figure 5. (A) Schémas de préparation des nanoparticules fluorescentes PEGylées. (B) Structures des trois PEG cliquables testés dans la préparation de nanoparticules furtives. (C) Résistance à l'agrégation dans des conditions de haute salinité des nanoparticules fonctionnalisées avec des chaînes de PEG.

Les NPs PEGylées ont d'abord été testées par diffusion dynamique de la lumière (DLS) et *spectroscopie de corrélation de fluorescence* (FCS) en vérifiant leur résistance à l'agrégation dans des conditions physiologique (tampon salin phosphate -PBS), puis sur des cellules HeLa par cytométrie et par microscopie à fluorescence. Nous avons trouvé que contrairement aux NPs nues, les NPs PEGylées ne s'agrègent pas dans le PBS (Figure 5C) et ne se lient pas aux cellules HeLa après incubation à température ambiante pendant 30 min (Figure 6).

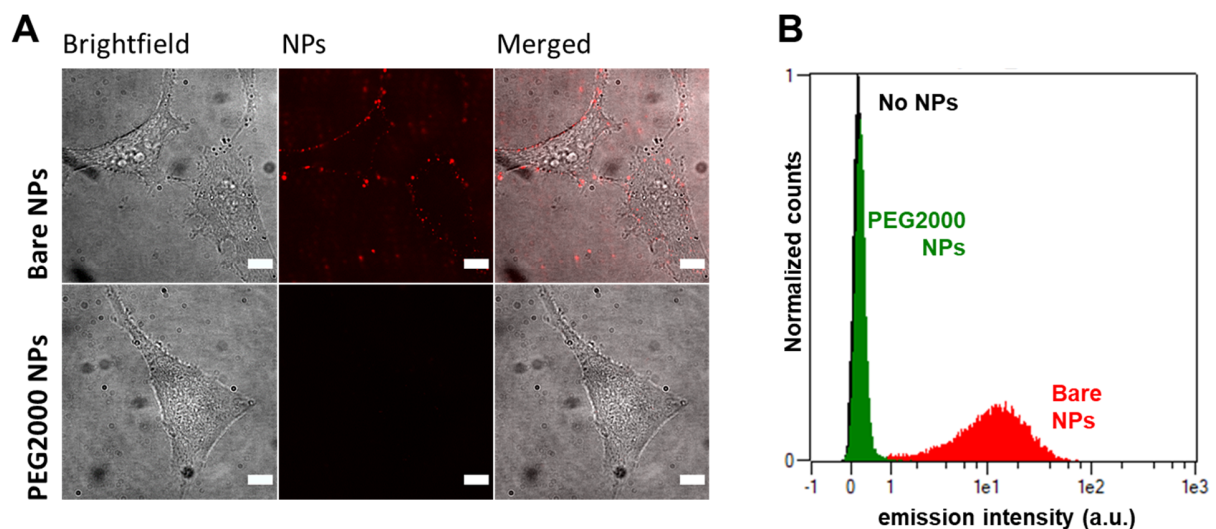


Figure 6. Nanoparticules PEGylées furtives. (A) Image de microscopie confocale de fluorescence de cellules HeLa incubées avec des NPs non fonctionnalisées (haut) et des NPs PEGylées furtives (bas). (B) Histogrammes d'intensité de fluorescence de cellules HeLa obtenues par cytométrie en flux : (i) sans NPs, (ii) incubées avec des NPs PEGylées furtives, (iii) incubées avec des NPs non fonctionnalisées. Barres d'échelle : 10 µm.

Par la suite nous avons synthétisés des chaînes PEG2000 portant un groupe DBCO à une extrémité et une unité de ciblage à l'autre. Deux unités de ciblage ont été choisies : des dérivés d'acide orthoacétyl boronique (APBA) qui se lie avec phosphatidyléthanolamine (PE) (présents sur la couche externe du plasma des membranes dans les bactéries et des cellules apoptotiques eucaryotes) (Bandyopadhyay et al., 2015) et la carbétocine un analogue de l'ocytocine qui se lie sur le récepteur couplé à la protéine G de l'ocytocine (Karpenko et al., 2015) (GPCR).

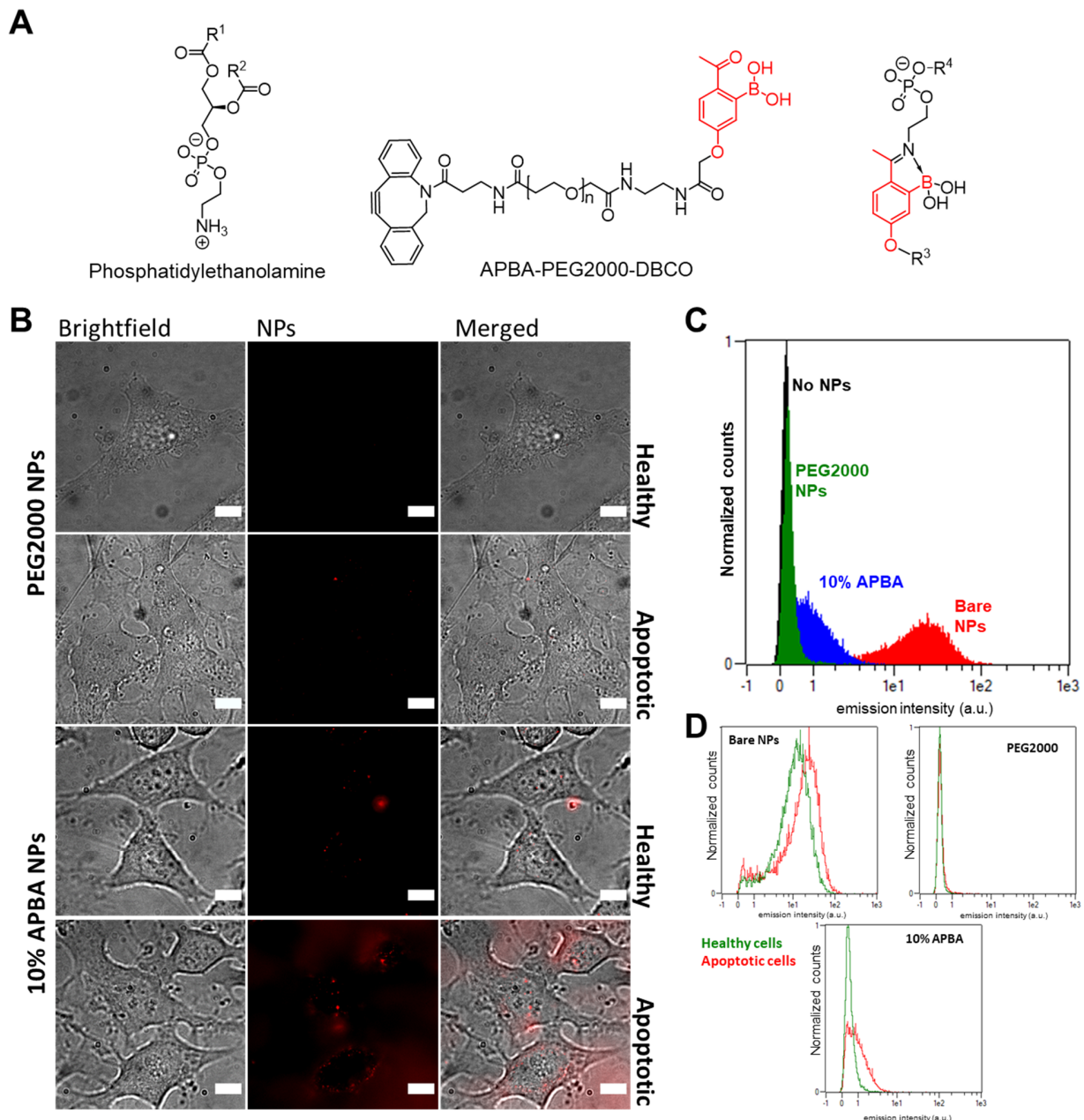


Figure 7. Nanoparticules ciblant les cellules apoptotiques. (A) Structure de la phosphatidyléthanolamine (PE) et du dérivé cliquable de l'APBA, et le mécanisme de liaison covalente de l'APBA avec la PE. (B) Images de microscopie à fluorescence de cellules HeLa normales et apoptotiques incubées avec des NPs PEGylées (haut) et des NPs portant de l'APBA (bas). (C) Cytométrie en flux des cellules HeLa apoptotiques. (D) Cytométrie en flux des cellules normales et des cellules apoptotiques incubées avec des nanoparticules furtives et des nanoparticules portant l'APBA. Barres d'échelle : 10 μ m.

Les NPs portant le groupement acide boronique ont été préparées et leur capacité à cibler les cellules apoptotiques a été testée par cytométrie de flux et par microscopie à fluorescence (Figure 7). Il a été trouvé qu'elles étaient capables de cibler sélectivement les cellules apoptotiques,

tandis que les simples NPs PEG2000 ne peuvent pas distinguer les cellules saines des cellules apoptotiques. D'autre part, les NPs fonctionnalisées avec la carbétocine montrent une meilleure capacité à se lier aux cellules exprimant le GPCR de l'ocytocine (OTR) (Figure 8).

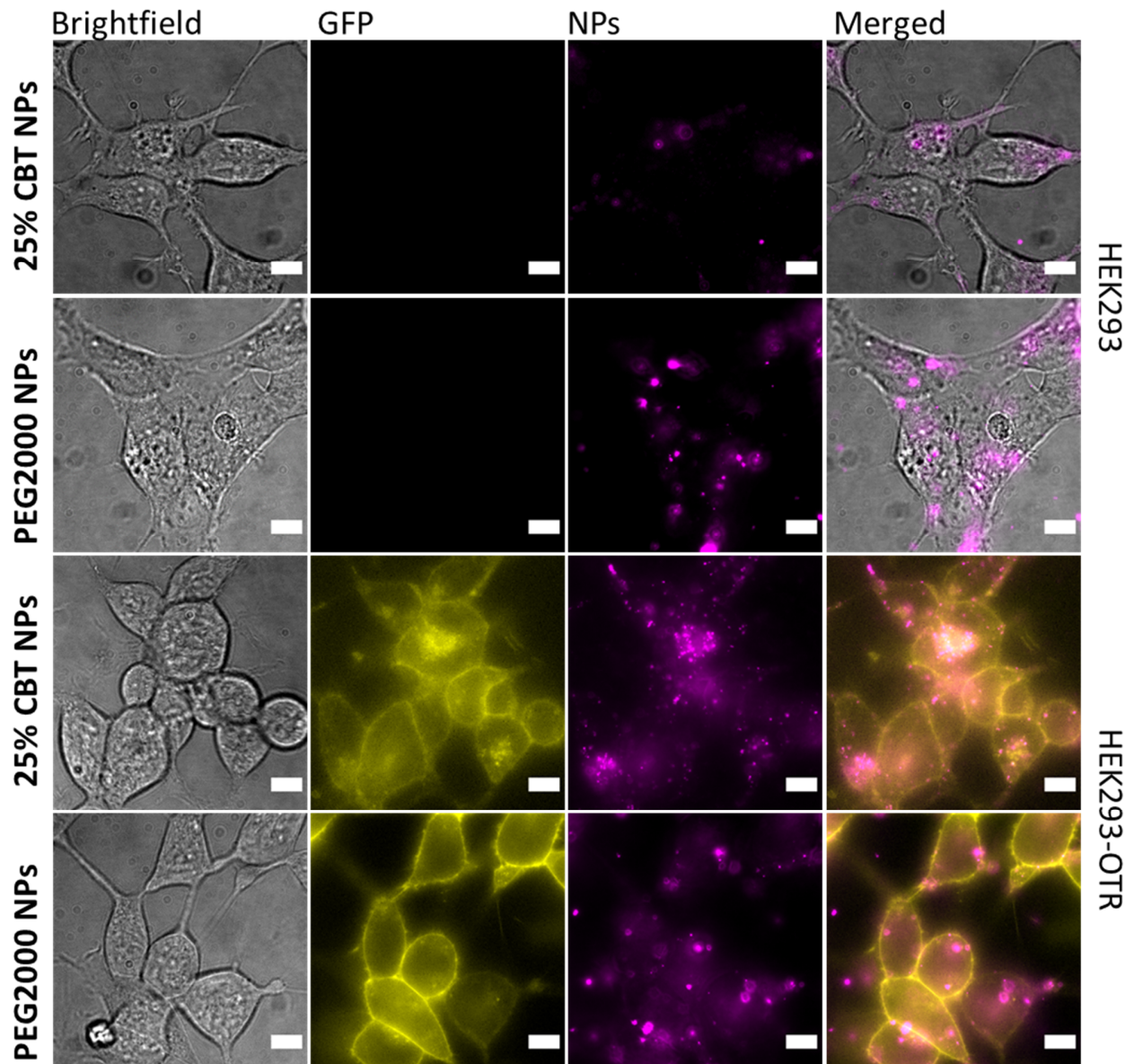


Figure 8. Nanoparticules pour le ciblage de l'OTR. Des cellules HEK293 exprimant l'OTR fusionné avec la GFP (bas) et de cellules HEK293 control qui n'expriment pas l'OTR (haut) étaient incubées avec des NPs PEGylés furtives et des NPs portant la CBT. Les cellules incubées avec les NPs étaient imagées avec la microscopie à épifluorescence en deux canaux : un canal vert (excitation à 470 nm) et un canal rouge (excitation à 550 nm). Barres d'échelle : 10 μ m.

Nanoparticules de ciblage avec une surface de type protéine

La possibilité de synthétiser des nanoparticules polymères chargées avec un colorant et possédant une affinité envers une cible spécifique soulève de nombreuses questions : serait-il possible de produire des nanoparticules avec une surface complexe de type protéine ? Une quelconque activité biologique pourrait-elle apparaître d'un tel système ? Les nanoparticules ayant ces surfaces complexes pourraient-elles être programmées vers une cible biologique spécifique ?

Pour créer des NPs avec une surface de type protéine, nous avons sélectionné huit acides aminés (AAs) avec des propriétés différentes afin de faire varier celles des NPs obtenues. (i) AAs chargés positivement : histidine (His), arginine (Arg), lysine (Lys) ; (ii) AAs chargés négativement : acide aspartique (Asp) ; (iii) AAs polaires avec une chaîne latérale neutre : serine (Ser) et asparagine (Asn) ; (iv) AAs hydrophobes : tyrosine (Tyr) et leucine (Leu). Chaque acide aminé a été greffé à la fois sur le poly(méthacrylate de méthyle-co-acide méthacrylique) (PMMA-COOH 1.6%) et le poly(méthacrylate d'éthyle-co-acide méthacrylique) (PEMA-COOH 5%) (Figure 9A). Ce modèle assure l'exposition des acides aminés à la surface des NPs après nanopréciipitation.

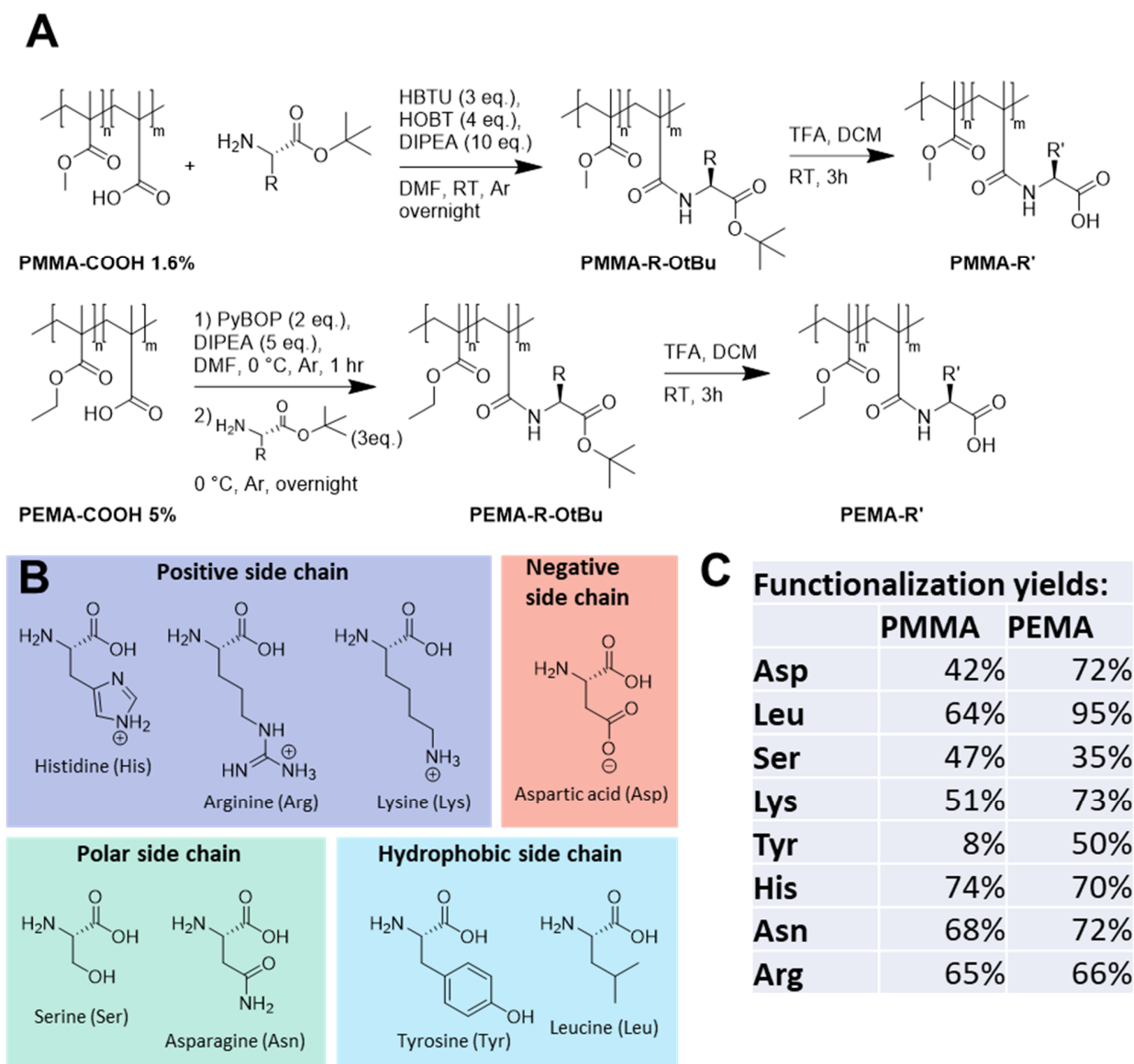


Figure 9. (A) Schémas de synthèse des poly méthacrylates portant des acides aminés : couplage du PMMA (haut) et couplage du PEMA (bas). (B) Huit acides aminés étaient choisis en fonction de leurs différentes propriétés. (C) Rendements de fonctionnalisation de chaque couplage (calculé en intégrant le signal du *tert*-Butyl au RMN).

Ces composés ont ensuite été utilisés pour formuler des nanoparticules (Figure 10A) et tester leurs capacités à i) survivre à des conditions drastiques ii) cibler spécifiquement des biomolécules d'intérêt. Les nanoparticules préparées avec des AA greffés sur du PMMA (PMMA-AA NPs) ont montré des diamètres généralement grands et une forte tendance à s'agréger dans des conditions de haute salinité (Figure 10B), tandis que les PEMA-AA NPs étaient généralement plus

petites (exceptés PEMA-Lys and PEMA-His qui ont donné de grands agrégats) et résistaient bien aux conditions de haute salinité (Figure 10C).

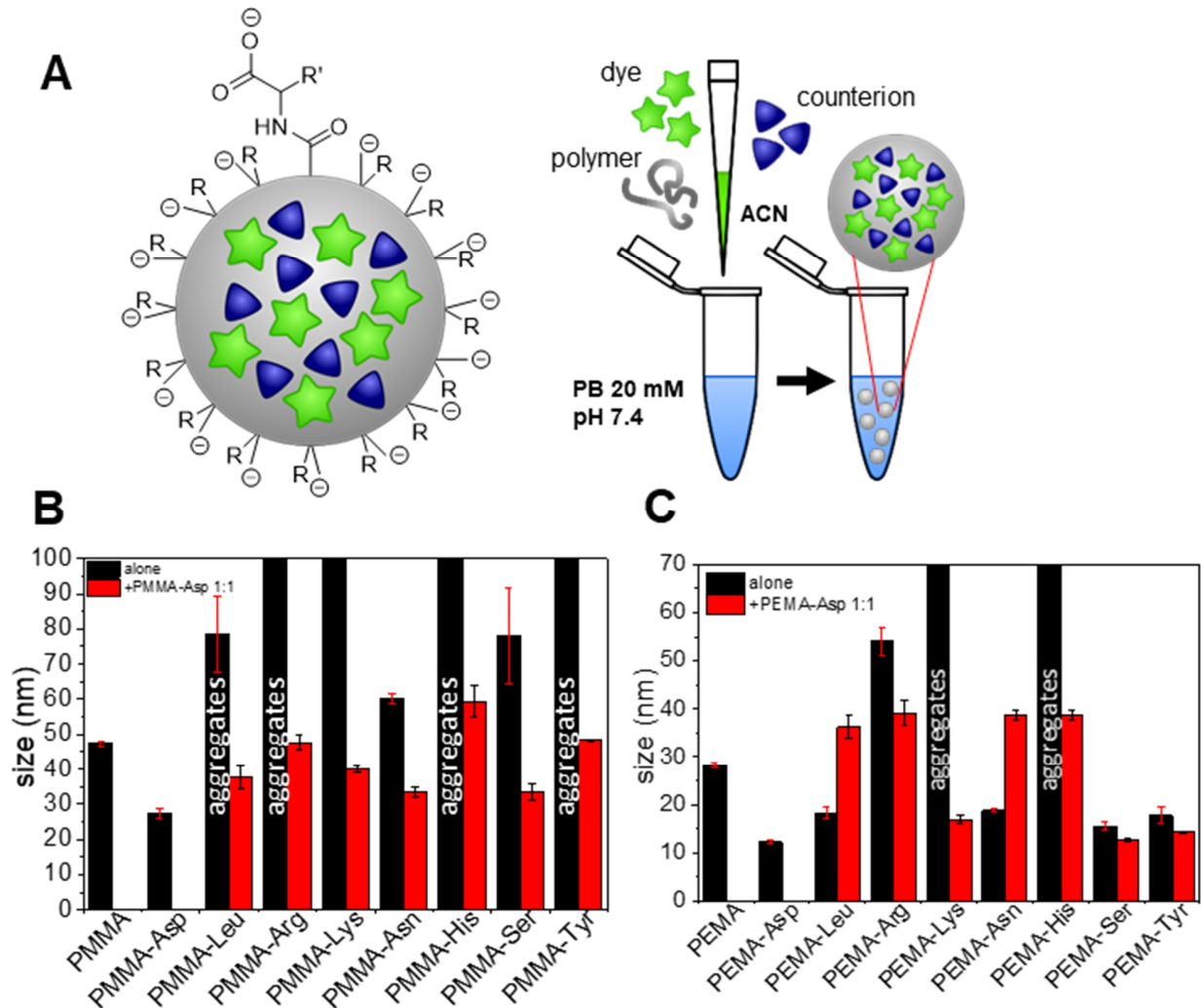


Figure 10. (A) Schéma de la surface des nanoparticules formulées avec des polymères portant des acides aminés (gauche) et schéma de préparation des nanoparticules par nanoprécipitation (gauche). Diamètres obtenu par DLS des NPs formulées avec des polymères portant des acides aminés : (B) PMMA-AA et (C) PEMA-AA.

3) Conclusions

Au cours de ce travail, nous nous sommes d'abord concentrés sur le contrôle des propriétés optiques des nanoparticules polymères chargés avec un colorant en changeant la composition chimique du cœur de la particule. Une nouvelle famille de nanoparticules fluorescentes émettrices dans le vert a été synthétisée et a été employée pour concevoir des nanosondes pour la détection

Résumé de la thèse en français

ADN assistée par smartphone. De plus, des NPs fluorescentes dopés au gadolinium ont été synthétisées. Ces systèmes montrent une bonne fluorescence et pourraient potentiellement être employés dans l'imagerie multimodale. Dans une seconde étape, nous nous sommes focalisés sur le contrôle des propriétés cibles des NPs. Ici, nous avons poursuivi une approche « classique » basée sur le greffage de PEG furtif et de groupes biologiquement actifs à la surface des NPs ainsi qu'une approche plus « motivée par la curiosité » basée sur la génération de NPs avec des surfaces complexes semblables à des protéines pour étudier leurs interactions non-spécifiques et leurs capacités de ciblage.

References

- Alivisatos, A.P., 1996. Semiconductor Clusters, Nanocrystals, and Quantum Dots. *Science* 271, 933–937. <https://doi.org/10.1126/science.271.5251.933>
- Alivisatos, P., 2004. The use of nanocrystals in biological detection. *Nature Biotechnology* 22, 47–52. <https://doi.org/10.1038/nbt927>
- Altieri, D.C., 2003. Survivin, versatile modulation of cell division and apoptosis in cancer. *Oncogene* 22, 8581–8589. <https://doi.org/10.1038/sj.onc.1207113>
- Alves, I.P., Reis, N.M., 2019. Microfluidic smartphone quantitation of *Escherichia coli* in synthetic urine. *Biosensors and Bioelectronics* 145, 111624. <https://doi.org/10.1016/j.bios.2019.111624>
- Ambrosini, S., Beyazit, S., Haupt, K., Tse Sum Bui, B., 2013. Solid-phase synthesis of molecularly imprinted nanoparticles for protein recognition. *Chemical Communications* 49, 6746. <https://doi.org/10.1039/c3cc41701h>
- Andreiuk, B., Reisch, A., Bernhardt, E., Klymchenko, A.S., 2019. Fighting Aggregation-Caused Quenching and Leakage of Dyes in Fluorescent Polymer Nanoparticles: Universal Role of Counterion. *Chemistry – An Asian Journal* 14, 836–846. <https://doi.org/10.1002/asia.201801592>
- Andreiuk, B., Reisch, A., Lindecker, M., Follain, G., Peyri ras, N., Goetz, J.G., Klymchenko, A.S., 2017a. Fluorescent Polymer Nanoparticles for Cell Barcoding In Vitro and In Vivo. *Small* 13, 1701582. <https://doi.org/10.1002/smll.201701582>
- Andreiuk, B., Reisch, A., Pivovarenko, V.G., Klymchenko, A.S., 2017b. An aluminium-based fluorinated counterion for enhanced encapsulation and emission of dyes in biodegradable polymer nanoparticles. *Materials Chemistry Frontiers* 1, 2309–2316. <https://doi.org/10.1039/C7QM00248C>
- Anselmo, A.C., Mitragotri, S., 2019. Nanoparticles in the clinic: An update. *Bioengineering & Translational Medicine* 4, e10143. <https://doi.org/10.1002/btm2.10143>
- Aparin, I.O., Melnychuk, N., Klymchenko, A.S., 2020. Ionic Aggregation-Induced Emission: Bulky Hydrophobic Counterions Light Up Dyes in Polymeric Nanoparticles. *Advanced Optical Materials* 8, 2000027. <https://doi.org/10.1002/adom.202000027>
- Arts, R., den Hartog, I., Zijlema, S.E., Thijssen, V., van der Beelen, S.H.E., Merckx, M., 2016. Detection of Antibodies in Blood Plasma Using Bioluminescent Sensor Proteins and a Smartphone. *Analytical Chemistry* 88, 4525–4532. <https://doi.org/10.1021/acs.analchem.6b00534>
- Balzani, V., Ceroni, P., Juris, A., 2014. *Photochemistry and Photophysics : Concepts, Research, Applications*. Wiley-VCH.
- Bandyopadhyay, A., McCarthy, K.A., Kelly, M.A., Gao, J., 2015. Targeting bacteria via iminoboronate chemistry of amine-presenting lipids. *Nature Communications* 6. <https://doi.org/10.1038/ncomms7561>
- Basabe-Desmonts, L., Ramstrom, S., Meade, G., O'Neill, S., Riaz, A., Lee, L.P., Ricco, A.J., Kenny, D., 2010. Single-Step Separation of Platelets from Whole Blood Coupled with Digital Quantification by Interfacial Platelet Cytometry (iPC). *Langmuir* 26, 14700–14706. <https://doi.org/10.1021/la9039682>
- Benson, C.R., Kacenauskaite, L., VanDenburgh, K.L., Zhao, W., Qiao, B., Sadhukhan, T., Pink, M., Chen, J., Borgi, S., Chen, C.-H., Davis, B.J., Simon, Y.C., Raghavachari, K., Laursen,

References

- B.W., Flood, A.H., 2020. Plug-and-Play Optical Materials from Fluorescent Dyes and Macrocycles. *Chem* 6, 1978–1997. <https://doi.org/10.1016/j.chempr.2020.06.029>
- Bernacki, R.J., Kim, U., 1977. Concomitant elevations in serum sialyltransferase activity and sialic acid content in rats with metastasizing mammary tumors. *Science* 195, 577–580. <https://doi.org/10.1126/science.835014>
- Bonacchi, S., Genovese, D., Juris, R., Montalti, M., Prodi, L., Rampazzo, E., Zaccheroni, N., 2011. Luminescent Silica Nanoparticles: Extending the Frontiers of Brightness. *Angewandte Chemie International Edition* 50, 4056–4066. <https://doi.org/10.1002/anie.201004996>
- Bonakdar, S., Mahmoudi, M., Montazeri, L., Taghipoor, M., Bertsch, A., Shokrgozar, M.A., Sharifi, S., Majidi, M., Mashinchian, O., Hamrang Sekachaei, M., Zolfaghari, P., Renaud, P., 2016. Cell-Imprinted Substrates Modulate Differentiation, Redifferentiation, and Transdifferentiation. *ACS Appl. Mater. Interfaces* 8, 13777–13784. <https://doi.org/10.1021/acsami.6b03302>
- Braeken, Y., Cheruku, S., Ethirajan, A., Maes, W., 2017. Conjugated Polymer Nanoparticles for Bioimaging. *Materials* 10, 1420. <https://doi.org/10.3390/ma10121420>
- Breslauer, D.N., Maamari, R.N., Switz, N.A., Lam, W.A., Fletcher, D.A., 2009. Mobile Phone Based Clinical Microscopy for Global Health Applications. *PLOS ONE* 4, e6320. <https://doi.org/10.1371/journal.pone.0006320>
- Brouwer, A.M., 2011. Standards for photoluminescence quantum yield measurements in solution (IUPAC Technical Report). *Pure and Applied Chemistry* 83, 2213–2228. <https://doi.org/10.1351/PAC-REP-10-09-31>
- Bwambok, D.K., El-Zahab, B., Challa, S.K., Li, M., Chandler, L., Baker, G.A., Warner, I.M., 2009. Near-Infrared Fluorescent NanoGUMBOS for Biomedical Imaging. *ACS Nano* 3, 3854–3860. <https://doi.org/10.1021/nn9010126>
- Çakir, P., Cutivet, A., Resmini, M., Bui, B.T.S., Haupt, K., 2013. Protein-Size Molecularly Imprinted Polymer Nanogels as Synthetic Antibodies, by Localized Polymerization with Multi-initiators. *Adv. Mater.* 25, 1048–1051. <https://doi.org/10.1002/adma.201203400>
- Calabria, D., Caliceti, C., Zangheri, M., Mirasoli, M., Simoni, P., Roda, A., 2017. Smartphone-based enzymatic biosensor for oral fluid L-lactate detection in one minute using confined multilayer paper reflectometry. *Biosensors and Bioelectronics* 94, 124–130. <https://doi.org/10.1016/j.bios.2017.02.053>
- Canfarotta, F., Lezina, L., Guerreiro, A., Czulak, J., Petukhov, A., Daks, A., Smolinska-Kempisty, K., Poma, A., Piletsky, S., Barlev, N.A., 2018. Specific Drug Delivery to Cancer Cells with Double-Imprinted Nanoparticles against Epidermal Growth Factor Receptor. *Nano Letters* 18, 4641–4646. <https://doi.org/10.1021/acs.nanolett.7b03206>
- Cardoso Dos Santos, M., Runser, A., Bartenlian, H., Nonat, A.M., Charbonnière, L.J., Klymchenko, A.S., Hildebrandt, N., Reisch, A., 2019. Lanthanide-Complex-Loaded Polymer Nanoparticles for Background-Free Single-Particle and Live-Cell Imaging. *Chem. Mater.* 31, 4034–4041. <https://doi.org/10.1021/acs.chemmater.9b00576>
- Chandrasekharan, N., Kelly, L.A., 2001. A Dual Fluorescence Temperature Sensor Based on Perylene/Exciplex Interconversion. *Journal of the American Chemical Society* 123, 9898–9899. <https://doi.org/10.1021/ja016153j>
- Chang, D., Kim, K.T., Lindberg, E., Winssinger, N., 2020. Smartphone DNA or RNA Sensing Using Semisynthetic Luciferase-Based Logic Device. *ACS Sensors* 5, 807–813. <https://doi.org/10.1021/acssensors.9b02454>

- Chen, G., Qiu, H., Prasad, P.N., Chen, X., 2014. Upconversion Nanoparticles: Design, Nanochemistry, and Applications in Theranostics. *Chemical Reviews* 114, 5161–5214. <https://doi.org/10.1021/cr400425h>
- Chen, L., Wang, X., Lu, W., Wu, X., Li, J., 2016. Molecular imprinting: perspectives and applications. *Chem. Soc. Rev.* 45, 2137–2211. <https://doi.org/10.1039/C6CS00061D>
- Chen, W., Yu, H., Sun, F., Ornob, A., Brisbin, R., Ganguli, A., Vemuri, V., Strzebonski, P., Cui, G., Allen, K.J., Desai, S.A., Lin, W., Nash, D.M., Hirschberg, D.L., Brooks, I., Bashir, R., Cunningham, B.T., 2017. Mobile Platform for Multiplexed Detection and Differentiation of Disease-Specific Nucleic Acid Sequences, Using Microfluidic Loop-Mediated Isothermal Amplification and Smartphone Detection. *Analytical Chemistry* 89, 11219–11226. <https://doi.org/10.1021/acs.analchem.7b02478>
- Chen, Y.-X., Huang, K.-J., Niu, K.-X., 2018. Recent advances in signal amplification strategy based on oligonucleotide and nanomaterials for microRNA detection—a review. *Biosensors and Bioelectronics* 99, 612–624. <https://doi.org/10.1016/j.bios.2017.08.036>
- Chi, J., Gao, B., Sun, M., Zhang, F., Su, E., Liu, H., Gu, Z., 2017. Patterned Photonic Nitrocellulose for Pseudopaper ELISA. *Analytical Chemistry* 89, 7727–7733. <https://doi.org/10.1021/acs.analchem.7b01732>
- Cho, S., Islas-Robles, A., Nicolini, A.M., Monks, T.J., Yoon, J.-Y., 2016. In situ, dual-mode monitoring of organ-on-a-chip with smartphone-based fluorescence microscope. *Biosensors and Bioelectronics* 86, 697–705. <https://doi.org/10.1016/j.bios.2016.07.015>
- Clerc, O., Greub, G., 2010. Routine use of point-of-care tests: usefulness and application in clinical microbiology. *Clinical Microbiology and Infection* 16, 1054–1061. <https://doi.org/10.1111/j.1469-0691.2010.03281.x>
- Coelho, M., Maghelli, N., Tolić-Nørrelykke, I.M., 2013. Single-molecule imaging *in vivo*: the dancing building blocks of the cell. *Integrative Biology* 5, 748–758. <https://doi.org/10.1039/c3ib40018b>
- Collot, M., Schild, J., Fam, K.T., Bouchaala, R., Klymchenko, A.S., 2020. Stealth and Bright Monomolecular Fluorescent Organic Nanoparticles Based on Folded Amphiphilic Polymer. *ACS Nano* 14, 13924–13937. <https://doi.org/10.1021/acsnano.0c06348>
- Coskun, A.F., Nagi, R., Sadeghi, K., Phillips, S., Ozcan, A., 2013. Albumin testing in urine using a smart-phone. *Lab Chip* 13, 4231–4238. <https://doi.org/10.1039/c3lc50785h>
- Cranfill, P.J., Sell, B.R., Baird, M.A., Allen, J.R., Lavagnino, Z., de Gruiter, H.M., Kremers, G.-J., Davidson, M.W., Ustione, A., Piston, D.W., 2016. Quantitative assessment of fluorescent proteins. *Nature Methods* 13, 557–562. <https://doi.org/10.1038/nmeth.3891>
- Dal Molin, M., Verolet, Q., Colom, A., Letrun, R., Derivery, E., Gonzalez-Gaitan, M., Vauthey, E., Roux, A., Sakai, N., Matile, S., 2015. Fluorescent Flippers for Mechanosensitive Membrane Probes. *Journal of the American Chemical Society* 137, 568–571. <https://doi.org/10.1021/ja5107018>
- Danylchuk, D.I., Jouard, P.-H., Klymchenko, A.S., 2021. Targeted Solvatochromic Fluorescent Probes for Imaging Lipid Order in Organelles under Oxidative and Mechanical Stress. *Journal of the American Chemical Society* 13.
- Daubendiek, S.L., Ryan, K., Kool, E.T., 1995. Rolling-Circle RNA Synthesis: Circular Oligonucleotides as Efficient Substrates for T7 RNA Polymerase. *J Am Chem Soc* 117, 7818–7819. <https://doi.org/10.1021/ja00134a032>
- Dennis, J., Waller, C., Timpl, R., Schirrmacher, V., 1982. Surface sialic acid reduces attachment of metastatic tumour cells to collagen type IV and fibronectin. *Nature* 300, 274–276. <https://doi.org/10.1038/300274a0>

References

- Ding, D., Li, K., Liu, B., Tang, B.Z., 2013. Bioprobes Based on AIE Fluorogens. *Accounts of Chemical Research* 46, 2441–2453. <https://doi.org/10.1021/ar3003464>
- Dong, Y., Wang, R., Li, H., Shao, J., Chi, Y., Lin, X., Chen, G., 2012. Polyamine-functionalized carbon quantum dots for chemical sensing. *Carbon* 50, 2810–2815. <https://doi.org/10.1016/j.carbon.2012.02.046>
- Duan, Y., Wu, M., Hu, D., Pan, Y., Hu, F., Liu, Xingang, Thakor, N., Ng, W.H., Liu, Xin, Sheng, Z., Zheng, H., Liu, B., 2020. Biomimetic Nanocomposites Cloaked with Bioorthogonally Labeled Glioblastoma Cell Membrane for Targeted Multimodal Imaging of Brain Tumors. *Adv. Funct. Mater.* 10.
- Dukhno, O., Przybilla, F., Muhr, V., Buchner, M., Hirsch, T., Mély, Y., 2018. Time-dependent luminescence loss for individual upconversion nanoparticles upon dilution in aqueous solution. *Nanoscale* 10, 15904–15910. <https://doi.org/10.1039/C8NR03892A>
- Egloff, S., Melnychuk, N., Reisch, A., Martin, S., Klymchenko, A.S., 2021. Enzyme-free amplified detection of cellular microRNA by light-harvesting fluorescent nanoparticle probes. *Biosensors and Bioelectronics* 179, 113084. <https://doi.org/10.1016/j.bios.2021.113084>
- Fernández-Dueñas, V., Llorente, J., Gandía, J., Borroto-Escuela, D.O., Agnati, L.F., Tasca, C.I., Fuxe, K., Ciruela, F., 2012. Fluorescence resonance energy transfer-based technologies in the study of protein–protein interactions at the cell surface. *Methods* 57, 467–472. <https://doi.org/10.1016/j.ymeth.2012.05.007>
- Floyd, D.L., Ragains, J.R., Skehel, J.J., Harrison, S.C., van Oijen, A.M., 2008. Single-particle kinetics of influenza virus membrane fusion. *Proceedings of the National Academy of Sciences* 105, 15382–15387. <https://doi.org/10.1073/pnas.0807771105>
- Fratini, A., Richards, G., Larder, E., Swavey, S., 2008. Neodymium, Gadolinium, and Terbium Complexes Containing Hexafluoroacetylacetonate and 2,2'-Bipyrimidine: Structural and Spectroscopic Characterization. *Inorg. Chem.* 47, 1030–1036. <https://doi.org/10.1021/ic701805t>
- Fuster, M.M., Esko, J.D., 2005. The sweet and sour of cancer: glycans as novel therapeutic targets. *Nature Reviews Cancer* 5, 526–542. <https://doi.org/10.1038/nrc1649>
- Geiger, W.E., Barrière, F., 2010. Organometallic Electrochemistry Based on Electrolytes Containing Weakly-Coordinating Fluoroarylborate Anions. *Accounts of Chemical Research* 43, 1030–1039. <https://doi.org/10.1021/ar1000023>
- Ghosh, K.K., Burns, L.D., Cocker, E.D., Nimmerjahn, A., Ziv, Y., Gamal, A.E., Schnitzer, M.J., 2011. Miniaturized integration of a fluorescence microscope. *Nature Methods* 8, 871–878. <https://doi.org/10.1038/nmeth.1694>
- Giepmans, B.N.G., 2006. The Fluorescent Toolbox for Assessing Protein Location and Function. *Science* 312, 217–224. <https://doi.org/10.1126/science.1124618>
- Grazon, C., Rieger, J., Charleux, B., Clavier, G., Méallet-Renault, R., 2014. Ultrabright BODIPY-Tagged Polystyrene Nanoparticles: Study of Concentration Effect on Photophysical Properties. *The Journal of Physical Chemistry C* 118, 13945–13952. <https://doi.org/10.1021/jp502790w>
- Grazon, C., Rieger, J., Méallet-Renault, R., Charleux, B., Clavier, G., 2013. Ultrabright Fluorescent Polymeric Nanoparticles Made from a New Family of BODIPY Monomers. *Macromolecules* 46, 5167–5176. <https://doi.org/10.1021/ma400590q>
- Groff, L.C., Wang, X., McNeill, J.D., 2013. Measurement of Exciton Transport in Conjugated Polymer Nanoparticles. *J. Phys. Chem. C* 117, 25748–25755. <https://doi.org/10.1021/jp407065h>

- Gubala, V., Harris, L.F., Ricco, A.J., Tan, M.X., Williams, D.E., 2012. Point of Care Diagnostics: Status and Future. *Anal. Chem.* 84, 487–515. <https://doi.org/10.1021/ac2030199>
- Guo, Y., Zhang, Y., Ma, J., Li, Q., Li, Y., Zhou, X., Zhao, D., Song, H., Chen, Q., Zhu, X., 2018. Light/magnetic hyperthermia triggered drug released from multi-functional thermo-sensitive magnetoliposomes for precise cancer synergetic theranostics. *Journal of Controlled Release* 272, 145–158. <https://doi.org/10.1016/j.jconrel.2017.04.028>
- Haidekker, M.A., Theodorakis, E.A., 2007. Molecular rotors—fluorescent biosensors for viscosity and flow. *Org. Biomol. Chem.* 5, 1669–1678. <https://doi.org/10.1039/B618415D>
- Hardman, R., 2006. A Toxicologic Review of Quantum Dots: Toxicity Depends on Physicochemical and Environmental Factors. *Environmental Health Perspectives* 114, 165–172. <https://doi.org/10.1289/ehp.8284>
- Haupt, K., Medina Rangel, P.X., Bui, B.T.S., 2020. Molecularly Imprinted Polymers: Antibody Mimics for Bioimaging and Therapy. *Chemical Reviews* 120, 9554–9582. <https://doi.org/10.1021/acs.chemrev.0c00428>
- Hildebrandt, N., Spillmann, C.M., Algar, W.R., Pons, T., Stewart, M.H., Oh, E., Susumu, K., Díaz, S.A., Delehanty, J.B., Medintz, I.L., 2017. Energy Transfer with Semiconductor Quantum Dot Bioconjugates: A Versatile Platform for Biosensing, Energy Harvesting, and Other Developing Applications. *Chem. Rev.* 117, 536–711. <https://doi.org/10.1021/acs.chemrev.6b00030>
- Hong, X., Nagarajan, V.K., Mugler, D.H., Yu, B., 2016. Smartphone microendoscopy for high resolution fluorescence imaging. *Journal of Innovative Optical Health Sciences* 09, 1650046. <https://doi.org/10.1142/S1793545816500462>
- Hong, Y., Lam, J.W.Y., Tang, B.Z., 2011. Aggregation-induced emission. *Chemical Society Reviews* 40, 5361. <https://doi.org/10.1039/c1cs15113d>
- Hossain, A., Canning, J., Ast, S., Cook, K., Rutledge, P.J., Jamalipour, A., 2015. Combined “dual” absorption and fluorescence smartphone spectrometers. *Optics Letters* 40, 1737. <https://doi.org/10.1364/OL.40.001737>
- Hosu, O., Ravalli, A., Lo Piccolo, G.M., Cristea, C., Sandulescu, R., Marrazza, G., 2017. Smartphone-based immunosensor for CA125 detection. *Talanta* 166, 234–240. <https://doi.org/10.1016/j.talanta.2017.01.073>
- Hou, L., Qin, Y., Li, J., Qin, S., Huang, Y., Lin, T., Guo, L., Ye, F., Zhao, S., 2019. A ratiometric multicolor fluorescence biosensor for visual detection of alkaline phosphatase activity via a smartphone. *Biosensors and Bioelectronics* 143, 111605. <https://doi.org/10.1016/j.bios.2019.111605>
- Howes, P.D., Chandrawati, R., Stevens, M.M., 2014. Colloidal nanoparticles as advanced biological sensors. *Science* 346, 1247390. <https://doi.org/10.1126/science.1247390>
- Hu, D., Sheng, Z., Fang, S., Wang, Y., Gao, D., Zhang, P., Gong, P., Ma, Y., Cai, L., 2014. Folate Receptor-Targeting Gold Nanoclusters as Fluorescence Enzyme Mimetic Nanoprobes for Tumor Molecular Colocalization Diagnosis. *Theranostics* 4, 142–153. <https://doi.org/10.7150/thno.7266>
- Hu, F., Li, J., Zhang, Z., Li, M., Zhao, S., Li, Z., Peng, N., 2020. Smartphone-Based Droplet Digital LAMP Device with Rapid Nucleic Acid Isolation for Highly Sensitive Point-of-Care Detection. *Analytical Chemistry* 92, 2258–2265. <https://doi.org/10.1021/acs.analchem.9b04967>
- Huang, J.-Y., Lin, H.-T., Chen, T.-H., Chen, C.-A., Chang, H.-T., Chen, C.-F., 2018. Signal Amplified Gold Nanoparticles for Cancer Diagnosis on Paper-Based Analytical Devices. *ACS Sens.* 3, 174–182. <https://doi.org/10.1021/acssensors.7b00823>

References

- Huang, X., Song, J., Yung, B.C., Huang, Xiaohua, Xiong, Y., Chen, X., 2018. Ratiometric optical nanoprobe enable accurate molecular detection and imaging. *Chem. Soc. Rev.* 47, 2873–2920. <https://doi.org/10.1039/C7CS00612H>
- Hynes, R.O., 2002. Integrins: Bidirectional, Allosteric Signaling Machines. *Cell* 110, 673–687. [https://doi.org/10.1016/S0092-8674\(02\)00971-6](https://doi.org/10.1016/S0092-8674(02)00971-6)
- Jia, M., Bandini, M., 2015. Counterion Effects in Homogeneous Gold Catalysis. *ACS Catalysis* 5, 1638–1652. <https://doi.org/10.1021/cs501902v>
- Jia, M.-Y., Wu, Q.-S., Li, H., Zhang, Y., Guan, Y.-F., Feng, L., 2015. The calibration of cellphone camera-based colorimetric sensor array and its application in the determination of glucose in urine. *Biosensors and Bioelectronics* 74, 1029–1037. <https://doi.org/10.1016/j.bios.2015.07.072>
- Jiang, Y., McNeill, J., 2017. Light-Harvesting and Amplified Energy Transfer in Conjugated Polymer Nanoparticles. *Chemical Reviews* 117, 838–859. <https://doi.org/10.1021/acs.chemrev.6b00419>
- Kamen, B., 2004. A review of folate receptor alpha cycling and 5-methyltetrahydrofolate accumulation with an emphasis on cell models in vitro. *Advanced Drug Delivery Reviews* 56, 1085–1097. <https://doi.org/10.1016/j.addr.2004.01.002>
- Kang, M.K., Mao, W., Lee, J.B., Yoo, H.S., 2017. Epidermal growth factor (EGF) fragment-guided anticancer theranostic particles for pH-responsive release of doxorubicin. *International Journal of Pharmaceutics* 519, 104–112. <https://doi.org/10.1016/j.ijpharm.2017.01.017>
- Karpenko, I.A., Collot, M., Richert, L., Valencia, C., Villa, P., Mély, Y., Hibert, M., Bonnet, D., Klymchenko, A.S., 2015. Fluorogenic Squaraine Dimers with Polarity-Sensitive Folding As Bright Far-Red Probes for Background-Free Bioimaging. *Journal of the American Chemical Society* 137, 405–412. <https://doi.org/10.1021/ja5111267>
- Karpenko, I.A., Kreder, R., Valencia, C., Villa, P., Mendre, C., Mouillac, B., Mély, Y., Hibert, M., Bonnet, D., Klymchenko, A.S., 2014. Red Fluorescent Turn-On Ligands for Imaging and Quantifying G Protein-Coupled Receptors in Living Cells. *ChemBioChem* 15, 359–363. <https://doi.org/10.1002/cbic.201300738>
- Khalin, I., Heimburger, D., Melnychuk, N., Collot, M., Groschup, B., Hellal, F., Reisch, A., Plesnila, N., Klymchenko, A.S., 2020. Ultrabright Fluorescent Polymeric Nanoparticles with a Stealth Pluronic Shell for Live Tracking in the Mouse Brain. *ACS Nano* 14, 9755–9770. <https://doi.org/10.1021/acsnano.0c01505>
- Klymchenko, A.S., 2017. Solvatochromic and Fluorogenic Dyes as Environment-Sensitive Probes: Design and Biological Applications. *Accounts of Chemical Research* 50, 366–375. <https://doi.org/10.1021/acs.accounts.6b00517>
- Klymchenko, A.S., Kreder, R., 2014. Fluorescent Probes for Lipid Rafts: From Model Membranes to Living Cells. *Chemistry & Biology* 21, 97–113. <https://doi.org/10.1016/j.chembiol.2013.11.009>
- Klymchenko, A.S., Liu, F., Collot, M., Anton, N., 2021. Dye-Loaded Nanoemulsions: Biomimetic Fluorescent Nanocarriers for Bioimaging and Nanomedicine. *Adv. Healthcare Mater.* 10, 2001289. <https://doi.org/10.1002/adhm.202001289>
- Klymchenko, A.S., Mély, Y., Demchenko, A.P., Duportail, G., 2004. Simultaneous probing of hydration and polarity of lipid bilayers with 3-hydroxyflavone fluorescent dyes. *Biochimica et Biophysica Acta (BBA) - Biomembranes* 1665, 6–19. <https://doi.org/10.1016/j.bbamem.2004.06.004>

- Knowlton, S., Joshi, A., Syrrist, P., Mastergabin, G.C., Coskun, A.F., Tasoglu, S., 2017. 3D-printed smartphone-based point of care tool for fluorescence- and magnetophoresis-based cytometry. *Lab on a Chip* 17, 2839–2851. <https://doi.org/10.1039/C7LC00706J>
- Kondo, T., Chen, W.J., Schlau-Cohen, G.S., 2017. Single-Molecule Fluorescence Spectroscopy of Photosynthetic Systems. *Chem. Rev.* 117, 860–898. <https://doi.org/10.1021/acs.chemrev.6b00195>
- Koydemir, H.C., Gorocs, Z., Tseng, D., Cortazar, B., Feng, S., Chan, R.Y.L., Burbano, J., McLeod, E., Ozcan, A., 2015. Rapid imaging, detection and quantification of *Giardia lamblia* cysts using mobile-phone based fluorescent microscopy and machine learning. *Lab on a Chip* 15, 1284–1293. <https://doi.org/10.1039/C4LC01358A>
- Koynov, K., Butt, H.-J., 2012. Fluorescence correlation spectroscopy in colloid and interface science. *Current Opinion in Colloid & Interface Science* 17, 377–387. <https://doi.org/10.1016/j.cocis.2012.09.003>
- Krossing, I., 2001. The Facile Preparation of Weakly Coordinating Anions: Structure and Characterisation of Silverpolyfluoroalkoxyaluminates $\text{AgAl}(\text{ORF})_4$, Calculation of the Alkoxide Ion Affinity. *Chemistry* 7, 490–502. [https://doi.org/10.1002/1521-3765\(20010119\)7:2<490::AID-CHEM490>3.0.CO;2-I](https://doi.org/10.1002/1521-3765(20010119)7:2<490::AID-CHEM490>3.0.CO;2-I)
- Krossing, I., Raabe, I., 2004. Noncoordinating Anions—Fact or Fiction? A Survey of Likely Candidates. *Angewandte Chemie International Edition* 43, 2066–2090. <https://doi.org/10.1002/anie.200300620>
- Kühnemund, M., Wei, Q., Darai, E., Wang, Y., Hernández-Neuta, I., Yang, Z., Tseng, D., Ahlford, A., Mathot, L., Sjöblom, T., Ozcan, A., Nilsson, M., 2017. Targeted DNA sequencing and in situ mutation analysis using mobile phone microscopy. *Nature Communications* 8. <https://doi.org/10.1038/ncomms13913>
- Kuno, M., Fromm, D.P., Hamann, H.F., Gallagher, A., Nesbitt, D.J., 2000. Nonexponential “blinking” kinetics of single CdSe quantum dots: A universal power law behavior. *The Journal of Chemical Physics* 112, 3117–3120. <https://doi.org/10.1063/1.480896>
- Lakowicz, J.R., Masters, B.R., 2008. Principles of Fluorescence Spectroscopy, Third Edition. *Journal of Biomedical Optics* 13, 029901. <https://doi.org/10.1117/1.2904580>
- Lauks, I.R., 1998. Microfabricated Biosensors and Microanalytical Systems for Blood Analysis. *Acc. Chem. Res.* 31, 317–324. <https://doi.org/10.1021/ar9700670>
- Lavis, L.D., Raines, R.T., 2008. Bright Ideas for Chemical Biology. *ACS Chemical Biology* 3, 142–155. <https://doi.org/10.1021/cb700248m>
- Lee, W.-I., Shrivastava, S., Duy, L.-T., Yeong Kim, B., Son, Y.-M., Lee, N.-E., 2017. A smartphone imaging-based label-free and dual-wavelength fluorescent biosensor with high sensitivity and accuracy. *Biosensors and Bioelectronics* 94, 643–650. <https://doi.org/10.1016/j.bios.2017.03.061>
- Li, K., Liu, B., 2014. Polymer-encapsulated organic nanoparticles for fluorescence and photoacoustic imaging. *Chem. Soc. Rev.* 43, 6570–6597. <https://doi.org/10.1039/C4CS00014E>
- Lim, S.Y., Shen, W., Gao, Z., 2015. Carbon quantum dots and their applications. *Chemical Society Reviews* 44, 362–381. <https://doi.org/10.1039/C4CS00269E>
- Lippincott-Schwartz, J., Snapp, E., Kenworthy, A., 2001. Studying protein dynamics in living cells. *Nature Reviews Molecular Cell Biology* 2, 444–456. <https://doi.org/10.1038/35073068>
- Liu, R., Cui, Q., Wang, C., Wang, X., Yang, Y., Li, L., 2017. Preparation of Sialic Acid-Imprinted Fluorescent Conjugated Nanoparticles and Their Application for Targeted Cancer Cell

References

- Imaging. *ACS Applied Materials & Interfaces* 9, 3006–3015. <https://doi.org/10.1021/acsami.6b14320>
- Liu, Y., Yang, Lou, Xu, Wu, 2011. Investigation of folate-conjugated fluorescent silica nanoparticles for targeting delivery to folate receptor-positive tumors and their internalization mechanism. *International Journal of Nanomedicine* 2023. <https://doi.org/10.2147/IJN.S24792>
- Liu, Z., Lavis, L.D., Betzig, E., 2015. Imaging Live-Cell Dynamics and Structure at the Single-Molecule Level. *Molecular Cell* 58, 644–659. <https://doi.org/10.1016/j.molcel.2015.02.033>
- Lu, W., Wang, Y., Song, S., Chen, C., Yao, B., Wang, M., 2018. A fishhook probe-based rolling circle amplification (FP-RCA) assay for efficient isolation and detection of microRNA without total RNA extraction. *The Analyst* 143, 5046–5053. <https://doi.org/10.1039/C8AN01544A>
- Luo, P.G., Sahu, S., Yang, S.-T., Sonkar, S.K., Wang, J., Wang, H., LeCroy, G.E., Cao, L., Sun, Y.-P., 2013. Carbon “quantum” dots for optical bioimaging. *Journal of Materials Chemistry B* 1, 2116. <https://doi.org/10.1039/c3tb00018d>
- Luppa, P.B., Müller, C., Schlichtiger, A., Schlebusch, H., 2011. Point-of-care testing (POCT): Current techniques and future perspectives. *TrAC Trends in Analytical Chemistry* 30, 887–898. <https://doi.org/10.1016/j.trac.2011.01.019>
- Lurje, G., Lenz, H.-J., 2009. EGFR signaling and drug discovery. *Oncology* 77, 400–410. <https://doi.org/10.1159/000279388>
- Ma, D., Duan, L., Qiu, Y., 2016. Orange-red- and white-emitting diodes fabricated by vacuum evaporation deposition of sublimable cationic iridium complexes. *J. Mater. Chem. C* 4, 5051–5058. <https://doi.org/10.1039/C6TC00738D>
- Magennis, E.P., Fernandez-Trillo, F., Sui, C., Spain, S.G., Bradshaw, D.J., Churchley, D., Mantovani, G., Winzer, K., Alexander, C., 2014. Bacteria-instructed synthesis of polymers for self-selective microbial binding and labelling. *Nature Materials* 13, 748–755. <https://doi.org/10.1038/nmat3949>
- Mahmoudi, M., Bonakdar, S., Shokrgozar, M.A., Aghaverdi, H., Hartmann, R., Pick, A., Witte, G., Parak, W.J., 2013. Cell-Imprinted Substrates Direct the Fate of Stem Cells. *ACS Nano* 7, 8379–8384. <https://doi.org/10.1021/nn403844q>
- Marchyk, N., Maximilien, J., Beyazit, S., Haupt, K., Sum Bui, B.T., 2014. One-pot synthesis of iniferter-bound polystyrene core nanoparticles for the controlled grafting of multilayer shells. *Nanoscale* 6, 2872. <https://doi.org/10.1039/c3nr05295h>
- Mashinchian, O., Bonakdar, S., Taghinejad, H., Satarifard, V., Heidari, M., Majidi, M., Sharifi, S., Peirovi, A., Saffar, S., Taghinejad, M., Abdolahad, M., Mohajezadeh, S., Shokrgozar, M.A., Rezayat, S.M., Ejtehadi, M.R., Dalby, M.J., Mahmoudi, M., 2014. Cell-Imprinted Substrates Act as an Artificial Niche for Skin Regeneration. *ACS Appl. Mater. Interfaces* 6, 13280–13292. <https://doi.org/10.1021/am503045b>
- McGonigle, A., Wilkes, T., Pering, T., Willmott, J., Cook, J., Mims, F., Parisi, A., 2018. Smartphone Spectrometers. *Sensors* 18, 223. <https://doi.org/10.3390/s18010223>
- Medintz, I.L., Uyeda, H.T., Goldman, E.R., Mattoussi, H., 2005. Quantum dot bioconjugates for imaging, labelling and sensing. *Nature Materials* 4, 435–446. <https://doi.org/10.1038/nmat1390>
- Melnychuk, N., Egloff, S., Runser, A., Reisch, A., Klymchenko, A.S., 2020. Light-Harvesting Nanoparticle Probes for FRET-Based Detection of Oligonucleotides with Single-Molecule Sensitivity. *Angewandte Chemie International Edition*. <https://doi.org/10.1002/anie.201913804>

- Melnychuk, N., Klymchenko, A.S., 2018. DNA-Functionalized Dye-Loaded Polymeric Nanoparticles: Ultrabright FRET Platform for Amplified Detection of Nucleic Acids. *Journal of the American Chemical Society* 140, 10856–10865. <https://doi.org/10.1021/jacs.8b05840>
- Michalet, X., 2005. Quantum Dots for Live Cells, in Vivo Imaging, and Diagnostics. *Science* 307, 538–544. <https://doi.org/10.1126/science.1104274>
- Miki, K., Oride, K., Inoue, S., Kuramochi, Y., Nayak, R.R., Matsuoka, H., Harada, H., Hiraoka, M., Ohe, K., 2010. Ring-opening metathesis polymerization-based synthesis of polymeric nanoparticles for enhanced tumor imaging in vivo: Synergistic effect of folate-receptor targeting and PEGylation. *Biomaterials* 31, 934–942. <https://doi.org/10.1016/j.biomaterials.2009.10.005>
- Minagawa, Y., Ueno, H., Tabata, K.V., Noji, H., 2019. Mobile imaging platform for digital influenza virus counting. *Lab on a Chip* 19, 2678–2687. <https://doi.org/10.1039/C9LC00370C>
- Mochalin, V.N., Shenderova, O., Ho, D., Gogotsi, Y., 2012. The properties and applications of nanodiamonds. *Nature Nanotechnology* 7, 11–23. <https://doi.org/10.1038/nnano.2011.209>
- Moerner, W.E., Fromm, D.P., 2003. Methods of single-molecule fluorescence spectroscopy and microscopy. *Review of Scientific Instruments* 74, 3597–3619. <https://doi.org/10.1063/1.1589587>
- Montalti, M., Prodi, L., Rampazzo, E., Zaccheroni, N., 2014. Dye-doped silica nanoparticles as luminescent organized systems for nanomedicine. *Chem. Soc. Rev.* 43, 4243–4268. <https://doi.org/10.1039/C3CS60433K>
- Müller, V., Sousa, J.M., Ceylan Koydemir, H., Veli, M., Tseng, D., Cerqueira, L., Ozcan, A., Azevedo, N.F., Westerlund, F., 2018. Identification of pathogenic bacteria in complex samples using a smartphone based fluorescence microscope. *RSC Advances* 8, 36493–36502. <https://doi.org/10.1039/C8RA06473C>
- Mullis, K., Faloona, F., Scharf, S., Saiki, R., Horn, G., Erlich, H., 1986. Specific Enzymatic Amplification of DNA In Vitro: The Polymerase Chain Reaction. *Cold Spring Harb Symp Quant Biol* 51, 263–273. <https://doi.org/10.1101/SQB.1986.051.01.032>
- Nakamura, J. (Ed.), 2006. *Image sensors and signal processing for digital still cameras*. Taylor & Francis, Boca Raton, Fla.
- Niemz, A., Ferguson, T.M., Boyle, D.S., 2011. Point-of-care nucleic acid testing for infectious diseases. *Trends in Biotechnology* 29, 240–250. <https://doi.org/10.1016/j.tibtech.2011.01.007>
- Notomi, T., Okayama, H., Masubuchi, H., Yonekawa, T., Watanabe, K., Amino, N., Hase, T., 2000. Loop-mediated isothermal amplification of DNA. *Nucleic Acids Research* 28, 7.
- Novotny, L., van Hulst, N., 2011. Antennas for light. *Nature Photonics* 5, 83–90. <https://doi.org/10.1038/nphoton.2010.237>
- Ochmann, S.E., Vietz, C., Trofymchuk, K., Acuna, G.P., Lalkens, B., Tinnefeld, P., 2017. Optical Nanoantenna for Single Molecule-Based Detection of Zika Virus Nucleic Acids without Molecular Multiplication. *Anal. Chem.* 89, 13000–13007. <https://doi.org/10.1021/acs.analchem.7b04082>
- Pan, J., Chen, W., Ma, Y., Pan, G., 2018. Molecularly imprinted polymers as receptor mimics for selective cell recognition. *Chemical Society Reviews* 47, 5574–5587. <https://doi.org/10.1039/C7CS00854F>
- Panagiotopoulou, M., Kunath, S., Medina-Rangel, P.X., Haupt, K., Tse Sum Bui, B., 2017. Fluorescent molecularly imprinted polymers as plastic antibodies for selective labeling and

References

- imaging of hyaluronan and sialic acid on fixed and living cells. *Biosensors and Bioelectronics* 88, 85–93. <https://doi.org/10.1016/j.bios.2016.07.080>
- Papkovsky, D.B., Dmitriev, R.I., 2013. Biological detection by optical oxygen sensing. *Chemical Society Reviews* 42, 8700. <https://doi.org/10.1039/c3cs60131e>
- Park, Y.I., Lee, K.T., Suh, Y.D., Hyeon, T., 2015. Upconverting nanoparticles: a versatile platform for wide-field two-photon microscopy and multi-modal in vivo imaging. *Chemical Society Reviews* 44, 1302–1317. <https://doi.org/10.1039/C4CS00173G>
- Petryayeva, E., Algar, W.R., 2015. Single-step bioassays in serum and whole blood with a smartphone, quantum dots and paper-in-PDMS chips. *The Analyst* 140, 4037–4045. <https://doi.org/10.1039/C5AN00475F>
- Petryayeva, E., Algar, W.R., 2014. Multiplexed Homogeneous Assays of Proteolytic Activity Using a Smartphone and Quantum Dots. *Analytical Chemistry* 86, 3195–3202. <https://doi.org/10.1021/ac500131r>
- Petryayeva, E., Algar, W.R., 2013. Proteolytic Assays on Quantum-Dot-Modified Paper Substrates Using Simple Optical Readout Platforms. *Analytical Chemistry* 85, 8817–8825. <https://doi.org/10.1021/ac4020066>
- Piletsky, Stanislav, Canfarotta, F., Poma, A., Bossi, A.M., Piletsky, Sergey, 2020. Molecularly Imprinted Polymers for Cell Recognition. *Trends in Biotechnology* 38, 368–387. <https://doi.org/10.1016/j.tibtech.2019.10.002>
- Poma, A., Guerreiro, A., Whitcombe, M.J., Piletska, E.V., Turner, A.P.F., Piletsky, S.A., 2013. Solid-Phase Synthesis of Molecularly Imprinted Polymer Nanoparticles with a Reusable Template-“Plastic Antibodies.” *Advanced Functional Materials* 23, 2821–2827. <https://doi.org/10.1002/adfm.201202397>
- Prasher, D.C., Eckenrode, V.K., Ward, W.W., Prendergast, F.G., Cormier, M.J., 1992. Primary structure of the *Aequorea victoria* green-fluorescent protein. *Gene* 111, 229–233. [https://doi.org/10.1016/0378-1119\(92\)90691-H](https://doi.org/10.1016/0378-1119(92)90691-H)
- Preus, S., Wilhelmsson, L.M., 2012. Advances in Quantitative FRET-Based Methods for Studying Nucleic Acids. *ChemBioChem* 13, 1990–2001. <https://doi.org/10.1002/cbic.201200400>
- Priye, A., Ball, C.S., Meagher, R.J., 2018. Colorimetric-Luminance Readout for Quantitative Analysis of Fluorescence Signals with a Smartphone CMOS Sensor. *Analytical Chemistry* 90, 12385–12389. <https://doi.org/10.1021/acs.analchem.8b03521>
- Qi, J., Liu, D., Liu, X., Guan, S., Shi, F., Chang, H., He, H., Yang, G., 2015. Fluorescent pH Sensors for Broad-Range pH Measurement Based on a Single Fluorophore. *Analytical Chemistry* 87, 5897–5904. <https://doi.org/10.1021/acs.analchem.5b00053>
- Raabe, I., Wagner, K., Guttsche, K., Wang, M., Grätzel, M., Santiso-Quiñones, G., Krossing, I., 2009. Tetraalkylammonium Salts of Weakly Coordinating Aluminates: Ionic Liquids, Materials for Electrochemical Applications and Useful Compounds for Anion Investigation. *Chemistry - A European Journal* 15, 1966–1976. <https://doi.org/10.1002/chem.200800417>
- Raj, D.B.A., Biju, S., Reddy, M.L.P., 2008. One-, Two-, and Three-Dimensional Arrays of Eu^{3+} - 4,4,5,5,5-pentafluoro-1-(naphthalen-2-yl)pentane-1,3-dione complexes: Synthesis, Crystal Structure and Photophysical Properties. *Inorg. Chem.* 47, 8091–8100. <https://doi.org/10.1021/ic8004757>
- Recommendations for the definition, estimation and use of the detection limit, 1987. . *The Analyst* 112, 199. <https://doi.org/10.1039/an9871200199>

- Reisch, A., Didier, P., Richert, L., Oncul, S., Arntz, Y., Mély, Y., Klymchenko, A.S., 2014. Collective fluorescence switching of counterion-assembled dyes in polymer nanoparticles. *Nature Communications* 5. <https://doi.org/10.1038/ncomms5089>
- Reisch, A., Heimbürger, D., Ernst, P., Runser, A., Didier, P., Dujardin, D., Klymchenko, A.S., 2018. Protein-Sized Dye-Loaded Polymer Nanoparticles for Free Particle Diffusion in Cytosol. *Advanced Functional Materials* 28, 1805157. <https://doi.org/10.1002/adfm.201805157>
- Reisch, A., Klymchenko, A.S., 2016a. Fluorescent Polymer Nanoparticles Based on Dyes: Seeking Brighter Tools for Bioimaging. *Small* 12, 1968–1992. <https://doi.org/10.1002/sml.201503396>
- Reisch, A., Klymchenko, A.S., 2016b. Fluorescent Polymer Nanoparticles Based on Dyes: Seeking Brighter Tools for Bioimaging. *Small* 12, 1968–1992. <https://doi.org/10.1002/sml.201503396>
- Reisch, A., Runser, A., Arntz, Y., Mély, Y., Klymchenko, A.S., 2015. Charge-Controlled Nanoprecipitation as a Modular Approach to Ultrasmall Polymer Nanocarriers: Making Bright and Stable Nanoparticles. *ACS Nano* 9, 5104–5116. <https://doi.org/10.1021/acs.nano.5b00214>
- Rocha-Lima, C.M., Soares, H.P., Raez, L.E., Singal, R., 2007. EGFR Targeting of Solid Tumors. *Cancer Control* 14, 295–304. <https://doi.org/10.1177/107327480701400313>
- Rochat, S., Swager, T.M., 2013. Conjugated Amplifying Polymers for Optical Sensing Applications. *ACS Appl. Mater. Interfaces* 5, 4488–4502. <https://doi.org/10.1021/am400939w>
- Roda, A., Michelini, E., Zangheri, M., Di Fusco, M., Calabria, D., Simoni, P., 2016. Smartphone-based biosensors: A critical review and perspectives. *TrAC Trends in Analytical Chemistry, Past, Present and Future challenges of Biosensors and Bioanalytical tools in Analytical Chemistry: a tribute to Prof Marco Mascini* 79, 317–325. <https://doi.org/10.1016/j.trac.2015.10.019>
- Rosenbaum, D.M., Rasmussen, S.G.F., Kobilka, B.K., 2009. The structure and function of G-protein-coupled receptors. *Nature* 459, 356–363. <https://doi.org/10.1038/nature08144>
- Runser, A., Dujardin, D., Ernst, P., Klymchenko, A.S., Reisch, A., 2020. Zwitterionic Stealth Dye-Loaded Polymer Nanoparticles for Intracellular Imaging. *ACS Appl. Mater. Interfaces* 12, 117–125. <https://doi.org/10.1021/acsami.9b15396>
- Rupp, A., Roznyatovskaya, N., Scherer, H., Beichel, W., Klose, P., Sturm, C., Hoffmann, A., Tübke, J., Koslowski, T., Krossing, I., 2014. Size Matters! On the Way to Ionic Liquid Systems without Ion Pairing. *Chem. Eur. J.* 20, 9794–9804. <https://doi.org/10.1002/chem.201400168>
- Rupp, A.B.A., Krossing, I., 2015. Ionic Liquids with Weakly Coordinating $[M^{III}(OR^F)_4]^-$ Anions. *Accounts of Chemical Research* 48, 2537–2546. <https://doi.org/10.1021/acs.accounts.5b00247>
- Schmidt, D., Stolte, M., Süß, J., Liess, A., Stepanenko, V., Würthner, F., 2019. Protein-like Enwrapped Perylene Bisimide Chromophore as a Bright Microcrystalline Emitter Material. *Angewandte Chemie International Edition* 58, 13385–13389. <https://doi.org/10.1002/anie.201907618>
- Schmied, J.J., Raab, M., Forthmann, C., Pibiri, E., Wünsch, B., Dammeyer, T., Tinnefeld, P., 2014. DNA origami-based standards for quantitative fluorescence microscopy. *Nature Protocols* 9, 1367–1391. <https://doi.org/10.1038/nprot.2014.079>

References

- Schwille, P., Bieschke, J., Oehlenschläger, F., 1997. Kinetic investigations by fluorescence correlation spectroscopy: The analytical and diagnostic potential of diffusion studies. *Biophysical Chemistry* 66, 211–228. [https://doi.org/10.1016/S0301-4622\(97\)00061-6](https://doi.org/10.1016/S0301-4622(97)00061-6)
- Sega, E.I., Low, P.S., 2008. Tumor detection using folate receptor-targeted imaging agents. *Cancer and Metastasis Reviews* 27, 655–664. <https://doi.org/10.1007/s10555-008-9155-6>
- Seifner, A., Lieberzeit, P., Jungbauer, C., Dickert, F.L., 2009. Synthetic receptors for selectively detecting erythrocyte ABO subgroups. *Analytica Chimica Acta* 651, 215–219. <https://doi.org/10.1016/j.aca.2009.08.021>
- Shinde, S., El-Schich, Z., Malakpour, A., Wan, W., Dizeyi, N., Mohammadi, R., Rurack, K., Gjörlöf Wingren, A., Sellergren, B., 2015. Sialic Acid-Imprinted Fluorescent Core–Shell Particles for Selective Labeling of Cell Surface Glycans. *Journal of the American Chemical Society* 137, 13908–13912. <https://doi.org/10.1021/jacs.5b08482>
- Shulov, I., Arntz, Y., Mély, Y., Pivovarenko, V.G., Klymchenko, A.S., 2016a. Non-coordinating anions assemble cyanine amphiphiles into ultra-small fluorescent nanoparticles. *Chemical Communications* 52, 7962–7965. <https://doi.org/10.1039/C6CC03716J>
- Shulov, I., Oncul, S., Reisch, A., Arntz, Y., Collot, M., Mely, Y., Klymchenko, A.S., 2015. Fluorinated counterion-enhanced emission of rhodamine aggregates: ultrabright nanoparticles for bioimaging and light-harvesting. *Nanoscale* 7, 18198–18210. <https://doi.org/10.1039/C5NR04955E>
- Shulov, I., Rodik, R.V., Arntz, Y., Reisch, A., Kalchenko, V.I., Klymchenko, A.S., 2016b. Protein-Sized Bright Fluorogenic Nanoparticles Based on Cross-Linked Calixarene Micelles with Cyanine Corona. *Angewandte Chemie International Edition* 55, 15884–15888. <https://doi.org/10.1002/anie.201609138>
- Shynkar, V.V., Klymchenko, A.S., Kunzelmann, C., Duportail, G., Muller, C.D., Demchenko, A.P., Freyssinet, J.-M., Mely, Y., 2007. Fluorescent Biomembrane Probe for Ratiometric Detection of Apoptosis. *Journal of the American Chemical Society* 129, 2187–2193. <https://doi.org/10.1021/ja068008h>
- Sivaraman, G., Anand, T., Chellappa, D., 2014. Pyrene based selective–ratiometric fluorescent sensing of zinc and pyrophosphate ions. *Anal. Methods* 6, 2343–2348. <https://doi.org/10.1039/C3AY42057D>
- Smith, Z.J., Chu, K., Espenson, A.R., Rahimzadeh, M., Gryshuk, A., Molinaro, M., Dwyre, D.M., Lane, S., Matthews, D., Wachsmann-Hogiu, S., 2011. Cell-Phone-Based Platform for Biomedical Device Development and Education Applications. *PLoS ONE* 6, e17150. <https://doi.org/10.1371/journal.pone.0017150>
- Snow, J.W., Ceylan Koydemir, H., Karınca, D.K., Liang, K., Tseng, D., Ozcan, A., 2019. Rapid imaging, detection, and quantification of *Nosema ceranae* spores in honey bees using mobile phone-based fluorescence microscopy. *Lab on a Chip* 19, 789–797. <https://doi.org/10.1039/C8LC01342J>
- Srinivasarao, M., Low, P.S., 2017. Ligand-Targeted Drug Delivery. *Chem. Rev.* 117, 12133–12164. <https://doi.org/10.1021/acs.chemrev.7b00013>
- Stedtfeld, R.D., Tourlousse, D.M., Seyrig, G., Stedtfeld, T.M., Kronlein, M., Price, S., Ahmad, F., Gulari, E., Tiedje, J.M., Hashsham, S.A., 2012. Gene-Z: a device for point of care genetic testing using a smartphone. *Lab on a Chip* 12, 1454. <https://doi.org/10.1039/c2lc21226a>
- Stöber, W., Fink, A., Bohn, E., 1968. Controlled growth of monodisperse silica spheres in the micron size range. *Journal of Colloid and Interface Science* 26, 62–69. [https://doi.org/10.1016/0021-9797\(68\)90272-5](https://doi.org/10.1016/0021-9797(68)90272-5)

- Stobiecka, M., Ratajczak, K., Jakiela, S., 2019. Toward early cancer detection: Focus on biosensing systems and biosensors for an anti-apoptotic protein survivin and survivin mRNA. *Biosensors and Bioelectronics* 137, 58–71. <https://doi.org/10.1016/j.bios.2019.04.060>
- Thomas, S.W., Joly, G.D., Swager, T.M., 2007. Chemical Sensors Based on Amplifying Fluorescent Conjugated Polymers. *Chemical Reviews* 107, 1339–1386. <https://doi.org/10.1021/cr0501339>
- Tian, Z., Shaller, A.D., Li, A.D.Q., 2009. Twisted perylenedyes enable highly fluorescent and photostable nanoparticles. *Chem. Commun.* 180–182. <https://doi.org/10.1039/B815507K>
- Tran, M.V., Susumu, K., Medintz, I.L., Algar, W.R., 2019. Supraparticle Assemblies of Magnetic Nanoparticles and Quantum Dots for Selective Cell Isolation and Counting on a Smartphone-Based Imaging Platform. *Analytical Chemistry* 91, 11963–11971. <https://doi.org/10.1021/acs.analchem.9b02853>
- Trofymchuk, K., Glembockyte, V., Grabenhorst, L., Steiner, F., Vietz, C., Close, C., Pfeiffer, M., Richter, L., Schütte, M.L., Selbach, F., Yaadav, R., Zähringer, J., Wei, Q., Ozcan, A., Lalkens, B., Acuna, G.P., Tinnefeld, P., 2020. Addressable Nanoantennas with Cleared Hotspots for Single-Molecule Detection on a Portable Smartphone Microscope (preprint). *Biophysics*. <https://doi.org/10.1101/2020.04.09.032037>
- Trofymchuk, K., Reisch, A., Didier, P., Frasc, F., Gilliot, P., Mely, Y., Klymchenko, A.S., 2017. Giant light-harvesting nanoantenna for single-molecule detection in ambient light. *Nature Photonics* 11, 657–663. <https://doi.org/10.1038/s41566-017-0001-7>
- Trofymchuk, K., Reisch, A., Shulov, I., Mély, Y., Klymchenko, A.S., 2014. Tuning the color and photostability of perylene diimides inside polymer nanoparticles: towards biodegradable substitutes of quantum dots. *Nanoscale* 6, 12934–12942. <https://doi.org/10.1039/C4NR03718A>
- Trofymchuk, K., Valanciunaite, J., Andreiuk, B., Reisch, A., Collot, M., Klymchenko, A.S., 2019. BODIPY-loaded polymer nanoparticles: chemical structure of cargo defines leakage from nanocarrier in living cells. *Journal of Materials Chemistry B* 7, 5199–5210. <https://doi.org/10.1039/C8TB02781A>
- Uzun, L., Turner, A.P.F., 2016. Molecularly-imprinted polymer sensors: realising their potential. *Biosensors and Bioelectronics* 76, 131–144. <https://doi.org/10.1016/j.bios.2015.07.013>
- Van Blaaderen, A., Vrij, A., 1992. Synthesis and characterization of colloidal dispersions of fluorescent, monodisperse silica spheres. *Langmuir* 8, 2921–2931. <https://doi.org/10.1021/la00048a013>
- Vashist, S.K., van Oordt, T., Schneider, E.M., Zengerle, R., von Stetten, F., Luong, J.H.T., 2015. A smartphone-based colorimetric reader for bioanalytical applications using the screen-based bottom illumination provided by gadgets. *Biosensors and Bioelectronics* 67, 248–255. <https://doi.org/10.1016/j.bios.2014.08.027>
- Wagh, A., Qian, S.Y., Law, B., 2012. Development of Biocompatible Polymeric Nanoparticles for in Vivo NIR and FRET Imaging. *Bioconjugate Chemistry* 23, 981–992. <https://doi.org/10.1021/bc200637h>
- Wang, J., Cormack, P.A.G., Sherrington, D.C., Khoshdel, E., 2003. Monodisperse, Molecularly Imprinted Polymer Microspheres Prepared by Precipitation Polymerization for Affinity Separation Applications. *Angew. Chem. Int. Ed.* 42, 5336–5338. <https://doi.org/10.1002/anie.200352298>
- Wang, N.X., von Recum, H.A., 2011. Affinity-Based Drug Delivery. *Macromol. Biosci.* 11, 321–332. <https://doi.org/10.1002/mabi.201000206>

References

- Wang, S., Zheng, L., Cai, G., Liu, N., Liao, M., Li, Y., Zhang, X., Lin, J., 2019. A microfluidic biosensor for online and sensitive detection of *Salmonella typhimurium* using fluorescence labeling and smartphone video processing. *Biosensors and Bioelectronics* 140, 111333. <https://doi.org/10.1016/j.bios.2019.111333>
- Wang, Y., Ren, S., Jiang, H., Peng, Y., Bai, J., Li, Q., Li, C., Gao, Z., Ning, B., 2017. A label-free detection of diethylstilbestrol based on molecularly imprinted polymer-coated upconversion nanoparticles obtained by surface grafting. *RSC Adv.* 7, 22215–22221. <https://doi.org/10.1039/C6RA26999K>
- Warsinke, A., Benkert, A., Scheller, F.W., 2000. Electrochemical immunoassays. *Fresenius J Anal Chem* 366, 622–634. <https://doi.org/10.1007/s002160051557>
- Watermann, A., Gieringer, R., Bauer, A.-M., Kurch, S., Kiesslich, R., Tremel, W., Gosepath, J., Brieger, J., 2019. Fluorescein- and EGFR-Antibody Conjugated Silica Nanoparticles for Enhancement of Real-time Tumor Border Definition Using Confocal Laser Endomicroscopy in Squamous Cell Carcinoma of the Head and Neck. *Nanomaterials* 9, 1378–1394. <https://doi.org/10.3390/nano9101378>
- Wei, Q., Acuna, G., Kim, S., Vietz, C., Tseng, D., Chae, J., Shir, D., Luo, W., Tinnefeld, P., Ozcan, A., 2017. Plasmonics Enhanced Smartphone Fluorescence Microscopy. *Sci Rep* 7, 1–10. <https://doi.org/10.1038/s41598-017-02395-8>
- Wei, Q., Luo, W., Chiang, S., Kappel, T., Mejia, C., Tseng, D., Chan, R.Y.L., Yan, E., Qi, H., Shabbir, F., Ozkan, H., Feng, S., Ozcan, A., 2014. Imaging and Sizing of Single DNA Molecules on a Mobile Phone. *ACS Nano* 8, 12725–12733. <https://doi.org/10.1021/nn505821y>
- Wei, Q., Qi, H., Luo, W., Tseng, D., Ki, S.J., Wan, Z., Göröcs, Z., Bentolila, L.A., Wu, T.-T., Sun, R., Ozcan, A., 2013. Fluorescent imaging of single nanoparticles and viruses on a smart phone. *ACS Nano* 7, 9147–9155. <https://doi.org/10.1021/nn4037706>
- Whitcombe, M.J., Chianella, I., Larcombe, L., Piletsky, S.A., Noble, J., Porter, R., Horgan, A., 2011. The rational development of molecularly imprinted polymer-based sensors for protein detection. *Chem. Soc. Rev.* 40, 1547–1571. <https://doi.org/10.1039/C0CS00049C>
- Wilhelmsson, L.M., 2010. Fluorescent nucleic acid base analogues. *Quarterly Reviews of Biophysics* 43, 159–183. <https://doi.org/10.1017/S0033583510000090>
- Wolfbeis, O.S., 2015. An overview of nanoparticles commonly used in fluorescent bioimaging. *Chem. Soc. Rev.* 44, 4743–4768. <https://doi.org/10.1039/C4CS00392F>
- Wöll, D., 2014. Fluorescence correlation spectroscopy in polymer science. *RSC Adv.* 4, 2447–2465. <https://doi.org/10.1039/C3RA44909B>
- Wong, M.L., Medrano, J.F., 2005. Real-time PCR for mRNA quantitation. *BioTechniques* 39, 75–85. <https://doi.org/10.2144/05391RV01>
- Wong, R.C., Tse, H.Y., 2005. *Drugs of abuse body fluid testing*. Humana Press, Totowa, N.J.
- Wong, Y.-P., Othman, S., Lau, Y.-L., Radu, S., Chee, H.-Y., 2018. Loop-mediated isothermal amplification (LAMP): a versatile technique for detection of micro-organisms. *Journal of Applied Microbiology* 124, 626–643. <https://doi.org/10.1111/jam.13647>
- Wu, C., Chiu, D.T., 2013. Highly Fluorescent Semiconducting Polymer Dots for Biology and Medicine. *Angewandte Chemie International Edition* 52, 3086–3109. <https://doi.org/10.1002/anie.201205133>
- Würth, C., Grabolle, M., Pauli, J., Spieles, M., Resch-Genger, U., 2013. Relative and absolute determination of fluorescence quantum yields of transparent samples. *Nat Protoc* 8, 1535–1550. <https://doi.org/10.1038/nprot.2013.087>

- Würth, C., Kaiser, M., Wilhelm, S., Grauel, B., Hirsch, T., Resch-Genger, U., 2017. Excitation power dependent population pathways and absolute quantum yields of upconversion nanoparticles in different solvents. *Nanoscale* 9, 4283–4294. <https://doi.org/10.1039/C7NR00092H>
- Xie, X., Gutiérrez, A., Trofimov, V., Szilagy, I., Soldati, T., Bakker, E., 2015. Charged Solvatochromic Dyes as Signal Transducers in pH Independent Fluorescent and Colorimetric Ion Selective Nanosensors. *Anal. Chem.* 87, 9954–9959. <https://doi.org/10.1021/acs.analchem.5b02566>
- Xiong, L., Chen, Z., Tian, Q., Cao, T., Xu, C., Li, F., 2009. High Contrast Upconversion Luminescence Targeted Imaging in Vivo Using Peptide-Labeled Nanophosphors. *Anal. Chem.* 81, 8687–8694. <https://doi.org/10.1021/ac901960d>
- Xu, H., Xia, A., Wang, D., Zhang, Y., Deng, S., Lu, W., Luo, J., Zhong, Q., Zhang, F., Zhou, L., Zhang, W., Wang, Y., Yang, C., Chang, K., Fu, W., Cui, J., Gan, M., Luo, D., Chen, M., 2020. An ultraportable and versatile point-of-care DNA testing platform. *Science Advances* 6, eaaz7445. <https://doi.org/10.1126/sciadv.aaz7445>
- Xu, W., Lu, S., Chen, Y., Zhao, T., Jiang, Y., Wang, Y., Chen, X., 2015. Simultaneous color sensing of O₂ and pH using a smartphone. *Sensors and Actuators B: Chemical* 220, 326–330. <https://doi.org/10.1016/j.snb.2015.05.088>
- Yan, L., Zhou, J., Zheng, Y., S. Gamson, A., T. Roembke, B., Nakayama, S., O. Sintim, H., 2014. Isothermal amplified detection of DNA and RNA. *Molecular BioSystems* 10, 970–1003. <https://doi.org/10.1039/C3MB70304E>
- Yang, Y., Niu, H., Zhang, H., 2016. Direct and Highly Selective Drug Optosensing in Real, Undiluted Biological Samples with Quantum-Dot-Labeled Hydrophilic Molecularly Imprinted Polymer Microparticles. *ACS Applied Materials & Interfaces* 8, 15741–15749. <https://doi.org/10.1021/acsami.6b04176>
- Yang, Y.-K., Cho, H.J., Lee, J., Shin, I., Tae, J., 2009. A Rhodamine–Hydroxamic Acid-Based Fluorescent Probe for Hypochlorous Acid and Its Applications to Biological Imagings. *Organic Letters* 11, 859–861. <https://doi.org/10.1021/ol802822t>
- Yang, Z., Cao, J., He, Y., Yang, J.H., Kim, T., Peng, X., Kim, J.S., 2014. Macro-/micro-environment-sensitive chemosensing and biological imaging. *Chem. Soc. Rev.* 43, 4563–4601. <https://doi.org/10.1039/C4CS00051J>
- Yao, H., Ashiba, K., 2011. Highly fluorescent organic nanoparticles of thiocyanine dye: A synergetic effect of intermolecular H-aggregation and restricted intramolecular rotation. *RSC Adv.* 1, 834. <https://doi.org/10.1039/c1ra00497b>
- Ye, L., Cormack, P.A.G., Mosbach, K., 1999. Molecularly imprinted monodisperse microspheres for competitive radioassay. *Analytical Communications* 36, 35–38. <https://doi.org/10.1039/a809014i>
- Yetisen, A.K., Akram, M.S., Lowe, C.R., 2013. Paper-based microfluidic point-of-care diagnostic devices. *Lab Chip* 13, 2210–2251. <https://doi.org/10.1039/C3LC50169H>
- Yetisen, A.K., Jiang, N., Tamayol, A., Ruiz-Esparza, G.U., Zhang, Y.S., Medina-Pando, S., Gupta, A., Wolffsohn, J.S., Butt, H., Khademhosseini, A., Yun, S.-H., 2017. Paper-based microfluidic system for tear electrolyte analysis. *Lab on a Chip* 17, 1137–1148. <https://doi.org/10.1039/C6LC01450J>
- Yu, H., Tan, Y., Cunningham, B.T., 2014. Smartphone Fluorescence Spectroscopy. *Analytical Chemistry* 86, 8805–8813. <https://doi.org/10.1021/ac502080t>

References

- Yu, Q., Xue, L., Hiblot, J., Griss, R., Fabritz, S., Roux, C., Binz, P.-A., Haas, D., Okun, J.G., Johnsson, K., 2018. Semisynthetic sensor proteins enable metabolic assays at the point of care. *Science* 361, 1122–1126. <https://doi.org/10.1126/science.aat7992>
- Zaki, N.M., Tirelli, N., 2010. Gateways for the intracellular access of nanocarriers: a review of receptor-mediated endocytosis mechanisms and of strategies in receptor targeting. *Expert Opinion on Drug Delivery* 7, 895–913. <https://doi.org/10.1517/17425247.2010.501792>
- Zeinhom, M.M.A., Wang, Y., Song, Y., Zhu, M.-J., Lin, Y., Du, D., 2018. A portable smart-phone device for rapid and sensitive detection of *E. coli* O157:H7 in Yoghurt and Egg. *Biosensors and Bioelectronics* 99, 479–485. <https://doi.org/10.1016/j.bios.2017.08.002>
- Zeng, Z., Hoshino, Y., Rodriguez, A., Yoo, H., Shea, K.J., 2010. Synthetic Polymer Nanoparticles with Antibody-like Affinity for a Hydrophilic Peptide. *ACS Nano* 4, 199–204. <https://doi.org/10.1021/nn901256s>
- Zhai, X., Zhang, P., Liu, C., Bai, T., Li, W., Dai, L., Liu, W., 2012. Highly luminescent carbon nanodots by microwave-assisted pyrolysis. *Chemical Communications* 48, 7955. <https://doi.org/10.1039/c2cc33869f>
- Zhang, B., Soleimaninejad, H., Jones, D.J., White, J.M., Ghiggino, K.P., Smith, T.A., Wong, W.W.H., 2017. Highly Fluorescent Molecularly Insulated Perylene Diimides: Effect of Concentration on Photophysical Properties. *Chem. Mater.* 29, 8395–8403. <https://doi.org/10.1021/acs.chemmater.7b02968>
- Zhang, D., Liu, Q., 2016. Biosensors and bioelectronics on smartphone for portable biochemical detection. *Biosensors and Bioelectronics* 75, 273–284. <https://doi.org/10.1016/j.bios.2015.08.037>
- Zhang, Xiaoyong, Wang, K., Liu, M., Zhang, Xiqi, Tao, L., Chen, Y., Wei, Y., 2015. Polymeric AIE-based nanoprobe for biomedical applications: recent advances and perspectives. *Nanoscale* 7, 11486–11508. <https://doi.org/10.1039/C5NR01444A>
- Zhang, Xiqi, Zhang, Xiaoyong, Tao, L., Chi, Z., Xu, J., Wei, Y., 2014. Aggregation induced emission-based fluorescent nanoparticles: fabrication methodologies and biomedical applications. *Journal of Materials Chemistry B* 2, 4398. <https://doi.org/10.1039/c4tb00291a>
- Zhang, Y., Li, S., Ma, X.-T., He, X.-W., Li, W.-Y., Zhang, Y.-K., 2020. Carbon dots-embedded epitope imprinted polymer for targeted fluorescence imaging of cervical cancer via recognition of epidermal growth factor receptor. *Microchim Acta* 187, 228. <https://doi.org/10.1007/s00604-020-4198-7>
- Zhao, M., Deng, Z., Tang, J., Zhou, X., Chen, Z., Li, X., Yang, L., Ma, L.-J., 2016. 2-(1-Pyrenyl) benzimidazole as a ratiometric and “turn-on” fluorescent probe for iron(III) ions in aqueous solution. *The Analyst* 141, 2308–2312. <https://doi.org/10.1039/C5AN02565F>
- Zhou, B., Shi, B., Jin, D., Liu, X., 2015. Controlling upconversion nanocrystals for emerging applications. *Nature Nanotechnology* 10, 924–936. <https://doi.org/10.1038/nnano.2015.251>
- Zhu, H., Mavandadi, S., Coskun, A.F., Yaglidere, O., Ozcan, A., 2011. Optofluidic Fluorescent Imaging Cytometry on a Cell Phone. *Analytical Chemistry* 83, 6641–6647. <https://doi.org/10.1021/ac201587a>
- Zhu, H., Sikora, U., Ozcan, A., 2012. Quantum dot enabled detection of *Escherichia coli* using a cell-phone. *The Analyst* 137, 2541. <https://doi.org/10.1039/c2an35071h>

List of publications

Severi, C., Melnychuk, N. & Klymchenko, A. S. Smartphone-assisted detection of nucleic acids by light-harvesting FRET-based nanoprobe. *Biosensors and Bioelectronics* 168, 112515 (2020). DOI: 10.1016/j.bios.2020.112515

Khalin, I., Severi, C., Heimbürger, D., Wehn, A., Hellal, F., Reisch, A., Klymchenko, A. S. & Plesnila, N. Highly fluorescent biodegradable PLGA nano-carriers allow real-time tracking of individual particles in vivo. *BioRxiv*. DOI : doi.org/10.1101/2020.11.19.385062

List of presentations

Severi C., Melnychuk N., Klymchenko A. S. Synthesis and characterization of new organic nanoantennas for FRET-based molecular detection. Journées Campus Illkirch 2018, 15-16 May 2018, Illkirch-Graffenstaden, France. (Poster)

Severi C., Melnychuk N., Klymchenko A. S. Synthesis and characterization of new organic nanoantennas for FRET-based detection of nucleic acids by RGB camera. Journées Campus Illkirch 2019, 1-2 April 2019, Illkirch-Graffenstaden, France (poster)

Severi C., Klymchenko A. S., Bright fluorescent probes for bioimaging based on dyes and nanoparticles. 102nd Canadian Chemistry Conference and Exhibition (CCCE 2019), 3-7 June 2019, Québec City, Canada. (Oral presentation)

Severi C., Melnychuk N., Klymchenko A. S. New organic nanoantennas for FRET-based detection of nucleic acids. 16th conference on Methods and Applications in Fluorescence (MAF 2019), 20-24 August 2019, La Jolla, California, United States. (Poster)

Severi C., Imai M., Karpenko I., Melnychuk N., Bonnet D., Reisch A., Niko Y., Klymchenko A. S., Ultrabright fluorescent dye-loaded polymeric nanoparticles for targeting lipids and proteins. The SFNano – Cnano joint meeting 2019. 10-12 December 2019, Dijon, France. (Poster)

Synthèse de nanoparticules polymères fluorescentes récolteuses de lumière et leurs applications dans la biodétection et la bioimagerie

Résumé

La présente étude porte sur le développement de nouvelles nanoparticules (NPs) polymères fluorescentes récolteuses de lumière. D'une part, nous ciblons l'amélioration des propriétés photophysiques de ces systèmes : (i) de nouveaux colorants ont été testés, créant des nanoparticules émettrices dans le vert permettant la préparation de capteurs ADN compatibles avec la caméra RGB de smartphone, (ii) de nouveaux contre-ions contenant des lanthanides ont été testés, créant une potentielle plateforme d'imagerie multimodal couplant l'utilisation de fluorophores avec la diffusion d'électrons. D'autre part, nous avons cherché à obtenir des NPs avec des propriétés de ciblage via les approches suivantes : (i) La greffe de groupes de ciblage à la surface des NPs et (ii) la conjugaison de groupes d'acides aminés aux polymères puis l'utilisation de ces polymères dans la formulation de nanoparticules afin d'obtenir des NPs avec une surface similaire aux protéines.

Mots-clés : nanoparticules polymères fluorescents, nano-antennes récolteuses de lumière, nanoparticules ciblant

Résumé en anglais

The present work focuses on developing new polymer-based fluorescent nanoantennas. On the one hand, we aimed to improve the photophysical properties of these systems: (i) new dyes were tested, creating a new family of green-emitting nanoparticles, which allowed the preparation of a DNA-sensor compatible with and the RGB camera of a smartphone, (ii) new lanthanide-based counterions were tested, synthesizing a potentially multimodal imaging platform, which couples fluorescent dyes with electron-scattering heavy atom complex. On the other hand, we aimed to control targeting properties of NP by two approaches: (i) grafting targeting groups on the NPs surface, and (ii) conjugating amino-acid groups to polymers and using the as-synthesized polymers in nanoparticle formulation, thus obtaining NPs with a protein-like surface.

Keywords : fluorescent polymeric nanoparticles, light-harvesting nanoantennas, targeting nanoparticles